energies

Special Issue Reprint

Solar Energy and Resource Utilization

2nd Edition

Edited by
Fabio Montagnaro and Roberto Solimene

mdpi.com/journal/energies

MDPI

Solar Energy and Resource Utilization—2nd Edition

Solar Energy and Resource Utilization—2nd Edition

Guest Editors

Fabio Montagnaro
Roberto Solimene

MDPI

Basel • Beijing • Wuhan • Barcelona • Belgrade • Novi Sad • Cluj • Manchester

Guest Editors

Fabio Montagnaro
Department of Chemical Sciences
University of Naples Federico II
Naples
Italy

Roberto Solimene
Institute of Sciences and Technologies for Sustainable Energy and Mobility (STEMS)
National Research Council (CNR)
Napoli
Italy

Editorial Office
MDPI AG
Grosspeteranlage 5
4052 Basel, Switzerland

This is a reprint of the Special Issue, published open access by the journal *Energies* (ISSN 1996-1073), freely accessible at: https://www.mdpi.com/journal/energies/special_issues/KHV4SW8WF5.

For citation purposes, cite each article independently as indicated on the article page online and as indicated below:

Lastname, A.A.; Lastname, B.B. Article Title. *Journal Name* **Year**, *Volume Number*, Page Range.

ISBN 978-3-7258-8707-1 (Hbk)
ISBN 978-3-7258-8708-8 (PDF)
https://doi.org/10.3390/books978-3-7258-8708-8

© 2026 by the authors. Articles in this reprint are Open Access and distributed under the Creative Commons Attribution (CC BY) license. The reprint as a whole is distributed by MDPI under the terms and conditions of the Creative Commons Attribution-NonCommercial-NoDerivs (CC BY-NC-ND) license (https://creativecommons.org/licenses/by-nc-nd/4.0/).

Contents

About the Editors . . . . . **vii**

Fabio Montagnaro and Roberto Solimene
Solar Energy and Resource Utilization—2nd Edition
Reprinted from: *Energies* **2026**, *19*, 3283, https://doi.org/10.3390/en19143283 . . . . . **1**

MyeongSeob Sim, Yejin Gu, Donghwan Kim and Yoonmook Kang
Unveiling the Hydrogen Diffusion During Degradation of Silicon Solar Cells
Reprinted from: *Energies* **2025**, *18*, 3090, https://doi.org/10.3390/en18123090 . . . . . **4**

Martin Beer and Radim Rybár
Enhancing Solar Thermal Energy Storage via Torsionally Modified TPMS Structures Embedded in Sodium Acetate Trihydrate
Reprinted from: *Energies* **2025**, *18*, 3234, https://doi.org/10.3390/en18133234 . . . . . **16**

Byeong-Hwa An, Kwang-Am Moon, Seong-Bhin Kim and Hwi-Ung Choi
Analysis of Heat Transfer and Fluid Flow in a Solar Air Heater with Sequentially Placed Rectangular Obstacles on the Fin Surface
Reprinted from: *Energies* **2025**, *18*, 3811, https://doi.org/10.3390/en18143811 . . . . . **33**

Pawel Znaczko, Norbert Chamier-Gliszczynski and Kazimierz Kaminski
Experimental Study of Solar Hot Water Heating System with Adaptive Control Strategy
Reprinted from: *Energies* **2025**, *18*, 3904, https://doi.org/10.3390/en18153904 . . . . . **47**

Mamadou Sow and Lavinia Grosu
Energy and Exergy Assessment of a Solar Driven Single Effect H_2O-LiBr Absorption Chiller Under Moderate and Hot Climatic Conditions
Reprinted from: *Energies* **2025**, *18*, 4553, https://doi.org/10.3390/en18174553 . . . . . **65**

Krishan Chopra, M. K. Shah, K. R. Niazi, Gulshan Sharma and Pitshou N. Bokoro
Optimizing Solar-Powered EV Charging: A Techno-EconomicAssessment Using Horse Herd Optimization
Reprinted from: *Energies* **2025**, *18*, 4556, https://doi.org/10.3390/en18174556 . . . . . **86**

Akash Kumar, Nijanth Kothandapani, Sai Tatapudi, Sagar Bhoite and GovindaSamy TamizhMani
Height-Dependent Inter-Array Temperature Difference and Position-Dependent Intra-Array Temperature Gradient
Reprinted from: *Energies* **2026**, *19*, 111, https://doi.org/10.3390/en19010111 . . . . . **108**

Marian Kampik, Krzysztof Bodzek, Arkadiusz Domoracki and Grzegorz Jarek
Instantaneous Power Generation of Monofacial and Bifacial Photovoltaic Modules Under Tracker-Induced Albedo Variations
Reprinted from: *Energies* **2026**, *19*, 2641, https://doi.org/10.3390/en19112641 . . . . . **119**

About the Editors

Fabio Montagnaro

Fabio Montagnaro is a Full Professor in Chemical Plants at the University of Naples Federico II, Italy. His main research interests are: chemical processes in fluidised bed reactors; thermochemical solar energy storage; reactivation aimed at the re-use of solid wastes of different nature; solids (e.g., traditional and biomass) thermoconversion processes aimed at the production of energy, with removal of pollutants (e.g., CO_2, SO_2); synthesis of non-traditional binders; liquid–solid and gas–solid adsorption processes; and design and modelling of chemical reactors and plants, investigated within international and national projects and collaboration networks. He served as Chair and Member of the Scientific Committee for International Conferences, and is the Italian Delegate to the European Federation of Chemical Engineering (Working Party on Comminution and Classification).

Roberto Solimene

Roberto Solimene is a Senior Researcher at the Institute of Sciences and Technologies for Sustainable Energy and Mobility, National Research Council, Naples, Italy. His main research interests are: combustion, gasification and pyrolysis of solid fuels with a high content of volatile materials; development of new configurations of multiple fluidised bed systems aimed at chemical looping with oxygen uncoupling process; and development of new fluidised bed configurations aimed at converting concentrated solar energy into electrical energy and/or materials (chemical storage, solar fuels), investigated within international and national projects and collaboration networks. He is a Member of the Board of the Italian Section of the Combustion Institute, and the Italian Member of the SolarPACES International Particle Technology Working Group. He has participated in international conferences as a plenary and keynote speaker.

energies

MDPI

Editorial

Solar Energy and Resource Utilization—2nd Edition

Fabio Montagnaro [1,*] and Roberto Solimene [2]

[1] Department of Chemical Sciences, University of Naples Federico II, 80126 Naples, Italy
[2] Institute of Sciences and Technologies for Sustainable Energy and Mobility (STEMS), National Research Council (CNR), 80125 Naples, Italy; roberto.solimene@stems.cnr.it
* Correspondence: fabio.montagnaro@unina.it

The ongoing global energy transition places solar energy at the centre of an increasingly diversified portfolio of low-carbon technologies. Reducing greenhouse gas emissions is not only a scientific imperative but a socio-political priority, shaping investment flows and research agendas. Concentrating solar power, photovoltaic conversion, and solar thermal systems are converging towards higher efficiencies, smarter controls, and deeper integration with energy storage and end-use sectors [1–7]. This Second Edition of the Special Issue "Solar Energy and Resource Utilization" collects eight contributions that, taken together, trace a coherent arc spanning from the materials and component level up to full system integration and application, offering a panoramic view of where solar energy research stands and where it is headed.

The first cluster of contributions addresses solar thermal energy collection and storage, which remains a cornerstone challenge: efficiently harvesting solar heat and retaining it beyond the hours of irradiation. For example, the thermo-hydraulic performance of a solar air heater featuring sequentially placed rectangular obstacles on finned surfaces is investigated using computational fluid dynamics. Studies quantify the interplay between heat transfer enhancement and the inevitable pressure penalty introduced by the obstacles, identifying the optimal obstacle height-to-pitch ratio that maximises the thermo-hydraulic performance factor. The derived correlations for the Nusselt number and friction factor provide practical design tools for engineers seeking to upgrade solar air heaters without resorting to complex or costly modifications. At a different scale, researchers address latent heat storage using sodium acetate trihydrate as a phase change material. The work highlights the growing synergy between advanced additive manufacturing and thermal energy storage engineering, opening a promising route towards compact, high-performance storage units compatible with solar thermal systems.

A second cluster examines photovoltaic energy conversion at both the cell and array levels. Authors probe the mechanisms of light- and elevated-temperature-induced degradation in monocrystalline passivated emitter rear contact silicon solar cells. By directly tracking hydrogen redistribution within the silicon wafer using dynamic secondary ion mass spectrometry and correlating it with carrier lifetime measurements and quantum efficiency spectra, the authors identify hydrogen diffusion as a primary driver. Moving from the cell to the array, scholars have conducted a controlled field experiment in a hot, arid desert environment to disentangle two geometric effects that are often conflated in the literature: the inter-array temperature difference arising from mounting height, and the intra-array edge-to-centre thermal gradient along a single-row configuration. Results have direct implications for racking design and thermal performance modelling in climates where natural convection governs module cooling. In another paper, authors add a further

spatial dimension by examining the instantaneous power output of bifacial versus monofacial modules installed on a single-axis tracking platform over five distinct ground surfaces. Albedo is shown to be neither constant nor spatially homogeneous. The work challenges the assumption of a fixed albedo coefficient embedded in most simulation tools and calls for spatially resolved albedo characterisation.

A third cluster turns to solar energy utilisation in thermal end-use applications. Researchers propose and experimentally validate an adaptive control strategy for a solar hot water heating system that dynamically selects among three control modes, based on a real-time daily classification of solar irradiance conditions into four categories. The result underscores the value of intelligent control even within relatively simple solar thermal installations, where weather-aware decision logic can significantly outperform fixed-parameter strategies. Other authors broaden the climatic scope by performing an energy and exergy analysis of a single-effect H_2O-LiBr absorption chiller driven by solar thermal collectors, comparing performance under moderate and hot conditions of different geographical areas. Optimal operating temperatures substantially differ between the two climates, a finding of practical importance as solar cooling technologies expand simultaneously towards regions with the highest cooling demand and the highest solar resource.

Completing the picture, researchers address the integration of solar photovoltaics with electric vehicle charging infrastructure, a nexus that is rapidly gaining prominence as both technologies scale. Using a population-based metaheuristic that outperforms both genetic algorithms and particle swarm optimisation, the study simultaneously optimises the siting of residential, commercial, and industrial fast-charging stations and the sizing of rooftop photovoltaic systems.

Taken as a whole, the eight papers collected in this Special Issue illustrate the breadth and vitality of contemporary solar energy research. The contributions span length scales from the nanometre-level hydrogen profile in a silicon wafer to the system-level optimisation of a multi-node distribution grid; they investigate methods from computational fluid dynamics and numerical thermal analysis to field experiments and metaheuristic optimisation; and they address applications from building heating and cooling to electric mobility. Several cross-cutting themes emerge and deserve further investigation. The role of material innovation (whether in phase change materials, silicon passivation layers, or solar collector geometries) continues to be pivotal. Intelligent, weather-aware control is proving its worth across both photovoltaic and solar thermal systems. Spatial heterogeneity, whether of albedo, temperature, or irradiance, cannot be neglected at the system level. And the coupling of solar energy with storage and with demand-side technologies such as electric vehicles is reshaping the boundaries of what solar research must encompass. We trust that Readers will find in these contributions both rigorous engineering insights and inspiration for future lines of investigation.

Author Contributions: F.M. and R.S. have equally contributed to the writing of this editorial. All authors have read and agreed to the published version of the manuscript.

Conflicts of Interest: The authors declare no conflict of interest.

References

1. Di Lauro, F.; Tregambi, C.; Montagnaro, F.; Molignano, L.; Salatino, P.; Solimene, R. Influence of fluidised bed inventory on the performance of limestone sorbent in calcium looping for thermochemical energy storage. *Energies* **2023**, *16*, 6942. [CrossRef]
2. Behar, O. Solar thermal power plants—A review of configurations and performance comparison. *Renew. Sustain. Energy Rev.* **2018**, *92*, 608–627. [CrossRef]
3. Green, M.A.; Dunlop, E.D.; Yoshita, M.; Kopidakis, N.; Bothe, K.; Siefer, G.; Hao, X.; Jiang, J.Y. Solar cell efficiency tables (version 65). *Prog. Photovolt. Res. Appl.* **2025**, *33*, 3–15. [CrossRef]

https://doi.org/10.3390/en19143283

4. Kwasi-Effaha, C.C.; Okpako, O. Comprehensive review of emerging trends in thermal energy storage mechanisms, materials and applications. *Front. Energy Res.* **2025**, *13*, 1651471. [CrossRef]
5. Adeyinka, A.M.; Esan, O.C.; Ijaola, A.O.; Farayibi, P.K. Advancements in hybrid energy storage systems for enhancing renewable energy-to-grid integration. *Sustain. Energy Res.* **2024**, *11*, 26. [CrossRef]
6. Deng, Z.; Zhu, B.; Davis, S.J.; Ciais, P.; Guan, D.; Gong, P.; Liu, Z. Global carbon emissions and decarbonization in 2024. *Nat. Rev. Earth Environ.* **2025**, *6*, 231–233. [CrossRef]
7. Wen, Y.; Wu, J.; Lin, P.; Low, Y.M. The role of offshore wind and solar PV resources in global low-carbon transition. *Sci. Adv.* **2025**, *11*, eadx5580. [CrossRef] [PubMed]

Disclaimer/Publisher's Note: The statements, opinions and data contained in all publications are solely those of the individual author(s) and contributor(s) and not of MDPI and/or the editor(s). MDPI and/or the editor(s) disclaim responsibility for any injury to people or property resulting from any ideas, methods, instructions or products referred to in the content.

https://doi.org/10.3390/en19143283

energies

MDPI

Article

Unveiling the Hydrogen Diffusion During Degradation of Silicon Solar Cells

MyeongSeob Sim [1], Yejin Gu [1], Donghwan Kim [1] and Yoonmook Kang [2,*]

[1] Department of Materials Science and Engineering, Korea University, Seoul 02841, Republic of Korea; audtjq03@korea.ac.kr (M.S.); 99yejin5s@korea.ac.kr (Y.G.); solar@korea.ac.kr (D.K.)
[2] Graduate School of Energy and Environment, Korea University, Seoul 02841, Republic of Korea
* Correspondence: ddang@korea.ac.kr

Abstract: We investigated monocrystalline passivated emitter rear contact cells for light- and elevated-temperature-induced degradation. Among the cell performance factors, a short current density results in a significant decrease in the short term. The quantum efficiency is also affected by carrier recombination-active defects, especially in the case of the reference cell, which has a decreased quantum efficiency across the wavelength, unlike the commercial cell. The front side of the cell has a diffuse hydrogen distribution, and it is related to LeTID. We observe how the hydrogen changes during each process and the changes in the profile during the degradation. The hydrogen appears to redistribute within the silicon wafer and saturate at a certain equilibrium state. The hydrogen distribution is correlated with the changes in the lifetime and, finally, short current density. Regeneration occurs depending on the hydrogen concentration within the emitter, and the closer the concentration is to saturation, the less degradation occurs.

Keywords: hydrogen; silicon; diffusion; carrier induced degradation; solar cell

1. Introduction

Photovoltaic (PV) energy is the fastest-growing renewable energy, accounting for more than 80% of the newly increased renewable energy production as of 2024 [1]. Among them, crystalline silicon-based solar cells account for 97% of the total PV energy portion, with high conversion efficiency and stability [2]. Over the past 30 years, the efficiency of crystalline silicon solar cells has increased by 3%p [3], but the efficiency decreases due to degradation during outdoor operation of solar cells by up to 3%p (~12.7%rel) [4]. The efficiency of solar cells decreases during operation due to many degradation phenomena, such as light-induced degradation (LID), light- and elevated-temperature-induced degradation (LeTID), and potential-induced degradation (PID) [5,6]. LeTID, which has recently attracted attention, occurs in almost all types of wafers [7–10], and the cause is believed to be hydrogen diffused during the process [7,11–19]. However, as the wafer thickness has decreased [20] and the wafer characteristics improved [21], the degradation was significantly reduced, and in particular, it has been almost eliminated through the firing process [22–29]. Recently, it has also been reported that LeTID and surface degradation are almost non-existent below a certain hydrogen amount [30]. However, as LeTID was found in the LID experiment [31], it is important to clearly understand the LeTID mechanism. It was mainly studied in a p-type silicon PERC cell, and degradation occurred in all factors of V_{oc}, J_{sc}, and FF [11,32–35]. The decrease in FF and J_{sc} is notable [24], and in the case of J_{sc},

there was a decrease in both short-wavelength and long-wavelength quantum efficiency (QE) [21,32]. Therefore, we can see that the defect of LeTID is close to the front and back surfaces, which is related to the passivation layer [9,36].

Therefore, in this study, we compared J_{sc}, which mostly changes the solar cells' factor, before and after degradation through QE analysis and compared the difference between commercial cells, that is, cells with and without the Anti-LeTID process. We confirmed the location of the LeTID phenomenon at the cell level by wavelength range. By directly observing how the hydrogen near the surface behaves in a degradation environment, we identified a more fundamental principle of LeTID. We analyzed when hydrogen diffusion occurs during the solar cell manufacturing process and how the hydrogen profile changes in a degradation environment by comparing it with the carrier lifetime. Through the relationship between hydrogen and degradation, the relationship between the current LeTID removal method and the hydrogen profile can be identified, which can be an important clue to a more comprehensive understanding of degradation and hydrogen.

2. Experimental Section

2.1. Sample Preparation

The Czochralski (Cz) boron-doped Si wafer is M2-size (156.75 × 156.75 mm) with similar resistivity (2.2 ± 0.2 Ω·cm). The wafers had a thickness of 180 ± 5 μm. The saw damage etching is performed by KOH solution before the RCA cleaning process. Subsequently, the wafers were placed in a furnace tube with a high temperature (870 °C, $POCl_3$ and O_2 gas) to form an emitter (80 Ω/sq). The phosphosilicate glass layer of the samples was removed by dilute HF. SiN_x:H was deposited by using plasma-enhanced chemical vapor deposition (Tes Co., Ltd. 2374-36 Jungbudaero, Yangji-Myun, Cheoin-Gu, Yongin-Si, Gyeonggi-Do, Republic of Korea). The SiN_x:H deposition conditions were as follows: 500 sccm SiH, 200 sccm NH_3, 2000 sccm N_2, and 150 sccm hydrogen at a temperature of 420 °C with a plasma power of 40 W. The firing process is conducted by a rapid thermal process (SNTEK, RTP5000, 176-25, Seotan 2-Ro Seotan-Myeon, Pyeongtaek-Si, Gyeonggi-Do, Republic of Korea), followed by annealing (peak temperature = 700 °C, N_2:O_2 flow = 0.7:0.3). Finally, the wafers were cut into 40 × 40 mm samples for the lifetime experiment. Before the firing process, the electrodes are screen-printed on the same wafer, and a reference cell is produced through the same firing process [37].

2.2. Measurement

The LeTID tester for the degradation test of the fabricated samples consisted of a solar simulator with a light source, a thermal controller, and a Keithley source meter (2651A). The light source of the LeTID tester (white LED, Class A < ±2%, 1000 W/m^2, WWSIM-2001, Woowon Tech, 19th Floor, Parkview Tower, 248 Jeongjail-ro, Bundang-du, Seongnam-si, Gyeonggi-do, Republic of Korea) is shown in Figure 1a. The light wavelength range is 400–775 nm, which is more concentrated in the visible wavelength range than the solar spectrum represented by air mass 1.5 global (AM1.5G), and there is less light in the infrared wavelength range. The thermal controller can be controlled by setting the board temperature on which the sample is placed, which was set to 85 °C. In addition, the degradation of the solar cell was measured in situ with a Keithley source meter (2651A) using a 5 BusBar (BB) probe, and V_{oc} and J_{sc} were automatically adjusted according to the temperature and light source. QE is measured from 300 to 1200 nm.

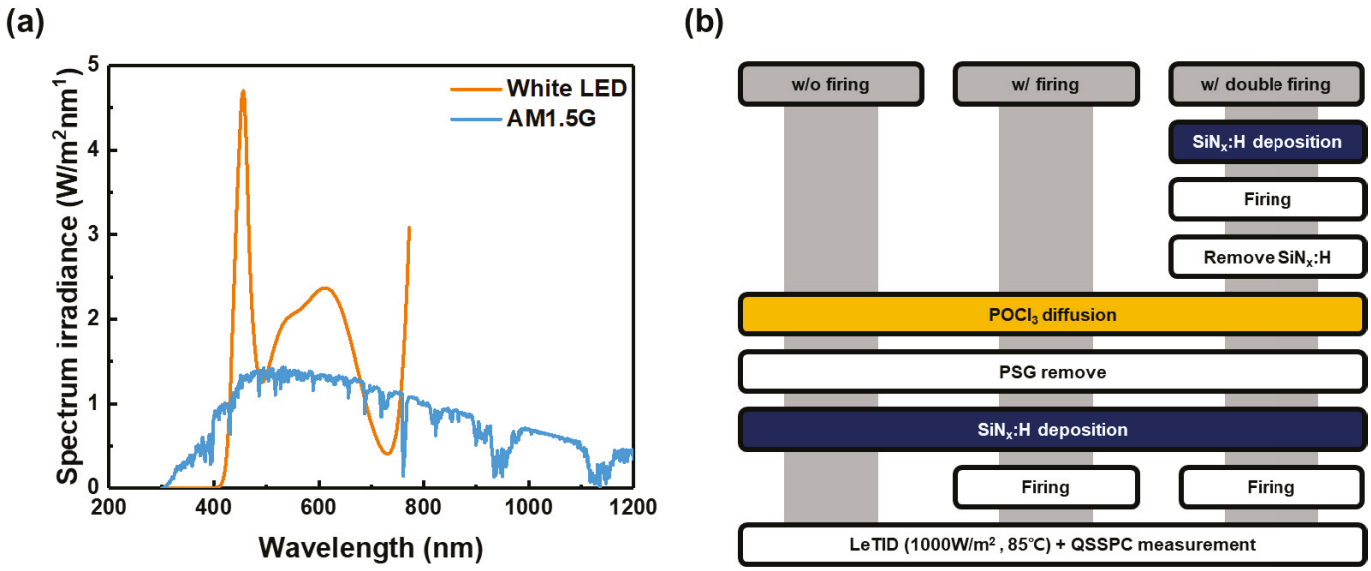

Figure 1. (**a**) Comparison of spectral irradiance of AM1.5G and the white LED used in this paper according to wavelength. (**b**) The process flow of the lifetime sample is used to figure out the hydrogen distribution and degradation.

The injection-dependent lifetime was evaluated using quasi-steady-state photoconductance (QSSPC, Sinton instrument lifetime tester WCT-120) for over 1000 h. The effective lifetime is measured at 20 °C and typically reported at an excess carrier concentration of $\Delta n = 1 \times 10^{14}$–$1 \times 10^{16}$ cm^{-3}. The apparent defect concentration (N^*_{app}) can be calculated from

$$N^*_{app}(t) = \frac{1}{\tau(t)} - \frac{1}{\tau(t=0)} \quad (1)$$

where $\tau(t)$ is the measured carrier effective lifetime at time t, and τ ($t = 0$) is the initial lifetime before degradation. The inverse of the effective lifetime is used for the recombination-active defect-affected SRH recombination. The hydrogen concentration was determined using dynamic SIMS (D-SIMS; 4FE7, AMETEK Korea, 105 Gwanggyo-ro, Yeongtong-gu, Suwon-si, Gyeonggi-do, Republic of Korea). Quantitative analysis was performed using the standard specimen. The hydrogen concentration in Si can be calculated as

$$C_{standard} = RSF \times \frac{I_{dopant,standard}}{I_{matrix,standard}},\ C_B = RSF \times \frac{I_{B,\ sample}}{I_{Si,sample}} \quad (2)$$

where RSF is the relative sensitivity factor, which is the conversion factor from the secondary ion intensity to the atom concentration; $C_{standard}$ is the atom concentration in the standard specimen; C_B is the atom concentration in the sample; and Intensity(I) is the impurity isotope secondary ion intensity in counts of the doping atom and matrix intensity measured using D-SIMS. The surface morphology of the silicon wafer, relative to the dynamic SIMS sputtering beam, can have a considerable impact on the measured location of the maximum point. However, it was not possible to completely quantitatively analyze the hydrogen in the textured silicon with these factors, and comparative analysis was performed on the same sample and measurement. The thickness and refractive index of the SiN_x layer were measured using an ellipsometer (Rudolph AutoEL from Entrepix, 4717 E Hilton Avenue Ste 200, Phoenix, AZ, USA).

3. Results and Discussion

3.1. Commercial Cell Degradation

Figure 2a–d shows the changes in degradation of commercial and reference cells in the LeTID environment by dividing them into each cell parameter. In the case of the commercial cell, there is an initial decrease in V_{oc} and FF due to the temperature effect, and after V_{oc} and FF also decrease by less than 1%. Therefore, it seems that the decrease in efficiency is almost due to J_{sc} drop. Reference cells also have a similar tendency to FF and J_{sc}. However, the V_{oc} decreases significantly compared to the commercial cell during the first 10 h in the LeTID environment. It shows a recovery pattern by regeneration occurring at about 5 h. Although it is not shown in the figure in the text, the reason why the degradation time was set short was because the sample showed the most degradation at around 10 h when it was maximally degraded for 200 h in Figure S1.

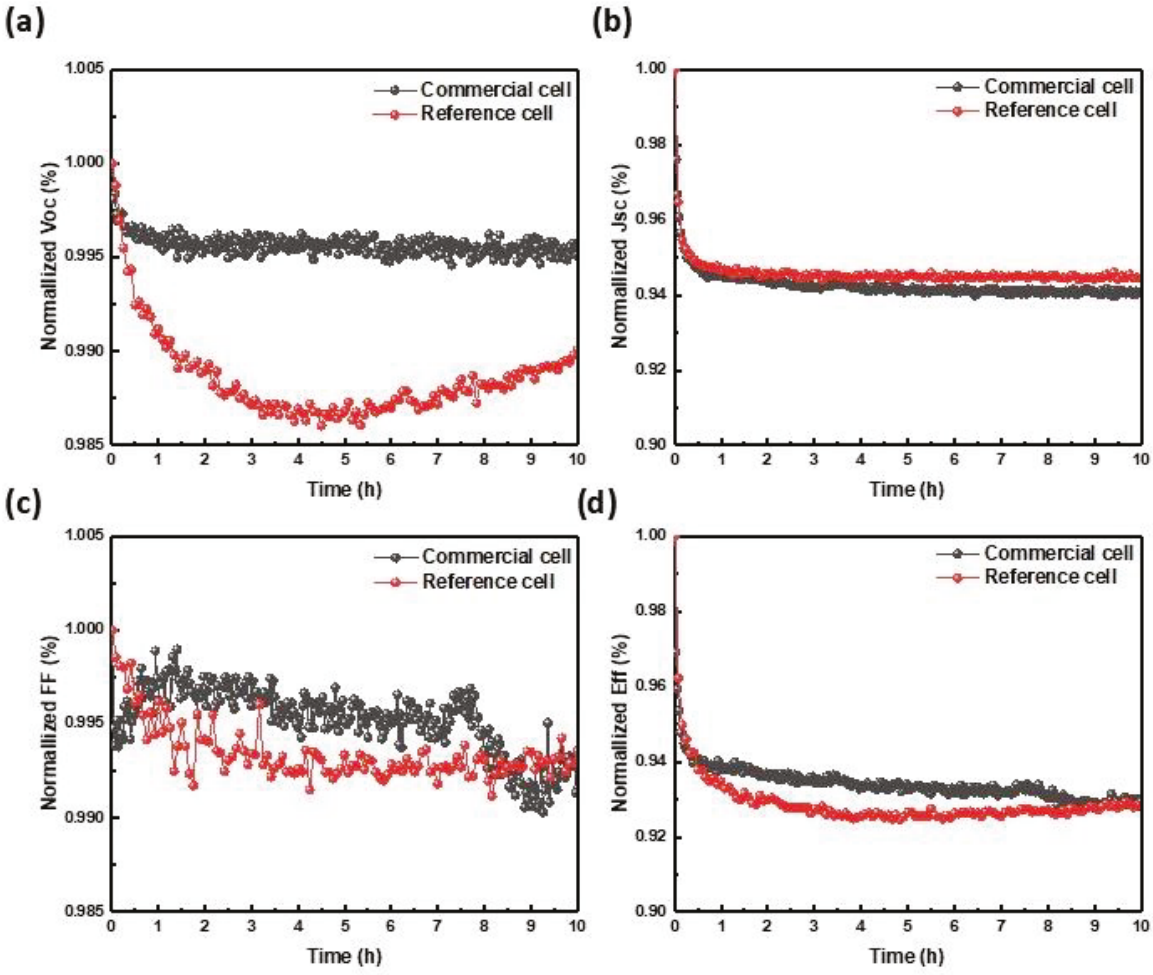

Figure 2. Degradation comparison between commercial and reference cells in LeTID environment. The change of cell performance parameters over the light soaking time normalized (**a**) open circuit voltage, (**b**) short current density, (**c**) fill factor, and (**d**) efficiency.

This result means that the photo-generated carrier collection efficiency is reduced by the influence of LeTID. This suggests that the reference cell is more vulnerable to LeTID. Because the commercial cell may have additionally included an anti-LeTID process such as a change in the firing process or light soaking. To further analyze the cause of the J_{sc} degradation, QE was measured and compared, as shown in Figure 3.

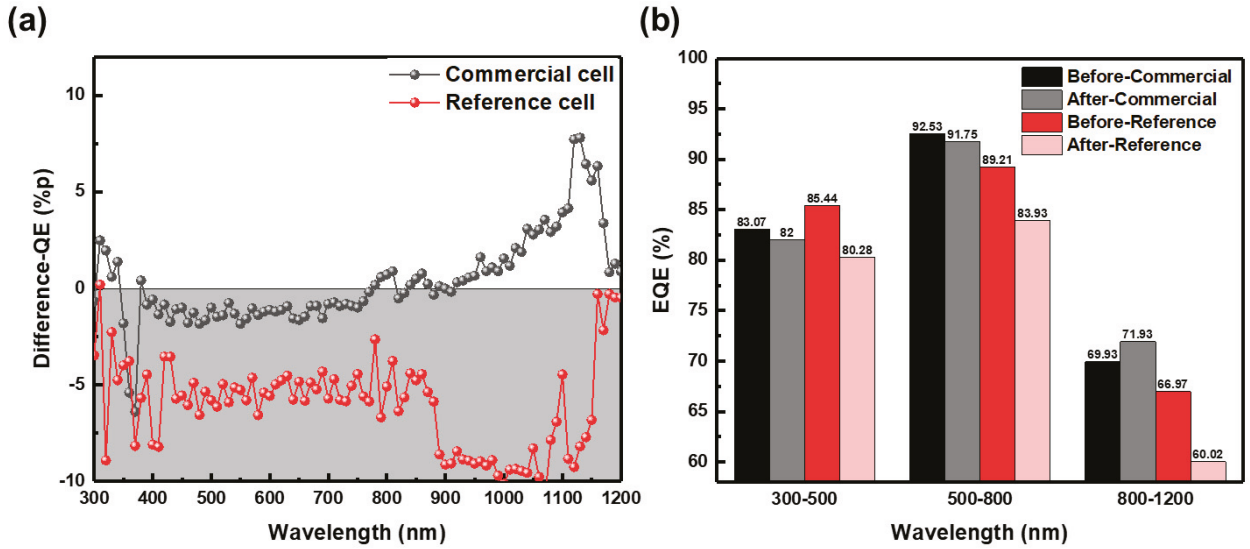

Figure 3. (**a**) QE value by wavelength before and after degradation. (**b**) Changes due to QE value degradation for each wavelength range: Short wavelength range (300–500 nm), middle wavelength range (500–800 nm), and long wavelength range (800–1200 nm).

Assuming that there is no change in the reflectance of the sample due to the LeTID environment, it is reasonable to think that the trends of external quantum efficiency (EQE) and internal quantum efficiency (IQE) are the same. Only EQE measurement can quantify the photo-generated carrier concentration and collection probability without reflectance measurement. Figure 3a measures how the EQE value of each cell changes before and after LeTID. Positive numbers on the *y*-axis indicate an increase, and negative numbers indicate a decrease. The commercial cell shows a slight decrease in the short and medium wavelength ranges but a significant increase in the long wavelength range. The reference cell shows a decrease in almost all wavelengths, and the difference from the commercial cell is clearly shown in the long wavelength range, especially. Figure 3b shows the change in the average value by wavelength. The commercial cell showed a decrease of 1.07%p in the short wavelength band and about 0.67%p in the medium wavelength band, but a 2%p increase was observed in the long wavelength band. Unlike the commercial cell, the reference cell showed a large decrease of 7%p in the wavelength range of 800–1200 nm due to the large loss at 900–1100 nm. This is similar to the results seen in previous literature [20]. Therefore, we will try to check the difference on the front surface, which is a short wavelength. Interestingly, the decrease in J_{sc} occurred in the commercial cell in Figure 2 but not in the QE results. Of course, since the I-V is an in-situ result, it was continuously measured at 85 °C, so the defects shown in LeTID may have a greater effect at 85 °C. Therefore, for a more detailed analysis, the measurements were made while applying a bias to the QE.

In Table 1, the QE value of the commercial cell does not change before and after the degradation. However, when the reverse voltage is applied, the overall QE value also decreases rapidly between 0.4 and 0.5 V due to degradation. This indicates a decrease in V_{mpp}, which seems to be due to the increase in the bulk defect or J_0 of the surface. Interestingly, it has a lower QE value than the reference cell at 0.6 V, despite the commercial cells showing high QE values at the initial state. The QE value of the reference cell shows a noticeable decrease at 0.2–0.4 V, and the decrease is larger than that of the commercial cell. It seems that this is probably due to more defects in the bulk. However, even with this measurement, the clear cause of the cell degradation and J_{sc} decrease cannot be identified.

Table 1. Changes in QE value depending on applied bias.

Applied Bias (V)	0	0.2	0.4	0.5	0.6
Before Commercial	39.01	39.19	35.51	26.26	15.44
After Commercial	39.01	39.04	37.77	28.85	14.78
Difference	0	−0.15	−2.26	−2.59	−0.66
Before Reference	37.46	38.68	35.69	28.70	16.85
After Reference	34.68	34.69	30.67	25.27	14.71
Difference	−2.78	−3.99	−5.02	−3.43	−2.14

3.2. Quantitative Hydrogen Analysis

Figure 4a shows the hydrogen profiles near the front surface of the commercial cell and the reference cell before and after degradation. The thickness of the front anti-reflection coating (ARC) layer of the Reference and commercial cells is different. Because, in the SIMS measurement, the concentration peaks represent the interface by the matrix effect. Compared to the commercial cell, the hydrogen concentration of the reference cell is reduced, and most of the hydrogen profile changes are shown on the surface just below the SiN_x:H, not the bulk. In contrast, the commercial cell shows little change in the diffusion graph itself, and rather, the concentration in the bulk increases slightly after degradation. In addition, the diffusion amount itself is qualitatively higher in the commercial cell, even after passing the saturation point.

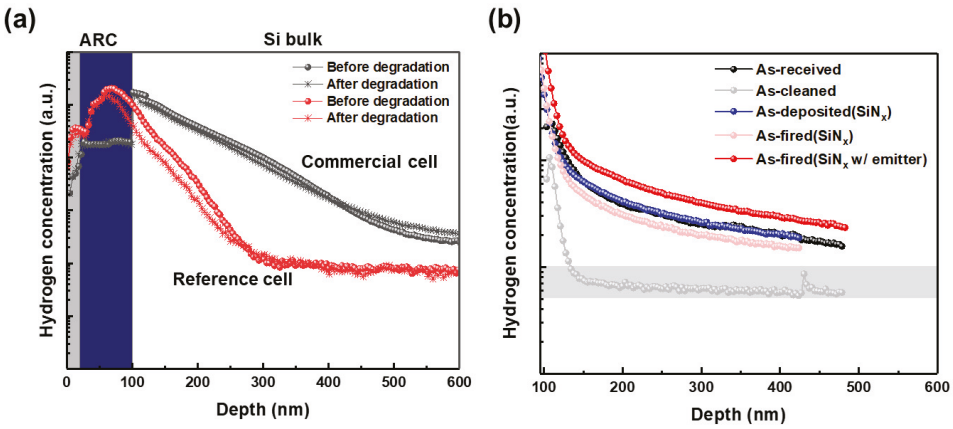

Figure 4. (**a**) Hydrogen profile of commercial and reference cells before and after degradation. A double anti-reflection layer is located on the front of the cells. The thickness seems to be different. (**b**) Shift of hydrogen profile for solar cell manufacturing processes by dynamic SIMS. 'As-received' and 'As-cleaned' samples were shifted to match the thickness of the SiN_x film to 80 nm.

Figure 4b shows the hydrogen profiles that change with the silicon solar cell fabrication process. After cleaning the silicon wafer, the surface and bulk hydrogen contents decrease compared to before the cleaning process (as received). And it shows the saturated profile with zero slope, unlike diffusion profiles. After SiN_x:H deposition, the hydrogen concentration returns to the level of the concentration profile before cleaning. It shows the same amount of hydrogen concentration as the as-received sample, with the SiN_x:H layer shifted by 80 nm calculated. The hydrogen concentration is measured to decrease slightly during the firing process above 700 °C. Considering that the hydrogen concentration in a

typical solar cell is 1×10^{14}–1×10^{16}/cm^{-3} [16,29], this difference is not so much that the amount of hydrogen increase due to the firing process is dominant compared to the SiN_x:H deposition process. However, it is confirmed that the hydrogen concentration increases compared to the firing process in the presence of a typical emitter, which is similar to the existing literature that the firing process is necessary as an additional factor for hydrogen diffusion. Although it has been shown in much literature that hydrogen diffused from SiN_x:H is the primary cause of LeTID, the hydrogen concentration can also be increased by plasma deposition at high temperatures, and additional hydrogen concentration can be obtained during the sintering process.

Figure 5a shows the hydrogen concentration in the SiN_x:H layer of the samples that were conducted according to the experimental flow shown in Figure 1b. The hydrogen concentration of the SiN_x:H layer does not change significantly due to firing, and as can be seen in Figure S2, there is no significant change in the hydrogen concentration of the SiN_x:H layer before and after degradation. This suggests that there is no change in the refractive index of the SiN_x:H layer, and thus, it can explain the correlation between the EQE data and the IQE data previously claimed in Section 3.1. In addition, looking at the hydrogen profile in Figure 5a, we can see that the slope is different depending on the presence or absence of firing, which is presumed to be out-diffusion.

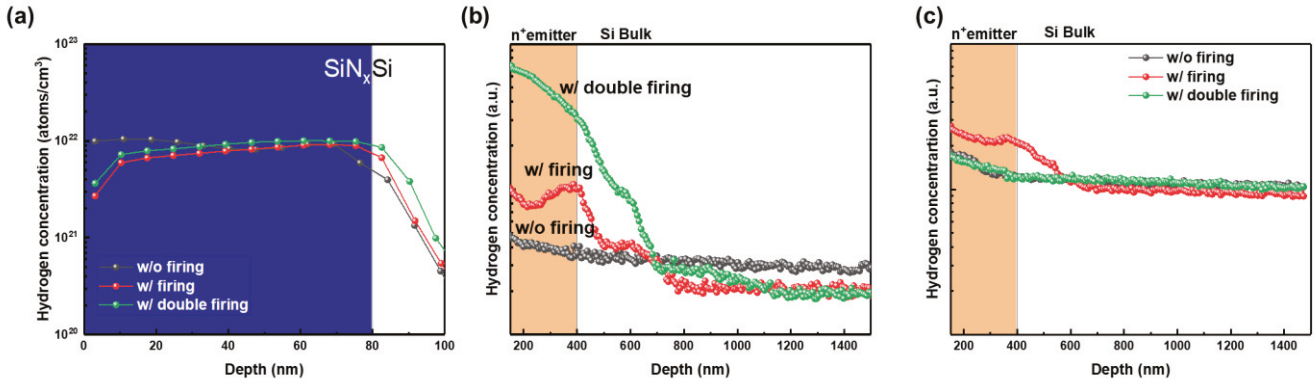

Figure 5. (**a**) The hydrogen profile changes in the SiN_x layer. Hydrogen profile (**b**) before degradation and (**c**) after degradation.

Figure 5b shows the hydrogen concentration distribution before degradation, and we can see that the amount of hydrogen increases with the firing process. As can be seen in Figure 4b, the firing co-occurrence in the presence of an emitter caused the greatest hydrogen diffusion, and in addition, the w/double firing sample showed the greatest amount of hydrogen. The emitter thickness is estimated to be approximately 300 nm. Approximately 300 nm depth corresponds to the junction depth where phosphorus and boron concentrations are equal based on the dopant (~1.0×10^{16} cm^{-3}) in S.I. This is likely due to the slight hill-like shape of the firing sample in Figure 5b, creating a hydrogen peak in the depletion region. It appears that a hydrogen aggregation region is formed in the depletion region of the n_+ emitter and the p-type wafer, like the interface. Figure 5c shows the hydrogen profiles of each sample after 1000 h of thermal annealing; all of them are saturated at a certain concentration. The hydrogen concentration decreased in w/double firing samples just below the SiN_x:H layer but increased in other samples. This implies that one of two things occurs: Either hydrogen diffuses from the SiN_x:H layer, or hydrogen diffuses from the bulk to the surface. Of these two, the latter case appears to be a more convincing mechanism when compared with the existing literature and the pre- and post-diffusion of the SiN_x:H layer in Figure S2.

Figure 6a shows the variation of the apparent defect density using the lifetime change in the LeTID environment for 1000 h. After 1000 h, the results can be largely divided into two groups: The w/o firing sample is one group, and the w/firing and double firing samples are the other. The w/o firing has more defects and shorter lifetimes than the initial state. On the other hand, the second group has fewer defects than the initial amount. All samples show degradation for 1 h. In addition, the w/o firing sample exhibiting hydrogen-deficient samples shows a higher level of degradation without regeneration. The second group, consisting of hydrogen-rich samples, shows degradation and regeneration. Comparing processes #2 and #4, the degradation is suppressed in process #4. The more the hydrogen profile has a gradient along the emitter, such as the commercial cell in Figure 4, the more immune to LeTID it is. It may not necessarily be the case that excessive hydrogen worsens LeTID.

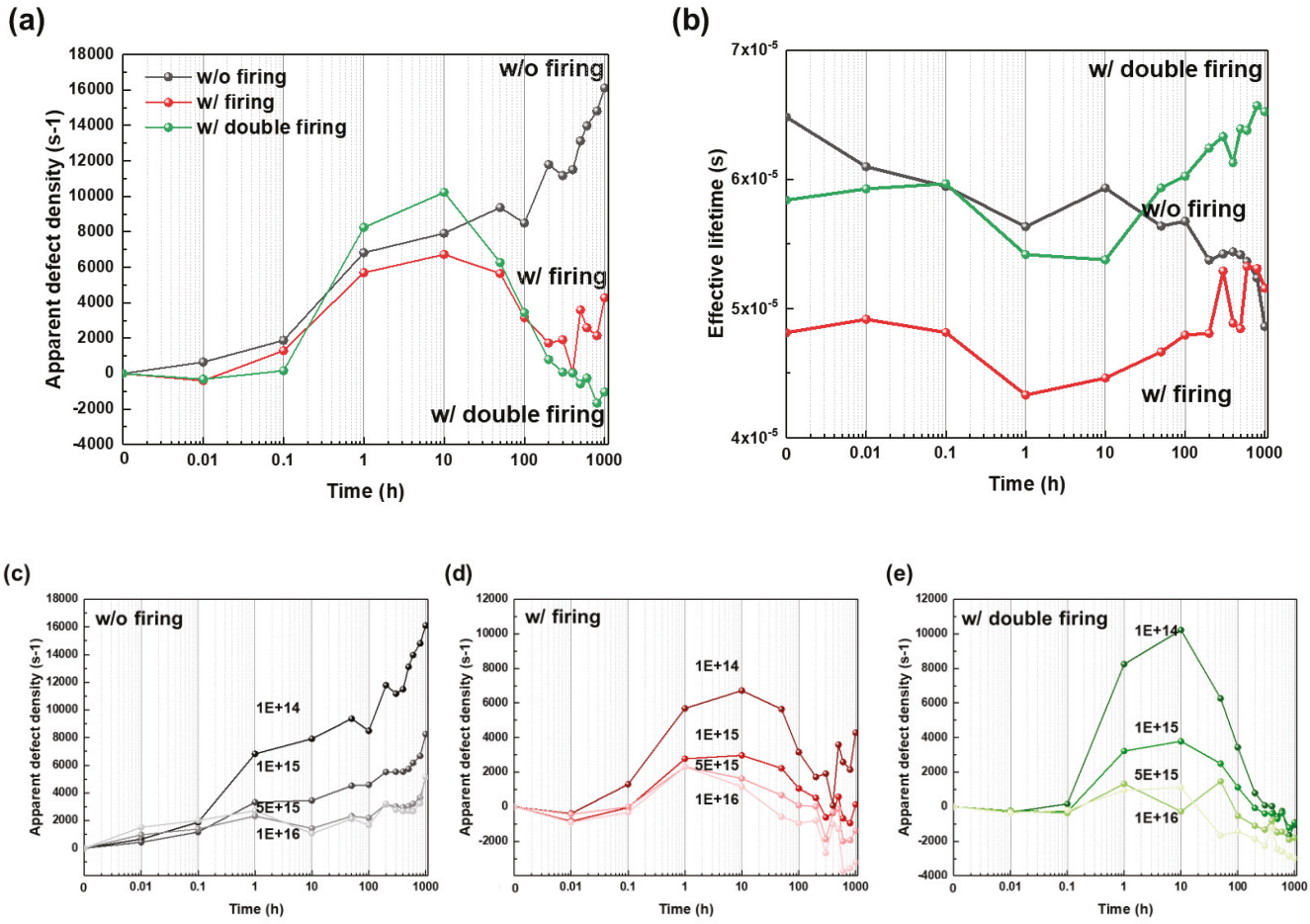

Figure 6. (**a**) Apparent defect density of sample with log-scale of *x*-axis, (**b**) Absolute lifetime over time (1000 W/m^2, 85 °C, 1000 h, MCD = 1 × 10^{14} cm^{-3}). The apparent defect density of the sample with various MCDs, (**c**) w/o firing, (**d**) w/firing, and (**e**) w/double firing.

Figure 6b shows the absolute lifetime. The initial lifetime of the w/o firing sample and the w/w/firing sample is higher in the w/o firing sample, but the lifetimes of the two samples become almost similar during 1000 h of degradation. In the case of the w/double firing, the initial lifetime is slightly lower than the w/o firing sample, but it recovers after 10 h and shows the highest lifetime. It even has a longer lifetime than the initial lifetime. Although firing is thought to be the main cause of LeTID, considering the hydrogen concentration distribution and the decrease in lifetime, it is thought that the

hydrogen diffused by the high-temperature PECVD, as shown in Figure 4b, also affects the degradation. In addition, the lifetime change according to the MCD was analyzed to determine the presence or absence of regeneration.

If the QSSPC results are divided according to MCD, the degree of degradation of the sample can be seen more clearly. For each sample, the smaller the MCD value, the larger the apparent defect density value. In particular, in the case of w/o firing samples, a very large degradation phenomenon is shown to the extent that the y-axis is different. However, in MCDs above 5×10^{15}, not much degradation is shown. Therefore, in the case of the w/o firing sample, it seems to have an effect on LID rather than LeTID. This is because in the case where there is very little hydrogen, it seems to be vulnerable to B-O complexes and therefore vulnerable to bulk defects, as can be seen in the case of low MCD. In the case of the w/o firing sample, it can be seen that it shows two or more degradation phenomena compared to other samples, since it shows a regeneration phenomenon at 10 h at high MCD.

In the case of the w/firing and w/double firing samples, it seems that the faster the hydrogen concentration in the emitter, the faster the degradation, but the faster the regeneration phenomenon is shown before 10 h. The w/firing sample with a constant hydrogen concentration shows the least maximum degradation phenomenon. Therefore, the degradation can be reduced by optimizing the hydrogenation process and firing process that control the amount of hydrogen on the surface, and it is also necessary to calculate the amount of saturated hydrogen required for the bulk and apply it to the passivation process.

4. Conclusions

In conclusion, this study focused on directly measuring the hydrogen depth profile to elucidate the specific relationship between the hydrogen profile and degradation due to LeTID. A significant loss of J_{sc} was observed during the first 10 h of degradation, which contributed most to the overall efficiency reduction. The commercial cell showed less short-wavelength QE decrease compared to the reference cell. This was due to the front side of the cell, especially the emitter region, where the hydrogen profile in the emitter under the degradation environment of the commercial cell showed little change. In contrast, the hydrogen profile in the emitter environment of the reference cell showed a change. Based on this, we hypothesized that the hydrogen profile plays a key role in the J_{sc} loss associated with LeTID. To verify this, degradation tests were performed on samples with various hydrogen profiles obtained through changes in the solar cell process. We confirmed that the high-temperature plasma process increased hydrogen diffusion during the firing and that additional diffusion occurred throughout the firing stage. In addition, after 1000 h of LeTID exposure, hydrogen was observed to migrate from the bulk to the surface, and the surface areas of almost all samples reached the saturated equilibrium hydrogen concentration. In particular, the lower the difference between the initial released hydrogen concentration and the equilibrium concentration, the lower the degree of degradation, especially in terms of J_{sc} loss. Since regeneration generally starts after the degradation reaches saturation (approximately 10 h), less degraded samples showed improved regeneration potential. These results suggest that implementing an optimized equilibrium hydrogen concentration through process control can improve both LeTID and LID resistance and passivation quality. However, these characteristics have limitations in that they cannot interpret the reversible phenomenon due to dark annealing, which is one of the major characteristics of degradation.

Supplementary Materials: The following supporting information can be downloaded at: https://www.mdpi.com/article/10.3390/en18123090/s1, Figure S1. Efficiency degradation of reference cell for 200 h; Figure S2. Cell efficiency parameter degradation of reference cell for 200 h; Figure S3. Hydrogen profile measured by D-SIMS in SiNx:H/Si interface. (a) Processing, (b) before degradation, and (c) after degradation. Figure S3b matches Figure 5a in the paper; Figure S4. Phosphorus profile measured by D-SIMS: the concentration measurement limitation of D-SIMS is 1E17 cm^{-3}, and the junction depth is considered 300 nm; Figure S5. Lifetime change for 1000 h with MCD (1×10^{14}–1×10^{16}).

Author Contributions: Conceptualization, M.S.; methodology, M.S.; validation, Y.G.; data curation, Y.G.; writing—original draft preparation, M.S.; writing—review and editing, Y.G.; supervision, D.K.; project administration, Y.K.; funding acquisition, D.K. All authors have read and agreed to the published version of the manuscript.

Funding: This research received no external funding.

Data Availability Statement: The data used in this study are provided in the text and its Supporting Information.

Acknowledgments: This research was supported by the New & Renewable Energy Core Technology Program of the Korea Institute of Energy Technology Evaluation and Planning (KETEP) and supported by the Ministry of Trade, Industry, and Energy of the Republic of Korea (No. RS-2023-00236715) and This research was supported by the Korea Evaluation Institute of Industrial Technology (KEIT, grant no. 20015762) of the Ministry of Trade, Industry and Energy (MOTIE; and the Development Program of the Korea Institute of Energy Research.

Conflicts of Interest: The authors declare that they have no known competing financial interests or personal relationships that could have appeared to influence the work reported in this paper.

Declaration of generative AI and AI-assisted technologies in the writing process: During the preparation of this work, the author(s) used ChatGPT in order to check English grammar. After using this ChatGPT, the author reviewed and edited the content as needed and take(s) full responsibility for the publication's content.

References

1. Walburga Hemetsberger, M.S. Sonia Dunlop. In *Global Market Outlook*; Intersolar Europe, Global Solar Council (GSC): Munich, Germany, 2025; pp. 6–12.
2. Fischer, M. *International Technology Roadmap for Photovoltaics*, 15th ed.; VDMA: Frankfurt, Germany, 2024.
3. NREL Best Research-Cell Efficiency Chart. Available online: https://www.nrel.gov/pv/cell-efficiency (accessed on 12 May 2025).
4. Chan, C.E.; Payne, D.N.R.; Hallam, B.J.; Abbott, M.D.; Fung, T.H.; Wenham, A.M. Rapid Stabilization of High-Performance Multicrystalline P-type Silicon PERC Cells. *IEEE J. Photovolt.* **2016**, *6*, 1473–1479. [CrossRef]
5. Lee, S.; Lee, K.D.; Bae, S.; Kang, Y.; Kim, D.; Lee, H.-S. Prevention of potential-induced degradation using a moisture barrier in crystalline silicon photovoltaic modules. *Prog. Photovolt. Res. Appl.* **2024**, *32*, 390–398. [CrossRef]
6. Lindroos, J.; Savin, H. Review of light-induced degradation in crystalline silicon solar cells. *Sol. Energy Mater. Sol. Cells* **2016**, *147*, 115–126. [CrossRef]
7. Petter, K.; Hubener, K.; Kersten, F.; Bartzsch, M.; Fertig, F.; Kloter, B.; Muller, J. Dependence of LeTID on brick height for different wafer suppliers with several resistivities and dopants. *Int. Work. Cryst. Silicon Sol. Cells* **2016**, *6*, 1–17.
8. Chen, D.; Hamer, P.; Kim, M.; Chan, C.; nee Wenham, A.C.; Rougieux, F.; Zhang, Y.; Abbott, M.; Hallam, B. Hydrogen-induced degradation: Explaining the mechanism behind light- and elevated temperature-induced degradation in n- and p-type silicon. *Sol. Energy Mater. Sol. Cells* **2020**, *207*, 110353. [CrossRef]
9. Winter, M.; Bordihn, S.; Peibst, R.; Brendel, R.; Schmidt, J. Degradation and Regeneration of n^+-Doped Poly-Si Surface Passivation on *p*-Type and *n*-Type Cz-Si Under Illumination and Dark Annealing. *IEEE J. Photovolt.* **2020**, *10*, 423–430. [CrossRef]
10. Zerfaß, R.; Simon, J.; Herguth, A.; Hahn, G. Impact of Hydrogen in Ga-Doped Silicon on Maximum LeTID Defect Density. *Sol. RRL* **2023**, *7*, 2300501. [CrossRef]

11. Kersten, F.; Engelhart, P.; Ploigt, H.-C.; Stekolnikov, A.; Lindner, T.; Stenzel, F.; Bartzsch, M.; Szpeth, A.; Petter, K.; Heitmann, J.; et al. Degradation of multicrystalline silicon solar cells and modules after illumination at elevated temperature. *Sol. Energy Mater. Sol. Cells* **2015**, *142*, 83–86. [CrossRef]
12. Niewelt, T.; Selinger, M.; Grant, N.E.; Kwapil, W.; Murphy, J.D.; Schubert, M.C. Light-induced activation and deactivation of bulk defects in boron-doped float-zone silicon. *J. Appl. Phys.* **2017**, *121*, 185702. [CrossRef]
13. Varshney, U.; Abbott, M.; Ciesla, A.; Chen, D.; Liu, S.; Sen, C. Evaluating the Impact of SiN_x Thickness on Lifetime Degradation in Silicon. *IEEE J. Photovolt.* **2019**, *9*, 601–607. [CrossRef]
14. nee Wenham, A.C.; Wenham, S.; Chen, R.; Chan, C.; Chen, D.; Hallam, B. Hydrogen-Induced Degradation. In Proceedings of the 2018 IEEE 7th World Conference on Photovoltaic Energy Conversion (WCPEC) (A Joint Conference of 45th IEEE PVSC, 28th PVSEC & 34th EU PVSEC), Waikoloa, HI, USA, 10–15 June 2018.
15. Sio, H.C.; Wang, H.; Wang, Q.; Sun, C.; Chen, W.; Jin, H.; Macdonald, D. Light and elevated temperature induced degradation in p-type and n-type cast-grown multicrystalline and mono-like silicon. *Sol. Energy Mater. Sol. Cells* **2018**, *182*, 98–104. [CrossRef]
16. Hammann, B.; Rodrigues, P.V.; Aßmann, N.; Kwapil, W.; Schindler, F.; Schubert, M.C.; Glunz, S.W. Deciphering the Role of Hydrogen in the Degradation of Silicon Solar Cells under Light and Elevated Temperature. *Sol. RRL* **2024**, *8*, 2400457. [CrossRef]
17. Schön, J.; Hamer, P.; Hammann, B.; Zechner, C.; Kwapil, W.; Schubert, M.C. Hydrogen in Silicon Solar Cells: The Role of Diffusion. *Sol. RRL* **2025**, *9*, 2400668. [CrossRef]
18. Jordan, D.; Sulas-Kern, D.B.; Jonhston, S.; Moutinho, H.R.; Xiao, C.; Jiang, C.S.; Young, M.; Norman, A.G.; Deline, C.; Repins, I.; et al. *High Efficiency Silicon Module Degradation—From Atoms to Systems: Preprint*; National Renewable Energy Lab. (NREL): Golden, CO, USA, 2020.
19. Ma, S.; Gao, P.; Xu, J.; Li, W.; Guo, Y.; Qiao, D.; Ma, B.; Yuan, W.; Ye, T. Light and elevated temperature induced degradation (LeTID) of N-type TOPCon solar cells. *Solar Energy* **2025**, *296*, 113573. [CrossRef]
20. Bredemeier, D.; Walter, D.C.; Schmidt, J. Possible Candidates for Impurities in mc-Si Wafers Responsible for Light-Induced Lifetime Degradation and Regeneration. *Sol. RRL* **2018**, *2*, 1700159. [CrossRef]
21. Maischner, F.; Maus, S.; Greulich, J.; Lohmuller, S.; Lohmuller, E.; Saint-Cast, P.; Ourinson, D.; Vahlman, H.; Hergert, K.; Riepe, S. LeTID mitigation via an adapted firing process in p-type PERC cells from SMART cast-monocrystalline, Czochralski and high-performance multicrystalline silicon. *Prog. Photovolt. Res. Appl.* **2022**, *30*, 123–131. [CrossRef]
22. Chakraborty, S.; Huang, Y.; Wilson, M.; Aberle, A.G.; Li, J.B. Mitigating Light and Elevated Temperature Induced Degradation in Multicrystalline Silicon Wafers and PERC Solar Cells Using Phosphorus Diffusion Gettering. *Phys. Status Solidi A* **2018**, *215*, 1800160. [CrossRef]
23. Zuschlag, A.; Skorka, D.; Hahn, G. Degradation and regeneration in mc-Si after different gettering steps. *Prog. Photovolt. Res. Appl.* **2017**, *25*, 545–552. [CrossRef]
24. Sharma, R.; Chong, A.P.; Li, J.B.; Aberle, A.G.; Huang, Y. Role of post-metallization anneal sequence and forming gas anneal to mitigate light and elevated temperature induced degradation of multicrystalline silicon solar cells. *Sol. Energy Mater. Sol. Cells* **2019**, *195*, 160–167. [CrossRef]
25. Wang, L.; Koh, D.; Hamer, P.; Pollard, M.; Chan, C. *Suppression of LeTID in p-Type Multi-Crystalline PERC Silicon Solar Cells by Biased Annealing Process*; AIP Publishing: Melville, NY, USA, 2022.
26. Varshney, U.; Hallam, B.; Hamer, P.; Ciesla, A.; Chen, D.; Liu, S. Controlling Light- and Elevated-Temperature-Induced Degradation With Thin Film Barrier Layers. *IEEE J. Photovolt.* **2020**, *10*, 19–27. [CrossRef]
27. Wang, Z.; Shen, H.; Hu, D.; Wei, Q.; Ni, Z.; Li, Y.; Sun, L.; Qian, H. Influence of double current injection annealing on anti-LID effect in mono-like cast silicon PERC solar cells. *J. Mater. Sci. Mater. Electron.* **2020**, *31*, 3221–3227. [CrossRef]
28. Sen, C.; Chan, C.; Hamer, P.; Wright, M.; Varshney, U.; Liu, S.; Chen, D.; Samadi, A.; Ciesla, A.; Chong, C.; et al. Annealing prior to contact firing: A potential new approach to suppress LeTID. *Sol. Energy Mater. Sol. Cells* **2019**, *200*, 109938. [CrossRef]
29. Eberle, R.; Kwapil, W.; Schindler, F.; Schubert, M.C.; Glunz, S.W. Impact of the firing temperature profile on light induced degradation of multicrystalline silicon. *Phys. Status Solidi (RRL)–Rapid Res. Lett.* **2016**, *10*, 861–865. [CrossRef]
30. Hammann, B.; Schindler, F.; Schon, J.; Kwapil, W.; Schubert, M.C.; Glunz, S.W. Review on hydrogen in silicon solar cells: From its origin to its detrimental effects. *Solar Energy Mater. Sol. Cells* **2025**, *282*, 113432.
31. Ramspeck, K.; Zimmermann, S.; Nagel, H.; Metz, A.; Gassenbauer, Y.; Birkmann, B.; Seidl, A. Light induced degradation of rear passivated mc-Si solar cells. In Proceedings of the 27th European Photovoltaic Solar Energy Conference and Exhibition, Frankfurt, Germany, 24–28 September 2012.
32. Resmi, E.; KSreejith, P.; Kottantharayil, A. Analysis of variation in recombination characteristics due to light and heat in industrial silicon solar cells. *Sol. Energy* **2023**, *252*, 127–133.
33. Fokuhl, E.; Naeem, T.; Schmid, A.; Gebhardt, P.; Geipel, T.; Philipp, D. LeTID—A comparison of test methods on module level. In Proceedings of the In 36th European PV Solar Energy Conference and Exhibition, Marseille, France, 9–13 September 2019.

34. Chan, C.; Fung, T.H.; Abbott, M.; Payne, D.; Wenham, A.; Hallam, B.; Chen, R.; Wenham, S. Modulation of Carrier-Induced Defect Kinetics in Multi-Crystalline Silicon PERC Cells Through Dark Annealing. *Sol. RRL* **2017**, *1*, 1600028. [CrossRef]
35. Zhang, D.; Yao, Z.; Wu, J.; Jiang, F. Application of current injection to LeTID monitoring in industrial PERC cell production. In Proceedings of the 2020 47th IEEE Photovoltaic Specialists Conference (PVSC), Calgary, AB, Canada, 15 June–21 August 2020.
36. Sperber, D.; Graf, A.; Skorka, D.; Herguth, A.; Hahn, G. Degradation of Surface Passivation on Crystalline Silicon and Its Impact on Light-Induced Degradation Experiments. *IEEE J. Photovolt.* **2017**, *7*, 1627–1634. [CrossRef]
37. Choi, D.; Park, H.; Bae, S.; Shin, S.H.; Han, H.; Kloter, B.; Kim, D.; Lee, H.-S.; Kang, Y. Lowering firing temperature of a p-type passivated emitter rear contact Si solar cell via current injection. *Sol. Energy Mater. Sol. Cells* **2022**, *239*, 111587. [CrossRef]

Disclaimer/Publisher's Note: The statements, opinions and data contained in all publications are solely those of the individual author(s) and contributor(s) and not of MDPI and/or the editor(s). MDPI and/or the editor(s) disclaim responsibility for any injury to people or property resulting from any ideas, methods, instructions or products referred to in the content.

energies

MDPI

Article

Enhancing Solar Thermal Energy Storage via Torsionally Modified TPMS Structures Embedded in Sodium Acetate Trihydrate

Martin Beer * and Radim Rybár

Institute of Earth Sources, Faculty of Mining, Ecology, Process Technologies and Geotechnology, Technical University of Košice, Letná 9, 042 00 Košice, Slovakia; radim.rybar@tuke.sk
* Correspondence: martin.beer@tuke.sk

Abstract: This study focuses on the numerical analysis of the impact of geometric modifications of sheet-gyroid structures on heat transfer in thermal energy storage systems utilizing sodium acetate trihydrate as a phase change material. The aim was to enhance the thermal conductivity of SAT, which is inherently low in the solid phase, by embedding a thermally conductive metallic structure made of aluminum alloy 6061. The simulations compared four gyroid configurations with different degrees of torsional deformation (0°, 90°, 180°, and 360°) alongside a reference model without any structure. Using numerical analysis, the study evaluated the time required to heat the entire volume of SAT above its phase transition temperature (58 °C) as well as the spatial distribution of the temperature field. The results demonstrate that all gyroid configurations significantly reduced the charging time compared with the reference case, with the highest efficiency achieved by the 360° twisted structure. Temperature maps revealed a more uniform thermal distribution within the phase change material and a higher heat flux into the volume. These findings highlight the strong potential of TPMS-based structures for improving the performance of latent heat thermal energy storage systems.

Keywords: TPMS; sheet-gyroid; sodium acetate trihydrate; numerical analysis

1. Introduction

The rapid advancement of additive manufacturing technologies over the past decade has opened new dimensions in the design and fabrication of engineering components with complex internal geometries. Thanks to additive techniques such as selective laser melting (SLM) [1], Stereolithography (SLA) [2], and metal powder sintering [3], it is now possible to produce three-dimensional structures that were previously unfeasible using conventional manufacturing processes [4–7]. These technologies enable the precise formation of internal cavities, channels, and surfaces with extremely high geometric complexity while maintaining the mechanical integrity and functional performance of the final product. Among the geometries that particularly benefit from the capabilities of additive manufacturing are the so-called Triply Periodic Minimal Surfaces (TPMSs). These mathematically defined surfaces possess zero mean curvature and exhibit spatial periodicity in all three orthogonal directions [8]. One of the most well-known TPMS geometries is the gyroid [9], originally discovered as a solution to a variational problem of surface area minimization under specific boundary conditions. The gyroid structure is characterized by a high surface-to-volume ratio [10], a three-dimensionally interconnected channel network [11], and intrinsic

symmetry, which is advantageous for both heat transfer and laminar flow. From a practical standpoint, gyroid structures are increasingly being employed in thermal processes as thermally conductive fillers [12], heat exchange surfaces [13], and passive mixing elements [14]. The application of TPMS structures as heat exchangers or thermal flow distributors is particularly attractive in systems where enhanced heat transfer is required.

An example of such an application is the use of phase change materials, which serve as heat storage media in low-temperature thermal energy storage systems [15]. Among the various materials classified as phase change material (PCM), sodium acetate trihydrate (SAT) stands out as a particularly attractive candidate due to its combination of favorable properties—it is non-toxic, cost-effective, chemically stable, and exhibits a relatively high latent heat capacity [16]. At a temperature of approximately 58 °C [17], SAT undergoes a phase transition from solid to liquid, during which it absorbs or releases a significant amount of thermal energy with only a minimal change in temperature. This phenomenon is advantageous for the design of compact thermal storage units, which can serve either as a heat source during discharging or as a thermal buffer to stabilize the temperature during transient demand conditions.

However, a fundamental limitation in the application of SAT and similar PCMs lies in their inherently low thermal conductivity, particularly in the solid phase. Reported thermal conductivity values for solid SAT typically range from 0.4 to 0.7 $W \cdot m^{-1} \cdot K^{-1}$ [18], which results in slow charging and discharging rates within thermal accumulators. Heat is transferred into the PCM volume primarily by conduction through its boundary, leading to temperature gradients and thermally "dead" zones that diminish the overall efficiency and performance of the storage unit. This issue has been addressed in the literature through several enhancement strategies, including the addition of metal foams, graphite, and nanoparticles and the implementation of thermally conductive inserts.

Sodium acetate trihydrate (SAT) was selected for this study due to its combination of desirable thermal and practical properties. It possesses a melting temperature of approximately 58 °C, which aligns well with the operational range of solar thermal systems and low-grade waste heat applications. SAT also provides a high latent heat of fusion (~264 kJ/kg), minimal supercooling, and relatively low thermal expansion during phase transition, reducing mechanical stress on storage containers. Its non-toxic nature, chemical stability over multiple thermal cycles, and low material cost further enhance its suitability for scalable thermal energy storage systems. Compared with other hydrated salts or paraffinic PCMs, SAT offers a strong balance between thermal performance and operational safety, making it a robust candidate for experimental and industrial deployment.

Garay Ramirez et al. [19] focused their research on improving the thermophysical properties of SAT by incorporating a mixture of carboxymethyl cellulose, silica gel, and silver nanoparticles. Their primary objective was to enhance the latent heat capacity. Wang et al. [20] conducted experiments aimed at evaluating the thermal and technical performance of PCM by using a composite based on expanded graphite. This material contributed to an increase in the amount of stored heat and accelerated both the charging and discharging processes. Myat et al. [21] investigated the effects of adding polyethylene glycol to PCM, reporting that the modified thermal conductivity of the mixture resulted in an approximately 25% reduction in the time required for charging and discharging the storage unit. Liu et al. [22] aimed to improve PCM performance by embedding a porous structure that acted as a conductive framework, thereby achieving more efficient thermal charging and discharging times. Hassan et al. [23] proposed a solution for passive cooling of electronic components using PCM enhanced with nanoparticles and copper foam with extremely high porosity (97%). Falcone et al. [24] highlighted a substantial im-

provement in the thermal conductivity of paraffin-based PCM after the inclusion of copper foam—specifically, an increase from 0.2 to 7 $W \cdot m^{-1} \cdot K^{-1}$. Al-Najjar et al. [25] introduced a thermal storage concept incorporating a metallic foam layer with various configurations, which allowed for control over the duration of the charging phase. Chen et al. [26] analyzed the impact of arc-shaped fins in a shell-and-tube heat exchanger, where their presence improved the temperature distribution and accelerated the melting of the PCM. Zhao et al. [27] designed a thermal storage unit combining SAT with copper metal foam, and their experimental results demonstrated a significant influence of the specific spatial configuration on the thermal behavior of the system.

One of the most effective and simultaneously technologically feasible solutions is the embedding of a thermally conductive metallic structure with a high surface area into the PCM volume. Such a structure acts as an element that conducts heat throughout the entire material. A geometrically ideal candidate for this role is the sheet-gyroid—a type of gyroid that forms a continuous wall rather than discrete voids or lattice networks. Compared with the skeletal-gyroid, the sheet-gyroid contains a greater volume of solid material and a continuous surface network, enabling more efficient thermal contact with the surrounding PCM. Moreover, its periodic structure can be further geometrically modified to increase the total heat exchange surface area. From a manufacturing perspective, the use of aluminum alloy 6061 is highly relevant, as it is widely adopted in industry for its favorable balance between thermal conductivity, mechanical strength, and corrosion resistance. Modern additive manufacturing (AM) techniques—particularly selective laser melting (SLM)—enable the precise fabrication of intricate TPMS structures such as the sheet-gyroid from aluminum alloys, which are otherwise difficult to produce by conventional methods. This technological feasibility supports the potential integration of such structures in commercial thermal storage units. Moreover, sodium acetate trihydrate (SAT) is already utilized in practical applications such as portable hand warmers and domestic thermal buffers, owing to its low cost, non-toxicity, and latent heat capacity. The combination of AM-produced aluminum structures and SAT thus represents a promising direction for scalable latent heat thermal energy storage systems that align with current industry standards.

The present study focuses on a numerical analysis of the effect of implementing a sheet-gyroid structure into the volume of a thermal energy storage medium, with the aim of improving the charging efficiency of the system by enhancing its effective thermal conductivity. Moreover, due to the favorable phase change temperature of SAT and the potential for high thermal storage density, the proposed system is particularly well-suited for applications in solar thermal energy storage. The improved heat transfer dynamics facilitated by torsionally modified TPMS structures can significantly enhance the efficiency and responsiveness of compact latent heat storage units integrated into solar energy systems, including solar water heaters, thermal cookers, and buffer tanks for domestic heating. The study considers a specific geometric modification of the sheet-gyroid structure in the form of a full-body twist about its central axis by 90°, 180°, and 360°. This alteration changes the internal trajectory of heat propagation within the structure as well as the total heat transfer surface area, both of which may significantly affect the overall energy transfer rate. The motivation for this modification stems from previous research on gyroid structures [28–30], which demonstrated that geometric adjustments such as the so-called twisted gyroid can improve the thermophysical performance of heat exchange components. The current work builds on these findings and extends them by conducting a systematic comparison of different levels of torsion in the context of PCM storage unit charging.

2. Materials and Methods

As part of the present study, four variants of thermal energy storage structures were developed, each differing in the geometry of the embedded sheet-gyroid body. All variants were designed as three-dimensional models using the CAD software Solidworks 2024. The base of each structure consisted of a periodic gyroid geometry, represented analytically as a triply periodic minimal surface defined by Equation (1) [31].

$$\sin x \cos y + \sin y \cos z + \sin z \cos x = 0, \quad (1)$$

Using this equation, a base unit of the structure with dimensions of $10 \times 10 \times 10$ mm was generated. This unit was then regularly arranged and concatenated into a prismatic volume measuring $30 \times 30 \times 50$ mm. To create a solid body with a defined wall thickness, the resulting surface was transformed by applying a material thickness of 0.5 mm. For the purposes of subsequent numerical analysis, this volume was modified into a cylindrical shape with a base diameter of 20 mm. In addition to the baseline, unaltered sheet-gyroid geometry, three modified structures were also created. These were geometrically transformed by applying torsional deformation to the entire gyroid volume about its vertical axis by 90°, 180°, and 360°, respectively, resulting in variants with altered internal topology. In order to investigate the influence of torsional deformation on heat transfer performance, four gyroid configurations were created by applying a progressive twist to the base structure around its vertical axis. The twist angles selected—0°, 90°, 180°, and 360°—correspond to the cumulative angular displacement of the top face relative to the bottom face of the structure. These values were chosen to represent a systematic increase in torsional distortion, with 0° serving as the undeformed baseline and 360° representing the upper bound of feasible geometric complexity within the given design volume. The deformation was applied using the Twist feature in SolidWorks, which continuously rotates horizontal cross-sections along the structure's height. This approach allowed us to observe the thermal effects of increasing surface curvature and internal flow redirection while ensuring that the deformed structures remained suitable for potential fabrication using additive manufacturing techniques.

These modifications were introduced with the aim of influencing the heat transfer pathways within the solid body as well as potentially altering the temperature distribution during the heating phases. Figure 1 presents the 3D models of the applied gyroid structures in both front and side views. Each model used in the numerical analysis consisted of two primary components: a solid, thermally conductive body represented by a sheet-gyroid structure and a surrounding volume into which this body was embedded—the phase change material sodium acetate trihydrate. The model was designed to represent a compact form of an elementary thermal storage unit with well-defined dimensions, carefully chosen to balance simulation accuracy and computational efficiency.

The SAT volume was shaped as a cylinder with a diameter of 22 mm and a height of 52 mm, with its outer walls offset by 1 mm from the outermost points of the sheet-gyroid structure. This offset eliminated direct contact between the storage medium and the external environment, thus simulating conditions closer to thermal insulation in a closed system. For reference purposes, a comparison model without the sheet-gyroid structure—referred to as the "blank" model—was also created. In this case, a solid cylinder with the same volume as the sheet-gyroid structure was centrally placed within the SAT volume. By keeping the cylinder height fixed at 50 mm, the diameter was calculated to yield a total volume of 2397 mm^3, ensuring volumetric consistency across all configurations for meaningful comparison of heat transfer effects.

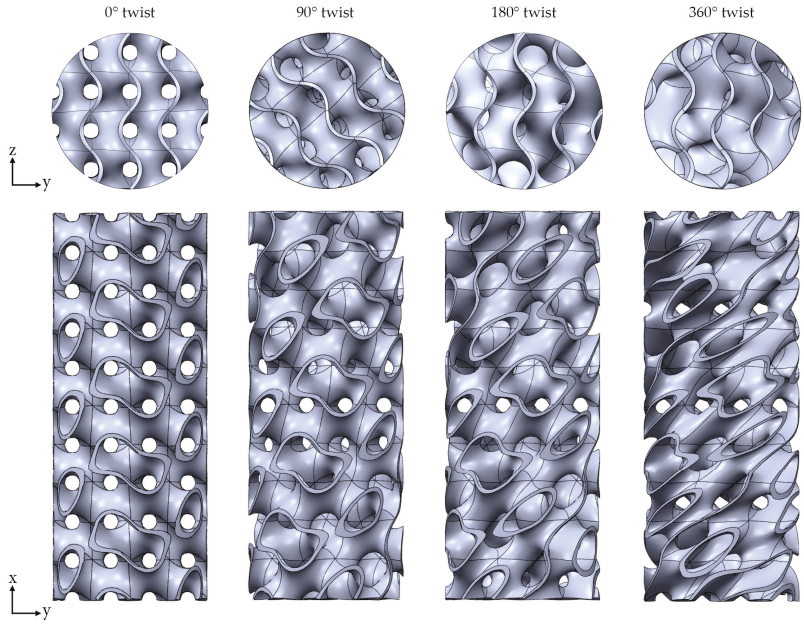

Figure 1. Front and side views of the four gyroid structures with 0°, 90°, 180°, and 360° torsional rotation about the vertical axis.

Table 1 summarizes the final values of volume and external surface area for the individual sheet-gyroid configurations, as well as the respective SAT volumes. For the sheet-gyroid, the listed values correspond to the volume and external surface area, which serves as the active heat transfer interface to the PCM. For the SAT, only the total volume of the storage medium is provided. The analysis of the tabulated data reveals that the volumes of the solid structures remain nearly identical across all configurations, with differences on the order of tenths of a cubic millimeter. In contrast, the external surface area of the sheet-gyroid structures—which serves as the heat transfer interface—increases noticeably with higher degrees of torsional deformation. The baseline (non-twisted) configuration exhibits a surface area of approximately 10,038 mm^2, while the 360° twisted structure reaches nearly 10,975 mm^2, corresponding to an increase of roughly 9%. On the other hand, the reference "blank" model without any embedded structure has a significantly smaller heat transfer surface (only 1326 mm^2), clearly illustrating the contrast between the plain configuration and the sheet-gyroid-filled models.

Table 1. Summary of the external surface area of the sheet-gyroid structure (i.e., the heat exchange surface) and the volumes of the sheet-gyroid structure and the SAT body for a cylindrical model with a diameter of 22 mm and a height of 52 mm denoted as a blank.

	Volume (mm^3)	**Surface Area (mm^2)**
	Sheet-gyroid	
0° twist	2396.52	10,038.39
90° twist	2396.73	10,100.31
180° twist	2397.02	10,282.63
360° twist	2397.60	10,975.28
blank	2397.36	1326.31
	SAT body	
0° twist	15,718.11	-
90° twist	15,717.37	-
180° twist	15,717.19	-
360° twist	15,719.42	-
blank	15,717.30	-

For the purposes of numerical simulation, the sheet-gyroid structure was modeled using aluminum alloy 6061, while the thermal storage medium was represented by sodium acetate trihydrate ($CH_3COONa{\cdot}3H_2O$). The fundamental thermophysical properties of both materials were adopted from the literature. For aluminum 6061, the following constant values were used: a thermal conductivity of 167 $W{\cdot}\ m^{-1}{\cdot}\ K^{-1}$, a specific heat capacity of 900 $J{\cdot}\ kg^{-1}{\cdot}\ K^{-1}$, and a density of 2700 $kg{\cdot}\ m^{-3}$. The thermophysical parameters of SAT were determined based on available correlations that express the temperature dependence of the relevant properties over the simulated operating range, which in this case involved a charging process beginning at 20 °C and concluding at 58 °C. The temperature-dependent specific heat capacity, thermal conductivity, and density of SAT were defined according to Equations (2)–(4), based on established sources [32,33]:

$$\rho_s = 8.07{\cdot}10^2 + 4.77T - 8.84{\cdot}10^{-3}T^2, \quad (2)$$

$$c_s = 1.43 + 2.03{\cdot}10^{-3}T, \quad (3)$$

$$k_s = 2.79 - 1.31{\cdot}10^{-2}T + 1.88{\cdot}10^{-5}T^2, \quad (4)$$

where ρ_s is the density of SAT in the solid phase ($kg{\cdot}m^{-3}$), T is the system temperature (°K), c_s is the specific heat capacity of solid SAT ($J{\cdot}kg^{-1}{\cdot}K^{-1}$), and k_s is the thermal conductivity of solid SAT ($W{\cdot}m^{-1}{\cdot}K^{-1}$). For the reference temperature of 20 °C, the following values were used: a thermal conductivity of 0.576 $W{\cdot}\ m^{-1}{\cdot}\ K^{-1}$, a specific heat capacity of 2015 $J{\cdot}kg^{-1}{\cdot}K^{-1}$, and a density of 1450 $kg{\cdot}\ m^{-3}$. The melting point of SAT was set at 58 °C, which represents a critical threshold temperature in terms of energy storage via latent heat.

All simulations were conducted as transient heat conduction problems without considering phase change or convection, meaning that only conductive heat transfer in the solid PCM was analyzed. The initial temperature of the entire system was uniformly set to 20 °C. A constant heat flux of 1000 $W{\cdot}m^{-2}$ was applied to the external surface of the sheet-gyroid structure, or to the cylindrical surface in the reference case with a solid cylinder, in order to evaluate the effectiveness of heat transfer from the metallic structure into the SAT volume. Outer walls were defined as thermally insulated (adiabatic), thereby eliminating parasitic heat losses to the surroundings and focusing the simulation exclusively on the efficiency of heat conduction through the structure and its distribution within the SAT volume. A representation of the boundary conditions used in the numerical analysis is shown in Figure 2.

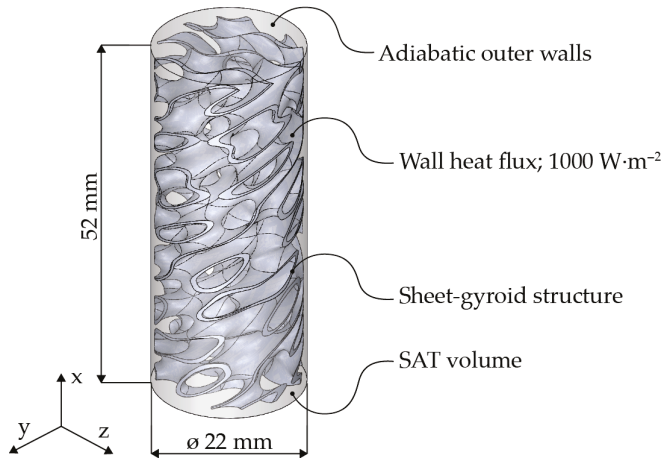

Figure 2. Boundary conditions of the numerical analysis and dimensions of the model.

The numerical analysis was conducted using SolidWorks Flow Simulation software, version 2024. Given the absence of a flowing medium, only the module enabling heat transfer analysis between two solid bodies was activated. During the simulation, no user-defined functions or external codes were employed to modify the computational algorithms. The simulation time domain was defined based on the time required for the minimum temperature of the SAT to reach 58 °C, representing the point at which the entire assessed volume of SAT exceeded its melting temperature. Once this temperature was reached, the calculation was terminated. Data logging was configured at intervals of 0.5 s. The numerical computations were performed using an implicit solver based on the finite volume method (FVM), with a convergence criterion set to 10^{-6} for all governing equations. The governing equation describing the phenomenon of anisotropic heat conduction in solid materials is expressed in Equation (5):

$$\frac{\partial \rho e}{\partial t} = \frac{\partial}{\partial x_i}\left(\lambda_i \frac{\partial T}{\partial x_i}\right) + Q_H, \tag{5}$$

where ρ is density, e is specific internal energy (e = C·T), C is specific heat, T is temperature, Q_H is specific heat release (or absorption) per unit volume, and λ_i are the eigenvalues of the thermal conductivity tensor. It is supposed that the heat conductivity tensor is diagonal in the considered coordinate system. For an isotropic medium, $\lambda_1 = \lambda_2 = \lambda_3 = \lambda$.

For the purposes of numerical simulation, the thermal storage unit model was transformed into a computational mesh, with meshing performed exclusively for regions representing solid bodies—namely, the aluminum sheet-gyroid structure and the volume of the phase change material (SAT) in its solid state. SolidWorks Flow Simulation utilizes a computational mesh based on a Cartesian coordinate system. With this meshing approach, it is not necessary to conform the mesh to the geometry itself; instead, the geometry is "immersed" into a regular grid of cuboidal cells. This allows for efficient meshing of highly complex and organic shapes, such as TPMS structures. Individual mesh cells may intersect multiple material regions, and when they cross the interface between two bodies, the software automatically applies appropriate boundary conditions through the immersed boundary method. This approach is particularly suitable for modeling heat conduction in solid bodies with intricate geometry and in the absence of fluid flow. Since the computational domain was limited exclusively to solid phases, the mesh density requirements were reduced, thereby shortening the overall computational time without compromising result accuracy. However, the effort to minimize computational time can, in some cases, result in reduced simulation accuracy due to an overly coarse mesh resolution. Such simplifications may lead to deviations in output values, not due to the physical characteristics of the model, but as a consequence of an inadequate spatial resolution. To avoid such inaccuracies, it is advisable to perform a mesh independence study, which helps verify whether changes in mesh density significantly affect the simulation results.

For the given geometric configurations, different levels of mesh refinement and optimization methods were sequentially applied, and, for each, the time required for the entire volume of SAT to reach a minimum temperature of 58 °C was evaluated. The results of this comparison are shown in Figure 3, where a clear stabilization of the evaluated variable can be observed with sufficiently refined mesh density, confirming that the simulation outcomes are not dependent on further mesh refinement.

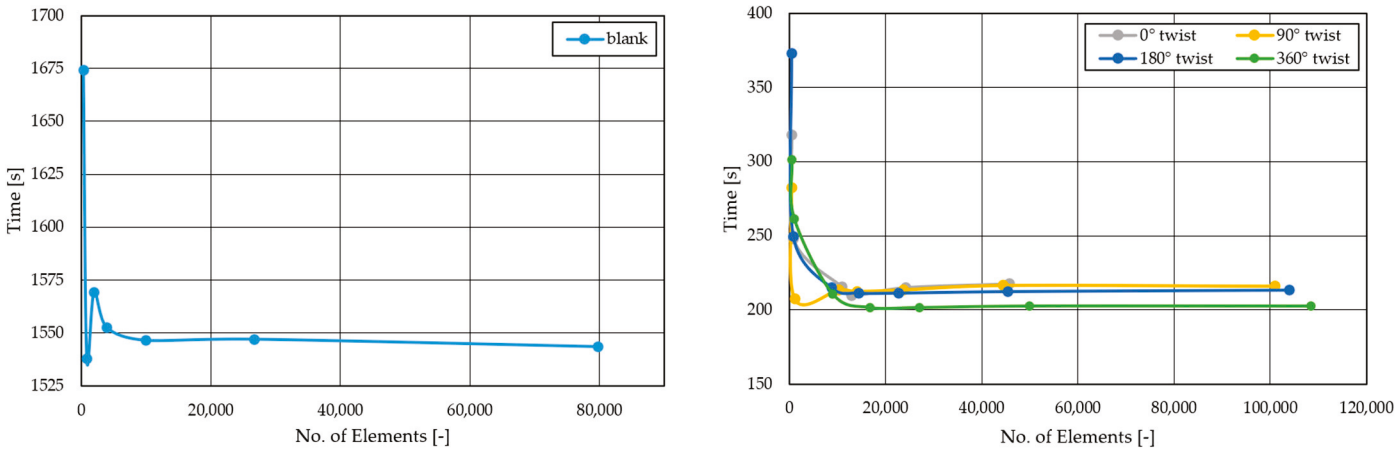

Figure 3. Results of the grid independence study for the reference case without the sheet-gyroid structure (**left**) and for the modeled cases with sheet-gyroid structures twisted by 0°, 90°, 180°, and 360° (**right**).

3. Results and Discussion

One of the main objectives of the numerical analysis was to quantitatively assess the influence of the geometric configuration of the sheet-gyroid structure on the dynamics of heat transfer within the solid phase of the SAT storage medium. Due to the specific thermal behavior of the material, the minimum temperature within the entire SAT volume was selected as the key reference variable. Particular attention was given to the time required to reach 58 °C, which corresponds to the onset of the phase transition from solid to liquid. The simulations were initiated with a uniform system temperature of 20 °C, and a constant heat flux was applied to the external surface of the sheet-gyroid structure (or to the cylindrical shell in the reference case). Throughout the calculation, the time-dependent values of the minimum temperature within the SAT volume were continuously monitored, enabling detailed tracking of the thermal response up to the point at which all regions of the PCM exceeded the phase transition threshold.

For the purposes of interpretation and visualization, the simulation results were processed at two levels of detail. The first graph (Figure 4) presents the complete thermal response over the time interval from 0 to 1600 s and includes all five evaluated configurations—namely, the four versions with the sheet-gyroid structure (rotated by 0°, 90°, 180°, and 360°) as well as the reference model without any structure (denoted as "blank"). The graph clearly demonstrates that embedding a thermally conductive metallic structure within the PCM volume has a significant positive impact on heating efficiency. While the structured cases reached the critical temperature within approximately the first 220 s, the reference model without the structure required around 1543 s to do so. This contrast highlights the effectiveness of using a metallic gyroid matrix in overcoming the limitations imposed by the low thermal conductivity of SAT in its solid state.

Since the differences among the individual versions of the gyroid structure manifested within a narrow time interval, a second visualization was created to better capture these subtle distinctions. The second graph (Figure 5) displays only the cases with sheet-gyroid structures and is zoomed in on the time interval from 180 to 220 s. This magnified time scale allows for precise differentiation of the times required to reach the 58 °C temperature in the whole SAT volume, depending on the specific geometric modification of the structure.

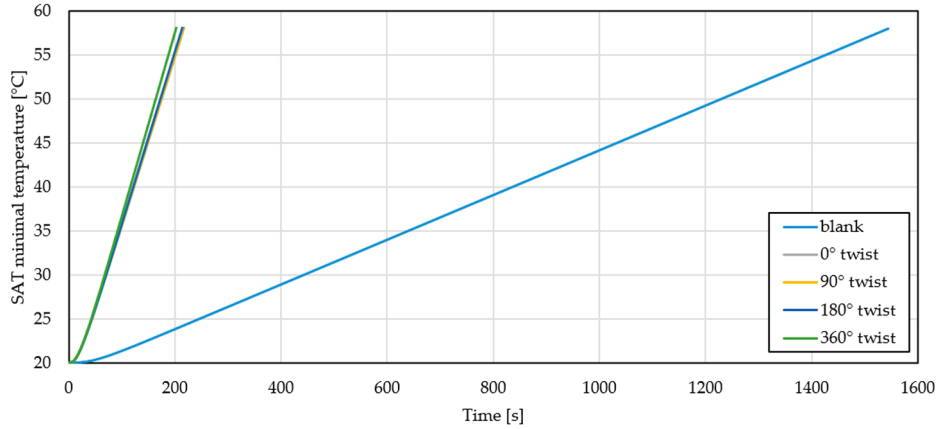

Figure 4. Time evolution of the minimum temperature in the SAT volume until reaching the phase change threshold of 58 °C.

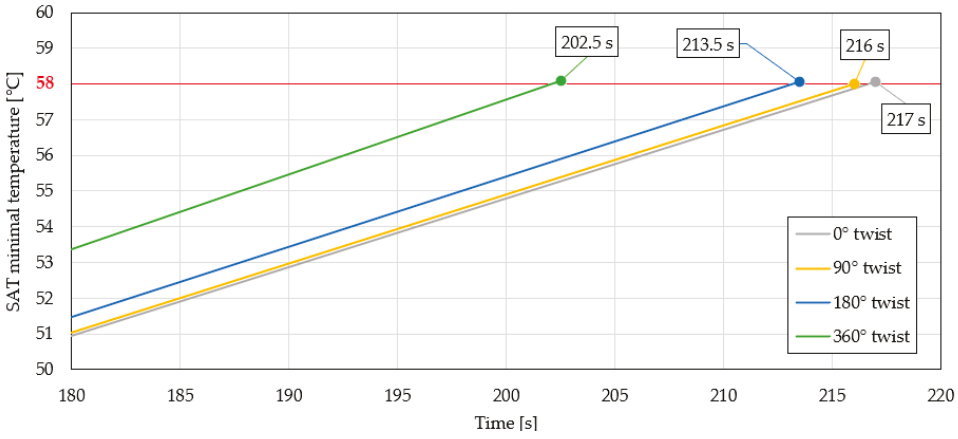

Figure 5. Time evolution of the minimum temperature in the SAT volume until reaching 58 °C for the four selected sheet-gyroid configurations, shown over the interval from 180 to 220 s.

The recorded trend indicates that torsional deformation of the gyroid structure has a positive effect on heat transfer efficiency. The reduction in the required heating time is attributed both to the increase in the active heat exchange surface area and to the altered internal heat flow paths resulting from the geometric reconfiguration of the structure. These results confirm that the geometric optimization of TPMS structures is not merely a structural design experiment but has a tangible impact on system performance, particularly in applications where the storage material has inherently low thermal conductivity.

In addition to the time required to reach the phase change temperature, the analysis also monitored the maximum temperature within the SAT volume at the moment when its minimum temperature reached 58 °C. This parameter provides supplementary insight into the uniformity of the temperature field within the PCM and indicates how effectively the supplied heat is distributed throughout the domain. Ideally, the difference between the minimum and maximum temperature should be as small as possible, as this signifies homogeneous heat transfer and minimizes the risk of local overheating or thermal gradients, factors that can negatively affect the mechanical stability and long-term cyclic durability of the PCM.

The results shown in Figure 6 demonstrate that, at the point when the minimum temperature reached 58 °C, the maximum temperature in the SAT volume varied depending on the structure's geometry. The highest temperature was observed in the 360° twisted structure (63.72 °C), followed by 180° (63.17 °C), 90° (62.94 °C), and the lowest in the base

0° configuration (62.88 °C). The difference between minimum and maximum temperatures thus ranged from 4.88 °C to 5.72 °C. Although these differences are relatively small, the trend suggests that a higher degree of torsion leads to faster heat transfer, but also to slightly higher local overheating. These findings highlight the importance of optimizing the design not only for heating rate but also for temperature uniformity throughout the PCM volume in order to minimize thermal stress and ensure phase change stability during cyclic operation. The spatial location of the temperature maximum can be observed in Figures 7 and 8. It consistently appears in the upper portions of the SAT domain, particularly near the outer boundary where the gyroid surface exhibits higher curvature and longer contact length. These regions are subjected to more intense localized heat transfer due to the proximity to the exposed structure and the tortuous geometry that enhances conductive paths. This thermal behavior explains why configurations with higher torsional deformation, such as the 360° twist, exhibit both faster heating and slightly elevated temperature gradients.

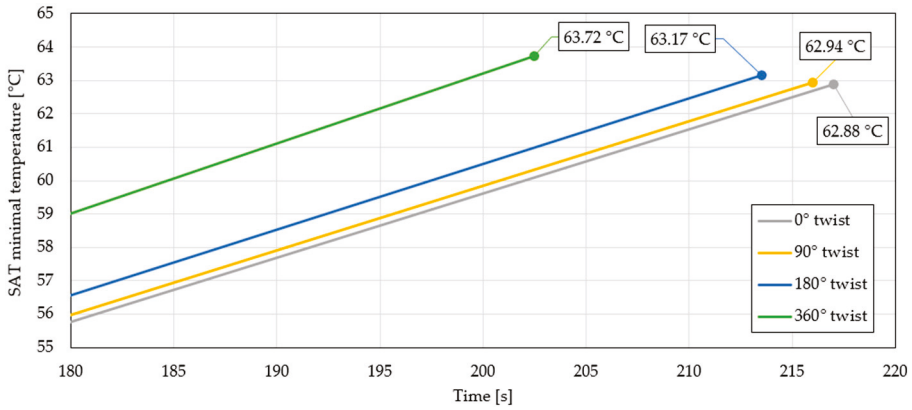

Figure 6. The maximum temperature in the SAT volume at the moment when the entire volume reaches the melting point.

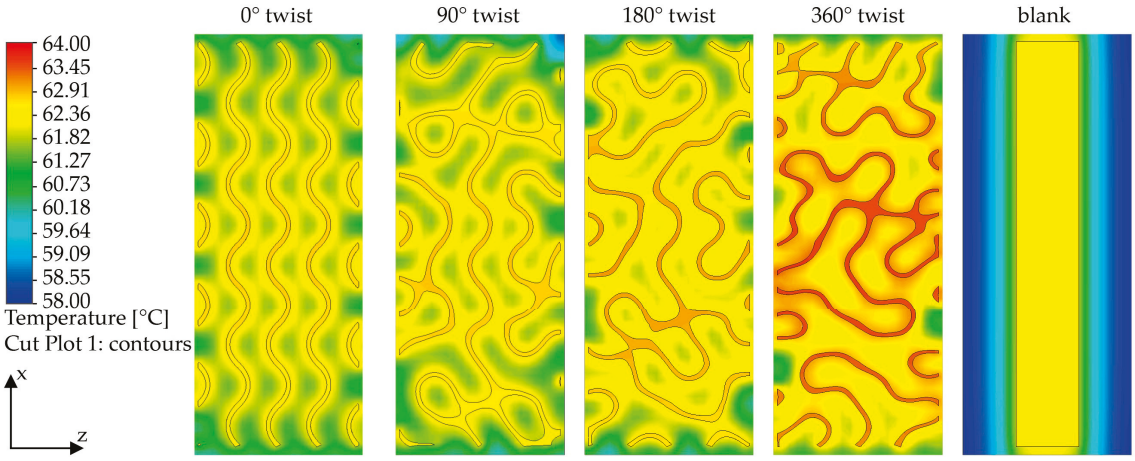

Figure 7. Temperature field distribution on the XZ plane at the center of the model.

As part of the numerical analysis, the heat transfer from the sheet-gyroid structure to the SAT volume was also evaluated quantitatively. Specifically, the heat flux was assessed across the surface of the sheet-gyroid structure that was in direct contact with the SAT. The integral heat transfer was calculated based on local temperature gradients and material properties, yielding the effective thermal power transferred into the adjacent volume. The obtained values served as an important supplementary parameter to the time-based

heating analysis and enabled a comparison of thermal transfer efficiency among different geometric configurations. The results show that the 360° twisted structure delivered the highest thermal power into the SAT—up to 9.596 W—followed by the 180° (8.995 W), 90° (8.849 W), and 0° (8.799 W) configurations. The reference "blank" model, which lacked an internal structure, transferred only 1.168 W—approximately eight times lower than the most efficient structure. These results confirm that increasing the active heat exchange area and altering the internal geometry of the structure have a direct impact on the intensity of energy transfer and that torsional modification of the sheet-gyroid can be an effective tool for optimizing thermal energy storage units.

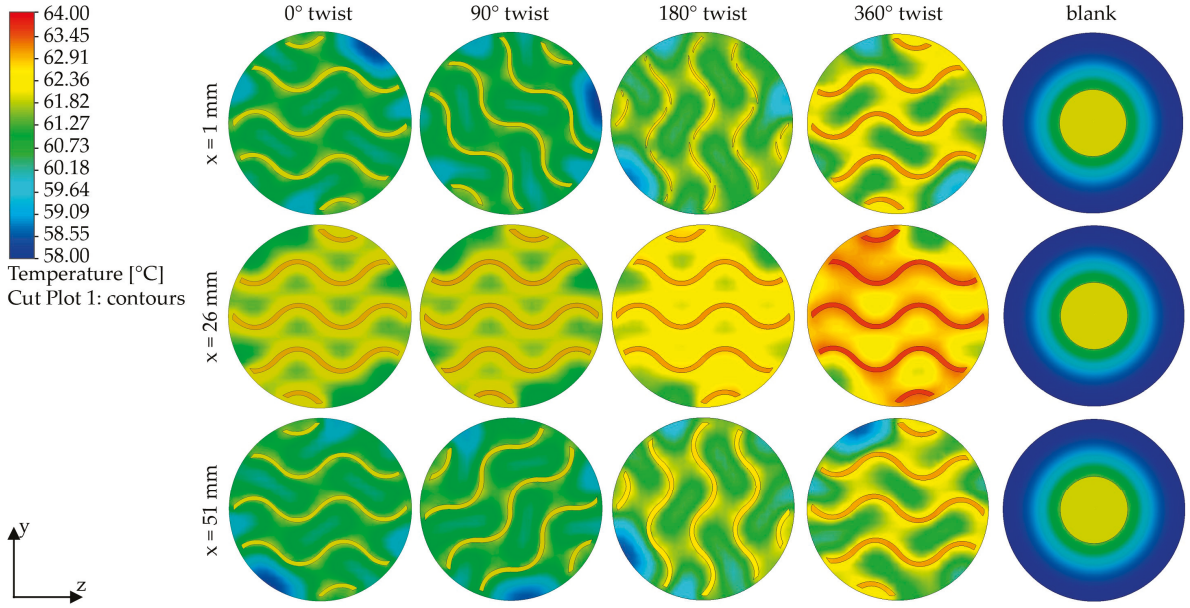

Figure 8. Temperature field distribution in transverse cross-sections of the model (YZ plane) at heights of 1 mm, 26 mm, and 51 mm from the model boundary.

To further investigate heat transfer within the PCM volume and compare the effectiveness of the different geometric configurations, detailed visualizations of the temperature field were generated from cross-sections of the models. These images provide spatial insight into the heat distribution during the charging phase. The first image (Figure 7) displays the temperature distribution on the XZ plane for all five analyzed cases—four with the sheet-gyroid structure and one reference "blank" model without structure. The XZ plane passes through the center of the SAT volume and captures the temperature field at the moment when the minimum temperature in the PCM reaches 58 °C. From the comparison of temperature fields, it is evident that greater torsional deformation of the structure results in more irregular and multi-directional contact areas between the structure and the PCM. This leads to more intensive and deeper heat penetration, visualized as broader regions of elevated temperature—particularly in the 360° configuration, where dominant zones exceeding 63 °C are clearly visible. Conversely, in the reference model without structure, the heat transfer geometry is simple and localized around the cylindrical heating core, with the temperature decreasing toward the outer boundaries. This configuration shows the lowest heat transfer efficiency and the greatest temperature non-uniformity.

The second image (Figure 8) illustrates cross-sections on the YZ plane at three vertical levels: 1 mm, 26 mm, and 51 mm from the base of the model. These cross-sections provide a representative view of the heat distribution along the vertical axis of the PCM. At each

height level, it is evident that configurations with higher torsional rotation ensure a more uniform temperature distribution across the width of the PCM.

Particularly in the 360° configuration, the structure intersects all levels in a multi-dimensional fashion and spans a larger volume, enabling faster and more homogeneous heat penetration into deeper PCM layers. In the 0° and 90° configurations, the structure appears more linear and aligned, resulting in lower heat transfer intensity in the Z-direction. Notably, in the reference case without structure, the isothermal zones are strictly concentric, once again confirming the slow and inefficient heat transfer toward the PCM core. These visualizations clearly demonstrate that not only the presence of a metallic structure but also its geometric modification significantly influence the spatial temperature distribution. The 360° twisted configuration proves to be the most effective, as it utilizes the model volume most efficiently for uniform heat transfer. These insights have direct implications for optimizing the design of phase change thermal energy storage systems, particularly with regard to the strategic geometry of embedded metallic inserts.

An additional important layer of comparison among the evaluated configurations is provided by the visualization of surface temperature on the sheet-gyroid structures, as shown in Figure 9. This visualization offers a three-dimensional overview of the temperature distribution directly on the surface of the metallic structure, which plays a crucial role in transferring heat to the storage medium SAT. Based on previous results, it has already been demonstrated that the degree of torsional deformation of the structure significantly influences the intensity and spatial extent of heat transfer. The surface temperature visualization clearly confirms these findings and provides further insight into the underlying mechanisms.

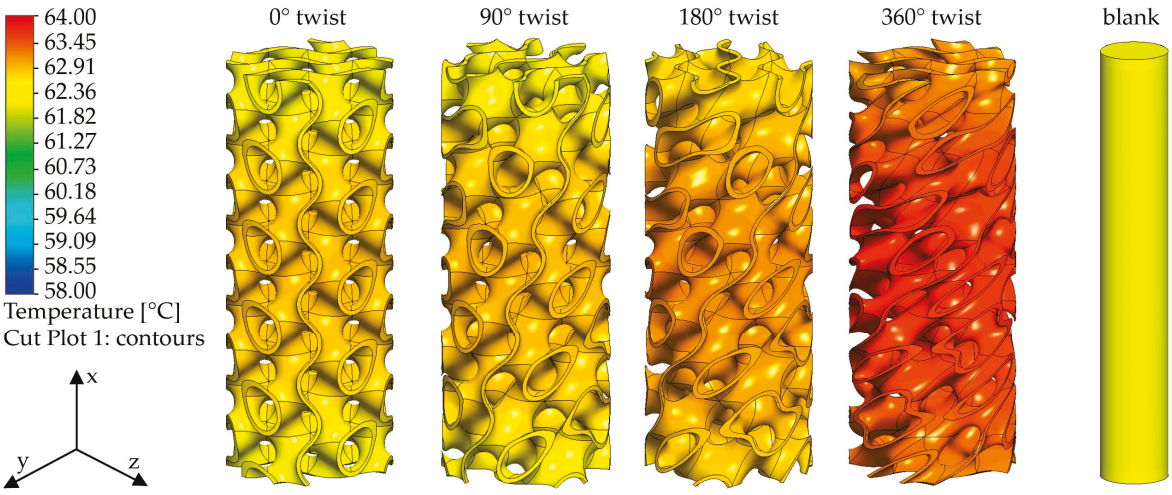

Figure 9. Temperature distribution on the outer surface of the heat exchange structure.

The 360° twisted configuration exhibits the highest surface temperature values—large areas of the structure reach up to 64 °C, the maximum temperature observed in the entire simulation. This phenomenon is associated with the effective "unfolding" of the heat exchange surface, which in this configuration is more geometrically curved, thereby increasing the contact area between the aluminum and the PCM while simultaneously shortening the thermal pathways required for heat to penetrate into the deeper layers of SAT. This effect has previously been supported by the recorded maximum heat transfer rate (9.596 W) and the shortest time to heat the entire SAT volume to 58 °C.

A gradual decrease in surface temperature intensity, visible as less intense coloration, is observed for configurations with lower degrees of twist (180°, 90°, and 0°), which correlates

directly with their lower recorded heat transfer rates and maximum temperatures in the PCM. Although the 180° and 90° configurations still exhibit slightly elevated surface temperatures compared with the base version (0°), the extent of their hottest surface zones (depicted in red to dark orange tones) is significantly smaller than in the 360° case. The base version without torsional deformation (0°) shows a uniformly distributed surface temperature with a significantly lower maximum and lower heat transfer dynamics, which is reflected in the longest heating time among all structured variants.

The reference case without any structure ("blank") appears as a uniformly yellow cylinder, indicating a stabilized and limited surface temperature resulting from poor heat transfer efficiency. This visualization aligns with the previously presented graphs, where the blank case was characterized by the lowest heat flux (1.168 W) and the fastest transition into thermal stagnation, caused by the insufficient dispersion of the input energy throughout the PCM volume.

In summary, the surface temperature visualization provides compelling evidence that the intensity and uniformity of structure heating are critical factors in the overall efficiency of heat storage in PCM. The 360° torsional configuration, in particular, demonstrates that proper geometric design of the structure not only increases the heat exchange surface area but also ensures higher local temperatures, thus promoting efficient and dynamic heat transfer into the thermal storage medium.

Based on the presented results, it can be concluded that the integration of a metallic sheet-gyroid structure into the volume of the thermal storage medium SAT significantly improves the dynamics of heat transfer. In all cases involving the structure, a reduction of more than 85% in the time required to reach the phase change temperature (58 °C) was observed compared with the reference model without the structure. The most effective configuration was the one with a 360° torsional twist, which achieved the target temperature in just 202.5 s. This variant also exhibited the highest heat flux and most intense surface heating of the structure, confirming the high efficiency of thermal energy transfer into the PCM volume. Graphical outputs further revealed that geometric modification of the structure affects not only the heating rate but also the temperature distribution within the PCM. Torsionally modified configurations ensured a more uniform distribution and more extensive coverage of the active volume. These findings clearly confirm the importance of the spatial arrangement of TPMS structures in optimizing the performance of phase change thermal energy storage systems.

Despite the significant improvements in heat transfer rate and temperature uniformity achieved by embedding sheet-gyroid structures in the SAT volume, certain limitations must be considered for their practical implementation in real-world storage systems. First, the geometric complexity of TPMS structures requires advanced manufacturing techniques, which can be technologically and economically demanding—especially for large-scale applications. The material and time-intensive production of components using metals like aluminum 6061 presents a barrier, particularly if the structures are intended to be integrated into compact modular units for commercial or residential use.

Another important consideration is the interaction between the metallic structure and the PCM. As an organic substance, SAT may undergo volumetric changes during repeated melting and solidification cycles, potentially causing mechanical stress at the interface with the structure and leading to material failure. In addition, fouling or chemical degradation within the narrow channels of the structure may reduce the effective heat exchange area over time and compromise the system's long-term stability. Air entrapment or improper PCM distribution during manufacturing and filling processes may also pose challenges, particularly in structures with very fine internal channels.

From a practical standpoint, successful implementation of sheet-gyroid structures requires optimization not only of their shape and placement but also of the enclosure design, PCM filling strategy, material compatibility, and thermal cycling performance. These aspects should be the subject of further experimental research focused on validating the mechanical, chemical, and thermal stability under long-term operating conditions, as well as evaluating the real-world feasibility of large-scale manufacturing and deployment.

While the present study focuses exclusively on torsional deformation of the sheet-gyroid structure, it is acknowledged that other forms of geometric modification—such as bending, expansion, or spatially localized distortion—could also affect the thermal conductivity and flow characteristics of the system. These deformation modes remain outside the scope of the current analysis but will be considered in future work to build a more comprehensive understanding of geometric influences on TPMS-based thermal storage systems.

4. Conclusions

The presented numerical study focused on evaluating the effect of various geometric configurations of sheet-gyroid structures on the efficiency of heat transfer in thermal energy storage systems utilizing sodium acetate trihydrate as a phase change material. The primary objective was to propose a solution to compensate for the low thermal conductivity of SAT in its solid phase, which significantly limits the rate of heat accumulation in such systems. The integration of a three-dimensional metallic sheet-gyroid structure made from aluminum 6061 was identified as a promising strategy for enhancing heat distribution throughout the PCM volume and accelerating the charging phase.

Four distinct geometric variants of the structure, differing in the degree of torsional deformation (0°, 90°, 180°, and 360°), were evaluated through simulation, along with a reference model without an embedded skeletal structure. The main evaluated output was the time required to raise the entire SAT volume to the minimum temperature of 58 °C, which marks the onset of the phase transition—a key milestone in latent heat storage. The results demonstrate that all four configurations with embedded structures significantly reduced the heating time compared with the reference case. While the blank model without a structure reached the threshold temperature after approximately 1560 s, the 360° twisted configuration achieved it in just about 202.5 s. The other geometries also exhibited high performance, reaching 58 °C in 213.5 s (180°), 216.0 s (90°), and 217.0 s (0°).

Supplementary analyses revealed that torsional modification not only affects the heating rate but also influences the temperature distribution within the PCM volume. Thermal maps from various cross-sections (XZ and YZ planes) demonstrated that configurations with greater torsion enable deeper spatial penetration of heat, a more uniform thermal energy distribution, and the minimization of cold zones. The visualization of surface temperatures on the structures confirmed that higher torsion resulted in higher local surface temperatures, indicating an increased instantaneous energy flux into the SAT. This observation was supported by quantitative heat flux data: the 360° configuration reached a thermal transfer rate of 9.596 W, followed by 8.995 W (180°), 8.849 W (90°), and 8.799 W (0°). The reference model without a structure yielded only 1.168 W, indicating significantly lower heat transfer efficiency into the PCM.

Despite the enhanced performance in terms of heat transfer and faster heating associated with higher torsion, a slight increase in the maximum temperature within the SAT was observed, suggesting the presence of increased thermal gradients. This phenomenon must be considered in the design of systems requiring high thermal homogeneity, such as those intended to prevent localized degradation of PCM or structural materials.

Based on the findings, it can be concluded that geometric optimization of TPMS structures—particularly through torsional deformation—represents an effective and viable approach for enhancing the performance of phase change thermal energy storage systems. The results demonstrate that the shape and spatial arrangement of the metallic insert are just as critical as its mere presence. From an application standpoint, this opens new opportunities for customized 3D-printed structures tailored to specific operational conditions and performance requirements. In the broader context of solar energy utilization, the demonstrated improvements in charging time and heat distribution position the investigated TPMS-based design as a promising candidate for latent heat storage units operating in solar thermal systems. The efficient and compact integration of these structures can support thermal buffering and load shifting in domestic or small-scale industrial solar applications, thereby contributing to more reliable and flexible use of renewable solar resources. In addition to solar thermal energy systems, the results of this study can be extrapolated to other application domains that require efficient and compact thermal regulation. For example, the enhanced heat transfer dynamics demonstrated by the torsionally modified TPMS structures are particularly beneficial in electronics cooling, where localized heat buildup must be rapidly dissipated, and in HVAC systems, where smart thermal buffering can help stabilize temperature fluctuations. The adaptability of the gyroid design and the scalability of additive manufacturing support the integration of this concept into modular systems across a wide range of operating temperatures and spatial constraints.

From an industrial point of view, the use of aluminum alloys such as Al 6061 is fully compatible with modern additive manufacturing processes, particularly selective laser melting (SLM), which allows for the fabrication of complex geometries like the sheet-gyroid with high precision. Regarding geometry, the proposed wall thickness of 0.5 mm lies near the lower limit of manufacturability for most metal AM systems, but remains feasible under controlled conditions. The torsional deformation introduced by the twist operation increases surface complexity, which may affect powder removal and support strategies during fabrication. Therefore, while technically achievable, such manufacturing requires careful orientation planning, laser path optimization, and possibly segmentation of the geometry for post-assembly. These considerations are critical for translating simulation concepts into physical prototypes and will be addressed in subsequent experimental work. The geometric flexibility offered by AM enables design-driven performance optimization without the limitations of traditional casting or machining. Furthermore, sodium acetate trihydrate is a commercially available and chemically stable PCM that has already found practical use in low- to medium-temperature thermal storage. Its well-documented safety, affordability, and recyclability make it suitable for large-scale deployment. Together, the choice of material and manufacturing method supports the practical realization of the proposed thermal storage concept in various industrial and residential energy systems.

It should be acknowledged that the current study does not include direct validation against analytical or experimental benchmarks. Due to the exclusion of latent heat modeling, the simulation represents a transient conduction problem in a complex 3D domain. While analytical or semi-analytical solutions exist for canonical cases, the highly intricate geometry of the embedded TPMS and the inclusion of conjugate heat transfer effects prevent straightforward comparison. Therefore, the presented results are intended for comparative evaluation across the investigated geometries rather than for absolute thermal prediction. In future work, experimental validation using 3D-printed gyroid structures and embedded thermocouples will be conducted to confirm the observed numerical trends.

Future research should focus on the experimental validation of the simulation results, particularly in the areas of the cyclic stability, repeated melting, and solidification

behavior of PCM, and verification of thermal field predictions via thermographic analysis. Further development could also explore the integration of torsionally modified structures with multi-material inserts, gradient geometries, or the design of hybrid storage systems employing multiphase mixtures.

Author Contributions: Conceptualization, M.B. and R.R.; methodology, M.B.; formal analysis, M.B.; investigation, M.B.; data curation, M.B.; writing—original draft preparation, M.B.; writing—review and editing, M.B.; visualization, M.B.; supervision, R.R.; project administration, R.R.; funding acquisition, R.R. All authors have read and agreed to the published version of the manuscript.

Funding: This research was funded by KEGA: 056TUKE-4/2024, a platform for the effective creation, evaluation, and transfer of innovations and the efficient management of university research outputs with a practical orientation.

Data Availability Statement: The original contributions presented in this study are included in the article. Further inquiries can be directed to the corresponding author.

Conflicts of Interest: The authors declare no conflicts of interest.

References

1. Véle, F.; Ackermann, M.; Macháček, J.; Šafka, J. Case Study of Additively Manufactured Mountain Bike Stem. *Materials* **2023**, *16*, 4717. [CrossRef] [PubMed]
2. Spirrett, F.; Ito, T.; Kirihara, S. High-Speed Alumina Stereolithography. *Appl. Sci.* **2022**, *12*, 9760. [CrossRef]
3. Moghimian, P.; Poirié, T.; Habibnejad-Korayem, M.; Arreguin Zavala, J.; Kroeger, J.; Marion, F.; Larouche, F. Metal powders in additive manufacturing: A review on reusability and recyclability of common titanium, nickel and aluminum alloys. *Addit. Manuf.* **2021**, *43*, 102017. [CrossRef]
4. Singh, R.; Pratap, R.; Narayanan, J.A.; Thangamani, G.; Krishnan, V.V.; Arjunan, A.; Hughes, D. Advances in additive manufacturing of fuel cells: A review of technologies, materials, and challenges. *Sustain. Mater. Technol.* **2025**, *43*, e01317. [CrossRef]
5. Tanwar, R.S.; Jhavar, S. Multi-wire additive manufacturing: A comprehensive review on materials, microstructure, methodological advances, and applications. *Results Eng.* **2025**, *26*, 104814. [CrossRef]
6. Rayhan, M.T.; Islam, M.A.; Khan, M.; Hasan, M.A.; Mobarak, M.H.; Rimon, M.I.H.; Hossain, N. Advances in additive manufacturing of nanocomposite materials fabrications and applications. *Eur. Polym. J.* **2024**, *220*, 113406. [CrossRef]
7. Liu, G.; Wang, Z.; Yan, C.; Shi, Y. Advances in additive manufacturing of SiC/Al composites: A review. *Rev. Mater. Res.* **2025**, *1*, 100041. [CrossRef]
8. Su, X.; Zhang, Y.; Rao, Y.; Yeranee, K.; Wang, X. Experimental and Numerical Study on Flow and Heat Transfer Characteristics of Additively Manufactured Triply Periodic Minimal Surface (TPMS) Heat Exchangers for Micro Gas Turbine. *Aerospace* **2025**, *12*, 416. [CrossRef]
9. Zhang, J.; Yang, X. Numerical Simulation of Convective Heat Transfer in Gyroid, Diamond, and Primitive Microstructures Using Water as the Working Fluid. *Energies* **2025**, *18*, 1230. [CrossRef]
10. Wang, Z.; Wang, C.; Wu, F.; Liu, Z.; Liu, L.; Wang, D. Design method of gyroid lattice structure based on the load paths direction and capacity. *Addit. Manuf.* **2025**, *97*, 104586. [CrossRef]
11. Samad, A.; Lai, W.-H. Experimental and simulation analysis of heat transfer in Gyroid heat exchangers with variable flow channels. *Int. J. Heat Mass Transf.* **2025**, *239*, 126530. [CrossRef]
12. Dassi, L.; Chatterton, S.; Parenti, P.; Pennacchi, P. Gyroid Lattice Heat Exchangers: Comparative Analysis on Thermo-Fluid Dynamic Performances. *Machines* **2024**, *12*, 922. [CrossRef]
13. Dam, S.; Khondoker, M.A.H. Design and Numerical Investigation of High-Performance Heat Exchangers Containing Triply Periodic Minimal Surface Lattice Structures. *Eng. Proc.* **2024**, *76*, 76. [CrossRef]
14. Alzoubi, M.A.; Al-Ketan, O.; Muthusamy, J.; Sasmito, A.P.; Poncet, S. Mixing performance of T-shape micromixers equipped with 3D printed Gyroid matrices: A numerical evaluation. *Results Eng.* **2023**, *17*, 100811. [CrossRef]
15. Çiçek, B. A numerical comparison of the thermal performances of nano-PCM heat sinks with Fe_3O_4, MgO, ZnO and xGNP nanoparticles: Key role of increased thermal conductivity. *Therm. Sci. Eng. Prog.* **2025**, *63*, 103712. [CrossRef]
16. Sharma, A.; Raaj, R.V.; Singh, S.; Kothadia, H. Inducing and controlling supercooling in industrial-grade sodium acetate trihydrate for long-term PCM based thermal energy storage system. *Energy* **2025**, *325*, 136164. [CrossRef]

17. Li, W.; Zhao, J.; Wang, J.; Li, S.; Zhang, X.; Zhao, J. Review of sodium acetate trihydrate as phase change material: Mechanism analysis, modification scheme and application. *J. Energy Storage* **2024**, *97*, 112923. [CrossRef]
18. Yang, H.; Bao, X.; Cui, H.; Lo, T.Y.; Chen, X. Optimization of supercooling, thermal conductivity, photothermal conversion, and phase change temperature of sodium acetate trihydrate for thermal energy storage applications. *Energy* **2022**, *254*, 124280. [CrossRef]
19. Garay Ramirez, B.M.L.; Glorieux, C.; San Martin Martinez, E.; Flores Cuautle, J.J.A. Tuning of thermal properties of SAT by blending with polymer and silver nanoparticles. *Appl. Therm. Eng.* **2014**, *62*, 838–844. [CrossRef]
20. Wang, Z.; Huang, G.; Jia, Z.; Gao, Q.; Li, Y.; Gu, Z. Eutectic Fatty Acids Phase Change Materials Improved with Expanded Graphite. *Materials* **2022**, *15*, 6856. [CrossRef]
21. Myat, L.P.; Ahmad, M.S.; Pulidindi, I.N.; Algarni, H.; Kumar, L.; Kalam, A.; Wageh, S.; Pandey, A.K.; Akbar, A.; Selvaraj, J. Effect of Polyethylene Glycol and Activated Carbon Macroparticles on Thermal Conductivity of Paraffin Wax for Thermal Storage Applications. *Polymers* **2022**, *14*, 4181. [CrossRef] [PubMed]
22. Liu, G.; Li, Y.; Wei, P.; Xiao, T.; Meng, X.; Yang, X. Thermo-Economic Assessments on a Heat Storage Tank Filled with Graded Metal Foam. *Energies* **2022**, *15*, 7213. [CrossRef]
23. Hassan, F.; Hussain, A.; Jamil, F.; Arshad, A.; Ali, H.M. Passive Cooling Analysis of an Electronic Chipset Using Nanoparticles and Metal-Foam Composite PCM: An Experimental Study. *Energies* **2022**, *15*, 8746. [CrossRef]
24. Falcone, M.; Rehman, D.; Dongellini, M.; Naldi, C.; Pulvirenti, B.; Morini, G.L. Experimental Investigation on Latent Thermal Energy Storages (LTESs) Based on Pure and Copper-Foam-Loaded PCMs. *Energies* **2022**, *15*, 4894. [CrossRef]
25. Al-Najjar, H.M.T.; Mahdi, J.M.; Bokov, D.O.; Khedher, N.B.; Alshammari, N.K.; Catalan Opulencia, M.J.; Fagiry, M.A.; Yaïci, W.; Talebizadehsardari, P. Improving the Melting Duration of a PV/PCM System Integrated with Different Metal Foam Configurations for Thermal Energy Management. *Nanomaterials* **2022**, *12*, 423. [CrossRef]
26. Chen, Q.; Wu, J.; Sun, K.; Zhang, Y. Numerical Study of Heat Transfer Enhancement by Arc-Shaped Fins in a Shell-Tube Thermal Energy Storage Unit. *Energies* **2022**, *15*, 7799. [CrossRef]
27. Zhao, L.; Xing, Y.; Liu, X.; Luo, Y. Thermal performance of SAT based composite phase change material for thermal energy storage. *Appl. Therm. Eng.* **2018**, *143*, 172–181. [CrossRef]
28. Beer, M.; Rybár, R. Numerical Investigation of Sheet-Gyroid Structure Modifications for Mixing Application in Renewable Energy Technologies. *Energies* **2025**, *18*, 2265. [CrossRef]
29. Beer, M.; Rybár, R. Optimisation of Heat Exchanger Performance Using Modified Gyroid-Based TPMS Structures. *Processes* **2024**, *12*, 2943. [CrossRef]
30. Beer, M.; Rybár, R. Numerical Study of Fluid Flow in a Gyroid-Shaped Heat Transfer Element. *Energies* **2024**, *17*, 2244. [CrossRef]
31. Al-Ketan, O.; Abu Al-Rub, R.K. Multifunctional Mechanical Metamaterials Based on Triply Periodic Minimal Surface Lattices. *Adv. Eng. Mater* **2019**, *21*, 1900524. [CrossRef]
32. Güémez, J.; Fiolhais, C.; Fiolhais, M. Quantitative experiments on supersaturated solutions for the undergraduate thermodynamics laboratory. *Eur. J. Phys.* **2005**, *26*, 25. [CrossRef]
33. Kenisarin, M.; Mahkamov, K. Salt hydrates as latent heat storage materials: Thermophysical properties and costs. *Sol. Energy Mater. Sol. Cells* **2016**, *145*, 255–286. [CrossRef]

Disclaimer/Publisher's Note: The statements, opinions and data contained in all publications are solely those of the individual author(s) and contributor(s) and not of MDPI and/or the editor(s). MDPI and/or the editor(s) disclaim responsibility for any injury to people or property resulting from any ideas, methods, instructions or products referred to in the content.

energies

MDPI

Article

Analysis of Heat Transfer and Fluid Flow in a Solar Air Heater with Sequentially Placed Rectangular Obstacles on the Fin Surface

Byeong-Hwa An [1], Kwang-Am Moon [1], Seong-Bhin Kim [2] and Hwi-Ung Choi [1,*]

[1] Department of Refrigeration and Air-Conditioning Engineering, Chonnam National University, Yeosu 59626, Republic of Korea; or7i16@naver.com (B.-H.A.); topo6785@naver.com (K.-A.M.)
[2] Department of Mechanical Engineering, Ulsan National Institute of Science and Technology, Ulsan 44919, Republic of Korea; tjdqls3821@unist.ac.kr
* Correspondence: choihu@jnu.ac.kr

Abstract: A solar air heater (SAH) converts solar energy into heated air without causing environmental pollution. It features a low initial cost and easy maintenance due to its simple design. However, owing to air's poor thermal conductivity, its thermal efficiency is relatively low compared to that of other solar systems. To improve its thermal performance, previous studies have aimed at either enlarging the heat transfer surface or increasing the convective heat transfer coefficient. In this study, a novel SAH with fins and sequentially placed obstacles on the fin surface—designed to achieve both surface extension through a finned channel and enhancement of the heat transfer coefficient via the obstacles—was investigated using computational fluid dynamics analysis. The results confirmed that the obstacles enhanced heat transfer performance by up to 2.602 times in the finned channel. However, the obstacles also caused a pressure loss. Therefore, the thermo-hydraulic performance was discussed, and it was concluded that the obstacles with a relative height of 0.12 and a relative pitch of 10 yielded the maximum THP values among the investigated conditions. Additionally, correlations for the Nusselt number and friction factor were derived and predicted the simulation values with good agreement.

Keywords: solar air heater; solar energy utilization; CFD; Nusselt number; friction factor

1. Introduction

As environmental pollution and energy depletion issues arise due to the significant increase in fossil fuel usage, interest in transitioning from traditional energy sources to renewable energy is growing worldwide. A solar air heater (SAH) is a renewable energy system that converts solar irradiance into heated air without causing environmental pollution. This system offers advantages in terms of initial cost, manufacturing, and maintenance owing to its uncomplicated configuration relative to other solar conversion devices. It can be utilized for several purposes, including space heating, food drying, pre-heating for industrial processes, and more [1]. However, the poor thermal conductivity of air decreases the convective heat transfer coefficient between the absorber and the flowing air in an SAH, thereby causing relatively lower thermal efficiency compared to other types of solar conversion systems [2,3]. Therefore, many studies have been conducted to address this issue.

One effective approach to augment the thermal performance of an SAH is to extend the surface area of the heat transfer in its air channel. Pakdaman et al. [4] integrated an SAH with longitudinal fins and experimentally evaluated its performance under natural convection. Their research showed that the inclusion of fins led to a notable increase in the SAH's performance. Fudholi et al. [5] compared double-pass SAHs with and without fins through numerical analysis and concluded that inserting fins effectively improves the thermal efficiency of an SAH. Priyam and Chand [6] investigated a wavy-finned SAH using a numerical method and confirmed that an SAH with a wavy fin achieved higher thermal efficiency compared to an SAH without a wavy fin. Kabeel et al. [7] experimentally assessed the daily thermal performance of a finned SAH with various fin heights. Their study revealed that higher fin heights led to higher efficiency. Chand et al. [8] suggested an SAH with louvered fins and conducted an experimental study. Their study concluded that incorporating louvered fins improved the thermal efficiency of a cumulative SAH by up to 106.7% compared to an SAH without fins. Karwa [9] established a numerical model of a finned SAH with a rectangular air flow channel and demonstrated that their SAH had about 31% higher thermal efficiency relative to the conventional SAH. Vengadesan et al. [10] proposed an SAH with discontinuous V-corrugated fins and rectangular tubes and found that the proposed SAH performed better than a conventional SAH, despite the increased pressure penalty. Elakrout et al. [11] compared a double-pass SAH with three different fin configurations—vertical, parallel, and opposed—using computational fluid dynamics (CFD). Their study indicated that the configuration of the fin provided the highest thermal performance among the fins investigated. In addition to these studies, various fin types, such as offset strip fins [12], C-shaped fins [13], and double triangular fins [14], have also been investigated.

Another method is to boost the heat transfer coefficient at the heated wall through the incorporation of ribs, obstacles, baffles, etc. [15]. Yadav and Bhagoria [16–18] demonstrated, through CFD analysis, that installing circular, triangular, or square ribs on the heated wall can effectively enhance heat transfer performance. Gawande et al. [19] analyzed heat transfer augmentation due to reverse L-shaped ribs. Their research found that the ribs improved the heat transfer coefficient at the heated wall by up to 2.827 times. Singh and Singh [20] investigated an SAH with square wave-profiled transverse ribs of various heights and pitches, and demonstrated that the ribs could improve heat transfer by up to 2.14 times. Singh et al. [21] experimentally and numerically evaluated the thermal behavior of an SAH with multiple broken transverse ribs. Their study demonstrated that the proposed ribs achieved maximum thermal enhancement by 3.24 times while increasing the pressure drop by 3.85 times. Kumar and Goel [22] performed a CFD analysis to evaluate an SAH with various rib shapes in a triangular airflow channel. Their research indicated that backward-chamfered rectangular ribs outperformed ribs of other shapes. Boussouar et al. [23] analyzed an SAH equipped with perforated baffles and indicated that incorporating baffles with holes enhances heat transfer performance while reducing pressure drop. Kumar et al. [24] evaluated an SAH with polygonal ribs using CFD analysis for various rib pitches and Reynolds numbers (*Re*), and reported that the polygonal rib enhanced thermal performance for all fin pitches and *Re* compared to an SAH without ribs. In addition, various designs, such as an SAH with plus-shaped baffles [25], dimples [26], triangular blocks [27], wavy ribs [28], one-eighth sphere vortex generators [29], and rotating cylindrical turbulators [30], have also been evaluated. Further studies can be found in comprehensive review articles [3,15,31–34].

So far, many studies have been conducted, as revealed in the aforementioned literature review. However, most of these studies have been conducted either by incorporating

extended surfaces or by enhancing the convective heat transfer coefficient. If obstacles are combined with a finned surface, the heat transfer coefficient at the finned surface can be improved while simultaneously extending the heat transfer surface area. Accordingly, in a previous study, the authors demonstrated that attaching obstacles to the finned channel improved heat transfer performance [35]. In this study, the installation locations of the base and side obstacles were restricted to the same position. Hence, in a further study, it was confirmed that the sequential installation of obstacles along the finned surface yielded the highest thermo-hydraulic performance [36]. However, the heat transfer and fluid flow characteristics can vary considerably depending on the obstacle height and pitch. Despite this, the effects of these geometric parameters have not yet been thoroughly analyzed for sequentially placed obstacles in a finned air channel.

To fill this research gap, this study investigates thermal and flow characteristics in a fin channel of an SAH with sequentially placed rectangular obstacles using CFD analysis. Heat transfer enhancement and pressure loss were evaluated for various obstacle heights and pitches under different *Re* values. The thermo-hydraulic performance was also assessed to account for both the improvement in heat transfer and the associated pressure drop. Additionally, correlations for the Nusselt number (Nu) and friction factor (f) were derived from the simulation results as dependent variables of geometric conditions and *Re*. The objective of this study is to explore how the height and pitch of sequentially placed obstacles affect heat transfer and pressure loss, and to identify the geometric conditions that yield the highest performance.

2. Methodology

2.1. Description of the Model

Figure 1 presents a schematic illustrating an SAH featuring sequentially placed obstacles in the finned air channel. The absorber is in contact with the base plate of the fin. The obstacles are sequentially placed on both the upper side and vertical faces of the fin, boosting convective heat transfer along the fin surfaces.

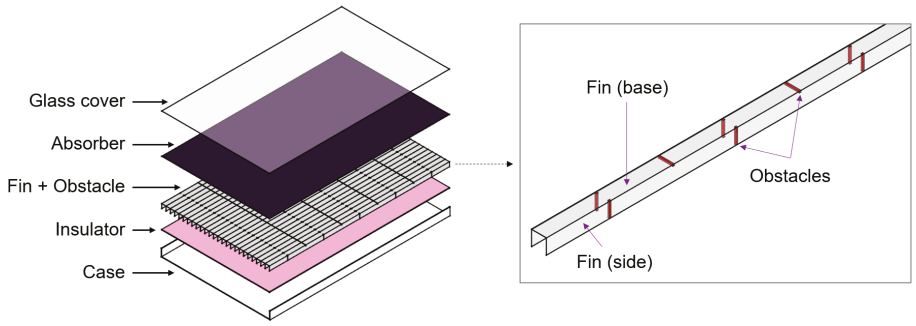

Figure 1. A schematic of an SAH with sequentially placed obstacles in a finned air channel.

This study aims to analyze the thermal and fluid flow characteristics with different configurations of obstacle height and pitch. Accordingly, one of these finned channels was selected for analysis. A symmetric condition was implemented along the mid-plane of the selected finned channel and the fin's lateral surface to minimize the simulation domain. Figure 2 illustrates the computational domain developed using the commercial software ANSYS Fluent 2023 R1, including the specified boundary conditions. The computational domain consists of an entrance section which is 120 mm long, a test section which is 1000 mm long, and an exit section which is 60 mm long. The finned air channel and obstacles are located in the test section. Four different relative heights, ranging from 0.04 to

0.28, and four different relative pitches, ranging from 10 to 34, were used, selected based on related previous research [17,20,25,28], while the width and height of the finned channel remained fixed. Five different *Re* values, varying from 3000 to 15,000, were used for each configuration. As a result, a total of 80 cases were investigated. Table 1 summarizes the values of the geometric conditions for the investigated computational domain.

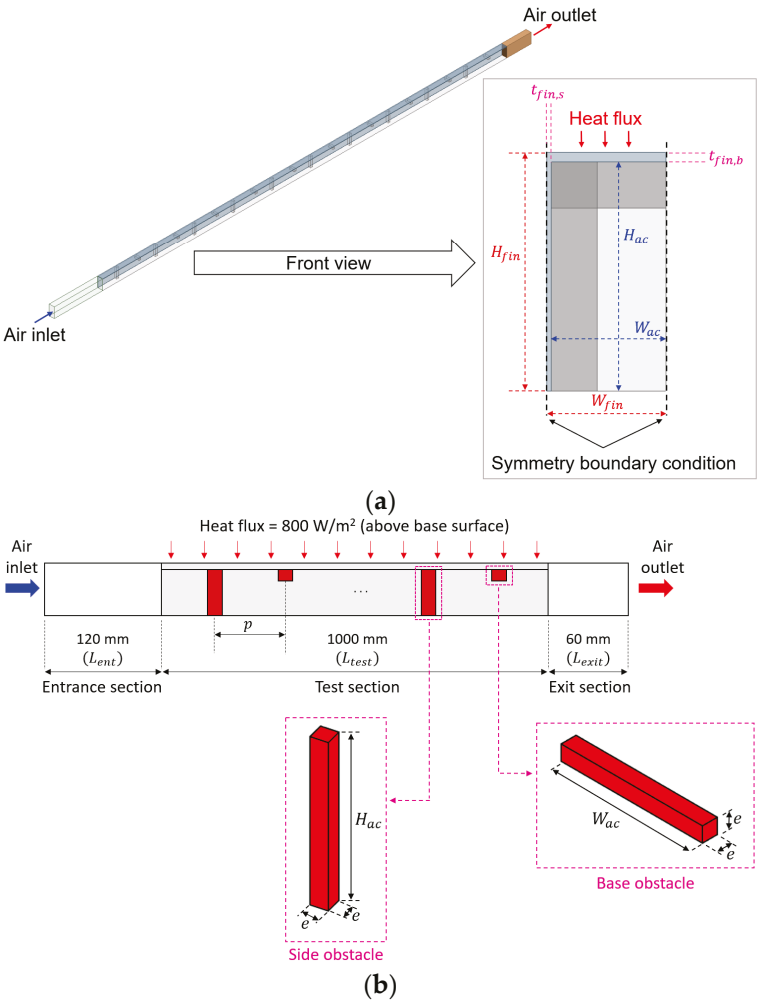

Figure 2. The computational domain of the SAH: (**a**) isometric view; (**b**) side view.

Table 1. The geometric conditions of a computational domain.

Parameter	Nomenclature	Value
Length of entrance section (mm)	L_{ent}	120
Length of test section (mm)	L_{test}	1000
Length of exit section (mm)	L_{exit}	60
Height of fin (mm)	H_{fin}	25
Width of fin (mm)	W_{fin}	12.5
Height of finned channel (mm)	H_{ac}	24
Width of finned channel (mm)	W_{ac}	12
Thickness of side fin (mm)	$t_{fin,s}$	0.5
Thickness of base fin (mm)	$t_{fin,b}$	1
Hydraulic diameter of finned channel (mm)	D_h	24
Relative height (-)	e/D_h	0.04, 0.12, 0.20, 0.28
Relative pitch (-)	p/e	10, 18, 26, 34

2.2. Boundary Conditions and Solution Method

As boundary conditions, a constant velocity inlet with an air temperature of 300 K was specified. At the outlet, a constant pressure of 101.325 kPa was applied [19,22,28]. A heat flux of 800 W/m^2 was applied to the top surface of the base fin, which has commonly been used in similar studies [3,31,37,38], while the remaining walls were treated as adiabatic. Consequently, the air introduced at 300 K was heated in the finned air channel. Additionally, a no-slip condition was applied to all solid surfaces. Table 2 summarizes the boundary conditions adopted in the simulation.

Table 2. Boundary conditions.

Boundary	Condition	Value
Top of base surface	Heat flux (W/m^2)	800
Mid-plain of finned channel	Symmetry	-
Fin's side surface	Symmetry	-
Other walls	Adiabatic	-
Inlet	Reynolds number (-)	3000, 6000, 9000, 12,000, 15,000
	velocity (m/s)	1.683, 3.366, 5.048, 6.731, 8.414
Outlet	Pressure (kPa)	101.325

To solve the computational domain, the commercial software ANSYS Fluent was used. The continuity, momentum, energy, and turbulence equations were solved using the aforementioned boundary conditions, assuming steady-state and incompressible flow. To link the velocity and pressure, a coupled algorithm was adopted. The governing equations were discretized using a second-order upwind scheme. The convergence criteria were set to 10^{-6} for the energy equation and 10^{-5} for the other equations.

2.3. Grid Independence Test

A 3D model for the simulation was prepared using ANSYS Design Modeler, and a non-uniform mesh was generated with ANSYS ICEM CFD. The number of cells was increased from 1,381,060 to 8,486,004 to confirm grid independence. To ensure grid independence, the Nusselt number and friction factor were evaluated, similar to the other relative studies [22,30,39]. Table 3 presents the variations in Nusselt number at the base surface (Nu_b); Nusselt number at the side surface (Nu_s); and average friction factor (f_{avg}) with changes in cell number for a relative height (e/D_h) of 0.12, a relative pitch of 10 (P/e), and a Re of 9000. The results fluctuated with increasing cell number. However, the changes in results indicated that further increases in cell number beyond 5,250,974 led to changes in Nu_b, Nu_s, and f_{avg} of less than 1%. Therefore, a cell number of 5,250,974 was selected for further analysis. The computational domain with the chosen mesh density is shown in Figure 3.

Table 3. Changes in Nu_s, Nu_b, and f_{avg} with various cell numbers.

Cell Number	Nu_s(-)	Change in Nu_s (%)	Nu_b (-)	Change in Nu_b (%)	f_{avg} (-)	Change in f_{avg} (%)
1,381,060	59.62	-	63.41	-	0.07045	-
2,779,150	59.25	0.62	58.24	8.16	0.08425	19.59
5,250,974	59.98	1.23	58.99	1.29	0.08430	0.06
6,622,861	59.89	0.14	59.29	0.51	0.08396	0.40
8,486,004	60.35	0.77	59.65	0.61	0.08408	0.14

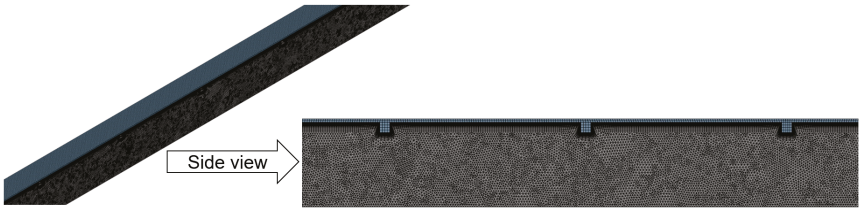

Figure 3. Meshed computational domain with selected cell number.

2.4. Turbulence Model Selection

Many studies on the CFD analysis of an SAH have selected an appropriate turbulence model and validated the developed model by comparing simulation results with empirical equation values [23,30,40]. Thus, this study also compared the simulated Nu and f values for a smooth-finned channel, obtained using various turbulence models, with empirical values to select the appropriate model. To obtain the empirical Nu values, Gnielinski and Dittus–Boelter correlations—widely used for SAH simulation—were employed, as shown in Equations (1) and (2) [20,35,40,41].

$$Nu_{ref} = \frac{(f_g/8)(Re - 1000)Pr}{1 + 12.7(f_g/8)^{1/2}\left(Pr^{2/3} - 1\right)} \text{ for } 3000 < Re < 10,000 \quad (1)$$

$$Nu_{ref} = 0.023Re^{0.8}Pr^{0.4} \text{ for } 10,000 < Re \quad (2)$$

Here, f_g represents the friction factor used in the Gnielinski correlation. It was calculated using Equation (3).

$$f_g = (0.79\ln Re - 1.64)^{-2} \quad (3)$$

Figure 4 compares the simulated average Nusselt number (Nu_{avg}) obtained using various turbulence models with empirical values. The figure confirms that the $k-\omega$ SST model yields the lowest mean absolute percentage error (MAPE) of 7.41% for Nu_{avg} between the simulated and empirical values. This result is consistent with the results reported in similar previous studies [26,42–46]. Therefore, the $k-\omega$ SST model was selected for further analysis.

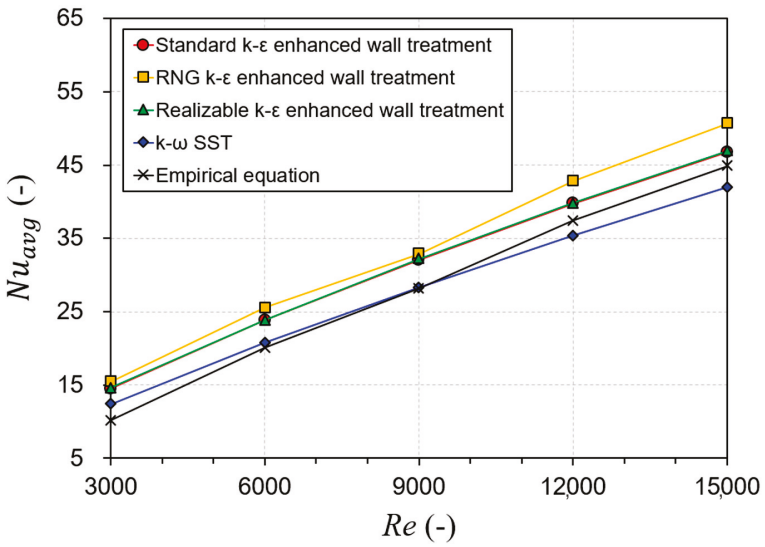

Figure 4. Comparison of simulated values obtained using various turbulence models with empirical values.

2.5. Performance Indices

This study sought to assess the heat transfer enhancement and associated pressure drop resulting from obstacles sequentially arranged on the fin surface. Heat transfer takes place on both the fin's upper and vertical surfaces. Accordingly, Nu_b and Nu_s were evaluated as follows:

$$Nu_b = \frac{h_b D_h}{k_{air}} \tag{4}$$

$$Nu_s = \frac{h_s D_h}{k_{air}} \tag{5}$$

The convective heat transfer corresponding to each fin surface was computed based on Equations (6) and (7).

$$h_b = \frac{\dot{Q}_b}{A_b(T_b - T_{air})} \tag{6}$$

$$h_s = \frac{\dot{Q}_s}{A_s(T_s - T_{air})} \tag{7}$$

The average Nu on the fin was obtained from Equation (8).

$$Nu_{avg} = \frac{h_{avg} D_h}{k_{air}} \tag{8}$$

The total fin-to-air heat transfer can be expressed as Equation (9).

$$\dot{Q}_t = h_{avg} A_t \left(T_{fin} - T_{air} \right) = \dot{Q}_b + \dot{Q}_s \tag{9}$$

Therefore, the average convective heat transfer coefficient can be obtained from Equation (10).

$$h_{avg} = \frac{h_b A_b (T_b - T_{air}) + h_s A_s (T_s - T_{air})}{A_t \left(T_{fin} - T_{air} \right)} \tag{10}$$

The average friction factor due to the obstacle was calculated using Equation (11) [47–49].

$$f_{avg} = \frac{(\Delta P / L_{ac}) D_h}{2 \rho_{air} {V_{air}}^2} \tag{11}$$

The rectangular obstacle installed on the fin surface not only improves heat transfer performance but also increases the pressure drop. Therefore, this study evaluates the thermo-hydraulic performance (THP) as a combined measure of both enhanced heat transfer and its resulting pressure penalty. The THP is calculated using Equation (12) [20,50–52].

$$\text{THP} = \frac{Nu_{avg} / Nu_{ref}}{\left(f_{avg} / f_{ref} \right)^{1/3}} \tag{12}$$

where f_{ref} represents the friction factor for a smooth-finned channel. A higher THP indicates more effective heat transfer enhancement under similar pressure drops.

3. Results and Discussion

3.1. Heat Transfer Performance

This subsection demonstrates heat transfer enhancement through the installation of obstacles with various heights and pitches. Figure 5 presents Nu on the base and side

surfaces. It is apparent that incorporating obstacles enhances heat transfer performance in a finned air channel. The values of Nu_b and Nu_s ranged from 11.14 to 98.96 and from 12.40 to 111.24, respectively. Both values increased with increasing Re, as a higher Re promotes turbulence generation near the hot surface, thereby enhancing convective heat transfer, as reported in several related studies [16–19,35,36].

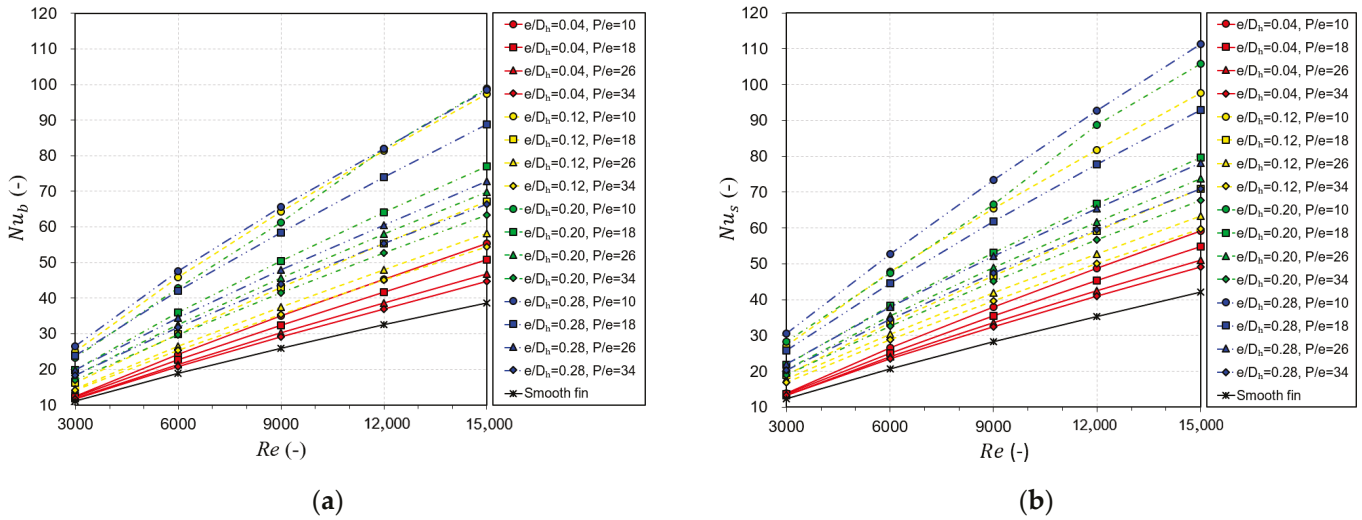

(**a**) (**b**)

Figure 5. Nu under varying relative heights and pitches: (**a**) base; (**b**) side.

It was also observed that a larger relative height (e/D_h) and a smaller relative pitch (P/e) resulted in greater heat transfer enhancement. This is because a larger relative height increases the turbulence kinetic energy, as shown in Figure 6, while a smaller relative pitch increases the total number of installed obstacles.

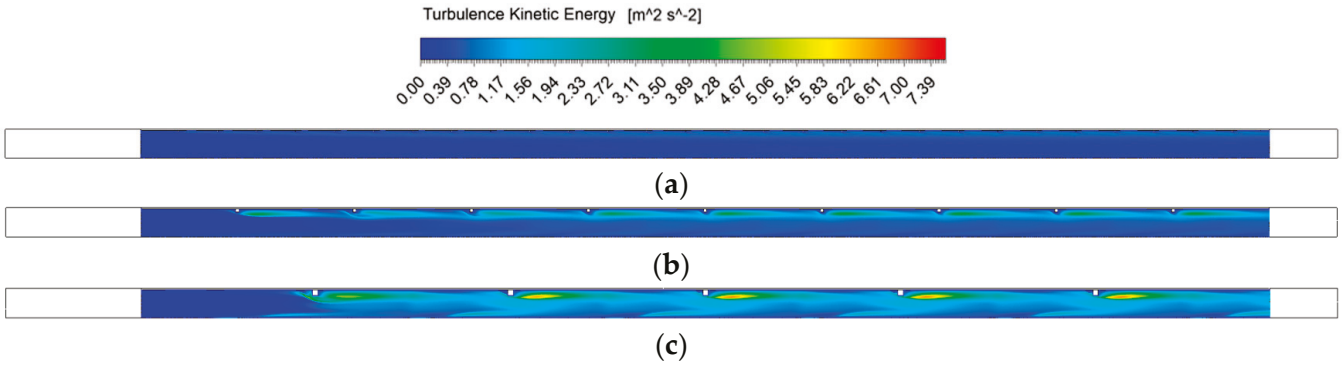

Figure 6. Contours of turbulence kinetic energy for different relative heights at fixed relative pitch of 18 and Re of 9000: (**a**) e/D_h = 0.04; (**b**) e/D_h = 0.12; (**c**) e/D_h = 0.20.

Figure 7 presents Nu_{avg} and its enhancement. The value of Nu_{avg} ranged from 11.97 to 106.28, varying with the relative height and pitch of the obstacle and Re. As shown previously, Nu_{avg} tended to increase with increasing relative height, decreasing relative pitch, and increasing Re.

Due to the presence of obstacles, Nu_{avg} was enhanced by a factor of 1.061 to 2.602 compared to the smooth-fin case. The minimum enhancement in Nu_{avg} was observed at a relative height of 0.04, a relative pitch of 34, and a Re of 3000, whereas the maximum enhancement occurred at 0.28, 10, and 15,000, respectively.

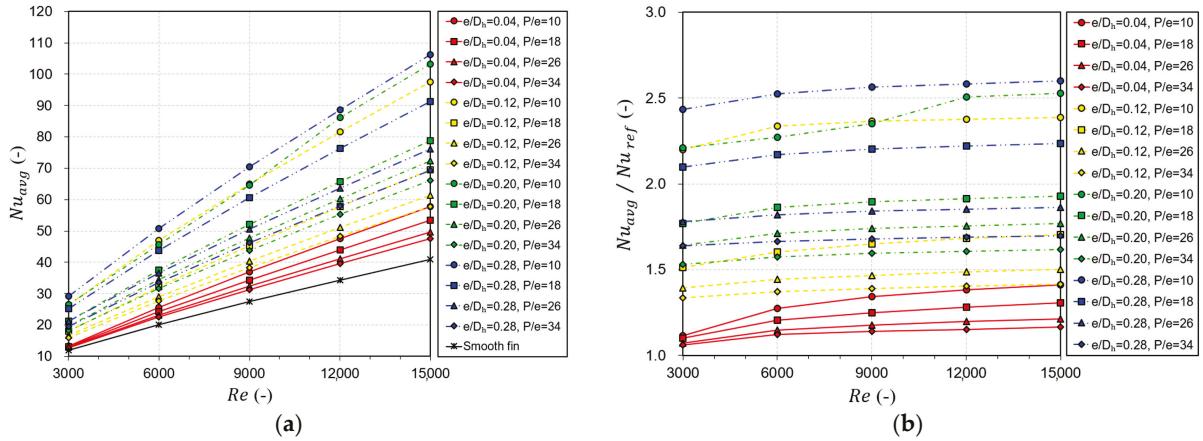

Figure 7. Nu_{avg} under varying relative heights and pitches: (**a**) Nu_{avg}; (**b**) enhancement in Nu_{avg}.

3.2. Fluid Friction

This section presents the friction factor, with the obstacle increasing the pressure drop in addition to enhancing heat transfer performance. Figure 8 shows f_{avg} and its increase. In all cases, the presence of obstacles led to an increase in f_{avg}. The value of f_{avg} ranged from 0.0117 to 0.2578, varying with the relative heights, relative pitches, and *Re*. It tended to rise with increasing relative height and decrements in relative pitch. The reason is that increasing the relative height and the number of obstacles resulting from a smaller relative pitch causes greater flow disruption, leading to an increased pressure drop. *Re* had a lesser effect on f_{avg} compared to the relative height and pitch. This is because the increase in pressure drop, which is proportional to f_{avg}, is similar to the velocity-squared increase, which is inversely proportional to f_{avg}, as *Re* increases.

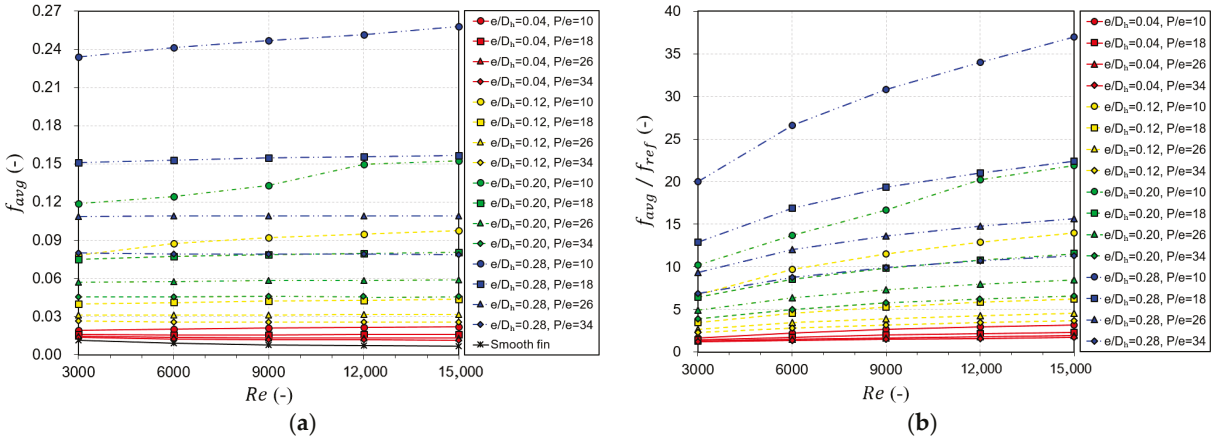

Figure 8. f_{avg} under varying relative heights and pitches: (**a**) f_{avg}; (**b**) increase in f_{avg}.

The increase in f_{avg} varied from 1.20 to 36.95 times. The minimum increase occurred at a relative height of 0.04, a relative pitch of 34, and a *Re* of 3000, whereas the maximum increase was observed at 0.28, 10, and 15,000, respectively.

3.3. Thermo-Hydraulic Performance

The results described in the previous subsections clearly show that a higher relative height and a smaller relative pitch not only enhance heat transfer performance, but also increase the pressure drop. Accordingly, the THP values, which reflect both heat transfer enhancement and the associated pressure drop, are presented in Figure 9.

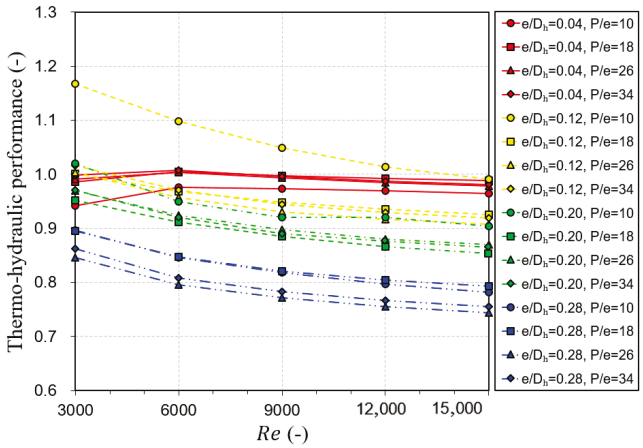

Figure 9. THP values under varying relative heights and pitches.

The value of THP ranged from 0.744 to 1.167. An increase in *Re* tended to decrease the THP value. This implies that the pressure penalty due to higher *Re* outweighed the corresponding enhancement in heat transfer. The highest THP values were observed when the relative height and relative pitch were 0.12 and 10, respectively, regardless of *Re*. Therefore, the combination of a relative height of 0.12 and a relative pitch of 10 was considered the most suitable geometric condition for the sequentially placed rectangular obstacles among the investigated cases. In contrast, the THP corresponding to a relative height of 0.28 exhibited the lowest values across all *Re* and relative pitch conditions, despite providing the highest heat transfer augmentation. This is because the increase in pressure drop outweighed the improvement in heat transfer. Accordingly, a relative height of 0.28 was identified as an unsuitable design parameter for obstacles in a finned SAH.

3.4. Correlation Derivation

Nu and f are essential for modeling the thermal behavior of an SAH and for predicting its thermal performance and fan power consumption. Therefore, this subsection derives the correlations for Nu and f as functions of relative height, relative pitch, and *Re*. The correlations were developed based on log–log plots, and the results are presented in Equations (13)–(15). A detailed description of the methodology can be found in related studies [1,35,51,53].

$$Nu_b = 0.10701 Re^{0.8483} (e/D_h)^{0.1503} (P/e)^{-0.5465} exp\left\{-0.0274[ln(e/D_h)]^2\right\} exp\left\{0.0395[ln(P/e)]^2\right\} \quad (13)$$

$$Nu_s = 0.20289 Re^{0.8106} (e/D_h)^{0.1384} (P/e)^{-0.7287} exp\left\{-0.0283[ln(e/D_h)]^2\right\} exp\left\{0.0738[ln(P/e)]^2\right\} \quad (14)$$

$$f_{avg} = 25.455 Re^{0.0228} (e/D_h)^{2.2881} (P/e)^{-1.2153} exp\left\{0.2659[ln(e/D_h)]^2\right\} exp\left\{0.0697[ln(P/e)]^2\right\} \quad (15)$$

Figure 10 compares the simulated values of Nu_b, Nu_s, and f_{avg} from the CFD analysis with the values predicted by the derived correlations under identical conditions. The results confirm that the predicted values are in good agreement with the simulated values, with MAPEs of 5.08% for Nu_b, 4.55% for Nu_s, and 9.66% for f_{avg}.

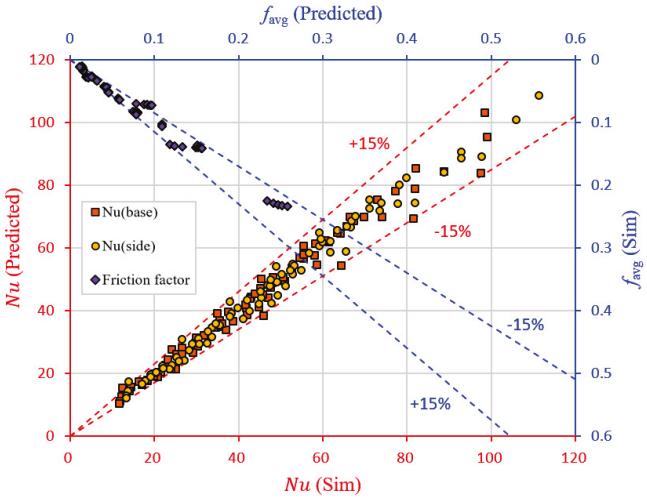

Figure 10. Comparison of simulated and predicted values of Nu_b, Nu_b, and f_{avg}.

4. Conclusions

In this work, the effects of the geometric conditions of sequentially placed obstacles in a finned channel, incorporated into an SAH, on thermal and flow characteristics were investigated through CFD analysis. The key findings are as follows:

(1) An increase in Nu_{avg} was observed with higher relative obstacle height, lower relative obstacle pitch, and higher Re. The sequentially placed obstacles enhanced Nu_{avg} by 2.602 times for the case where a relative height of 0.28, a relative pitch of 10, and a Re of 15,000 were used.

(2) Elevating the relative height and reducing the relative pitch led to an increment in f_{avg}, while Re had a comparatively smaller effect. The value of f_{avg} increased by 36.95 times compared to the smooth-fin case at a relative height of 0.28, a relative pitch of 10, and a Re of 3000.

(3) The THP values varied from 0.744 to 1.167. The highest THP was achieved at a relative height of 0.12 and a relative pitch of 10, regardless of Re. Therefore, these conditions were deemed the most suitable for the obstacles when considering both thermal performance and flow resistance.

(4) Correlations for Nu_s, Nu_b, and f_{avg} were derived as functions of relative height, relative pitch, and Re. The values of Nu_s, Nu_b, and f_{avg} were accurately predicted by the correlations with MAPEs of 5.08%, 4.55%, and 9.66%, respectively.

This study confirms that sequentially placed obstacles effectively enhance heat transfer in the finned channel of an SAH. However, the scope of this study was limited to the analysis of heat transfer and pressure penalty within the fluid domain. The temperature rise and thermal efficiency are the most important parameters for an SAH from a practical point of view. Therefore, future research will involve both experimental studies and numerical analyses of the proposed SAH to evaluate its performance, including air temperature rise and thermal efficiency. In addition, an economic analysis should be conducted to confirm the feasibility of the proposed design because the initial cost and fan power increase due to the use of the obstacles. The findings and derived correlations from this research are anticipated to offer useful information for further investigation.

Author Contributions: Conceptualization, B.-H.A. and S.-B.K.; methodology, B.-H.A.; software, B.-H.A., K.-A.M. and H.-U.C.; validation, B.-H.A.; investigation, B.-H.A. and H.-U.C.; data curation, K.-A.M. and S.-B.K.; writing—original draft preparation, B.-H.A. and H.-U.C.; writing—review

and editing, H.-U.C.; visualization, B.-H.A. and K.-A.M. All authors have read and agreed to the published version of the manuscript.

Funding: This research received no external funding.

Data Availability Statement: Data available on request.

Acknowledgments: This research was supported by the Regional Innovation System & Education (RISE) program, funded by the Ministry of Education and the Jeollanam-do Provincial Government.

Conflicts of Interest: The authors declare no conflicts of interest.

Nomenclature

A_b	Surface area of the base fin (m^2)
A_s	Surface area of the side fin (m^2)
A_t	Total surface area of the fin (m^2)
D_h	Hydraulic diameter (m)
f_{avg}	Average friction factor (-)
f_g	Friction factor for Gnielinski correlation (-)
f_{ref}	Smooth-finned air channel friction factor (-)
h_{avg}	Average convective heat transfer coefficient between the fin and the flowing air ($W/m^2 \cdot K$)
h_b	Convective heat transfer coefficient at the base surface of the fin ($W/m^2 \cdot K$)
h_s	Convective heat transfer coefficient at the side surface of the fin ($W/m^2 \cdot K$)
k_{air}	Thermal conductivity of the air ($W/m \cdot K$)
L_{ac}	Length of the finned air channel (m)
Nu_{avg}	Average Nusselt number at the fin–air interface (-)
Nu_b	Nusselt number on the fin base surface (-)
Nu_{ref}	Nusselt number for the smooth-finned air channel (-)
Nu_s	Nusselt number on the fin side surface (-)
ΔP	Pressure drop (Pa)
Pr	Prandtl number (-)
$\dot{Q}_b$	Heat transfer rate at the base surface of the fin (W)
$\dot{Q}_s$	Heat transfer rate at the side surface of the fin (W)
$\dot{Q}_t$	Total fin-to-air heat transfer rate (W)
Re	Reynolds number (-)
T_{air}	Temperature of the flowing air (°C)
T_b	Temperature at the base surface of the fin (°C)
T_{fin}	Average temperature of the base and side of the fin (°C)
T_s	Temperature on the side surface of the fin (°C)
V_{air}	Velocity of the air (m/s)
Greek symbol	
ρ_{air}	Air density (kg/m^3)

References

1. Chamoli, S.; Lu, R.; Xu, D.; Yu, P. Thermal performance improvement of a solar air heater fitted with winglet vortex generators. *Sol. Energy* **2018**, *159*, 966–983. [CrossRef]
2. Singh, V.P.; Jain, S.; Karn, A.; Kumar, A.; Dwivedi, G.; Meena, C.S.; Dutt, N.; Ghosh, A. Recent Developments and Advancements in Solar Air Heaters: A Detailed Review. *Sustainability* **2022**, *14*, 12149. [CrossRef]
3. Markam, B.; Maiti, S. Artificial enhancer for small-scale solar air heater—A comprehensive review. *Clean. Energy Syst.* **2023**, *4*, 100046. [CrossRef]
4. Fakoor Pakdaman, M.; Lashkari, A.; Basirat Tabrizi, H.; Hosseini, R. Performance evaluation of a natural-convection solar air-heater with a rectangular-finned absorber plate. *Energy Convers. Manag.* **2011**, *52*, 1215–1225. [CrossRef]

5. Fudholi, A.; Sopian, K.; Ruslan, M.H.; Othman, M.Y. Performance and cost benefits analysis of double-pass solar collector with and without fins. *Energy Convers. Manag.* **2013**, *76*, 8–19. [CrossRef]
6. Priyam, A.; Chand, P. Thermal and thermohydraulic performance of wavy finned absorber solar air heater. *Sol. Energy* **2016**, *130*, 250–259. [CrossRef]
7. Kabeel, A.E.; Hamed, M.H.; Omara, Z.M.; Kandeal, A.W. Influence of fin height on the performance of a glazed and bladed entrance single-pass solar air heater. *Sol. Energy* **2018**, *162*, 410–419. [CrossRef]
8. Chand, S.; Chand, P.; Kumar Ghritlahre, H. Thermal performance enhancement of solar air heater using louvered fins collector. *Sol. Energy* **2022**, *239*, 10–24. [CrossRef]
9. Karwa, R. Thermo-hydraulic performance of solar air heater with finned absorber plate forming multiple rectangular air flow passages in parallel under laminar flow conditions. *Appl. Therm. Eng.* **2023**, *221*, 119673. [CrossRef]
10. Vengadesan, E.; Arunkumar, T.; Krishnamoorthi, T.; Senthil, S. Thermal performance improvement in solar air heating: An absorber with continuous and discrete tubular and v-corrugated fins. *Therm. Sci. Eng. Prog.* **2024**, *48*, 102416. [CrossRef]
11. Elakrout, O.; Ghriss, O.; Bouabidi, A.; Garcia Castellanos, H.; Mohtaram, S.; Keçebaş, A.; Aryanfar, Y. Investigative analysis of the influence of diverse fin configurations on the performance of a dual pass solar air collector. *Therm. Sci. Eng. Prog.* **2024**, *50*, 102545. [CrossRef]
12. Yang, M.; Yang, X.; Li, X.; Wang, Z.; Wang, P. Design and optimization of a solar air heater with offset strip fin absorber plate. *Appl. Energy* **2014**, *113*, 1349–1362. [CrossRef]
13. Saravanan, A.; Parida, S.; Murugan, M.; Reddy, M.S.; Elumalai, P.V.; Kumar Dash, S. Thermal performance prediction of a solar air heater with a C-shape finned absorber plate using RF, LR and KNN models of Machine learning. *Therm. Sci. Eng. Prog.* **2023**, *38*, 101630. [CrossRef]
14. Albdoor, A.K.; Obaid, Z.A.H.; Kamel, M.S.; Azzawi, I.D.J. Energy, exergy, economic and environmental analysis of a solar air heater integrated with double triangular fins: Experimental investigation. *Int. J. Thermofluids* **2024**, *24*, 100979. [CrossRef]
15. Singh Bisht, V.; Kumar Patil, A.; Gupta, A. Review and performance evaluation of roughened solar air heaters. *Renew. Sustain. Energy Rev.* **2018**, *81*, 954–977. [CrossRef]
16. Yadav, A.S.; Bhagoria, J.L. A CFD (computational fluid dynamics) based heat transfer and fluid flow analysis of a solar air heater provided with circular transverse wire rib roughness on the absorber plate. *Energy* **2013**, *55*, 1127–1142. [CrossRef]
17. Yadav, A.S.; Bhagoria, J.L. A numerical investigation of square sectioned transverse rib roughened solar air heater. *Int. J. Therm. Sci.* **2014**, *79*, 111–131. [CrossRef]
18. Yadav, A.S.; Bhagoria, J.L. A CFD based thermo-hydraulic performance analysis of an artificially roughened solar air heater having equilateral triangular sectioned rib roughness on the absorber plate. *Int. J. Heat Mass Transf.* **2014**, *70*, 1016–1039. [CrossRef]
19. Gawande, V.B.; Dhoble, A.S.; Zodpe, D.B.; Chamoli, S. Experimental and CFD investigation of convection heat transfer in solar air heater with reverse L-shaped ribs. *Sol. Energy* **2016**, *131*, 275–295. [CrossRef]
20. Singh, I.; Singh, S. CFD analysis of solar air heater duct having square wave profiled transverse ribs as roughness elements. *Sol. Energy* **2018**, *162*, 442–453. [CrossRef]
21. Singh, I.; Vardhan, S.; Singh, S.; Singh, A. Experimental and CFD analysis of solar air heater duct roughened with multiple broken transverse ribs: A comparative study. *Sol. Energy* **2019**, *188*, 519–532. [CrossRef]
22. Kumar, R.; Goel, V. Unconventional solar air heater with triangular flow-passage: A CFD based comparative performance assessment of different cross-sectional rib-roughnesses. *Renew. Energy* **2021**, *172*, 1267–1278. [CrossRef]
23. Boussouar, G.; Rostane, B.; Aliane, K.; Ravi, D.; Gęca, M.J.; Gola, A. Study of the Thermal Performance of Solar Air Collectors with and without Perforated Baffles. *Energies* **2024**, *17*, 3812. [CrossRef]
24. Kumar, B.V.; Kanna, P.R.; Manikandan, G.; Taler, D.; Taler, J.; Sobota, T.; Nowak-Ocłoń, M. Investigation of Thermo-Hydraulic Performances of Artificial Ribs Mounted in a Rectangular Duct. *Energies* **2023**, *16*, 4404. [CrossRef]
25. Khanlari, A.; Güler, H.Ö.; Tuncer, A.D.; Şirin, C.; Bilge, Y.C.; Yılmaz, Y.; Güngör, A. Experimental and numerical study of the effect of integrating plus-shaped perforated baffles to solar air collector in drying application. *Renew. Energy* **2020**, *145*, 1677–1692. [CrossRef]
26. Alam, M.W.; Souayeh, B. Parametric CFD Thermal Performance Analysis of Full, Medium, Half and Short Length Dimple Solar Air Tube. *Sustainability* **2021**, *13*, 6462. [CrossRef]
27. Choi, H.; Choi, K. Parametric study of a novel air-based photovoltaic-thermal collector with a transverse triangular-shaped block. *Renew. Energy* **2022**, *201*, 96–110. [CrossRef]
28. Haldar, A.; Varshney, L.; Verma, P. Effect of roughness parameters on performance of solar air heater having artificial wavy roughness using CFD. *Renew. Energy* **2022**, *184*, 266–279. [CrossRef]
29. Hu, J.; Zhang, Y.; Xie, S.; Xiao, Y. Thermo-hydraulic performance of solar air heater with built-in one-eighth sphere vortex generators. *Appl. Therm. Eng.* **2024**, *245*, 122837. [CrossRef]

30. Singh, S.; Suman, S.; Mitra, S.; Kumar, M. Thermo-hydraulic performance enhancement of a solar air heater using rotating cylindrical turbulators. *Appl. Therm. Eng.* **2024**, *236*, 121748. [CrossRef]
31. Mahanand, Y.; Senapati, J.R. Implementation of hybrid rib-turbulators on the thermal performance of solar air heater duct: A collective review. *Sustain. Energy Technol. Assess.* **2022**, *52*, 102345. [CrossRef]
32. Hassan, A.; Nikbakht, A.M.; Fawzia, S.; Yarlagadda, P.; Karim, A. A Comprehensive Review of the Thermohydraulic Improvement Potentials in Solar Air Heaters through an Energy and Exergy Analysis. *Energies* **2024**, *17*, 1526. [CrossRef]
33. Nidhul, K.; Yadav, A.K.; Anish, S.; Kumar, S. Critical review of ribbed solar air heater and performance evaluation of various V-rib configuration. *Renew. Sustain. Energy Rev.* **2021**, *142*, 110871. [CrossRef]
34. Ghritlahre, H.K.; Verma, M.; Parihar, J.S.; Mondloe, D.S.; Agrawal, S. A detailed review of various types of solar air heaters performance. *Sol. Energy* **2022**, *237*, 173–195. [CrossRef]
35. Choi, H.-U.; Moon, K.-A.; Kim, S.-B.; Choi, K.-H. CFD Analysis of the Heat Transfer and Fluid Flow Characteristics Using the Rectangular Rib Attached to the Fin Surface in a Solar Air Heater. *Sustainability* **2023**, *15*, 5382. [CrossRef]
36. An, B.-H.; Choi, K.-H.; Choi, H.-U. Heat Transfer Augmentation and Friction Factor Due to the Arrangement of Rectangular Turbulators in a Finned Air Channel of a Solar Air Heater. *Energies* **2023**, *16*, 6891. [CrossRef]
37. Diana, L.; Safitra, A.G.; Muhammad, G. Numerical Investigation of Airflow in a Trapezoidal Solar Air Heater Channel. In Proceedings of the 2019 International Electronics Symposium (IES), Surabaya, Indonesia, 27–28 September 2019; pp. 248–253.
38. Al-Abbasi, O.; Sarac, B.; Ayhan, T. Experimental Investigation and CFD Modeling to Assess the Performance of Solar Air Humidifier. *Int. J. Heat Technol.* **2019**, *37*, 357–364. [CrossRef]
39. Qader, B.S.; Supeni, E.E.; Ariffin, M.K.A.; Talib, A.R.A. RSM approach for modeling and optimization of designing parameters for inclined fins of solar air heater. *Renew. Energy* **2019**, *136*, 48–68. [CrossRef]
40. Singh, S.; Singh, B.; Hans, V.S.; Gill, R.S. CFD (computational fluid dynamics) investigation on Nusselt number and friction factor of solar air heater duct roughened with non-uniform cross-section transverse rib. *Energy* **2015**, *84*, 509–517. [CrossRef]
41. Singh, A.; Singh, S. CFD investigation on roughness pitch variation in non-uniform cross-section transverse rib roughness on Nusselt number and friction factor characteristics of solar air heater duct. *Energy* **2017**, *128*, 109–127. [CrossRef]
42. Chaube, A.; Sahoo, P.K.; Solanki, S.C. Analysis of heat transfer augmentation and flow characteristics due to rib roughness over absorber plate of a solar air heater. *Renew. Energy* **2006**, *31*, 317–331. [CrossRef]
43. Alam, T.; Kim, M.-H. Heat transfer enhancement in solar air heater duct with conical protrusion roughness ribs. *Appl. Therm. Eng.* **2017**, *126*, 458–469. [CrossRef]
44. Kumar, S.; Verma, S.K. Heat transfer and fluid flow analysis of sinusoidal protrusion rib in solar air heater. *Int. J. Therm. Sci.* **2022**, *172*, 107323. [CrossRef]
45. Wongcharee, K.; Changcharoen, W.; Eiamsa-ard, S. Numerical Investigation of Flow Friction and Heat Transfer in a Channel with Various Shaped Ribs Mounted on Two Opposite Ribbed Walls. *Int. J. Chem. React. Eng.* **2011**, *9*, A26. [CrossRef]
46. Boulemtafes-Boukadoum, A.; Benzaoui, A. CFD based Analysis of Heat Transfer Enhancement in Solar Air Heater Provided with Transverse Rectangular Ribs. *Energy Procedia* **2014**, *50*, 761–772. [CrossRef]
47. Kumar, R.; Goel, V.; Kumar, A. Investigation of heat transfer augmentation and friction factor in triangular duct solar air heater due to forward facing chamfered rectangular ribs: A CFD based analysis. *Renew. Energy* **2018**, *115*, 824–835. [CrossRef]
48. Kim, S.-B.; Choi, H.-U. Numerical analysis of photovoltaic–thermal air collector with fins and rectangular turbulators. *Therm. Sci. Eng. Prog.* **2025**, *59*, 103393. [CrossRef]
49. Choi, H.-U. Dynamic analysis of air-based photovoltaic–thermal system with fins and rectangular obstacles. *Appl. Therm. Eng.* **2025**, *272*, 126412. [CrossRef]
50. Webb, R.L.; Eckert, E.R.G. Application of rough surfaces to heat exchanger design. *Int. J. Heat Mass Transf.* **1972**, *15*, 1647–1658. [CrossRef]
51. Kumar, R.; Kumar, A.; Goel, V. Performance improvement and development of correlation for friction factor and heat transfer using computational fluid dynamics for ribbed triangular duct solar air heater. *Renew. Energy* **2019**, *131*, 788–799. [CrossRef]
52. Gupta, A.D.; Varshney, L. Performance prediction for solar air heater having rectangular sectioned tapered rib roughness using CFD. *Therm. Sci. Eng. Prog.* **2017**, *4*, 122–132. [CrossRef]
53. Choi, H.-U.; Choi, K.-H. CFD Analysis on the Heat Transfer and Fluid Flow of Solar Air Heater having Transverse Triangular Block at the Bottom of Air Duct. *Energies* **2020**, *13*, 1099. [CrossRef]

Disclaimer/Publisher's Note: The statements, opinions and data contained in all publications are solely those of the individual author(s) and contributor(s) and not of MDPI and/or the editor(s). MDPI and/or the editor(s) disclaim responsibility for any injury to people or property resulting from any ideas, methods, instructions or products referred to in the content.

energies

MDPI

Article

Experimental Study of Solar Hot Water Heating System with Adaptive Control Strategy

Pawel Znaczko [1], Norbert Chamier-Gliszczynski [2,*] and Kazimierz Kaminski [1]

[1] Faculty of Mechanical and Energy Engineering, Koszalin University of Technology, 75-453 Koszalin, Poland; pawel.znaczko@tu.koszalin.pl (P.Z.); kazimierz.kaminski@tu.koszalin.pl (K.K.)
[2] Faculty of Economics Sciences, Koszalin University of Technology, 75-453 Koszalin, Poland
* Correspondence: norbert.chamier-gliszczynski@tu.koszalin.pl

Abstract: The efficiency of solar water heating systems is strongly influenced by variable weather conditions, making the optimization of control strategies essential for maximizing energy performance. This study presents the development and evaluation of a rule-based adaptive control strategy that dynamically selects one of three predefined control modes—ON–OFF, proportional, or indirect proportional control (IPC)—based on real-time weather classification. The classification algorithm assigns each day to one of four solar irradiance categories, enabling the controller to respond appropriately to current environmental conditions. The proposed adaptive controller was implemented and tested under real operating conditions and compared with a conventional commercial solar controller. Over a 40-day testing period, the adaptive system achieved a 12.7% increase in thermal energy storage efficiency. Specifically, despite receiving 4.8% less solar radiation (719 kWh vs. 755 kWh), the adaptive controller stored 453 kWh of heat in the water tank compared to 416 kWh with the traditional system. This corresponds to an efficiency improvement from 0.55 to 0.63. These results demonstrate the adaptive controller's superior ability to utilize available solar energy across all weather scenarios. The findings confirm that intelligent control strategies not only enhance technical performance but also improve the economic and environmental value of solar thermal systems.

Keywords: solar energy; adaptive control strategy; solar heating system; weather conditions

1. Introduction

The shift toward renewable energy stands as a central challenge of the 21st century, driven by the global need to address climate change, strengthen energy security [1], and support sustainable economic development. The European Union's Energy Strategy and Energy Union underscore the importance of building a secure, competitive, and sustainable energy system [2]. As part of this commitment, the EU has set an ambitious goal for renewable energy sources to account for 32% of its total energy mix by 2030 [3].

Renewable energy systems (RESs) are becoming increasingly common in everyday use [3–5]. They are used as an ecological [6] and economically more beneficial alternative to conventional energy sources [7,8]. Solar heating systems occupy a major place among them. Most often used for heating domestic hot water and heating residential spaces, they also have wider applications, such as agriculture, gardening [9], and industry [10]. Such systems support the heating of greenhouses, thus extending the growing season of plants. The use of solar energy to heat domestic hot water (DHWS) allows for a reduction

in greenhouse gas emissions [11] and lowers heating costs. However, the profitability and efficiency of photothermal systems depend largely on the operating conditions and the effectiveness of the control strategies used [12,13].

A solar hot water heating system (Figure 1) is an advanced system of several components that work together to collect, store, and distribute thermal energy [14]. The main elements of such systems are primarily as follows [15–17]:

- solar collector—responsible for efficiently capturing solar radiation energy,
- working medium—gas or liquid circulating in the hydraulic circuit, the purpose of which is to transport energy to the storage tank. This function is most often performed by glycol or water,
- storage tank—used to store the accumulated heat gains,
- heat exchanger—a component designed to transfer heat from the medium to either water,
- pump group—used to pump the medium in a closed circuit through the solar collector to the tank,
- solar regulator—the purpose of which in the system is to supervise the operation of the pump group and the pumping.

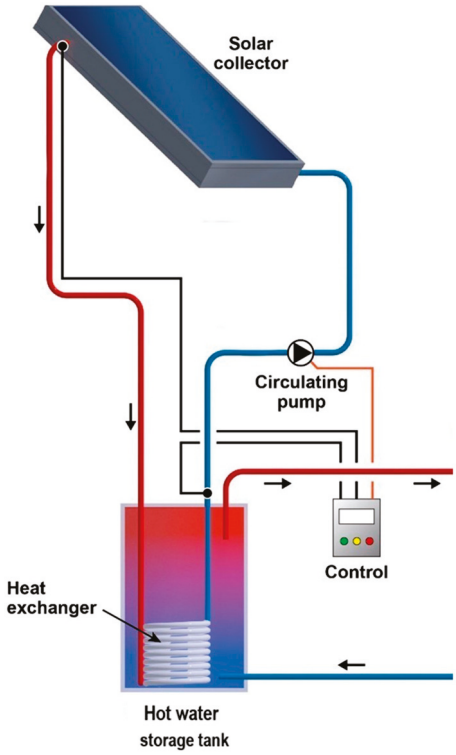

Figure 1. Simplified solar heating system diagram.

In recent years, research on solar thermal systems has focused on three key areas. The first area involves developments in energy storage technologies [18,19], particularly focusing on phase change materials (PCM) and related heat storage methods. This research aims to increase the performance of thermal systems by exploring ways to improve the capacity and efficiency of energy storage for practical use and economic feasibility [20,21]. Another area of interest is integrating systems with other renewable energy sources to create hybrid systems, such as combining thermal systems with biomass or geothermal

resources. Another objective is to enhance system sustainability under varying conditions, considering system [22] configurations and environmental impacts [23,24].

Finally, a strong emphasis is being placed on optimizing control methods for thermal systems [25,26]. Researchers are analyzing control strategies to assess their impact on overall system energy efficiency, particularly in terms of adapting to changing weather conditions while maximizing energy accumulation processes. Much of the research also involves conducting experiments and simulations to evaluate control strategies under both controlled conditions and real-world scenarios [27]. The results of these studies provide insight into the practical advantages and limitations of various control techniques [28]. The list of research work on solar thermal systems grouped into research areas is shown in Table 1.

Table 1. Research directions in solar thermal systems.

Research Area	Description	Research
Development of storage technologies	Investigation of materials and technologies aimed at enhancing the efficiency of thermal energy storage systems.	[29–36]
Hybrid systems design	Research on combining photothermal systems with other renewable energy systems to improve their independence from conditions	[37–44]
Optimization of control methods	Study of control strategies in solar thermal systems and their optimal selection based on specific operating conditions.	[45–53]

The literature mentions three main control concepts in solar heating installations: time, temperature, and differential control [54,55]. The simplest of them involves programming the system's operating parameters for specific hours when the best availability of solar energy is expected during the day [56,57]. This is especially useful when a repeatable pattern of solar operation can be identified or when the heating system is only scheduled to operate at specific times. However, in this case, there is no feedback that would make the operation of the system dependent on its operating conditions. A concept based on temperature measurements allows these conditions to be considered. It involves monitoring temperatures at specific points in the system (e.g., solar collectors, surroundings, tanks) and then activating or deactivating the circulation pump based on these measurements [57,58]. Simplicity, which is a natural advantage of this approach, also translates to the differential method, which allows the pump group to be switched on only when the logical condition based on the collector-storage tank temperature difference is met. The pump's operation is once again influenced by the system's operating conditions, but in a significantly more sophisticated manner. Additionally, it guarantees the minimization of pump operation in situations where heat transfer would not be beneficial from the point of view of energy efficiency [59,60].

One of the most important challenges related to the operation of heating systems equipped with solar collectors is their variable efficiency resulting from fluctuations in solar radiation intensity [56,57]. So far, many different control methods have been proposed and evaluated to minimize the impact of solar operation disruptions on the operation of the heating system. These strategies usually modify, to some extent, the way the pump group operates depending on the amount of available solar energy. A common approach is to use predictive methods that allow for optimization of the operating parameters of the heating system in terms of weather conditions in real time [61,62]. However, there are many obstacles to the effective use of such a strategy. The main problem is the uncertainty of the weather conditions, based on which the control strategy is implemented. Predictive

methods have difficulty in dynamically adapting to unpredictable and sudden changes in weather conditions. Moreover, a significant limitation of the applicability of these methods is their complexity and implementation cost [63,64]. The consequence of this is that the scope for using predictive control methods is limited despite their proven effectiveness. Fully understanding and solving these problems is crucial for the further development of photo-thermal technologies and increasing their efficiency and economic viability [65].

2. Subject of the Study

The main objective of the study was to determine the impact of an adaptive control strategy developed using the results of previous research [48,51]. A new adaptive controller will be designed and evaluated based on its impact on thermal energy collection efficiency in a solar heating system. In this study, efficiency is defined as the ratio of useful thermal energy stored in the tank to the total solar energy incident on the collector surface during the same period. The goal was to determine whether this new device could outperform the reference controller. The commercial solar controller Tech ST-402n manufactured by TECH Sterowniki (Wieprz, Poland) was used for comparison. Both controllers used in the study are presented in Figure 2. The Arduino Mega microcontroller, manufactured by Arduino (Turin, Italy) was selected for the adaptive controller due to its flexibility, substantial number of I/O ports, and sufficient processing capacity, which were essential during the development and testing phases. Although the final configuration used only a few inputs and outputs, the extended I/O capability allowed for easy integration of additional sensors and rapid prototyping without hardware modifications. This choice also ensured the reliable execution of the adaptive algorithm and left room for future system expansion or algorithm upgrades. The study involved data collection and analysis to evaluate the influence of the adaptive controller on the efficiency of energy conversion. The results were compared to those of a classic proportional control system to fully assess the benefits of this approach in improving solar heating performance.

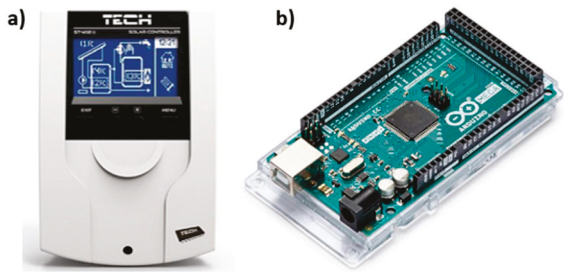

Figure 2. Controllers used for comparative studies: (**a**) classic proportional solar controller; (**b**) new adaptive controller.

To accomplish these research objectives, a test stand was constructed to monitor the operational parameters of solar collectors, following the guidelines outlined in the PN-EN ISO 9806:2017 standard [66]. This standard specifies testing procedures for evaluating the durability, reliability, safety, and thermal performance of liquid solar thermal collectors. The prescribed methods served as the basis for developing the laboratory testing procedures.

To meet the research goal, the following key aspects of the work carried out were identified:

- system design and configuration: a discussion of the design of the solar water heating system using solar panels and details of the technology used to capture and store energy. Reviewing the layout of system components, including buffer tanks, pumps, heat exchangers, and sensors,

- adaptive control approach: a characterization of the control strategy used to dynamically adjust system parameters in response to changing environmental conditions. Explanation of control algorithms that optimize pump operation based on sensor data to increase energy efficiency,
- experimental methodology: explanation of experimental test methodology including test conditions, location details, test duration, and measurement procedures. Identify information on the types and locations of measurement sensors, along with methods for data collection and analysis,
- analysis of results: presentation of the collected data, assessment of system performance, and evaluation of its overall effectiveness. This includes a comparative analysis between the proposed control strategy and traditional control methods,
- discussion: consideration of the impact of using an adaptive control strategy on system stability and reliability. The identification of potential improvements and future research directions to increase performance while reducing operating costs. The final element was a summary of the findings from the experimental studies and the formulation of suggestions for incorporating adaptive control techniques into solar thermal systems.

Average daily values were used instead of totals to normalize the influence of day-to-day variability in solar radiation and thermal dynamics. This approach enables a more representative comparison of the system's typical performance under each weather condition, minimizing the impact of outliers and ensuring methodological consistency across all control scenarios. The study seeks not only to assess how adaptive control influences the effectiveness of household water heating systems but also to offer practical advice for professionals enhancing renewable energy solutions.

3. Experimental Setup

The test stand built to measure the thermal efficiency of solar collectors was located at the Koszalin University of Technology. It consisted of two flat plate solar collectors (FPC). Figure 3 presents a setup featuring two collectors identified as SC 1 and SC 2. Cold water, known as Tin, enters these collectors while hot water, referred to as Tout, exits them. The controller (SC) oversees temperature readings from sensors T1, T2, and T3. Water passes through a BV valve and an FM1 flow meter, with circulation facilitated by pump PR1. The heated water is stored in a tank labelled ST, which includes a temperature sensor named TS. Additionally, the system is equipped with a cranial anemometer (AN1) and pyranometer (PR) for monitoring and control purposes. An important part of the test stand was also a data acquisition station comprising a computer (CPU) and a measurement card (DAQ).

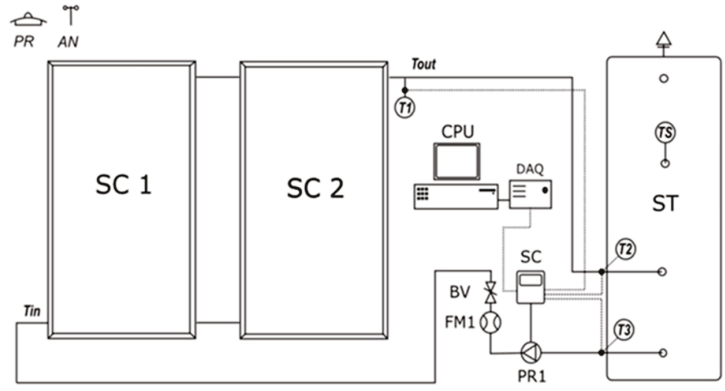

Figure 3. Diagram of heating system.

During the evaluation of the system efficiency, a method was created to ensure that the tasks performed could be repeated accurately while reducing error. This step was crucial considering the duration of the measurement process. Prior to commencing measurements, temperature sensors were routinely calibrated. This calibration aimed to adjust the readings of PT100 resistance sensors (manufactured by WIKA Polska, Włocławek, Poland) based on data from a set of mercury thermometers accurate to 0.1 K. Temperature corrections were applied at ten reference points within the tank, covering a range from 5 °C to 95 °C. By comparing temperatures recorded by the thermometers, we established the characteristics of PT100 sensors in relation to temperature. Figures 4 and 5 present the appearance of the test stand.



Figure 4. Test stand for solar heating systems: 1—computer console; 2—electromagnetic flow meters with control valves; 3—fuse box; 4—working medium circulation pump; 5—heating boiler; 6—measurement data acquisition system; 7—storage tanks; 8—water cooler.



Figure 5. Outdoor research platform with a battery of two flat-plate solar collectors.

Two KSH-2.0 flat-plate liquid solar collectors supplied for the research by KOSPEL S.A. (Koszalin, Poland) were used for the adaptive controller research work. They were combined into a single battery according to the presented schematic of the stand. Their total aperture area was almost 4 m^2. Table 2 outlines the main specifications of the solar collectors used in the study.

Table 2. Technical parameters of the collector.

Type of Solar Collector	Flat Liquid
Manufacturer/brand name	KOSPEL S.A./KSH-2.0
Gross area/aperture/absorber	2.27/1.98/2.00 (m^2)
Collector length/width/height	2.12/1.1/0.09 (m)
Empty collector mass	36.5 (kg)

Each measurement instrument was properly calibrated and overdriven under field conditions prior to the test work. All post-measurement values from the presented transducers were recorded using cDAQ-9174 (MS) post-measurement cards (National Instruments, Austin, TX, USA) and NI LabVIEW software (version 2023). The most important technical parameters of the sensors used for the study are summarized in Tables 3–6.

Table 3. Specifications of the pyranometer.

Transducer	Measuring Range (W/m^2)	Sensitivity ($\mu V/W/m^2$)	Spectral Range (nm)	Time Constant (s)
LP-PYRA-02, Delta OHM (Caselle di Selvazzano, Italy)	0 ÷ 2000	±10	305 ÷ 2800	<28

Table 4. Technical parameters of the anemometer.

Transducer	Range (m/s)	Accuracy (%)	Resolution (m/s)
LAMBRECHT 14577, Lambrecht meteo GmbH (Göttingen, Germany)	0.7 ÷ 50	±0.2	305 ÷ 2800

Table 5. Specifications of the PT100 RTD temperature sensor.

Transducer	Measurement Card	Measuring Range (K)	Measurement Accuracy (K)	Measurement Resolution (K)
PT100 RTD, WIKA Włocławek, Poland	NI 9217	±120	±0.1	0.02

Table 6. Specifications of the meteorological station.

Transducer	Humidity Range (°C)	Measurement Accuracy (K)	Measurement Resolution (K)
HD9008TR, Delta OHM (Caselle di Selvazano, Italy)	−40 ÷ 80	±0.1	0.05

4. Experimental Research Using an Adaptive Controller—Material and Methods

Based on the result of previous research work [51], indicators were developed to group research days by weather conditions. The first of the proposed coefficients contains information about the thermal conversion efficiency occurring in the solar heating system. It allows for determining the ratio of energy stored in the water storage tank to the energy available on the collector. It can be expressed in the form of the following formula:

$$X_{Sol} = \frac{E_z}{E_{rad}} \quad (1)$$

where E_z represents the quantity of thermal energy accumulated in the water tank over the course of the measurement day.

$$E_z = (T_k - T_p) \cdot c_f \cdot M_z \tag{2}$$

where T_k, T_p denote the initial and final temperatures, respectively; c_f represents the specific heat capacity of the working fluid, and M_z is its mass.

The value of the variable E_{rad}, which describes the amount of total solar energy on the collector surface during the specified test period, is calculated according to the following equation:

$$E_{rad} = \int_{t_0}^{t_f} G_\beta A_c \, dt \tag{3}$$

where G_β refers to the total amount of solar radiation incident on the surface of the collector, A_c is the aperture area of the collectors, and t_0 and t_f are the initial and final test times, respectively.

However, for the control strategy in the solar system, an equally important parameter is the dynamics of changes in the solar flux density. To describe these fluctuations during the measurement day, the following third coefficient was developed:

$$E_{var} = \frac{k_{var}}{k_t} \tag{4}$$

where k_t represents the total number of measurement time samples recorded during the test day, while k_{var} is the count of time intervals in which significant fluctuations in solar radiation intensity occurred, as defined by the specified condition:

$$t_{var} = \begin{cases} t_{var} \Rightarrow \left| G_{\beta_i} - G_{\beta_{i-1}} \right| < \Delta G_{cr} \\ t_{var} + 1 \Rightarrow \left| G_{\beta_i} - G_{\beta_{i-1}} \right| \geq \Delta G_{cr} \end{cases} \tag{5}$$

where the G_{β_i} represents the global solar radiation intensity measured at each time sample, and the ΔG_{cr} is the threshold value for changes in radiation intensity, set at a predefined level of $\Delta G_{cr} = 5 \left[\mathrm{W/m^2} \right]$.

The indicators determined in this way made it possible to create a kind of 4-state classifier of measurement days, forming groups of days with similar weather conditions. The proposed division was based on average values. As a result, the space was divided into four weather groups, each of which is characterized by different properties. Each of the groups included an appropriate number of days (at least 20), which usefully allowed the use of the results and drawing of reliable conclusions. This made it possible to classify the measurement days based on the most relevant weather parameters.

Grouping of measurement samples using the proposed four-state classifier is presented in Figure 6.

Created classifier allows for the distinction of four groups of days with similar parameters of solar operation. As a result of this division, groups of days of high solar radiation with low interference coefficient (I) and days with similar solar potential but burdened with large radiation fluctuations (II) were created. Group IV included measurement days with lower-than-average solar radiation during the day and with low interference. The last group (III) includes samples for which there was a low value of available radiation during the day and significant disturbances in solar operation. Example radiation profiles along with mass flow rate values for each of the defined groups are presented in Figure 7.

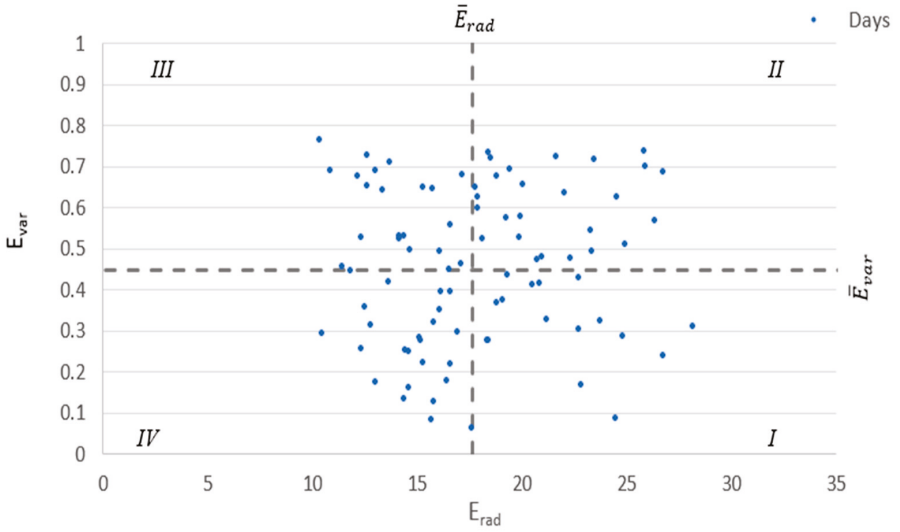

Figure 6. Space to separate days into weather groups.

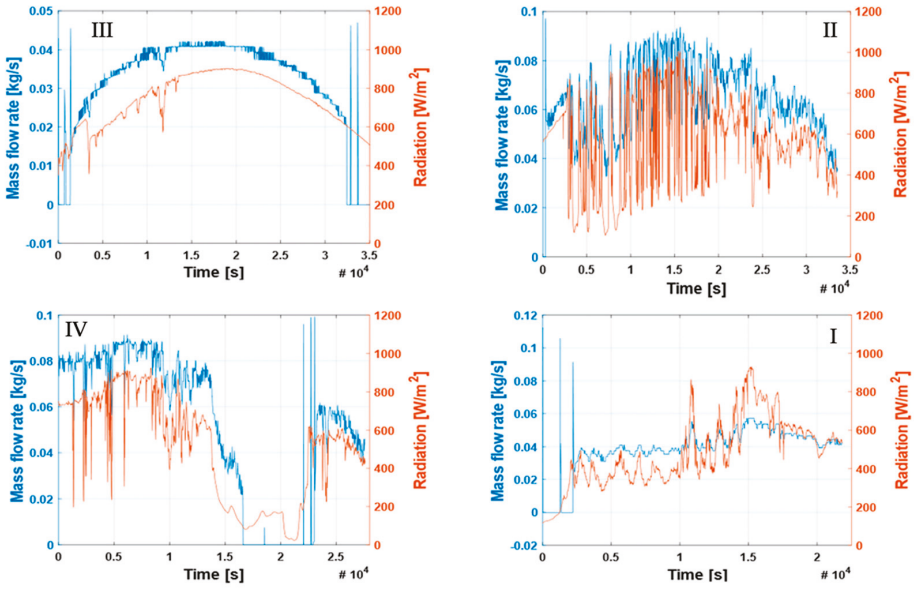

Figure 7. Measurement results for typical days in four defined weather groups: (I)—high solar radiation, low interference day; (II)—high radiation with strong fluctuations day; (III)—low radiation and high interference day; (IV)—below-average radiation, low interference day.

One article [48] discusses approaches to controlling solar thermal systems. Proportional control, ON–OFF control, and the new Indirect Proportional Control (IPC) method were tested. The experiments were conducted in real-world conditions using a method for measuring days. The results for all control methods regarding energy gains in storage tanks are presented, and based on the analysis, the following conclusions were drawn:

The analysis of energy gains in storage tanks across all control methods led to the following conclusions:

– Under conditions of high solar irradiance and low weather variability, the performance of all control strategies was comparable. However, the straightforward ON–OFF control achieved the greatest thermal energy accumulation under intense and stable sunlight. This outcome stems from its inherently high mass flow rate, which enhances heat transfer efficiency in such favorable conditions.

– When sunlight becomes more unpredictable, during periods of unstable sunlight, proportional control strategies become more effective. These methods are better suited to dynamic conditions and enable higher energy yields when solar availability is inconsistent. Under circumstances where solar input is high but thermal demand is low, the control task becomes more challenging. In such cases, standard proportional control often results in undesirable thermal drift. Methods that incorporate additional regulatory parameters—such as Indirect Proportional Control (IPC)—demonstrate improved performance. IPC minimizes energy losses caused by thermal drift and better utilizes the available solar radiation, leading to enhanced thermal efficiency.

The development of an adaptive controller aimed to enable the selection of an appropriate control method based on the current operating conditions of the solar heating system. To validate the conclusions drawn from the combined experimental and simulation research results, a new solar controller was programmed. The simulation model was based on several simplifying boundary conditions and operational assumptions to streamline the analysis of the solar thermal system. The thermophysical properties of the working fluid, including density and specific heat capacity, were assumed to be temperature-dependent but limited to single-phase liquid conditions, excluding saturation, phase change, or freezing states. Heat losses in the system were modeled using linear, temperature-dependent coefficients. It was assumed that no backflow or mass loss of the working fluid occurred in the hydraulic circuit. The model neglected external environmental influences such as wind speed, humidity, and atmospheric pressure. Finally, the pump model did not account for energy dissipation or fluid heating due to pump operation.

The new controller allowed for automatic changes in the control method by assessing 10-min time intervals. This was the final stage of the research, which enabled testing the formulated operational recommendations.

The adaptive controller was built using the Arduino Mega 2560, manufactured by Arduino (Turin, Italy), which is based on the Atmega microcontroller. The choice of this device for creating an adaptive controller was driven by several important advantages. It offers 54 digital I/O pins and 16 pins for analog signals, which is crucial given the complexity of the task and the need to manage numerous continuous signal sensors in the solar heating system.

The system was designed to accomplish two key tasks:

1. Switching the operating mode among the three tested control methods based on weather condition measurements from the last 10 min.
2. Assuming the role of a traditional solar controller in the heating system, specifically controlling the pump group operation according to the deltaT (temperature difference between the inlet and outlet of the solar collector) parameter and the selected algorithm.

The delay interval of 10 min was selected based on empirical observations gathered during preliminary testing phases. Various time intervals were evaluated to determine the optimal balance between system responsiveness and control stability. Shorter intervals—below 10 min—led to frequent and unnecessary switching between control modes, as the system reacted too sensitively to minor and transient fluctuations in solar radiation. This not only caused instability in the control process but also increased the wear on system components, particularly the circulation pump. Conversely, longer intervals—exceeding 10 min—resulted in the controller responding too slowly to actual changes in weather conditions. This delay reduced the system's ability to adapt promptly, leading to suboptimal energy harvesting during periods of rapidly changing solar irradi-

ance. As a compromise, a 10-min interval was identified as the most effective timeframe for assessing weather trends and adjusting control strategies accordingly. It provided sufficient temporal resolution to capture relevant changes while maintaining control stability and operational efficiency.

Implementing these functions required developing an adaptive controller operation algorithm capable of dynamically adjusting the pump group's operating parameters based on set conditions. This algorithm also needed to ensure the flexibility necessary for easy and rapid adaptation to dynamic control requirements. The conceptual diagram used in the development of the adaptive controller is presented in Figure 8.

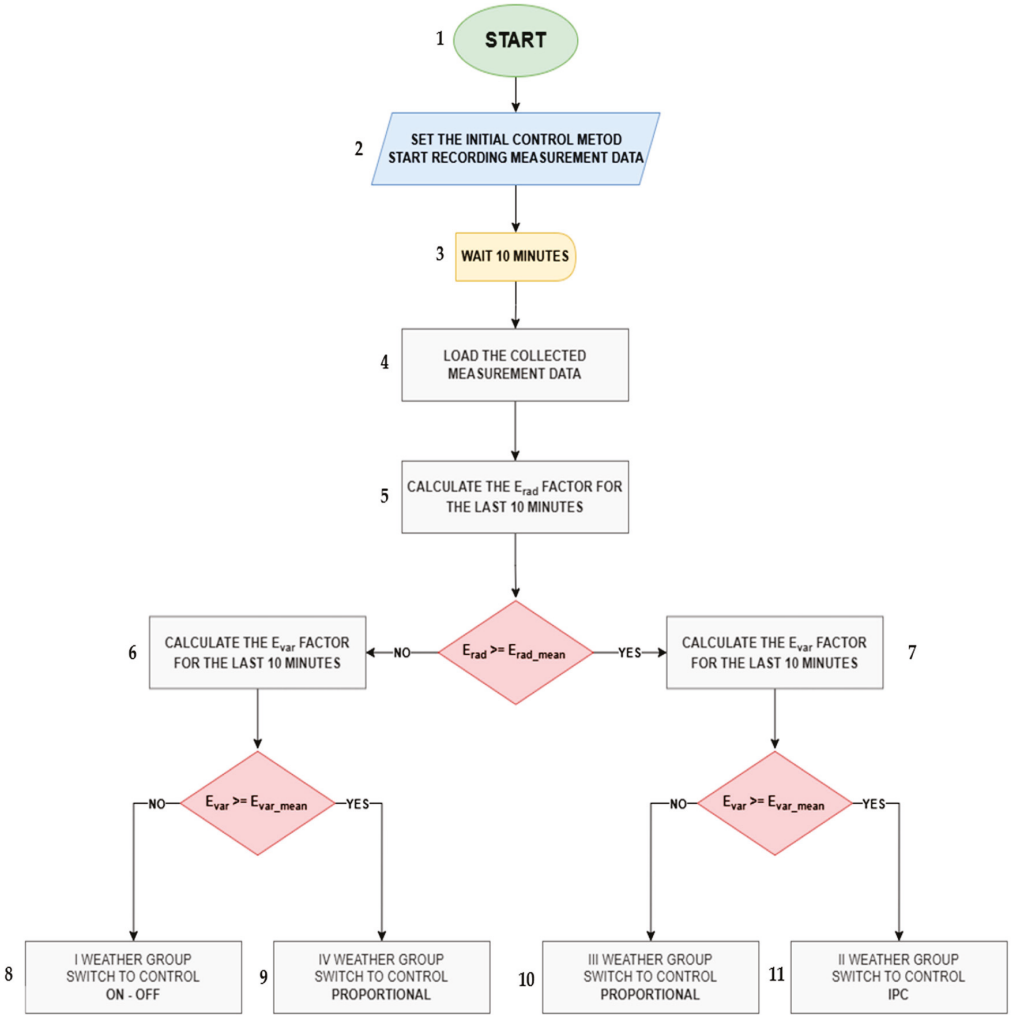

Figure 8. Algorithm of adaptive controller operation.

When the system is activated, the user selects the method of control for the work cycle. During this time, data on measurements from the heating system are gathered. The system runs for 10 min using parameters to collect data for adjusting the control method (4). After importing the measurement data, it computes an indicator to indicate the amount of energy received during the 10 min of operation (5). Comparing this information with the previously calculated average $E_{rad_{mean}}$ value determines its algorithmic step. Additionally, it compares the coefficient of variation in E_{var} with its average value from measurement samples—E_{var_mean}.

As a result of these two comparisons, the algorithm can classify and assign the analyzed time interval to one of four predefined weather groups using the proposed classifier.

Based on prior research and operational observations from the analysis of control methods in solar heating systems, a recommended control method for the specific weather group is then applied (8–11). Each method has been pre-programmed into the memory of the adaptive controller according to the parameters, algorithms, and operating characteristics discussed in previous chapters.

Following the classification of conditions and adjustment of control methods, another 10-min period is monitored irrespective of the identified weather category. This period serves as the foundation for the iteration in the work cycle. Throughout the measurement day, this iterative process continues with the controller. This setup enables the control method of heating systems to adapt to conditions effectively, thus optimizing solar energy utilization across different weather scenarios.

5. Results

The experiments were conducted at the test facility located at the Koszalin University of Technology (54°11′ N, 16°11′ E). Testing took place during the summer months (May–July 2023), covering a total of 53 measurement days. A subset of 40 days was selected for detailed analysis, ensuring complete datasets and representativeness within each weather classification group. The remaining days were excluded due to incomplete data, equipment malfunction, or non-representative weather conditions (e.g., prolonged overcast). The selected days were grouped by similar solar irradiance profiles to ensure consistent environmental conditions across control strategy comparisons. To assess the impact of the adaptive controller on the efficiency of the solar heating system, these data were compared with 40 previously collected samples. Reference samples were obtained using the classic proportional control method in the default operating mode of the ST-402n controller. The measurement results for both groups are summarized in Table 7. For each weather group, the average values of the indicators E_{rad} (energy available on the surface of solar collectors during the measurement day) and E_z (energy accumulated in the storage tank at the end of the measurement day) were calculated. Based on these values, the efficiency factor for the conversion of thermal energy in the solar heating system, X_{sol} was calculated for each group.

Specifically, the temperatures of the working fluid during both experimental and simulation periods are now described, with values ranging from 5 °C to 90 °C depending on the operational conditions. Furthermore, the system includes a high-efficiency circulation pump, ensuring that most of the consumed electrical energy is effectively converted into fluid flow. The hydraulic circuit features a mixing loop within the storage tank, which eliminates thermal stratification and maintains a uniform temperature distribution. The velocity of the working fluid within the hydraulic system ranges from 0 to 0.5 m/s, with smooth transitions and no abrupt changes, contributing to stable thermal conditions. The collector surface is assumed to be clean, and the optical parameters of the glass cover are uniform across the entire area, allowing for consistent performance under varying solar angles.

To assess the performance differences between control strategies, the average values of collected thermal energy and system efficiency were calculated, along with standard deviations. For instance, the adaptive IPC strategy achieved an average energy gain of 755 kWh $\pm$ 9.8 kWh, compared to 719 kWh $\pm$ 9.3 kWh for the ON–OFF method. A Student's *t*-test ($p < 0.05$) confirmed the statistical significance of these differences, supporting the robustness of the observed improvements.

Table 7. Summary results of comparative studies.

	Classic Proportional Solar Controller				**New Adaptive Controller**			
Number of days	40				40			
Weather group	**I**	**II**	**III**	**IV**	**I**	**II**	**III**	**IV**
Number of days in each group	10	10	10	10	10	10	10	10
Average E_{rad} value (energy available at the collector)	22.4 [kWh]	21.7 [kWh]	15.2 [kWh]	15.8 [kWh]	22.6 [kWh]	20.3 [kWh]	14.9 [kWh]	14.7 [kWh]
Average E_z value (energy collected in the tank)	13.8 [kWh]	10.4 [kWh]	7.8 [kWh]	9.0 [kWh]	15.2 [kWh]	12.6 [kWh]	9.1 [kWh]	8.8 [kWh]
$X_{Sol} = \frac{E_z}{E_{rad}}$	0.62	0.48	0.51	0.57	0.67	0.62	0.61	0.60
Difference between controller in a given group	-	-	-	-	+0.05 +8.1%	+0.14 +29.5%	+0.10 +19.0%	+0.03 +5.1%
$\sum E_{rad}$	755 [kWh] $\pm$ 9.8 kWh				719 [kWh] $\pm$ 9.3 kWh			
$\sum E_z$	416 [kWh]				453 [kWh]			
X_{Sol}	0.55				0.63			
Efficiency increase	-				**+12.7%**			

When using a classic solar controller, the average values of the E_{rad} index range from 15.8 to 22.4 kWh. As expected, a significantly higher potential for available energy is evident in the first two weather groups, which naturally experience higher solar radiation than average during the day. Similarly, the energy available in groups III and IV is correspondingly lower. Within each pair of groups, higher values of the E_{rad} are characteristic of groups with lower radiation variability. Regarding the energy stored in the tank, the values are more varied across the groups, ranging from 7.8 kWh to 13.8 kWh. This variation is due to differences in weather conditions among the groups and the varying efficiency of the heat collection process by a classic solar controller in each group. The highest amount of thermal energy collected was recorded in group I, while the lowest was observed in weather group IV.

The efficiency coefficients, which were calculated using these indicators, range from 0.48 to 0.62. This shows a variation in how effectively the solar heating system performs in different weather conditions. It is important to note that the highest and lowest efficiency ratings were found in groups I (0.62) and II (0.48). Despite both groups having energy potential, there was a difference in how efficiently the heating system operated between them. This difference is likely due to the variability in radiation levels; group II's high variability makes it more challenging to collect heat. A similar pattern can be seen in groups III and IV, although it is not as pronounced. In both cases, over half of the energy, during the day, was stored in the water tank. When using the designed controller, the E_{rad} values are slightly lower, ranging from 14.7 kWh, for group IV to 22.6 kWh for group I. It is important to note the difference in energy availability between groups I and II compared to groups III and IV. This difference, spanning several kilowatt-hours, results from the much higher solar radiation intensity during the days of the first two groups. In groups III and IV, there is an amount of available energy, whereas there is a 2.3 kWh difference between groups I and II.

In terms of stored energy, a wide range of measured values was observed, varying from 8.8 kWh for days in group IV to 15.2 kWh for days in group I. The X_{sol} coefficients calculated for each group are quite similar, ranging narrowly from 0.6 to 0.67. An adaptive controller maintained energy storage efficiency by minimizing the impact of weather

conditions on the energy storage process of the solar heating system. It was more effective in adjusting the system's operation to changing conditions than a standard solar controller, maximizing the stored energy. The energy efficiency coefficients X_{sol} measured during the tests using the controller show an increase compared to those obtained with the traditional controller across all weather categories. Figure 9 illustrates a comparison of the performance of both controllers in weather conditions.

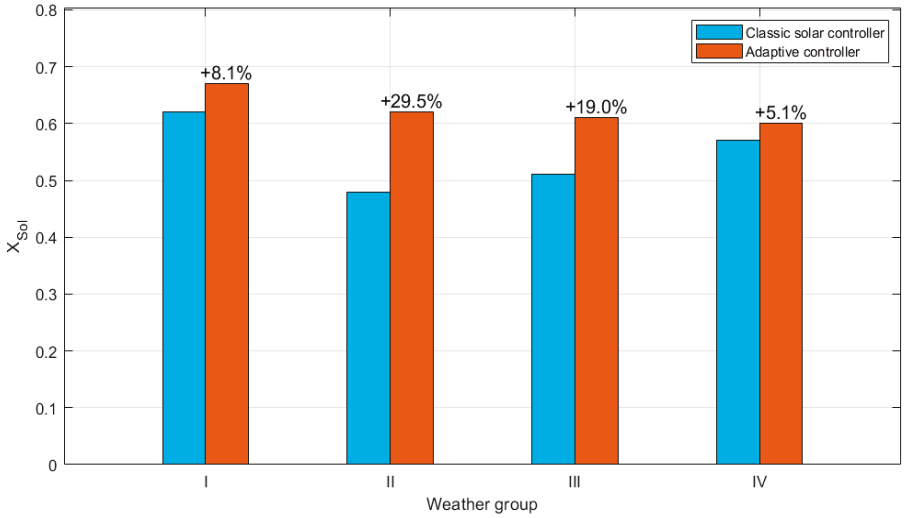

Figure 9. Comparison of the results obtained for the adaptive controller with the classical proportional controller in each weather group. Where the Y-axis represents the dimensionless coefficient expressing the ratio of actual solar energy gains to the theoretical maximum.

In each weather category analyzed, the adaptive controller demonstrated better efficiency in capturing solar energy from the collector surface and storing it in the water tank. It consistently outperformed the controller in terms of energy collection despite the latter being deemed superior in each category. This suggests that adjusting the control strategy based on weather conditions enhances system efficiency in varying weather scenarios.

The most significant increase in group II showed a 29.5% increase compared to the standard value. This substantial rise indicates that the adaptation mechanism works well in situations with intense and fluctuating solar radiation. Group III also experienced a smaller improvement of 19%, with the controller highlighting how radiation fluctuations can significantly enhance the advantages of employing adaptive techniques. Smaller enhancements of 8.1% and 5.1% were observed in groups I and IV, respectively. These modest variances suggest that both controllers perform under these circumstances. Nevertheless, it is crucial to stress that the adaptive control system continues to outshine the control method. These results underscore the validity and value of using an adaptive controller for managing the operation of a solar heating system.

6. Conclusions

The collected data and the conducted analyses provide convincing evidence that incorporating the findings from comparative studies on control strategies into the design of the adaptive controller led to a substantial performance enhancement over conventional control methods. Specifically, the adaptive controller achieved a 12.7% increase in solar energy collection efficiency, demonstrating its superiority in managing thermal energy in variable operating conditions. This improvement not only translates into enhanced overall system performance but also contributes to the economic and environmental viability of

solar thermal installations. For a standard residential system, the increased efficiency could result in annual energy savings of approximately 150–200 kWh, alongside a reduction in carbon dioxide emissions estimated at 50–70 kg. Such gains improve the return on investment by reducing operating costs and accelerating the payback period for the system.

Furthermore, these benefits align with broader sustainability and climate policy objectives, emphasizing the importance of maximizing energy use from renewable sources. Considering the growing global demand for efficient and intelligent renewable energy systems, the development, refinement, and implementation of advanced control strategies such as the one proposed in this study represent a crucial step toward achieving long-term energy transition goals.

As illustrated in Figure 10, the use of the adaptive controller resulted in more effective utilization of the available solar energy. During the operation of the conventional solar controller, the total solar radiation incident on the collector surface amounted to 755 kWh, of which approximately 416 kWh was stored in the water tanks, yielding an energy storage efficiency of 0.55. In comparison, when the adaptive controller was employed, the available solar radiation over the 40-day analysis period was lower, totaling 719 kWh. Nevertheless, the amount of thermal energy stored in the tanks increased to 453 kWh, corresponding to an efficiency factor of 0.63. These results indicate a marked improvement in energy collection efficiency associated with the adaptive control strategy. Notably, the adaptive controller enabled a higher thermal energy yield despite the reduced availability of solar energy, highlighting its effectiveness in optimizing system performance under variable operating conditions.

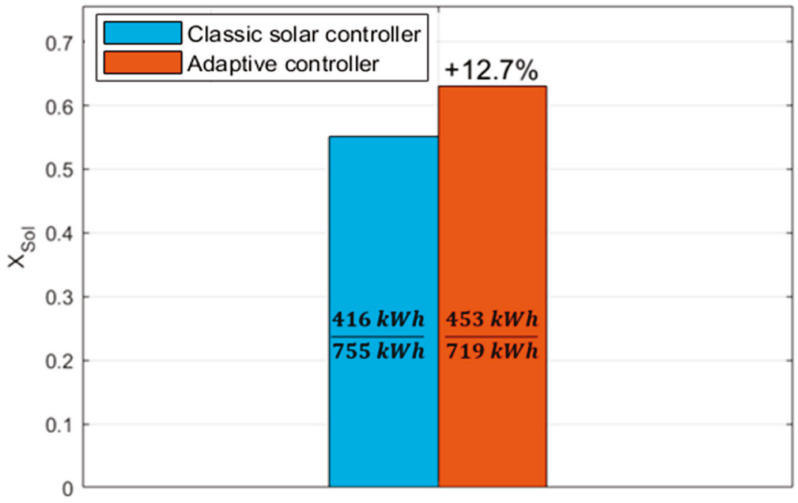

Figure 10. Summary values of acquired/available energy for both controllers. The Y-axis shows the solar gain coefficient, indicating system performance efficiency.

Moreover, the performance of the proposed method was contrasted with each constituent control method independently across weather categories. This comparative analysis revealed that no single fixed strategy consistently outperformed others in all conditions, underscoring the advantage of adaptive selection. In future research, the adaptive selection algorithm could be evaluated against a wider range of control strategies, such as fuzzy logic, PID controllers, or model predictive control, to further validate its versatility and effectiveness. While the present study focused on empirical performance under real-world operating conditions, incorporating a theoretical analysis from a control systems perspective could provide additional insight into the algorithm's decision-making mechanisms and stability characteristics.

Author Contributions: Conceptualization, P.Z., N.C.-G. and K.K.; methodology, N.C.-G., P.Z. and K.K.; software, P.Z. and K.K.; validation, N.C.-G. and P.Z.; formal analysis, N.C.-G., P.Z. and K.K.; investigation, P.Z., N.C.-G. and K.K.; resources, P.Z., K.K. and N.C.-G.; data curation, P.Z. and K.K.; writing—original draft preparation, P.Z., N.C.-G. and K.K.; writing—review and editing, P.Z., K.K. and N.C.-G.; visualization, P.Z. and K.K.; supervision, N.C.-G.; project administration, N.C.-G., P.Z. and K.K.; funding acquisition, N.C.-G. All authors have read and agreed to the published version of the manuscript.

Funding: This research received no external funding.

Data Availability Statement: Data are contained within this article.

Conflicts of Interest: The authors declare no conflicts of interest.

References

1. Olkiewicz, M.; Dyczkowska, J.A.; Olkiewicz, A.M. Financial Aspects of Energy Investments in the Era of Shaping Stable Energy Development in Poland: A Case Study. *Energies* **2023**, *16*, 7814. [CrossRef]
2. Bradac, J.; Folta, M.; Machuta, J.; Slaby, J.; Benes, M. Green Innovations in Foundry Production Processes of Automobile Castings. *Rocz. Ochr. Srodowiska* **2024**, *26*, 558–567. [CrossRef]
3. International Energy Agency (IEA). *Renewables 2023*; IEA: Paris, France, 2024. Available online: https://www.iea.org/reports/renewables-2023 (accessed on 12 April 2025).
4. Kelm, P.; Mieński, R.; Wasiak, I. Modular PV System for Applications in Prosumer Installations with Uncontrolled, Unbalanced and Non-Linear Loads. *Energies* **2024**, *17*, 1594. [CrossRef]
5. Kurz, D.; Bugała, A.; Głuchy, D.; Kasprzyk, L.; Szymenderski, J.; Tomczewski, A.; Trzmiel, G. The Use of Renewable Energy Sources in Road Construction and Public Transport: A Review. *Energies* **2024**, *17*, 2141. [CrossRef]
6. Kurz, D.; Dobrzycki, A.; Krawczak, E.; Jajczyk, J.; Mielczarek, J.; Woźniak, W.; Sąsiadek, M.; Orynycz, O.; Tucki, K.; Badzińska, E. An Analysis of the Increase in Energy Efficiency of Photovoltaic Installations by Using Bifacial Modules. *Energies* **2025**, *18*, 1296. [CrossRef]
7. Orosz, T.; Rassolkin, A.; Arsenio, P.; Poor, P.; Valme, D.; Sleisz, A. Current Challenges in Operation, Performance, and Maintenance of Photovoltaic Panels. *Energies* **2024**, *17*, 1306. [CrossRef]
8. Olchowik, W.; Bednarek, M.; Dąbrowski, T.; Rosiński, A. Application of the Energy Efficiency Mathematical Model to Diagnose Photovoltaic Micro-Systems. *Energies* **2023**, *16*, 6746. [CrossRef]
9. Wei, L.; Guo, X.; Zhang, L. Life-cycle assessments of solar water-heating systems: A review. *Proc. Inst. Civ. Eng. Energy* **2021**, *174*, 103–112. [CrossRef]
10. Tasmin, N.; Farjana, S.H.; Hossain, M.R.; Golder, S.; Mahmund, M.A.P. Integration of Solar Process Heat in Industries: A Review. *Clean Technol.* **2022**, *4*, 97–131. [CrossRef]
11. Bellos, E.; Tzivanidis, C. Investigation of a novel CO_2 transcritical organic rankine cycle driven by parabolic trough solar collectors. *Appl. Syst. Innov.* **2021**, *4*, 53. [CrossRef]
12. Ntsaluba, S.; Zhu, B.; Xia, X. Optimal flow control of a forced circulation solar water heating system with energy storage units and connecting pipes. *Renew. Energy* **2016**, *89*, 108–124. [CrossRef]
13. Zhang, G.; Hu, K.; Yan, C.; Shi, J.; Sheng, K.; Gong, Y.; Xu, Y. Optimal design and integration of multiple-function solar water heating systems based on a co-adaptive matchmaking method. *Energy Build.* **2021**, *252*, 111492. [CrossRef]
14. Liyew, K.W.; Louvet, Y.; Habtu, N.G.; Jordan, U. Experimental investigations of the operating behavior of a low-flow drainback solar heating system. *Energy Rep.* **2025**, *13*, 594–608. [CrossRef]
15. Duffie, J.A.; Beckman, W.A. *Solar Engineering of Thermal Processes*, 4th ed.; John Wiley & Sons: New York, NY, USA, 1991; ISBN 978-0-470-87366-3.
16. Brownson, J.R.S. *Solar Energy Conversion Systems*; Academic Press: London, UK, 2014; ISBN 9780123970213. [CrossRef]
17. Barone, G.; Buonomano, A.; Faninger, G.; Forzano, C.; Giuzio, G.F.; Kalogirou, S.A.; Palombo, A. Solar hot water heating systems. In *Comprehensive Renewable Energy*; Letcher, T.M., Ed.; Elsevier: Amsterdam, The Netherlands, 2022; pp. 463–500. [CrossRef]
18. Nguyen-Tuan, A.; Ta-Duy, B.; Nguyen-Duc, T.; Fujita, G. A novel approach to optimize and allocate battery energy storage system in distributed grid considering impact of demand response program. *Sustain. Energy Grids Netw.* **2025**, *43*, 101738. [CrossRef]
19. Nalina, B.S.; Chilambarasan, M.; Tamilselvi, S.; Al Alahmadi, A.A.; Alwetaishi, M.; Mujtaba, M.A.; Kalma, M.A. Design and Implementation of Embedded Controller-Based Energy Storage and Management System for Remote Telecom. *Electronics* **2023**, *12*, 341. [CrossRef]

20. Kamiński, K.; Znaczko, P.; Lyczko, M.; Krolikowski, T.; Knitter, R. Operational properties investigation of the flat-plate solar collector with poliuretane foam insulation. *Procedia Comput. Sci.* **2019**, *159*, 1730–1739. [CrossRef]
21. Kamiński, K.; Królikowski, T.; Błażejewski, A.; Knitter, R. Significant parameters identification for optimal modelling of the harp-type flat-plate solar collector. In *Sustainable Design and Manufacturing 2019*; Smart Innovation Systems and Technologies, Conference Paper; Springer: Singapore, 2019. [CrossRef]
22. Arkusz, K.; Pasiak, K.; Jedrzejewska, A.; Klekiel, T.; Wozniak, W.; Nycz, M.; Stryjski, R. Shedding light on the problem: Influence of the radiator power, source-sample distance, and exposure time on the performance of UVC lamps in laboratory and real-world conditions. *PLoS ONE* **2024**, *19*, e0302258. [CrossRef] [PubMed]
23. Mieński, R.; Wasiak, I.; Kelm, P. Integration of PV Sources in Prosumer Installations Eliminating Their Negative Impact on the Supplying Grid and Optimizing the Microgrid Operation. *Energies* **2023**, *16*, 3479. [CrossRef]
24. Olkiewicz, M.; Wolniak, R. Responsible pro-environmental management in an organization: A case study. *Rocz. Ochr. Srodowiska* **2020**, *22*, 763–780.
25. Xin, X.; Liu, Y.; Zhang, Z.; Zheng, H.; Zhou, Y. A day-ahead operational regulation method for solar district heating systems based on model predictive control. *Appl. Energy* **2025**, *377*, 124619. [CrossRef]
26. Bugała, A.; Bugała, D.; Jajczyk, J.; Dąbrowski, T. Statistical Analysis of Electrical and Non-Electrical Parameters of Photovoltaic Modules in Controlled Tracking Systems Artur Bugała. *Rocz. Ochr. Srodowiska* **2021**, *23*, 694–714. [CrossRef]
27. Krinitsky, M.; Averbukh, M. Control and Managing of Individual Solar Water Heating Systems in an Apartment Complex. *Electronics* **2024**, *13*, 2305. [CrossRef]
28. Grunt, M.; Pecolt, S.; Błazejewski, A.; Królikowski, T.; Kawa, K. Innovative Controller and Remote Battery Capacity Measurement System. *Procedia Comput. Sci.* **2024**, *246*, 4336–4346. [CrossRef]
29. Yang, M.; Moghimi, M.A.; Loillier, R.; Markides, C.N.; Kadivar, M. Design of a latent heat thermal energy storage system under simultaneous charging and discharging for solar domestic hot water applications. *Appl. Energy* **2023**, *336*, 120848. [CrossRef]
30. Congedo, P.M.; Baglivo, C.; Carrieri, L. Application of an unconventional thermal and mechanical energy storage coupled with the air conditioning and domestic hot water systems of a residential building. *Energy Build.* **2020**, *224*, 110234. [CrossRef]
31. Wu, W.; Dai, S.; Liu, Z.; Dou, Y.; Hua, J.; Li, M.; Wang, X.; Wang, X. Experimental study on the performance of a novel solar water heating system with and without PCM. *Sol. Energy* **2018**, *171*, 604–612. [CrossRef]
32. Abokersh, M.H.; El-Morsi, M.; Sharaf, O.; Abdelrahman, W. On-demand operation of a compact solar water heater based on U-pipe evacuated tube solar collector combined with phase change material. *Sol. Energy* **2017**, *155*, 1130–1147. [CrossRef]
33. Essa, M.A.; Mostafa, N.H.; Ibrahim, M.M. An experimental investigation of the phase change process effects on the system performance for the evacuated tube solar collectors integrated with PCMs. *Energy Convers. Manag.* **2018**, *177*, 1–10. [CrossRef]
34. Belz, K.; Kuznik, F.; Werner, K.F.; Schmidt, T.; Ruck, W.K.L. Thermal energy storage systems for heating and hot water in residential buildings. In *Advances in Thermal Energy Storage Systems*; Cabeza, L.F., Ed.; Woodhead Publishing: Cambridge, UK, 2015; pp. 441–465. [CrossRef]
35. Dincer, I.; Erdemir, D. Thermal energy storage systems. In *Solar Ponds*; Springer: Cham, Switzerland, 2024. [CrossRef]
36. Sarbu, I.; Sebarchievici, C. A comprehensive review of thermal energy storage. *Sustainability* **2018**, *10*, 191. [CrossRef]
37. Babaelahi, M.; Kazemi, A. Optimal energy system configuration for zero energy buildings using hybrid thermal-photovoltaic solar collector. *Environ. Dev. Sustain.* **2024**, *27*, 11047–11062. [CrossRef]
38. Pérez-Iribarren, E.; González-Pino, I.; Azkorra-Larrinaga, Z.; Odriozola-Maritorena, M.; Gómez-Arriarán, I. A mixed integer linear programming-based simple method for optimizing the design and operation of space heating and domestic hot water hybrid systems in residential buildings. *Energy Convers. Manag.* **2023**, *292*, 117326. [CrossRef]
39. Rahimi-Ahar, Z.; Khiadani, M.; Rahimi Ahar, L.; Shafieian, A. Performance evaluation of single stand and hybrid solar water heaters: A comprehensive review. Clean Technol. *Environ. Policy* **2023**, *25*, 2157–2184. [CrossRef]
40. Kalogirou, S.A.; Tripanagnostopoulos, Y. Hybrid PV/T solar systems for domestic hot water and electricity production. *Energy Convers. Manag.* **2006**, *47*, 3368–3382. [CrossRef]
41. Dudkiewicz, E.; Fidorów-Kaprawy, N. Hybrid domestic hot water system performance in industrial hall. *Resources* **2020**, *9*, 65. [CrossRef]
42. Barbu, M.; Darie, G.; Siroux, M. A parametric study of a hybrid photovoltaic thermal (PVT) system coupled with a domestic hot water (DHW) storage tank. *Energies* **2020**, *13*, 6481. [CrossRef]
43. Babu, C.; Ponnambalam, P. The role of thermoelectric generators in the hybrid PV/T systems: A review. *Energy Convers. Manag.* **2017**, *151*, 368–385. [CrossRef]
44. Zhou, X.; Wu, L.; Xiao, G.; Tong, Z.; Li, H. Experimental investigation and economic analysis on a solar pure water and hot water hybrid system. *Appl. Therm. Eng.* **2021**, *195*, 117182. [CrossRef]

45. Prud'homme, T.; Gillet, D. Advanced control strategy of a solar domestic hot water system with a segmented auxiliary heater. *Energy Build.* **2001**, *33*, 463–475. [CrossRef]
46. Araújo, A.; Pereira, V. Solar thermal modeling for rapid estimation of auxiliary energy requirements in domestic hot water production: On-off flow rate control. *Energy* **2017**, *119*, 637–651. [CrossRef]
47. Lapertot, A.; Segond, G.; Fasquelle, T.; Kadoch, B.; Le Métayer, O. Multi-criteria optimization of an experimental system for the production of domestic hot water. *Energy Convers. Manag.* **2022**, *267*, 115875. [CrossRef]
48. Znaczko, P.; Kaminski, K.; Chamier-Gliszczynski, N.; Szczepanski, E.; Gołda, P. Experimental analysis of control methods in solar water heating systems. *Energies* **2021**, *14*, 8258. [CrossRef]
49. Li, W.-T.; Thirugnanam, K.; Tushar, W.; Yuen, C.; Chew, K.T.; Tai, S. Improving the operation of solar water heating systems in green buildings via optimized control strategies. *IEEE Trans. Ind. Inform.* **2018**, *14*, 1646–1655. [CrossRef]
50. Yin, L.; Xiong, Y. Fast-apply deep autoregressive recurrent proximal policy optimization for controlling hot water systems. *Appl. Energy* **2024**, *367*, 123348. [CrossRef]
51. Znaczko, P.; Kaminski, K.; Chamier-Gliszczynski, N. A correlation study between weather conditions and the control strategy of a solar water heating system. In *Sustainable Design and Manufacturing 2020*; Smart Innovation, Systems and Technologies, 200; Scholz, S.G., Howlett, R.J., Setchi, R., Eds.; Springer: Singapore, 2021. [CrossRef]
52. Kicsiny, R.; Farkas, I. Improved differential control for solar heating systems. *Sol. Energy* **2012**, *86*, 3489–3498. [CrossRef]
53. Hongbing, C.; Yutong, G.; Haoyu, N.; Xiaoli, Y.; Xilin, C. Optimization and performance study of residential centralized solar domestic hot water system. *Energy Procedia* **2019**, *158*, 6431–6437. [CrossRef]
54. Rehman, H.; Hirvonen, J.; Sirén, K. Design of a simple control strategy for a community-size solar heating system with a seasonal storage. *Energy Procedia* **2016**, *91*, 486–495. [CrossRef]
55. Zhang, Z.; Zhou, Y.; Xin, X.; Qian, J.; Liu, Y. A day-ahead operation regulation method for solar water heating based on model predictive control. *Energy Build.* **2023**, *301*, 113715. [CrossRef]
56. Azhar, K.M.; Idres, A.H. Analysis of energy savings for residential electrical and solar water heating systems. *Case Stud. Therm. Eng.* **2021**, *27*, 101347. [CrossRef]
57. Al-Mamun, M.R.; Roy, H.; Islam, M.S.; Ali, M.R.; Hossain, M.I.; Aly, M.A.S.; Khan, M.Z.H.; Marwani, H.M.; Islam, A.; Haque, E.; et al. State-of-the-art in solar water heating (SWH) systems for sustainable solar energy utilization: A comprehensive review. *Sol. Energy* **2023**, *264*, 111998. [CrossRef]
58. Ghorab, M.; Entchev, E.; Yang, L. Inclusive analysis and performance evaluation of solar domestic hot water system (a case study). *Alex. Eng. J.* **2017**, *56*, 201–212. [CrossRef]
59. Li, W.T.; Tushar, W.; Yuen, C.; Ng, B.K.K.; Tai, S.; Chew, K.T. Energy efficiency improvement of solar water heating systems—An IoT based commissioning methodology. *Energy Build.* **2020**, *224*, 110231. [CrossRef]
60. Halam, R.; Raman, R. Enhancing Energy Efficiency in Solar Water Heating Systems for Sustainable Homes with IoT Technology. In Proceedings of the 2023 International Conference on Innovative Computing, Intelligent Communication and Smart Electrical Systems, ICSES 2023, Chennai, India, 14–15 December 2023. [CrossRef]
61. Unterberger, V.; Lichtenegger, K.; Kaisermayer, V.; Gölles, M.; Horn, M. An adaptive short-term forecasting method for the energy yield of flat-plate solar collector systems. *Appl. Energy* **2021**, *293*, 116891. [CrossRef]
62. Han, X.; Li, C.; Ma, H. Performance studies and energy-saving analysis of a solar water-heating system. *Processes* **2021**, *9*, 1536. [CrossRef]
63. Budea, S.; Bădescu, V. Improving the performance of systems with solar water collectors used in domestic hot water production. *Energy Procedia* **2017**, *112*, 398–403. [CrossRef]
64. *ISO 9806:2017*; Solar Energy—Solar Thermal Collectors—Test Methods. European Committee for Standardization: Brussels, Belgium, 2017.
65. Huang, B.J.; Ton, W.Z.; Wu, C.C.; Ko, H.W.; Chang, H.S.; Yen, R.H.; Wang, J.C. Maximum-power-point tracking control of solar heating system. *Sol. Energy* **2012**, *86*, 3278–3287. [CrossRef]
66. Svensen, J.L.; Bergsteinsson, H.G.; Madsen, H. Modeling and nonlinear predictive control of solar thermal systems in district heating. *Heliyon* **2024**, *10*, e31027. [CrossRef] [PubMed]

Disclaimer/Publisher's Note: The statements, opinions and data contained in all publications are solely those of the individual author(s) and contributor(s) and not of MDPI and/or the editor(s). MDPI and/or the editor(s) disclaim responsibility for any injury to people or property resulting from any ideas, methods, instructions or products referred to in the content.

energies

MDPI

Article

Energy and Exergy Assessment of a Solar Driven Single Effect H_2O-LiBr Absorption Chiller Under Moderate and Hot Climatic Conditions

Mamadou Sow and Lavinia Grosu *

Laboratory of Energetics Mechanics and Electromagnetism, University of Paris Nanterre, 50 rue de Sèvres, 92410 Ville d'Avray, France
* Correspondence: mgrosu@parisnanterre.fr

Abstract: This work mainly focuses on the energy and exergy analysis of a single-effect absorption cooling system operating with the couple H_2O-LiBr, under different climatic conditions in Senegal and France. A simulation model was developed, using the Engineering Equation Solver V10 (EES) software. Results indicate that the system can achieve a maximum COP of 0.76 and an exergy efficiency of 56%, which decreases as the generator temperature increases. Increasing the generator temperature from 87 to 95 °C significantly improves COP, but gains become marginal beyond 100 °C. The highest exergy destruction occurs in the generator, followed by the absorber, condenser, and evaporator. A temperature difference above 44 °C between the generator and the absorber is required to maintain H_2O-LiBr solution stability. Optimal temperatures for hot climates like Senegal are 90 °C (generator), 42 °C (absorber/condenser), and 7 °C (evaporator), while maximum exergy efficiency (56%) is reached at 81 °C, typical of moderate climates (France). Evaporator exergy efficiency increases from 16 to 52% with rising ambient temperature, while absorber and condenser efficiencies drop. Increasing the cooling water flow rate from 0.2 to 1.4 kg/s reduces exergy losses in the absorber and the condenser by up to 36%. The solution heat exchanger (SHE) optimal effectiveness of 0.75 reduces exergy consumption in the absorber and the generator.

Keywords: absorption chiller; energy; exergy; solar cooling; H_2O-LiBr; single effect

1. Introduction

With environmental challenges intensifying worldwide, the need for sustainable energy solutions has never been more urgent [1,2].

Heatwaves in Europe have already caused nearly 90,000 fatalities since 1980 [3]. Excessive urban heat causes residents to rely on electricity for cooling, resulting in high energy use, pollution, and economic strain, all of which being unsustainable.

In France, cooling demand in residential areas is limited to short periods during heat waves but cooling needs for the residential sector are expected to increase in the future [4]. There is a large demand for cooling in developing countries where there is no reliable electricity supply and fuels are difficult or too expensive to obtain [5]. In Senegal, a significant part of energy demand is dedicated to cooling, as ambient temperatures can reach over 43 °C in some areas. The three main areas in which there is a demand for cooling are vaccine storage, food preservation, and air conditioning. In addition, Senegal is commonly known as a good country for energy transitions with a high solar density

area with 1600 to 1800 kWh/m^2 per year of direct irradiation and appears to be an ideal candidate for solar applications. It was also stated that the photovoltaic solar system components (batteries, inverters, regulators) efficiency depends strongly on the ambient temperature and need to be cooled in this country to increase their lifespan [4]. In response to the challenges posed by building energy consumption, numerous research efforts are currently underway to enhance the energy performance of buildings [6].

Solar refrigeration technologies have the advantage of consuming less energy and using environmentally friendly fluids. One of these systems related to cooling and air conditioning is the absorption chiller. Instead of using shaft work, a heat source provides the energy to produce cooling in absorption chillers. Solar absorption cooling systems provide a viable option for reducing energy consumption, but their performance varies across different climatic conditions [7]. In recent years, many studies concerning these technologies have been reported.

Ketfi et al. [8] studied the performance of a Single Effect Solar Absorption Cooling System (LiBr-H_2O). The results showed a better COP with the increase in the generator and evaporator temperatures, and a lower one with the increase in the absorber and condenser temperatures.

Chen et al. [9] experimented an air-cooled single effect absorption chiller with a cooling capacity of about 6 kW. Under design conditions, the ambient temperature significantly affected the performance of the chiller. The COP decreased from 0.68 to 0.6 with the ambient temperature rising from 28 to 35 °C. Boukholda et al. [10] investigated a commercial absorption chiller using natural refrigerant R717 and powered by a Fresnel solar collector. Experimental results show that the temperature of the heat source fluid can reach 190 °C with the chilled water leaving the evaporator at −7.8 °C. The average coefficient of performance of the chiller is about 0.65. Pop et al. [11] operated a single effect ammonia-water absorption chiller with solar parabolic trough collectors for cold storage and the freezing of meat in a cold storage warehouse. The values of the COP were found higher when the refrigeration plant operates in the refrigeration regime in comparison to the freezing regime.

The configuration of absorption chillers depends on the particular demands of every system [12]. The efficiency of these systems increases with the effects number [11]. Absorption chillers could be found in single, double, and triple effect configurations. Generally, the configurations with a higher number of effects present higher coefficient of performance (COP) values, though their driving temperature levels are higher, as more effects are considered and the conversion of low or medium temperature heat sources is more efficient [13].

Most single effect absorption systems use flat or vacuum solar collectors [13]. In single effect absorption technology, a peak COP of around 0.7 is obtainable and the heat input temperature is in the range of 90–120 °C [14]. Double and triple effect chillers require driving temperatures of around 180–240 °C and can reach COPs of up to 1.4 and 1.8, respectively [15]. The multiples-effects absorption systems available on the market with higher temperatures than simple-effect ones can be obtained by concentrated solar collectors. The main factors affecting the performance of an absorption system are external temperature, solar irradiance, solar collector performance, cooling load scheduling, the system configurations, control logic of the whole system, and operational conditions [16–19].

Although the potential of solar-powered absorption chillers is well established, assessments under contrasting climatic conditions remain limited. This study addresses that gap by conducting a detailed energy and exergy analysis of a single-effect H_2O-LiBr absorption chiller operating in two distinct environments: France and Senegal, by simulating realistic

conditions including ambient temperature, solar irradiation, cooling water availability, and heat rejection potential. This work evaluates how the local climate influences system performance. The comparison is grounded in a technical feasibility perspective, highlighting the operational constraints and opportunities in each context. Particular attention is given to the main components, whose performance strongly depends on external conditions. The findings aim to support the optimal design and deployment of solar thermal cooling technologies in both developed and developing countries, reinforcing their adaptability and practical relevance across diverse climatic scenarios.

2. Materials and Methods

2.1. System Configuration

The components of the studied solar installation, shown in Figure 1, are listed in Table 1. The solar tank, the absorption machine, and the hydraulic network allowing the fluid circulation, are installed in the technical local situated near the solar collector. A 2-pipe hot water/chilled water supply network is situated between the technical local and the fan coils installed in the building.

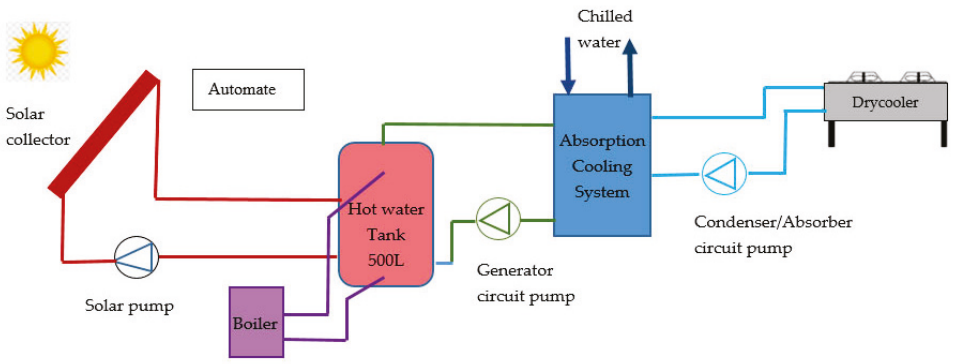

Figure 1. Schematic diagram of solar air conditioning installation.

Table 1. Components of the overall absorption cooling system.

Components and Arrangement	
Field of solar thermal collectors	Evacuated heat pipe tubes, with a total "input" surface area of 13 m^2, inclined at 30° and south orientation
Solar hot tank	Vertical type hot buffer tank with a capacity of 500 L
Chiller	Absorption machine with 17 kW of nominal refrigeration power
Drycooler	Adiabatic air cooler with a power adapted to the absorption machine, about 45 kW
Distribution network	Armaflex XG insulated multilayer pipes
Chilled water fan coils	3 WESPER Aquafan II AHC fan coils (cased ceiling light) with an average nominal cooling power of 6 kW

Solar irradiation is transformed into heat by solar thermal collectors and transported by a heat transfer fluid (monopropylene glycol) to a hot water tank placed between the solar collectors and the generator inlet of the absorption cooling system. This tank serves as a buffer tank, allowing the continuous operation of the installation, even during a cloudy period.

The solar circuit is self-draining. It includes a safety device that limits the risk of overheating. When the temperature in the solar tank is over a limit imposed value, the

solar primary pump is stopped. Solar collectors drain themselves by the action of gravity. The heat transfer fluid is then collected in the self-draining tank. The pump can then only be restarted when the temperature of the solar tank has dropped significantly.

The absorption cooling system uses the solar heat as an energy source and supplies the cooling load to the building. The operation of the absorption cooling system depends on the temperature levels of the heat exchangers. To operate, the system must be supplied with hot water at a temperature between 70 and 90 °C. The return from the air conditioning circuit must be bigger than 12 °C and intermediate cooling (Dry cooler) must be carried out between 20 and 35 °C.

The control and regulation of the air conditioning equipment is handled by a central controller, connected to the Ethernet network, having a user interface with remote access. The automaton also acts as a remote controller and logs are programmed.

The principles of regulating the solar production part are as follows. The solar primary pump which allows the circulation of fluid in the collectors, is activated according to a sunshine threshold. Anti-overheating safety is activated when the temperature at the top of the solar hot tank exceeds 95 °C.

The generator circuit pump is activated if the temperature at the top of the solar hot tank is higher than a set value of about 80 °C, allowing the absorption cooling system to operate with correct performance. As the generator circuit pump ensures the transfer of energy to the cooling system, it is only stopped when the temperature at the top of the solar hot tank is less than or equal to the minimum temperature necessary for the operation of the absorption cooling system.

2.2. Characteristics of Solar Thermal Collectors

The solar thermal collectors installed at the University of Paris Nanterre (Figure 2) connected to the absorption system (Figure 3) are evacuated tube collectors of the heat pipe type, certified with a valid CSTB Technical Approval and Solar Keymark certificate covered by a ten-year "good performance" guarantee. They are heating pipe vacuum tube types with a selectively coated metal absorber with a dry type of collector/heat pipe connection and a copper collector (1 inlet/1 outlet) on either side of the sensor, installed on supports inclined at 30° from the terrace roof. The characteristics of each collector are η_0 = 0.683 (optical efficiency), a_1 = 1.37 W/m^2. K (first-order heat loss coefficient), a_2 = 0.0041 W/m^2. K^2 (second-order heat loss coefficient) for an entrance surface of 3.26 m^2. The efficiency can then be estimated using the following expression $\eta = \eta_0 - a_1 \frac{T - T_{amb}}{G} - a_2 \frac{(T - T_{amb})^2}{G}$ where T is the average fluid temperature in the collector, T_{amb} refers to the ambient temperature and G represents global solar irradiance on the collector surface.



Figure 2. Photograph of the thermal solar field installed at the University of Paris Nanterre.



Figure 3. Photograph of the solar powered absorption system.

This equation allows for the estimation of thermal efficiency under variable climate and operating conditions.

2.3. Comparative Study (France vs. Senegal)

A comparative simulation study was conducted using the TRANSOL Pro 3.1 software to evaluate the thermal performance of the solar collector field currently installed in France against an identical system hypothetically installed in Senegal. The objective was to assess the impact of local climatic conditions, particularly solar irradiance and ambient temperature on the annual thermal energy output, collector efficiency, and overall system performance. Both configurations were modeled using the same collector specifications, orientation, tilt angle, and system design parameters to ensure a consistent basis for comparison.

The simulation results, summarized in Table 2, highlight the differences in solar energy availability and thermal yield between a temperate climate (France) and a hot, sunny climate (Senegal), providing insights into the system's potential for enhanced productivity under higher solar resource conditions.

Table 2. Evacuated tube solar collectors' performance: France vs. Senegal.

Month	Monthly Irradiation Duration [h]		Monthly Solar Irradiation [kWh/m^2]		Ambiant Temperature [°C]		Rendement	
	Ville d'Avray (France)	Ziguinchor (Senegal)	Ville d'Avray (France)	Ziguinchor (Senegal)	Ville d'Avray (France)	Ziguinchor (Senegal)	Ville d'Avray (France)	Ziguinchor (Senegal)
January	55.6	265.0	43.7	167.4	4	29	0.36	0.62
February	68.0	265.0	65.2	189.1	6.2	30	0.46	0.64
March	122.7	305.0	122.8	190.4	7.7	31	0.49	0.64
April	148.3	295.0	156.3	217.0	8.5	32	0.51	0.66
May	153.8	300.0	163.1	198.0	12.2	32	0.54	0.65
June	260.4	250.0	167.4	167.4	18.5	31	0.49	0.65
July	216.9	200.0	174.5	132.0	19	28	0.55	0.61
August	176.2	185.0	160.9	130.2	18.1	26	0.57	0.60
September	143.0	205.0	138.6	130.2	17.8	27	0.58	0.60
October	110.5	255.0	92.4	129.0	11.9	30	0.48	0.60
November	53.0	265.0	49.8	151.9	9.3	30	0.49	0.62
December	49.1	305.0	41.5	150.0	6.2	30	0.42	0.59

As expected, the solar collector efficiency would be higher under the climatic conditions in Senegal than in France, depending on the ambient temperature, the solar irradiation, and the daily duration of the irradiation. The inclination angle of the collector greatly

affects natural convection and heat transfer. Thus, the recommended inclination angle in Senegal is 20° with an incoming mean daily irradiance of about 550 W/m^2, while in France, the recommended inclination is 40° with the mean incoming daily irradiance equaling about 339 W/m^2.

3. Thermodynamic Analysis of the Absorption Cooling System

3.1. Method and Assumption

The method developed in this study is based on the energy and exergy analysis including the following steps:

- The studied system is divided into several sections (control volumes), depending on the depth of details and the desired understanding of the analysis.
- The mass, energy, entropy, and exergy balances are established on each section.
- The results are analysed to draw conclusions and make appropriate recommendations regarding the design and operation conditions of the system upgrades.

The analysis based on the first and second laws of thermodynamics applied to the single-effect H_2O-LiBr absorption cycle with a solution heat exchanger is carried out under the following assumptions and conditions:

- ➢ The system operates under steady-state conditions.
- ➢ The temperatures within the heat exchangers (generator, condenser, evaporator, and absorber) are assumed to be uniform throughout their respective volumes.
- ➢ The rich solution leaving the absorber is considered as saturated liquid at the corresponding absorber temperature and concentration.
- ➢ The poor solution exiting the generator is assumed to have a concentration in thermodynamic equilibrium with the generator's pressure and temperature.
- ➢ The refrigerant leaving the condenser is taken as saturated liquid at the corresponding temperature and pressure.
- ➢ The refrigerant at the evaporator outlet is considered as saturated vapour at the low pressure and temperature of the evaporator.
- ➢ Expansion processes (through throttling valves) are considered isenthalpic.
- ➢ Pressure drops throughout the system are assumed to be negligible.

Each of these aspects and the solution adopted in this work are presented below. The operating thermodynamic states of the absorption cycle are shown in Figure 4.

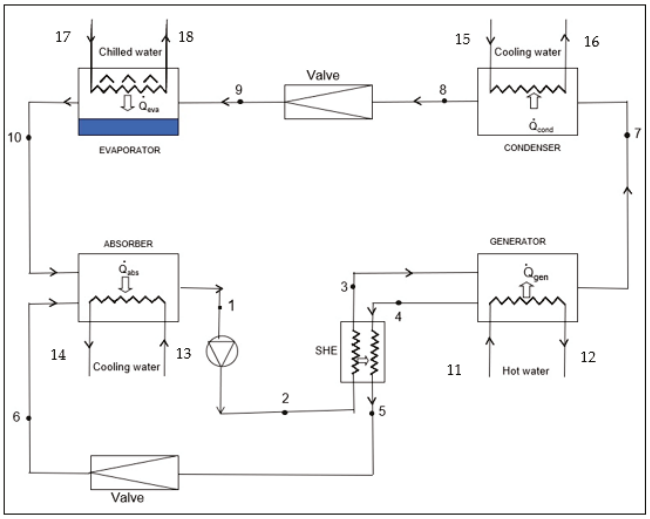

Figure 4. Schematic of the absorption cycle with operating thermodynamic states (from 1 to 18).

3.2. Energy and Mass Balances

The model of the absorption cooling system was built according to mass and energy balances, considering each of the components (generator, condenser, evaporator, solution heat exchanger, and absorber) as a control volume.

The energy balance is evaluated from the general following equation:

$$\frac{dE}{dt} = \sum \dot{Q} + \sum \dot{W} + \sum \dot{m}_i \left(h + \frac{v^2}{2} + gz \right)_i - \sum \dot{m}_e \left(h + \frac{v^2}{2} + gz \right)_e \quad (1)$$

The following hypotheses were considered:

- The regime is permanent.
- The variation in kinetic and potential energies is insignificant.

Therefore, Equation (1) becomes:

$$\sum \dot{Q} + \sum \dot{W} = \sum \dot{m}_e h_e - \sum \dot{m}_i h_i \quad (2)$$

The mass conservation law is applied as follows:

$$\frac{dm}{dt} = \sum \dot{m}_i - \sum \dot{m}_e \quad (3)$$

In addition, the regime being considered permanent, following this equation is obtained:

$$\sum \dot{m}_i - \sum \dot{m}_e = 0 \quad (4)$$

These mass and energy balances are written for each component of the absorption machine.

Absorber

In the absorber, the refrigerant (H_2O) is absorbed by the rich in LiBr solution during an exothermic process.

$$|q_{abs}| = (h_{10} - h_1) + f(h_6 - h_1) \quad (5)$$

$$\dot{m}_{10} + \dot{m}_6 - \dot{m}_1 = 0 \quad (6)$$

where f is the solution circulation ratio, defined by the ratio of the mass flow rate of the rich solution to the mass flow rate of the refrigerant.

$$f = \frac{\dot{m}_r}{(\dot{m}_p - \dot{m}_r)} \quad (7)$$

Generator

The role of the generator is to separate the refrigerant (H_2O) from the poor in LiBr solution (diluted solution) during an endothermic process. Required heat energy is provided by the solar panels. The poor in LiBr solution enters in the generator, releases the refrigerant, and returns to the absorber concentrated in LiBr.

$$q_{gen} = (h_7 - h_3) + f(h_4 - h_3) \quad (8)$$

$$\dot{m}_3 - \dot{m}_4 - \dot{m}_7 = 0 \quad (9)$$

Condenser

In the condenser, the refrigerant transfers the heat energy to the cooling fluid. Mass and energy balances are written as follows:

$$|q_{cond}| = (h_7 - h_8) \tag{10}$$

$$\dot{m}_7 - \dot{m}_8 = 0 \tag{11}$$

Evaporator

The role of the evaporator is to remove heat from an external fluid (chilled water). Mass and energy balances are written as follows:

$$q_{eva} = (h_{10} - h_9) \tag{12}$$

$$\dot{m}_9 - \dot{m}_{10} = 0 \tag{13}$$

Solution heat exchanger

At the solution heat exchanger, thermal equilibrium is assumed to be obtained and the heat flow released by the rich solution is assumed to be entirely received by the poor solution. Thus, the following equations are obtained:

$$q_{SHE} = f(h_4 - h_5) \tag{14}$$

$$(\dot{m}_2 + \dot{m}_4) - (\dot{m}_3 + \dot{m}_5) = 0 \tag{15}$$

The coefficient of performance (COP) of the absorption machine is defined by the ratio of the power absorbed by the evaporator to the power supplied to the generator to which is added the power of the solution pump:

$$COP = \frac{\dot{Q}_{eva}}{\dot{Q}_{gen} + \dot{W}_{pump}} \tag{16}$$

3.3. Exergy Analysis

If the energy analysis states the way the energy is converted from a form to another during a process, the exergy analysis provides information on the degradation of energy during the process.

Exergy analysis is based both on the first and second principles of thermodynamics. Every component is studied from an exergetic point of view, and so, for every component, the following elements are associated: a fuel (the exergetic resource supplied or the exergetic potential at the beginning of the process), a product (what the component offers from an exergetic point of view), and the irreversibility, meaning the exergy consumed (named also exergy destruction).

Thus, exergy analysis is used to estimate the exergy consumption (destructions) to point out the malfunctions occurring in each component of the system.

An exergy analysis, similar to a previous study conducted by [16–19] is carried out with the following parameters considered as the reference state conditions: $P_0 = 101.4$ kPa and $T_0 = 20$ °C in France, $T_0 = 35$ °C in Senegal.

The exergy balance is written as follows:

$$\frac{dEx}{dt} = \sum\left(1 - \frac{T_0}{T}\right)\dot{Q} + \sum\dot{W} + \sum\dot{m}_i ex_i - \sum\dot{m}_e ex_e - \dot{I} \tag{17}$$

where the index 0 represents the reference state. The terms ex_i and ex_e are, respectively, the specific exergies at the inlet and the exit of a component which are defined as the sum of thermo-mechanical and chemical specific exergies:

$$ex = ex^{TM} + ex^{CH} \tag{18}$$

For a state *i*, the thermo-mechanical exergy can be expressed by the following equation:

$$ex_i^{TM} = (h_i - h_0) - T_0(s_i - s_0) \tag{19}$$

where the parameters with subscript "0" represent the H_2O-LiBr solution with the same chemical concentration as the one at the considered state, but in a thermo-mechanical equilibrium with the environment (P_0, T_0).

Thus, its corresponding exergy flow is expressed as:

$$\dot{E}x_i = \dot{m}_i * ex_i \tag{20}$$

Considering a permanent regime, the exergy balance becomes:

$$\dot{I} = \sum\left(1 - \frac{T_0}{T}\right)\dot{Q} + \sum\dot{W} + \sum\dot{m}_i ex_i - \sum\dot{m}_e ex_e \tag{21}$$

where $\dot{I}$ represents the irreversibility flow (corresponding to the flow of the exergy consumption), the terms $\sum\dot{m}_i ex_i$ et $\sum\dot{m}_e ex_e$ are the exergy flows of the fluids entering and leaving the studied volume, the term $\sum\left(1 - \frac{T_0}{T}\right)\dot{Q}$ represents the exergy flows associated with the heat transfer, and $\sum\dot{W}$ is the mechanical power exchanged by the studied volume.

The exergy fuel (F), the exergy product (P_r), and the exergy consumed ($\dot{I}$) of each component of the system are given as follows.

Evaporator

$$P_{r_eva} = \dot{E}x_{18} - \dot{E}x_{17} \tag{22}$$

$$F_{eva} = \dot{E}x_9 - \dot{E}x_{10} = \dot{m}_{ref}(ex_9 - ex_{10}) \tag{23}$$

$$\dot{I}_{eva} = F_{eva} - P_{r_eva} \tag{24}$$

Condenser

$$F_{cond} = \dot{E}x_7 - \dot{E}x_8 \tag{25}$$

$$P_{rcond} = \dot{E}x_{16} - \dot{E}x_{15} \tag{26}$$

$$\dot{I}_{cond} = F_{cond} - P_{r_cond} \tag{27}$$

Generator

$$P_{r_gen} = \dot{E}x_7 + \dot{E}x_4 \tag{28}$$

$$F_{gen} = \dot{E}x_{11} - \dot{E}x_{12} + \dot{E}x_3 \tag{29}$$

$$\dot{I}_{gen} = F_{gen} - P_{r_gen} \tag{30}$$

Absorber

$$F_{abs} = \dot{E}x_{10} + \dot{E}x_6 \tag{31}$$

$$P_{r_abs} = \dot{E}x_{14} - \dot{E}x_{13} + \dot{E}x_1 \tag{32}$$

$$\dot{I}_{abs} = F_{abs} - P_{r_abs} \tag{33}$$

Solution Heat Exchanger (SHE)

$$P_{r_SHE} = \dot{E}x_3 - \dot{E}x_2 = \dot{m}_p(ex_3 - ex_2) \tag{34}$$

$$F_{SHE} = \dot{E}x_4 - \dot{E}x_5 = \dot{m}_r(ex_4 - ex_5) \tag{35}$$

$$\dot{I}_{SHE} = F_{SHE} - P_{r_SHE} \tag{36}$$

Thus, the exergy efficiency of the entire absorption cooling system (ACS) can be expresses as follows:

$$\eta_{ex_ACS} = \frac{F_{ACS}}{P_{r_ACS}} \tag{37}$$

With the following fuel and the product:

$$F_{ACS} = \dot{E}x_{11} - \dot{E}x_{12} \tag{38}$$

$$P_{r_ACS} = \dot{E}x_{18} - \dot{E}x_{17} \tag{39}$$

The maximum improvement in the exergy efficiency of a system is obtained for minimum internal and external irreversibilities. As a result, it is useful to employ the concept of exergy improvement potential when analysing different processes in a system. The improvement potential of a component is an avoidable part of the exergy destruction rate through the technological (design) improvement of the component. This potential for improvement in the form of a rate denoted (ε) is equal to:

$$\varepsilon = (\,1 - \eta_{ex}) * \dot{I}_{comp} \tag{40}$$

where η_{ex} is the exergy efficiency of each component and $\dot{I}_{comp}$ is the rate of exergy consumption in each component of the system.

4. Results and Discussions

Table 3 presents the key thermodynamic properties at each state point of the solar-driven LiBr-H_2O absorption cooling system, including temperature, pressure, specific

enthalpy, specific entropy, and lithium bromide mass concentration (x [%]). These values correspond to the steady-state conditions defined for a representative operating case, based on selected generator, condenser, and evaporator temperatures. They serve as a basis for energy and entropy balance calculations and for identifying major sources of irreversibility within the cycle.

Table 3. Thermodynamic properties at cycle state points.

		T_{gen} = 91 °C	T_{abs} = T_{cond} = 42 °C		T_{eva} = 7 °C
State	**Temperature (°C)**	**Pressure (kPa)**	**ξLiBr (%)**	**Enthalpy (kJ/kg)**	**Entropy (kJ/kg/K)**
1	42.35	1.002	57.83	110.8	0.2452
2	43.56	8.362	57.83	112.81	0.2497
3	64.46	8.362	57.83	154.3	0.3788
4	90.63	8.362	61.20	220.8	0.5018
5	57.35	8.362	61.20	174.8	0.3195
6	45.53	1.002	61.20	140.3	0.2579
7	88.84	8.362	0.00	2666	7.493
8	43.35	8.362	0.00	174.4	0.695
9	6.37	1.002	0.00	174.4	0.6363
10	7.00	1.002	0.00	2514	8.974

To validate the present model, the simulation results obtained in this work were compared with data reported in the literature.

Table 4 compares the heat loads of the main components and the COP with the literature data under identical operating conditions, with the evaporator cooling capacity fixed at 10 kW. The strong alignment observed confirms the validity of the proposed model.

Table 4. Energy flows through the main components.

Operating Parameters			
T_{gen} = 90 °C	T_{abs} = 34.9 °C	T_{cond} = 44.3 °C	T_{eva} = 6 °C
Heat loads (kW)			
Components	Florides et al. [20]	Marashli et al. [21]	Present study
Generator	14.2	14.2	14.21
Absorber	13.51	13.54	13.53
Condenser	10.78	10.67	10.67
Evaporator	10	10	10
COP	0.704	0.704	0.7039

Table 5 presents the exergy consumption rates of each component in the system, comparing the results obtained in this study with those reported by other researchers. This comparison highlights the consistency of the model and demonstrates its reliability for exergy analysis in absorption cooling systems.

Table 5. Simulation results of exergy consumption rate in [kW].

Components	**A.M. Blanco-Marigorta and J.D. Marcos [22]**	**R. Palacios-Bereche et al. [23]**	**W.J. Koehler et al. [24]**	**S. De Oliveira and P. Le Goff [25]**	**Present Study**
Absorber	0.36	0.40	0.46	0.91	0.39
SHE	0.19	0.19	0.19	0.19	0.19
Generator	0.55	0.50	0.45	0.01	0.52
Condenser	0.38	0.38	0.38	0.38	0.38
Evaporator	0.27	0.27	0.27	0.27	0.27
Total	1.75	1.74	1.75	1.74	1.75

The comparison reveals only minor discrepancies, primarily in the generator and absorber, which can be attributed to slight differences in modeling assumptions. Overall, the distribution of exergy destruction is consistent with trends reported in the literature. As shown in Table 5, the generator accounts for the highest exergy consumption, followed by the absorber and the condenser. These similarities confirm the validity and reliability of the present model for exergy analysis.

COP variation in the absorption cooling system is shown in Figure 5 as a function of the generator operating temperature. Assuming the absorption and condensation temperature is 42 °C, it is observed that the minimum generator temperature required to operate the system cannot be less than 87 °C, which is the cut off temperature. In addition, the required minimum generator temperature increases with the increase in condenser and absorber temperatures. This can be explained by the increase in the mass concentration of LiBr into the solution, leading to an increase in the heat demand at the generator for the same refrigeration load. For an absorption machine, crystallization may occur in a high solution concentration.

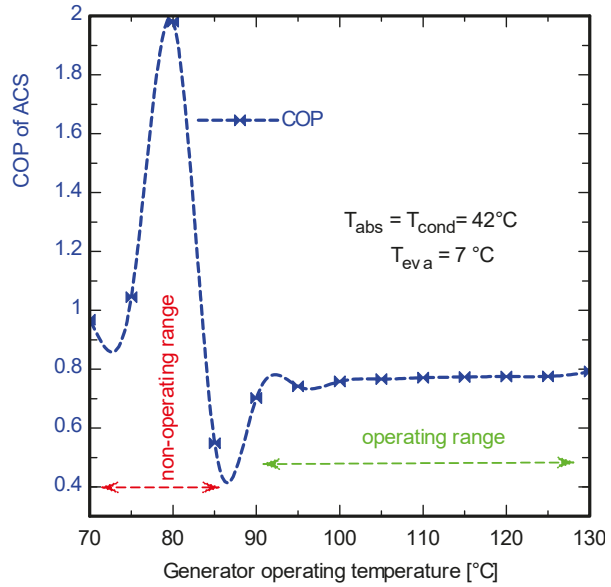

Figure 5. COP variation in the system function of the generator temperature.

It is also noticed that the COP of the system increases from 0.43 to 0.76 with the generator temperature increasing from 87 to 95 °C and then after, a very negligible variation is observed.

The system does not operate at generator and absorber temperature differences $(T_{gen} - T_{abs})$ below 44 °C as the solution at the entrance to the absorber approaches crystallization conditions at different lower temperatures for the generator and the absorber.

Enthalpy of superheated refrigerant steam marginally increases with generator temperature while enthalpy of weak and strong solution increases rapidly, hence lowering generator heat load. However, there is not much benefit from operating at generator temperatures above 100 °C because this leads to an increase in the global cost of the system versus a very small increase in the value of the COP.

To prevent the risk of crystallization, the generator temperature of the single-effect chiller is considered to vary from 70 to 100 °C.

Figure 6 shows the heat load variation in the main components with the absorption temperature increasing.

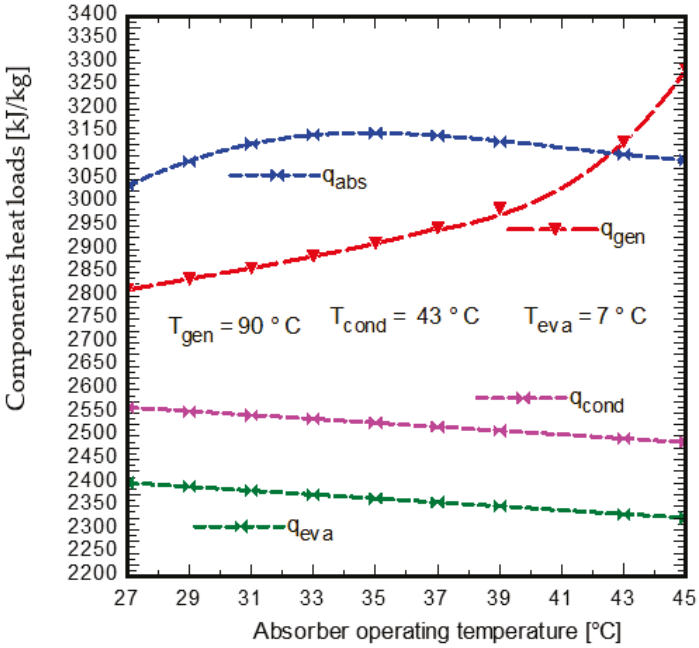

Figure 6. Main component heat loads variation with absorption temperature.

Raising the absorption temperature while the desorption temperature is kept constant leads to a significant increase in the circulation ratio (which means a significant solution concentration). With the generator temperature equal to 90 °C, it is imperative to not increase the absorption temperature to over 43 °C to avoid the risk of possible crystallization conditions. Furthermore, it could be observed that the condenser and evaporator heat loads are less than those of the generator and the absorber.

Figures 7 and 8 show COP and circulation ratio (f) variations as a function of the absorption temperature. An increase in the circulation ration (f) was observed, resulting from the increase in the mass flow rate of the solution and the decrease in the weak solution concentration in the absorber, during the absorber temperature elevating from 27 to 45 °C. Consequently, this leads to a decrease in the COP of the system from 0.835 to 0.56.

The increase in the condenser operating temperature while the vaporization temperature is kept constant leads to a decrease in the concentration of the weak solution leaving the absorber to the generator. This results in an increase in the circulation ratio as is shown in Figure 9, and in the heat required in the generator to separate the refrigerant from the absorbent. Consequently, the COP decreases. It can be observed that the rise in the condenser operating temperature from 27 to 45 °C reduces the COP of the system by 19%.

According to Figure 10, the performance of the system grows by increasing the evaporator temperature, contrary to the quality of energy effect which decreases the temperature, leading to a diminution of the exergy efficiency of the system (Figure 11). Figure 11 highlights that the increase in the evaporator temperature strictly decreases the exergy efficiency in the system. In other words, the useful effect (in terms of exergy) decreases in comparison with the input exergy flow in the generator.

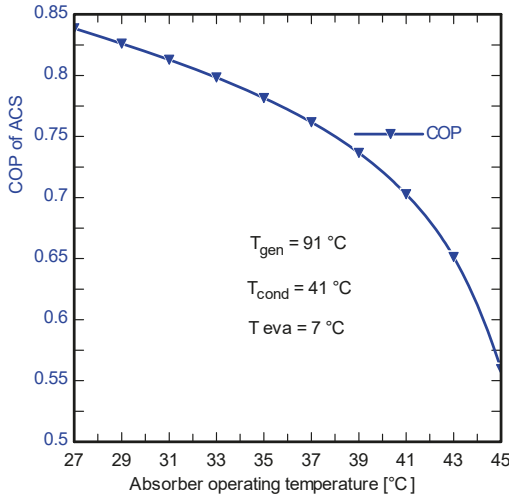

Figure 7. Effect of the absorption temperature on COP of the absorption cooling system.

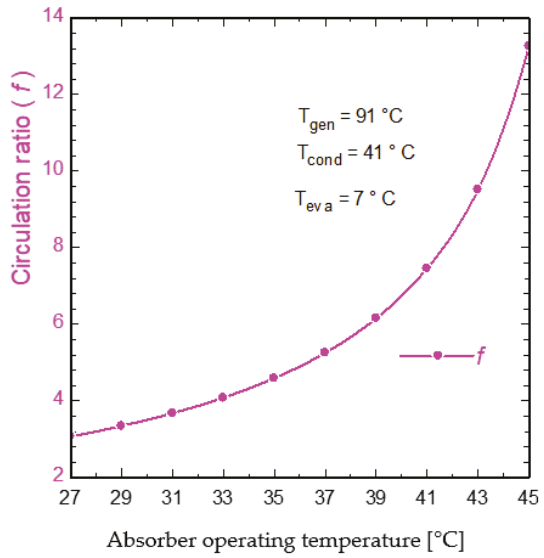

Figure 8. Circulation ratio variation with the absorption temperature.

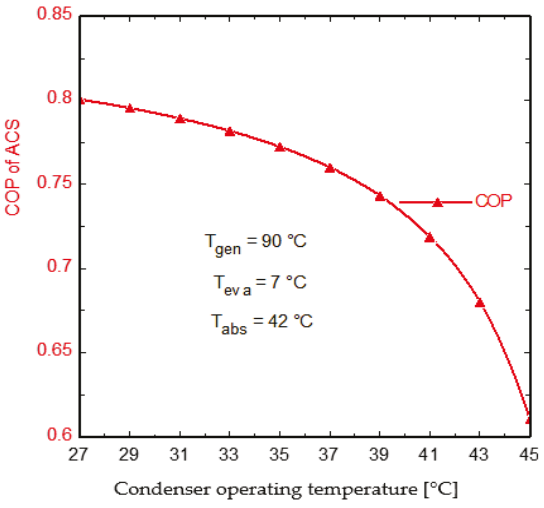

Figure 9. Effect of the condenser operating temperature on COP.

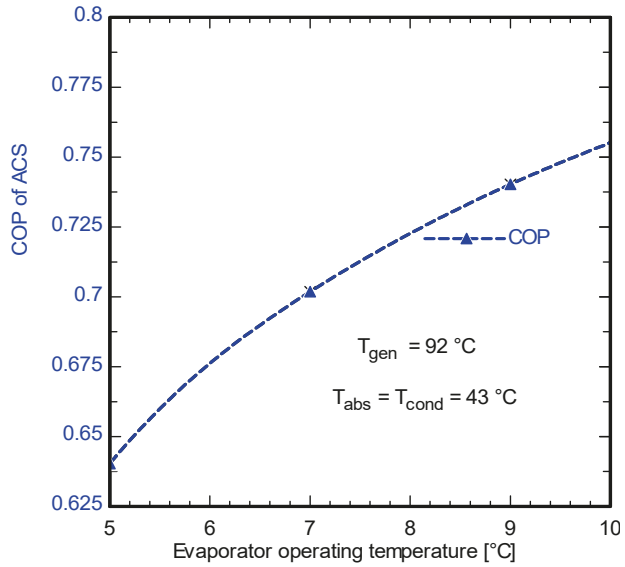

Figure 10. COP versus the evaporator temperature.

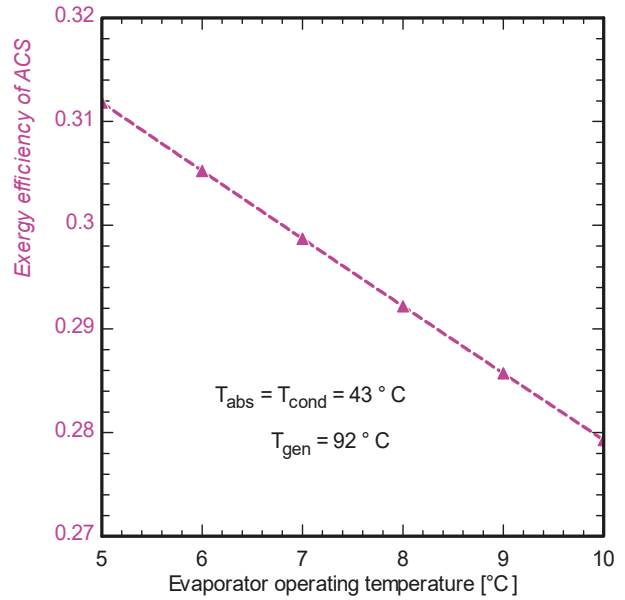

Figure 11. Exergy efficiency vs. evaporator temperature.

In Figure 12, it can be observed that the COP climb rapidly from 0.73 to 0.86 and then converge to a constant value of about 0.85. At the same conditions, exergy efficiency drops from 56 to 25% due to the exergy flow increasing in the generator. This can also be explained by the increase in the mass concentration of LiBr into the solution (Figure 13).

It should be noted that for a constant cooling load, the reduction in the thermal load of the generator leads to an initial increase in the COP. In this case, the optimum generator operating temperature is 86 °C corresponding to the maximum exergy efficiency.

Figure 14 shows the variation in the exergy efficiency of the main components as a function of the ambient temperature considering the following conditions: $T_{eva} = 10$ °C; $T_{gen} = 97$ °C; $T_{abs} = T_{cond} = 49$ °C.

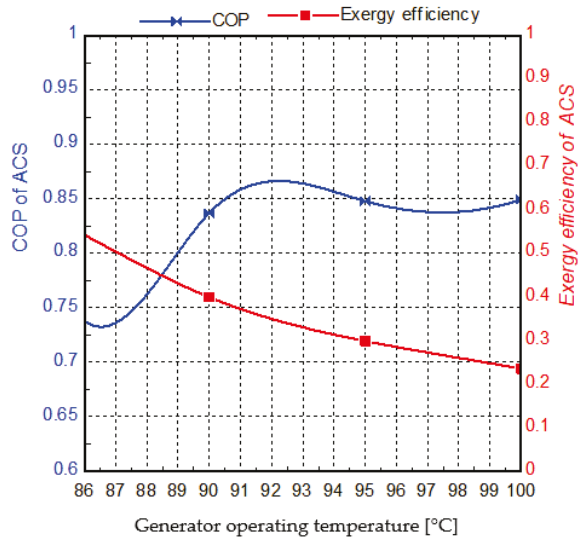

Figure 12. COP and exergy efficiency versus generator temperature for $T_{ab} = 32\ ^{\circ}\mathrm{C}$, $T_{ev} = 8\ ^{\circ}\mathrm{C}$.

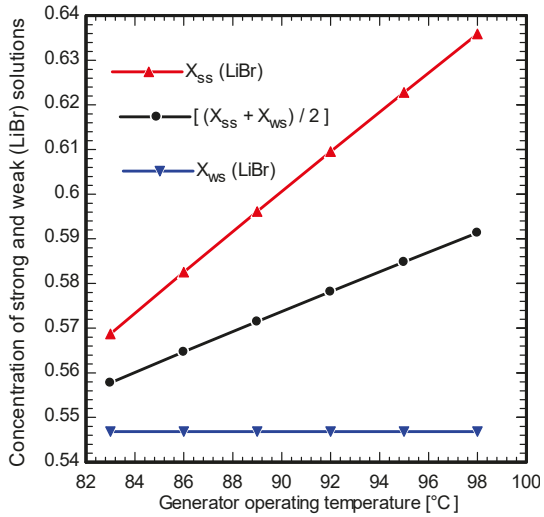

Figure 13. Concentration of weak and strong solutions as a function of the generator operating temperature.

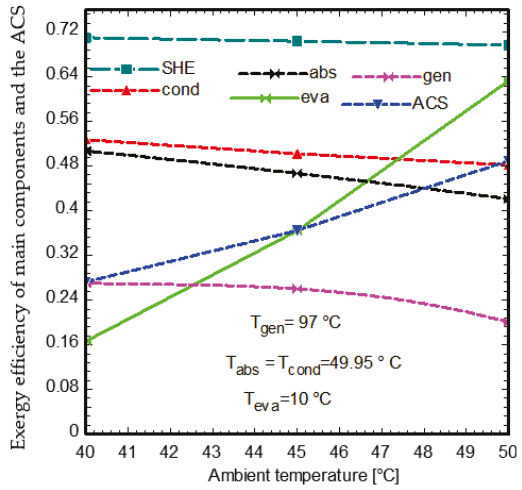

Figure 14. Exergy efficiencies of the main components versus the ambient temperature.

The exergy consumption is well distributed and is not negligible in any of the components. When the ambient temperature increases, the exergy consumption of the absorber and the condenser increases; thus, the exergy efficiency of these components decreases. In addition, the exergy consumed by the evaporator decreases significantly (exergy efficiency increases). It remains almost constant for the generator and the solution exchanger.

According to Figure 14, the evaporator exergy efficiency increases from 16 to 52% with the increasing ambient temperature from 40 to 48 °C. The reason is that with the increase in the ambient temperature, the difference between the ambient temperature and the evaporator operating temperature increases which means that the produced exergy flow of the chilled water is higher. Furthermore, the exergy efficiency of the system increases significantly, as is seen in Figure 15.

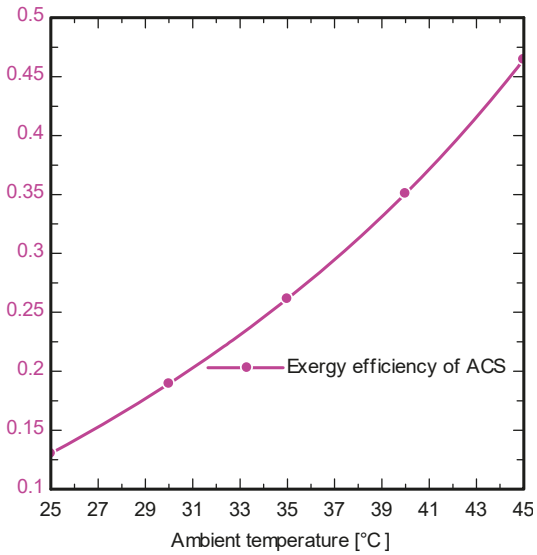

Figure 15. Exergy efficiency of the system versus the ambient temperature.

The absorber and condenser exergy efficiency decreasing implies an increasing in the potential of these components to improve their designs. Rising absorber and condenser cooling flow is therefore required. To improve the performance of the system, special attention must be paid to reduce the irreversibility that exists in the absorber, in addition to the generator.

The performance of the system can be improved by minimizing irreversibilities so that the entropy generation rate in the absorber and the generator is decreased. A solution heat exchanger is suitable as well as an accurate control of the cooling water flow in the absorber and the condenser. Figure 16 shows the variation in the exergy destruction in the absorber and the condenser versus the mass flow rate of the cooling water.

As absorption and condensation are exothermic processes, it is imperative to correctly evacuate the heat released during these processes. A low cooling water mass flow rate implies high irreversibility of the absorber, so the cooling flow should be automatically adjusted when the ambient temperature increases.

For this simulation, the absorber and the condenser are cooled with the same cooling water flow rate.

It was observed that when the cooling water flow rate increases from 0.2 to 1.4 kg/s, the exergy consumption of the two components is reduced by 36% due to the decrease in the temperature pinch.

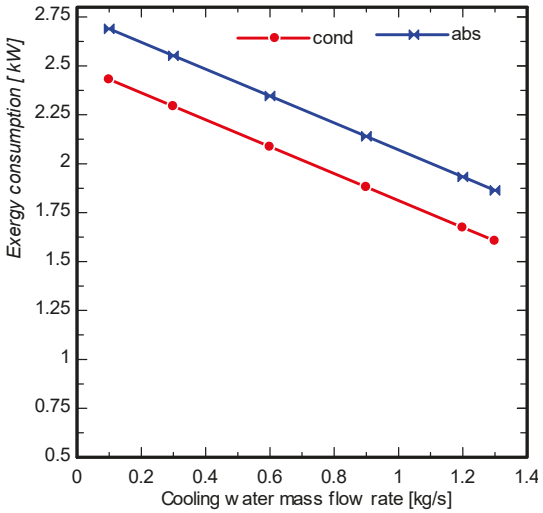

Figure 16. Absorber and condenser exergy consumption versus cooling water flow rate.

The solution heat exchanger helps to increase the temperature in the weak solution, which leaves the absorber, before entering the generator, thus reducing the temperature of the strong solution leaving the generator before entering the absorber. Further analyses were conducted to better understand what happens in the absorber and the generator when the effectiveness of the solution heat exchanger varies. As is shown in Figure 17, a solution heat exchanger having an efficiency of about 0.75 seems suitable to reduce the exergy consumption in both the generator and the absorber.

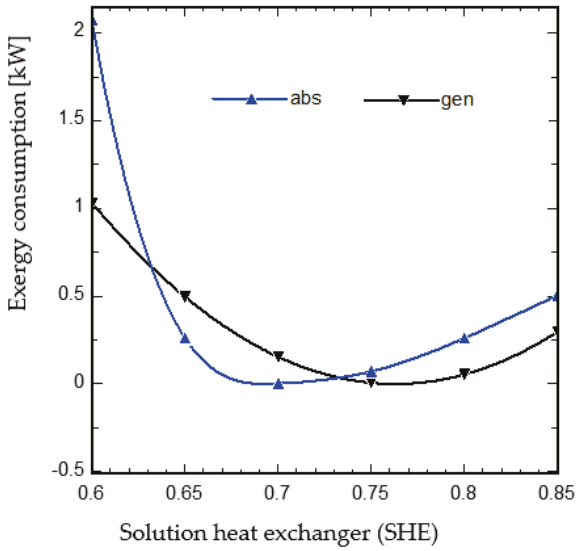

Figure 17. Impact of the effectiveness of the SHE on the absorber and generator exergy consumption.

With equal absorber and condenser operating temperatures, the system seems to have higher performances, hence, it is important to control the cooling water flow to assume the operating temperature of these two components.

Based on the analysis presented in Figure 17, several design improvements can be considered to enhance the overall performance and stability of the absorption cooling system. One key recommendation is the implementation of a generator equipped with advanced heat transfer surfaces, which can significantly improve thermal efficiency by enhancing the heat exchange between the heat source and the working fluid. Additionally, the adoption

of hybrid cooling systems for the absorber is proposed to optimize heat rejection, especially under fluctuating ambient conditions. These enhancements contribute to a more robust and efficient absorption chiller design suitable for real-world operating conditions.

5. Conclusions

This study conducted a comprehensive energy and exergy analysis of a single-effect H_2O-LiBr absorption chiller, operating under two contrasting climatic conditions: France (temperate) and Senegal (hot), using simulation data from EES software.

The results show that system performance is highly sensitive to component operating temperatures. The Coefficient of Performance (COP) increased from 0.672 to 0.776 with a generator temperature increasing from 85 to 95 °C, and by approximately 12.4% and 11.2% with absorber and condenser temperature reductions of 5 °C, respectively. The maximum COP reached was 0.802 in France versus 0.761 in Senegal, under identical generator and evaporator settings.

From the exergy perspective, the generator accounted for the largest share of exergy consumption (47.8%), followed by the absorber (27.4%), condenser (15.1%), and evaporator (9.7%). The total exergy destruction was higher in Senegal, mainly due to elevated ambient and cooling water temperatures, which impair heat rejection.

Cooling water mass flow rate played a critical role: increasing from 0.08 to 1.2 kg/s reduced absorber and condenser temperatures and improving exergy efficiency from 29.9 to 38.5%. Furthermore, raising the ambient temperature from 25 to 45 °C, while maintaining controlled flow conditions, resulted in a net exergy efficiency gain, due to the increase in chilled water exergy.

The analysis also demonstrated that optimal operating temperatures of system components are climate dependent. In France, lower ambient temperatures allowed absorber and condenser operation at more favorable setpoints (e.g., absorber at 27–35 °C vs. 35–43 °C in Senegal), leading to better system performance.

These results underscore the importance of adaptive thermal management strategies, including the automated control of flow rates and operating temperatures, to ensure efficient and flexible operation under varying environmental conditions.

Dynamic simulations considering economic factors are reserved for future investigation, following on from this evaluation of the feasibility and thermodynamic performances of the system, under steady-state conditions within a local context.

Author Contributions: Conceptualization, methodology, software, resources, investigation L.G. and M.S.; validation, L.G.; formal analysis, L.G.; writing—original draft preparation, M.S.; writing—review and editing, L.G.; supervision, L.G. All authors have read and agreed to the published version of the manuscript.

Funding: This research received no external funding.

Data Availability Statement: The original contributions presented in the study are included in the article, further inquiries can be directed to the corresponding author.

Conflicts of Interest: The authors declare no conflicts of interest.

Abbreviations

The following abbreviations are used in this manuscript:

ACS	Absorption Cooling System
EES	Engineering Equation Solver

Nomenclature

Symbols	
a_1	Conduction heat loss coefficient, $W \cdot m^{-2} \cdot K^{-1}$
a_2	Convection heat loss coefficient, $W \cdot m^{-2} \cdot K^{-2}$
COP	Coefficient of Performance, -
E	total energy, J
Ex	exergy, J
ex	specific exergy, $J \cdot kg^{-1}$
$\dot{E}x$	exergy flow, W
f	circulation factor, -
F	exergy fuel, W
h	specific enthalpy, $J \cdot kg^{-1}$
$\dot{I}$	irreversibility, W
m	mass, kg
$\dot{m}$	mass flow rate, kg
P	pressure, Pa
P_r	exergy product, W
q	specific heat, J
$\dot{Q}$	heat flow rate, W
s	specific entropy, $J \cdot kg^{-1} \cdot K^{-1}$
T	temperature, °C
t	time, s
$\dot{W}$	mechanical power, W
X	fraction of LiBr in the solution, %
Greek symbols	
η_{ex}	exergy efficiency, -
η_0	optical efficiency, -
ε	improvement potential, -
Subscripts	
abs	absorber
amb	ambient
comp	component
cond	condenser
e	exit
eva	evaporator
gen	generator
i	inlet
p	poor in LiBr (solution)
r	rich in LiBr (solution)
ref	refrigerant
s	solution
SHE	solution heat exchanger

References

1. Praveenkumar, S.; Kumar, A. Thermodynamic, environmental and economic analysis of solar photovoltaic panels using aluminium reflectors and latent heat storage units: An experimental investigation using passive cooling approach. *J. Energy Storage* **2025**, *112*, 115487. [CrossRef]
2. Alwan, N.T.; Majeed, M.H.; Shcheklein, S.E.; Ali, O.M.; PraveenKumar, S. Experimental Study of a Tilt Single Slope Solar Still Integrated with Aluminum Condensate Plate. *Inventions* **2021**, *6*, 77. [CrossRef]

3. Saikia, P.; Corcoran, L.; Ugalde-Loo, C.E.; Abeysekera, M. A cooling demand estimator for housing communities in a warming world. *Appl. Energy* **2025**, *377*, 124597. [CrossRef]
4. Patureau, R.; Tran, C.T.; Gavan, V.; Stabat, P. The new generation of District heating & cooling networks and their potential development in France. *Energy* **2021**, *236*, 121477. [CrossRef]
5. Metcalf, S.J.; Tamainot-Telto, Z.; Critoph, R.E. Application of a compact sorption generator to solar refrigeration: Case study of Dakar (Senegal). *Appl. Therm. Eng.* **2011**, *31*, 2197–2204. [CrossRef]
6. Babaharra, O.; Choukairy, K.; Faraji, H.; Khallaki, K.; Hamdaoui, S.; Bahammou, Y. Thermal performance analysis of hollow bricks integrated phase change materials for various climate zones. *Heat Transf.* **2024**, *53*, 2148–2172. [CrossRef]
7. González, R.C.; Díaz, A.J.; Rojas, O.D.; Sarmiento-Laurel, C. Assessing solar absorption chillers for data center cooling across diverse climatic conditions. *Energy Build.* **2025**, *331*, 115376. [CrossRef]
8. Ketfi, O.; Merzouk, M.; Merzouk, N.K.; Metenani, S.E. Performance of a Single Effect Solar Absorption Cooling System (Libr-H_2O). *Energy Procedia* **2015**, *74*, 130–138. [CrossRef]
9. Chen, J.F.; Dai, Y.J.; Wang, R.Z. Experimental and analytical study on an air-cooled single effect LiBr-H_2O absorption chiller driven by evacuated glass tube solar collector for cooling application in residential buildings. *Sol. Energy* **2017**, *151*, 110–118. [CrossRef]
10. Boukholda, I.; Ezzine, N.B.; Bellagi, A. Experimental investigation and simulation of commercial absorption chiller using natural refrigerant r717 and powered by Fresnel solar collector. *Int. J. Thermofluids* **2025**, *27*, 101213. [CrossRef]
11. Pop, O.G.; Dobrovicescu, A.; Serban, A.; Ciocan, M.; Zaaoumi, A.; Hiris, D.P.; Balan, M.C. Analytical modelling of food storage cooling with solar ammonia-water absorption system, powered by parabolic trough collectors. Method. *MethodsX* **2023**, *10*, 102013. [CrossRef]
12. Petersen, S.; Hausherr, C.; Hüls, W.; Paitazoglou, R.; Albers, J. Efficient absorption cooling for low district heating return temperatures. *Energy Rep.* **2021**, *7*, 88–96. [CrossRef]
13. Lubis, A.; Jeong, J.; Saito, K.; Giannetti, N.; Yabase, H.; Alhamid, M.I.; Nasruddin. Solar-assisted single-double-effect absorption chiller for use in Asian tropical climates. *Renew. Energy* **2016**, *99*, 825–835. [CrossRef]
14. Grossman, G. Solar-powered systems for cooling, dehumidification and air-conditioning. *Sol. Energy* **2002**, *72*, 53–62. [CrossRef]
15. Bataineh, K.; Taamneh, Y. Review and recent improvements of solar sorption cooling systems. *Energy Build.* **2016**, *128*, 22–37. [CrossRef]
16. Borge, D.; Colmenar, A.; Castro, M.; Martín, S.; Sancristobal, E. Exergy efficiency analysis in buildings climatized with LiCl–H_2O solar cooling systems that use swimming pools as heat sinks. *Energy Build.* **2011**, *43*, 3161–3172. [CrossRef]
17. Avanessian, T.; Ameri, M. Energy, exergy, and economic analysis of single and double effect LiBr–H_2O absorption chillers. *Energy Build.* **2014**, *73*, 26–36. [CrossRef]
18. Gomri, R. Investigation of the potential of application of single effect and multiple effect absorption cooling systems. *Energy Convers. Manag.* **2010**, *51*, 1629–1636. [CrossRef]
19. Grosu, L.; Dobrovicescu, A.; Untea, A. Energy and exergy analyses of a solar-driven absorption cooling system. *Int. J. Exergy* **2014**, *15*, 308–327. [CrossRef]
20. Florides, G.A.; Kalogirou, S.A.; Tassou, S.A.; Wrobel, L.C. Design and construction of a LiBr–water absorption machine. *Energy Convers. Manag.* **2003**, *44*, 2483–2508. [CrossRef]
21. Marashli, A.; Alfanatseh, E.; Shalby, M.; Gomaa, M.R. Modelling single-effect of Lithium Bromide-Water (LiBr–H_2O) driven by an evacuated solar tube collector in Ma'an city (Jordan) case study. *Case Stud. Therm. Eng.* **2022**, *37*, 102239. [CrossRef]
22. Blanco-Marigorta, A.M.; Marcos, J.D. Key issues on the exergetic analysis of H_2O/LiBr absorption cooling systems. *Case Stud. Therm. Eng.* **2021**, *28*, 101568. [CrossRef]
23. Palacios-Bereche, R.; Gonzales, R.; Nebra, S.A. Exergy calculation of lithium bromide–water solution and its application in the exergetic evaluation of absorption refrigeration systems LiBr-H_2O. *Int. J. Energy Res.* **2012**, *36*, 166–181. [CrossRef]
24. Koehler, W.J.; Ibele, W.E.; Soltes, J.; Winter, E.R. Availability simulation of a lithium bromide absorption heat pump. *Heat Recovery Syst. CHP* **1988**, *8*, 157–171. [CrossRef]
25. de Oliveira, S.; Le Goff, P. Analyse exergétique des processus de séparation et de mélangeage: Application aux thermotransformateurs. *Rev. Générale Therm.* **1994**, *33*, 385.

Disclaimer/Publisher's Note: The statements, opinions and data contained in all publications are solely those of the individual author(s) and contributor(s) and not of MDPI and/or the editor(s). MDPI and/or the editor(s) disclaim responsibility for any injury to people or property resulting from any ideas, methods, instructions or products referred to in the content.

energies

MDPI

Article

Optimizing Solar-Powered EV Charging: A Techno-Economic Assessment Using Horse Herd Optimization

Krishan Chopra [1], M. K. Shah [1], K. R. Niazi [1], Gulshan Sharma [2,*] and Pitshou N. Bokoro [2]

[1] Department of Electrical Engineering, Malaviya National Institute of Technology, Jaipur 302017, India; chopra.ee@gmail.com (K.C.); mkshah.ee@mnit.ac.in (M.K.S.); krniazi.ee@mnit.ac.in (K.R.N.)
[2] Department of Electrical and Electronics Engineering Technology, University of Johannesburg, Johannesburg 2006, South Africa; pitshoub@uj.ac.za
* Correspondence: gulshans@uj.ac.za

Abstract: Mass market adoption of EVs is critical for decreasing greenhouse gas emissions and dependence on fossil fuels. However, this transition faces significant challenges, particularly the limited availability of public charging infrastructure. Expanding charging stations and renewable integrated EV parking lots can accelerate the adoption of EVs by enhancing charging accessibility and sustainability. This paper introduces an integrated optimization framework to determine the optimal siting of a Residential Parking Lot (RPL), a Commercial Parking Lot (CPL), and an Industrial Fast Charging Station (IFCS) within the IEEE 33-bus distribution system. In addition, the optimal sizing of rooftop solar photovoltaic (SPV) systems on the RPL and CPL is addressed to enhance energy sustainability and reduce grid dependency. The framework aims to minimize overall power losses while considering long-term technical, economic, and environmental impacts. To solve the formulated multi-dimensional optimization problem, Horse Herd Optimization (HHO) is used. Comparative analyses on IEEE-33 bus demonstrate that HHO outperforms well-known optimization algorithms such as genetic algorithm (GA) and particle swarm optimization (PSO) in achieving lower energy losses. Case studies show that installing a 400-kW rooftop PV system can reduce daily energy expenditures by up to 51.60%, while coordinated vehicle scheduling further decreases energy purchasing costs by 4.68%. The results underscore the significant technical, economic, and environmental benefits of optimally integrating EV charging infrastructure with renewable energy systems, contributing to more sustainable and resilient urban energy networks.

Keywords: electric vehicle; renewable; charging infrastructure; parking lots; charging stations

1. Introduction

Electric vehicles (EVs) are a crucial solution for reducing greenhouse gas emissions from transportation and decreasing dependence on fossil fuels. As an environmentally friendly alternative to traditional vehicles, EVs have seen rapid adoption, with U.S. sales growing from 20,000 in 2010 to over 2 million by 2018 [1]. However, widespread adoption is still hindered by the limited availability of public charging infrastructure [2]. Although most EV charging occurs at home, public charging stations are crucial for overcoming range anxiety and enabling long-distance travel. With an estimated 100 million parking spaces at business locations across the U.S. [1], parking lots represent a promising opportunity for the deployment of electric vehicle supply equipment (EVSE). However, the strategic placement

of EVCS and parking lots is crucial for minimizing power losses and ensuring grid stability. Recent studies have employed advanced optimization techniques to determine optimal locations for various types of EV charging infrastructure. For instance, a study by Li et al. [3] proposed the whale optimization algorithm for EVCS locations aiming to minimize overall costs and carbon emissions, demonstrating the importance of incorporating dynamic demand patterns into location planning. Altaf et al. [4] utilized Particle Swarm Optimization (PSO) for the optimal placement of EVCS and effectively reduced both real and reactive power losses, improving voltage stability and unbalanced generation, highlighting the significance of optimally integrating EV charging stations in a radial distribution system. H Asghari Rad et al. proposed a model in [5] to determine the optimum location and capacity of a parking lot to maximize the benefit of the parking lot owner. However, these studies primarily focus on either residential or commercial zones and often do not simultaneously consider I-FCS. A study by Chakraborty et al. [6] focused on planning a fast-charging infrastructure for EVs employing a multi-objective PSO approach to minimize power loss and voltage deviations. The authors demonstrated that by using real time dynamic pricing, the benefit of the owner increased significantly. Other studies have focused on the grid impact and control strategies: In [7], the author used solar power in the EV parking lot so that the power drawn from the grid can be reduced in order to maximize the profit of the parking lot owner. The impact of a renewable integrated EV residential parking lot is analyzed in [8], and the effectiveness of the results is obtained by the PSO algorithm based on a parking lot. In [9], a study was conducted on a commercial parking lot, and results show the impact of the load of the parking lot on the distribution system. The importance of EV fast charging stations (FCSs) is analyzed in [10], and techno-economic comparison of FCSs is also performed. The impact of both home and public EVCS on the distribution system can be mitigated by smart charging [11]. In [12], Citroni, R. et al. highlight the potential for integrating self-sufficient, energy-efficient devices into urban energy networks, which can further reduce reliance on grid power and enhance the overall system sustainability. It may be worth noting that unplanned placement of an EV charging station may adversely affect the distribution system with consequent substantial power loss and an unsatisfactory voltage profile.

The exploration of the possible integration of solar photovoltaic (SPV) systems into the charging station is another important aspect. Integrating SPV systems into a charging station offers additional benefits as solar energy production aligns closely with daytime EV charging demand. The PV also reduces reliance on the utility grid, and provides shade and protection through solar canopies. While the initial investment remains significant, the value proposition of solar-powered EVSE in parking lots strengthens as EV adoption increases. Oruganti et al. [1] conducted extensive studies on solar PV and level 2 EV charging installation cost benefit design for a commercial workplace parking lot in Texas. The authors demonstrated that the financial viability of the project is not secure when assessed solely on the basis of direct cash flows. Deshmukh and Pearce [2] evaluated the viability of installing solar charge parking PV awnings over parking spaces with integrated EV chargers. The study also showed that the projects do not yet provide enough direct profits as power costs increase. Junid et al. [13] propose a model that has excess solar energy at telecom base stations to power public EV charging stations. This may provide considerable additional revenue for telecom operators in addition to cutting consumer charging costs. However, comprehensive cost–benefit analyses (CBAs) that simultaneously consider optimal location, PV sizing, and integration across different zones are scare in the current literature. In [14], A. Varone et al. presents an Al-designed software platform to efficiently power management at an SPV-powered parking lo; however, the study lacks in optimum

location of the parking lot. Despite these insights, the literature lacks comprehensive studies that integrate PV sizing with the optimal placement of EVCS, particularly in diverse zones such as residential, commercial, and industrial areas. Conducting a cost–benefit analysis is also vital for assessing the economic viability of integrating rooftop solar PV systems into commercial EV parking lots. Such analyses consider capital expenditures, operational costs, energy savings, and potential revenue streams.

The objectives of this paper are as follows:

1. Develop an optimization framework that determines the best locations for residential, commercial, and industrial EV charging infrastructure based on power loss minimization in the distribution systems.
2. Develop an optimization framework to determine the optimal size of rooftop solar PV systems for integration into residential and commercial parking lots.
3. In the literature, many algorithms such as PSO and GA have been applied to solve the above optimization problems. In this paper, HHO has been explored to solve the optimization problem.
4. Carry out a thorough cost–benefit analysis of the commercial EV parking lot in order to maximize the profit of the parking lot owner.

This study explores the potential of parking garages as sites for solar-powered EV charging, focusing on key factors such as economic feasibility, system design challenges, and long-term viability. Drawing from recent research, we present a cost–benefit analysis from the owner's perspective over a 30-year timeframe. The findings offer quantitative insights into the financial performance and design considerations necessary for implementing effective solar PV EVSE systems. In this research work, the HHO technique is employed to determine the optimal placement of various EV loads and the appropriate sizing of rooftop PV panels on parking lots. To the best of our knowledge, this optimization technique has not yet been applied in the context of power distribution systems, and therefore, we aim to explore its potential in this domain.

The HHO algorithm is a population-based, nature-inspired metaheuristic that emulates the social behavior and dynamics observed in horse herds. In the natural world, horses rely on cooperative group behavior, individual decision making, and strategic movement to achieve goals such as locating food sources, avoiding threats, and maintaining group cohesion. These behaviors are mathematically modeled in HHO to effectively balance exploration (global search) and exploitation (local search) in solving complex optimization problems. In this study, using the HHO algorithm, we propose a novel methodology for identify the most suitable locations for installing RPL, CPL, and I-FCS within a power distribution system along with the optimal sizing of rooftop solar PV systems at RPL and CPL. The motivation for utilizing HHO lies in its superior ability to handle complex, high-dimensional optimization problems. It demonstrates high efficiency in both the exploration of the global search space and the exploitation of local optima, achieving optimal solutions rapidly with low computational cost and complexity. Comparative results indicate that the proposed approach outperforms conventional optimization techniques such as GA and PSO in terms of both accuracy and efficiency.

The remainder of this paper is structured as follows: Section 2 describes the problem overview and formulation, including the objective function, constraints, and details of the solar rooftop photovoltaic system with its energy, economic, and environmental performance assessments. Section 3 outlines the proposed HHO methodology. Section 4 presents the case study, simulation results, and comparative analyses. Finally, Section 5

concludes the paper and outlines possible directions for future work. Nomenclatures and List of Acronyms presents the list of nomenclatures and list of acronyms.

2. Problem Overview and Formulation

In this paper, the IEEE 33 bus system is divided into three distinct zones: residential area, commercial area, and industrial area. Residential and commercial areas both have an EV parking lot, whereas FCS is installed in an industrial area. HHO (the flowchart is given in Figure 1) is used to find the optimal location for both EVPL and FCS. Both parking lots also have a rooftop SPV, and the optimum size for the SPV is also determined by the HHO. Analysis of energy performance, economic performance, and environmental performance for the rooftop SPV system is performed in Section 2.3. Cost–benefit analysis for the CPL is performed from the perspective of the parking lot. The summarized contributions of this study are as follows:

1. Proposed a framework to determine optimal locations where I-FCS, CPL, and RPL should be placed to minimize losses;
2. Developed HHO to solve the proposed optimization problem;
3. Provided the energy, economic, and environmental benefits of integrating PV with EVs in the distribution system.

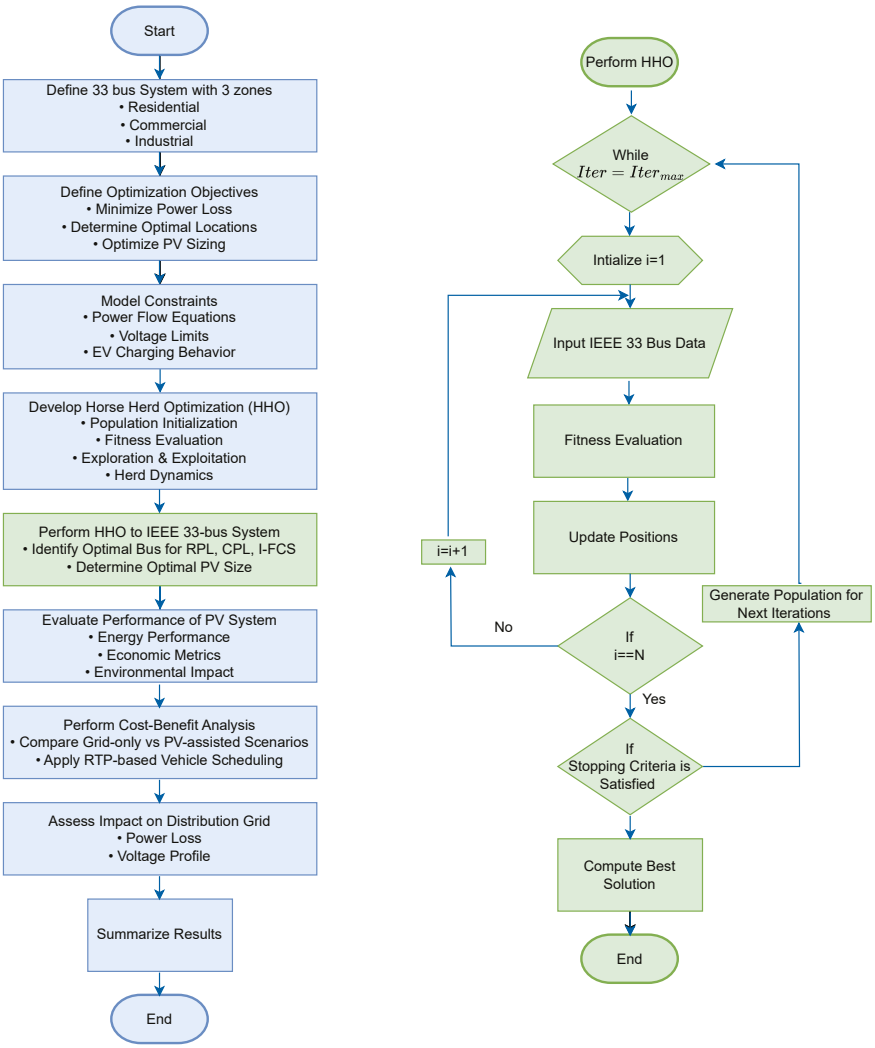

Figure 1. Flowchart of the proposed work using HHO.

2.1. Objective Function

The optimal locations of I-FCS, CPL, and RPL are determined through optimization of power loss. The objective function is represented mathematically by

$$P_{\text{Loss}} = \frac{1}{2}\sum_{k=1}^{24}\left[\sum_{i=1}^{N}\sum_{j=1}^{N} G_{i,j}\left(V_{i,k}^2 + V_{j,k}^2 - 2V_{i,k}V_{j,k}\cos(\delta_{j,k} - \delta_{i,k})\right)\right] \quad (1)$$

2.2. Constraints

The power balance and voltage constraint equations [15] are essential to power flow analysis because they guarantee that the system runs within stable bounds. Usually, power injections and bus admittance matrices are used to formulate these equations expressed as follows:

$$S_i = P_i + jQ_i \quad (2)$$

$$P_i = V_i \sum_{k=1}^{N} V_k |Y_{ik}| \cos(\theta_{ik} + \delta_k - \delta_i) \quad (3)$$

$$Q_i = V_i \sum_{k=1}^{N} V_k |Y_{ik}| \sin(\theta_{ik} + \delta_k - \delta_i) \quad (4)$$

$$V_{\min,i} \leq V_i \leq V_{\max,i} \quad (5)$$

where S_i is complex power, P_i and Q_i are real and reactive power injected at bus i, V_i and V_k are voltage magnitudes at buses i and k, δ_i and δ_k are voltage phase angles at buses i and k, $|Y_{ik}|$ and θ_{ik} are magnitude and phase angle of the admittance matrix element Y_{ik}, $V_{min,i}$ and $V_{max,i}$ are lower and upper voltage limits at bus i, and N is the number of total buses.

2.3. Solar Rooftop Photovoltaic System

The SPV system is assumed to install on the roof of a commercial parking lot in Jaipur, India. The system has a nominal capacity of 400 kW and comprises 1455 PV modules, all installed oriented southwards with a tilt angle of 25° and an azimuth angle of 180°. The modules are based on multi-crystalline silicon technology, specifically the ASP-7-320 model manufactured by Mundra Solar Pvt. Ltd. (Mundra, India). Each module has a rating of 275 Wp and has an efficiency of 16.32% under Standard Test Conditions (STCs). Collectively, the modules occupy a total surface area of 2850 sq. m, covering 1.96 m^2 by each individual module, which is approximately 90% of the total available area. Table 1 represents the Specifications of solar PV system.

Table 1. Specifications of solar PV system.

Particular	Specification
Location	Jaipur
Latitude	26.95
Longitude	75.85
DC System Size (kW)	400
Module Type	Standard
Array Type	Fixed
Tilt Angle	25°
Azimuth Angle	180°
System Losses (%)	14.08
DC-to-AC Size Ratio	1.2
Type of Inverter	Grid-tied string inverter
Inverter Efficiency (%)	96

2.3.1. Energy Performance

(i) Performance ratio (PR)

It serves as a PV system's energy-generating performance indicator. It explains all of a PV system's losses while it operates under actual circumstances.

$$PR = \frac{E_{\text{actual}}}{E_{\text{theoretical}}} \tag{6}$$

$$E_{\text{theoretical}} = \text{Installed Capacity} \times \text{Solar Irradiance} \tag{7}$$

where E_{actual} is actual energy output and $E_{theoretical}$ is theoretical energy output.

The performance ratio of a PV system reflects its operational efficiency. A higher PR indicates that the system is operating near its rated capacity, while a lower PR points to energy losses or potential faults within the system. Typically, the PR ranges between 60% and 90%, depending on varying environmental conditions [16].

(ii) Energy density (E_d)

It is described as the yearly power produced by a PV system's array per unit area. The available area's energy generation can be approximated using this parameter. It can also be used to contrast how well various PV systems perform in terms of energy. It is given by [17].

$$E_d = \frac{E_{a,\text{out}}}{A_a} \tag{8}$$

(iii) Energy payback time (EPBT)

"It refers to the amount of time required for the SPV system to recover the energy used in its manufacturing, installation, and maintenance over the course of its whole life." The net energy (NE) of the system is evaluated annually to determine the EPBT. The EPBT is the amount of time needed for the system's net energy to drop to zero.

$$E_{a,\text{out/year}} \cdot \sum_{t=1}^{n} (1-d)^{t-1} = E_{\text{em}} \tag{9}$$

Here, d denotes the degradation rate of the polycrystalline silicon modules, n represents the total lifespan of the system, and t indicates the time elapsed (in years).

The PV system's annual degradation rate was determined to be 0.6% in the current investigation [18]. The concept of NE has been established to determine the system's EPBT. The system's net energy is calculated annually until it equals zero, at which point the system's EPBP is determined.

(iv) Energy return on energy invested (EROI)

The ratio of the PV system's total power production to the total energy input used during its lifetime. It forecasts how well the installed PV system will use electricity.

$$\text{EROI} = \frac{n}{\text{EPBT}} \tag{10}$$

2.3.2. Economic Performance

(i) Cost of electricity (COE)

It is defined as the ratio of the whole life-cycle costs (LCCs) of the PV system to its lifetime energy production.

$$\text{COE} = \frac{\text{LCC}}{\text{Energy production over its lifetime}} \tag{11}$$

$$\text{Energy production over its lifetime} = \sum_{t=1}^{n} E_{a,\text{out}} \cdot (1-d)^{t-1} \tag{12}$$

$$\text{LCC} = C + C_{MR} + C_R - C_S \tag{13}$$

$$C_{MR} = M \cdot \left(\frac{(i+1)^n - 1}{i(i+1)^n} \right) \tag{14}$$

for a 15-year life of PCU,

$$C_R = R_{15} \cdot \left(\frac{1}{(i+1)^{15}} \right) \tag{15}$$

The salvage value of SPV systems is projected to be 20% of their capital cost at the end of their operational life. The value of capital cost after n years,

$$P_n = P_o \cdot (1-d)^n \tag{16}$$

$$C_S = 20\% \text{ of } P_n$$

where d is the depreciation rate and i is the annual interest rate/ inflation rate.

(ii) Payback period (PBP)

The calculation of the entire duration for the system to recover its initial investment serves as an assessment indication. The system's PBP has been computed using the net present value (NPV). The payback period is the amount of time required to bring the system's net present value to zero.

$$\text{NPV} = \sum_{t=0}^{n} \frac{\text{Annual Cash Flow}}{(1+i)^t} - \text{Initial Investment} \tag{17}$$

$$\text{Annual Cash Flow} = \sum_{j=0}^{n} \frac{E_{a,\text{out}}\left(\frac{\text{kWh}}{\text{year}}\right)}{(1+d)^j} \cdot C_E\left(\frac{\text{INR}}{\text{kWh}}\right) \tag{18}$$

2.3.3. Environmental Performance

(i) Carbon footprint emission (CF_e)

It includes the net greenhouse gas emissions produced throughout the manufacturing process of the various components of the photovoltaic system. The CO_2 discharge in India varies in the range of 0.82–0.91 kg per unit of energy generated by the thermal power plant [19]. Here, for approximation, the average is taken, i.e., 0.865 kg/kWh. In India, transmission and distribution losses are approximately 20.7% [19]. These losses raise the average emission per unit CO_2 to 1.09 kg.

$$\text{Carbon footprint emission by the system in the entire life} = E_{\text{em}}\,(\text{kWh}) \times 1.09 \quad (\text{in kg}) \tag{19}$$

$$\text{CF}_e = \frac{E_{\text{em}}\,(\text{kWh}) \times 1.09}{n\,(\text{years})} \quad (\text{in kg per year}) \tag{20}$$

(ii) Carbon footprint mitigation (CF_m)

It is defined as the reduction in CO_2 emission achieved by electricity generation from the photovoltaic system, compared with the emissions produced by a coal-fired thermal power plant to generate an equivalent amount of electricity.

$$\text{Annual } CO_2 \text{ mitigation} = \left[E_{a,\text{out}}\left(\frac{\text{kWh}}{\text{year}}\right) - \frac{E_{\text{em}}\,(\text{kWh})}{n\,(\text{years})}\right] \times 1.09 \quad (\text{in kg}) \tag{21}$$

The difference between CO_2 emissions and mitigation over the system's lifetime is used to determine the installed rooftop solar system's net mitigation of CO_2.

Net carbon footprint mitigation:

$$CF_m = \left[\sum_{t=1}^{n} E_{a,\text{out}}\left(\frac{\text{kWh}}{\text{yr}}\right) \cdot (1-d)^{t-1} - E_{\text{em}}\,(\text{kWh})\right] \times 1.09 \times 10^{-3} \quad (\text{in tons}) \tag{22}$$

1 Ton = 10^3 kg

Carbon footprint emission(before implying solar):

$$CF_{bs} = P_{bs} \times 1.09 \quad (\text{kg/day}) \tag{23}$$

Carbon footprint emission(after implying solar):

$$CF_{as} = P_{as} \times 1.09 + CF_e \quad (\text{per day}) \tag{24}$$

Net carbon footprint savings:

$$CF_{Net} = \left(\frac{\text{CF}_{\text{bs}} - \text{CF}_{\text{as}}}{\text{CF}_{\text{bs}}}\right) \times 100 \quad (\text{in \%}) \tag{25}$$

2.4. Mathematical Modeling of Cost–Benefit Analysis

2.4.1. EV Charging

The EV battery's State of Charge (SOC) determines how much energy is needed to charge it. A mathematical expression for charging and discharging an EV battery can be written as

$$E_{\text{req}} = V_c\left(\text{SOC}_{\text{req}} - \text{SOC}_{\text{cr}}\right) \tag{26}$$

$$E_T = \sum E_{\text{req}} \tag{27}$$

$$E_{\text{avl}} = V_c(\text{SOC}_{\text{cr}} - \text{SOC}_{\text{min}}) \tag{28}$$

$$T_c = \frac{E_{\text{req}}}{P_{\text{ch}}} \tag{29}$$

$$T_c = (\text{SOC}_2 - \text{SOC}_{\text{cr}})\left(\frac{\text{SOC}_2 - \text{SOC}_{\text{cr}}}{t_1}\right) + (t_3 - t_1) + \left(\text{SOC}_{\text{req}} - \text{SOC}_4\right)\left(\frac{\text{SOC}_5 - \text{SOC}_4}{t_4 - t_3}\right) \tag{30}$$

$$P_{L,k} = V_{c,k}\sum\left[\frac{\text{SOC}_2 - \text{SOC}_1}{t_1} + \frac{\text{SOC}_3 - \text{SOC}_2}{t_2 - t_1} + \frac{\text{SOC}_4 - \text{SOC}_3}{t_3 - t_2} + \frac{\text{SOC}_5 - \text{SOC}_4}{t_4 - t_3}\right] \tag{31}$$

2.4.2. Cost–Benefit Analysis

Following equations are used to perform cost benefit analysis at the CPL.

$$C_{\text{bs}} = \sum_{i=1}^{24} P_{\text{bs},i} \cdot \sigma_i \tag{32}$$

$$C_{\text{as}} = \sum_{i=1}^{24} P_{\text{as},i} \cdot \sigma_i + C_s \tag{33}$$

2.5. Scheduling of Vehicles

Efficient scheduling of electric vehicle (EV) charging from high-price periods to low-price periods is essential to maximize the profitability of an EVPL operator. In this study, any time slot where the electricity price exceeds 90% of the peak price is classified as a High Real-Time Pricing (RTP) Zone. If a vehicle is initially scheduled to charge during a high RTP zone, the charging schedule will be adjusted to shift charging from high RTP periods to low RTP periods—provided that there is sufficient remaining time before the vehicle's scheduled departure to complete the required charging. If such a shift is not feasible due to time constraints, charging will proceed even during high RTP periods to ensure that the vehicle is adequately charged. The classification of a high RTP zone is defined by the following condition:

$$P_H(t) = \begin{cases} 1, & \text{if } P(t) \geq 0.9 \cdot P_{\max} \\ 0, & \text{otherwise} \end{cases} \tag{34}$$

where

- $P_H(t)$: indicator for high RTP at time t;
- $P(t)$: electricity price at time t;
- $P_{\max}$: peak electricity price over the scheduling horizon;
- $P_H(t) = 1$: indicates a high RTP zone;
- $P_H(t) = 0$: indicates a low RTP zone.

Constraints

1. Charging or discharging of an EV should be in between arrival and departure time of that vehicle.
2. The SOC of an EV at any instant neither goes below the minimum SOC nor exceeds the required SOC value.
3. The charging rate of a battery at any instant should not exceed the charger rating.
4. The utilized solar power at any instant should not exceed the solar generation at that instant.

$$T_{\text{ar},k} \leq T_{\text{d},k} \leq T_{\text{dep},k} \tag{35}$$

$$\text{SOC}_{\min} \leq \text{SOC}_{k,t} \leq \text{SOC}_{\text{req},k} \tag{36}$$

$$\text{Ch}_{r,t} \leq \text{Ch}_{r_{\max},t} \tag{37}$$

$$P_{s,t} \leq P_{s_{\max},t} \tag{38}$$

3. Methodology

In this section, we will illustrate the detailed steps of the Horse Herd Optimization (HHO). Then, the proposed method based on HHO is used to solve the problem of optimal

location of EVPLs and FCS, later on the optimal size of SPV at the rooftop of EVPLs in a radial distribution network.

Horse Herd Optimization (HHO)

HHO is a metaheuristic optimization algorithm that draws inspiration from the social behaviors of horse herds. Horses exhibit group dynamics, cooperation, and individual decision making to achieve objectives such as finding food, avoiding predators, or maintaining group cohesion. These principles are abstracted and applied to optimization problems.

Algorithm Summary

1. Initialize the positions of horses randomly.
2. Evaluate fitness for all horses.
3. Repeat until termination:
   - Apply exploration or exploitation based on iteration progress.
   - Update positions using herd dynamics.
   - Evaluate fitness and update x_{best}.
4. Return x_{best} as the optimal solution.

3.1. Initialization

A population of horses is represented as

$$X = \{x_1, x_2, \ldots, x_n\}$$

where x_i is the position of the ith horse in a d-dimensional search space, as follows:

$$x_i = \{x_{i,1}, x_{i,2}, \ldots, x_{i,d}\}$$

3.2. Fitness Evaluation

The fitness of each horse is assessed based on the value obtained from the objective function $f(x)$. The best position in the herd is

$$x_{\text{best}} = \arg\min_{x \in X} f(x) \quad \text{(for minimization problems)}$$

3.3. Exploration Phase

In the exploration phase, the movement of a horse is given by

$$x_i(t+1) = x_i(t) + r_1 \cdot (x_j(t) - x_i(t)) + r_2 \cdot (x_k(t) - x_i(t))$$

where

- $x_j(t)$ and $x_k(t)$ are random positions of other horses in the herd;
- r_1 and r_2 are random variables between $[0, 1]$.

3.4. Exploitation Phase

In the exploitation phase, horses move towards the best-known position, as follows:

$$x_i(t+1) = x_i(t) + s \cdot (x_{\text{best}}(t) - x_i(t)) + \epsilon$$

where

- s is a scaling factor that decreases over iterations;
- ϵ is a small random value to avoid local optima.

3.5. Herd Dynamics

The influence of the leader (x_{best}) and social interactions is modeled as

$$x_i(t+1) = \alpha \cdot x_{\text{best}}(t) + (1-\alpha) \cdot x_i(t) + \beta \cdot \Delta$$

where

- α, β are weight factors
- Δ is a perturbation caused by neighboring horses.

3.6. Boundary Handling

To ensure that horses stay within the search space,

$$x_{i,j}(t+1) = \begin{cases} \text{lower_bound}_j, & \text{if } x_{i,j}(t+1) < \text{lower_bound}_j \\ \text{upper_bound}_j, & \text{if } x_{i,j}(t+1) > \text{upper_bound}_j \\ x_{i,j}(t+1), & \text{otherwise} \end{cases}$$

3.7. Termination Criteria

The algorithm stops if any of the following conditions are satisfied:

- A predefined maximum number of iterations is reached;
- The fitness reaches an acceptable error threshold.

4. Case Study and Results

In this section, the results obtained using the Horse Herd Optimization (HHO) algorithm for the IEEE 33-bus distribution network are presented. The system's peak load demand is 3.715 MW, and Figure 2 illustrates a single-line diagram of the system [20]. Simulations were carried out in MATLAB R2023b on a Windows 10-based personal laptop equipped with an Intel(R) Core(TM) i5 CPU @2.53 GHz and 6 GB of RAM. For this analysis, the distribution network is categorized into three consumer classes: residential (R), commercial (C), and industrial (I), as shown in Figure 2. Table 2 shows allocated nodes and class-specific demand.

System Description: The 33-bus distribution system was divided into the following three distinct zones:

Residential Area: contains an EVPL with a rooftop SPV;

Commercial Area: includes an EVPL equipped with a rooftop SPV;

Industrial Area: hosts a fast-charging station (FCS).

As shown in Figure 2, feeders 1 to 15 are dedicated for residential users; similarly, feeders from 22 to 29 are specified for industrial users, and feeders from 16 to 21 and 30 to 33 are allocated to commercial users. The line voltage of the system is 12.66 kV, whereas the nominal active and reactive demand of the system are 3715 kW and 2300 kVA, respectively.

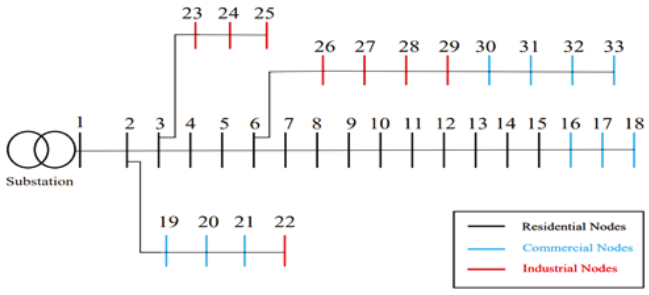

Figure 2. Radial distribution network of 33 buses.

Table 2. Customer's class-wise details.

Class	Allocation Demand (%)	Allocation Demand (kW)	Allocated Nodes
R	34.86	1295	1 to 15
C	29.60	1100	16 to 21, 30 to 33
I	35.54	1320	22 to 29

It is assumed that an EV parking lot with a capacity of 200 vehicles is located in a mixed-use area serving both residential and commercial purposes, while a fast-charging station is situated in an industrial zone. This study analyzes data from 204 vehicles at the Residential Parking Lot (RPL), 178 vehicles at the Commercial Parking Lot (CPL), and 500 vehicles at the Industrial Fast-Charging Station (I-FCS). Figures 3 and 4 illustrate the vehicle arrival and departure patterns at CPL [21] and RPL [22], respectively, whereas Figure 5 shows the arrival pattern of EVs at FCS [23]. At the RPL, peak vehicle arrivals occur in the evening, with departures predominantly in the morning. In contrast, the CPL experiences peak arrivals in the morning and departures in the evening. Details regarding battery capacity, initial and final State of Charge (SOC), charging efficiency, charger types, and quantities, as well as power ratings, are provided in Table 3. The battery charging behavior curves for AC level-2 chargers and fast chargers [24] are presented in Figure 6.

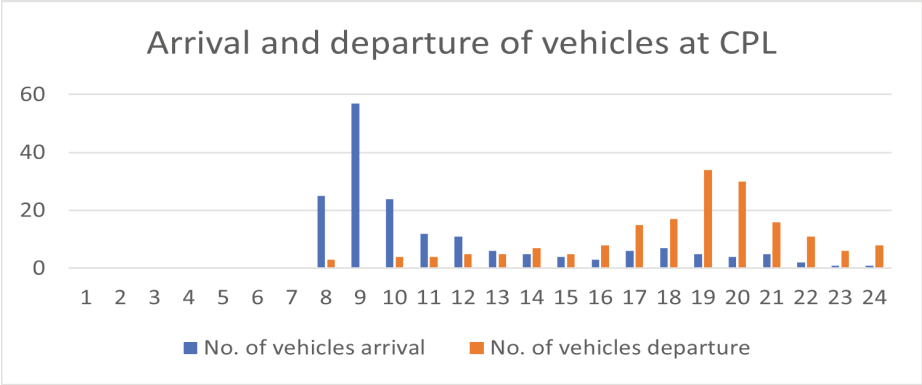

Figure 3. Arrival and departure pattern of EVs at CPL.

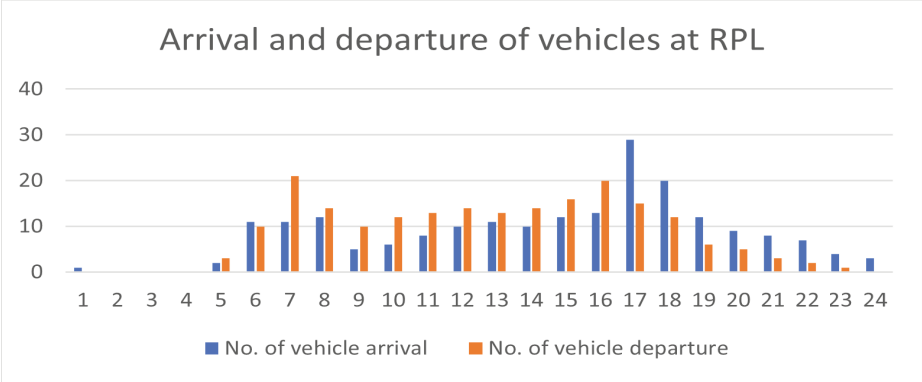

Figure 4. Arrival and departure pattern of EVs at RPL.

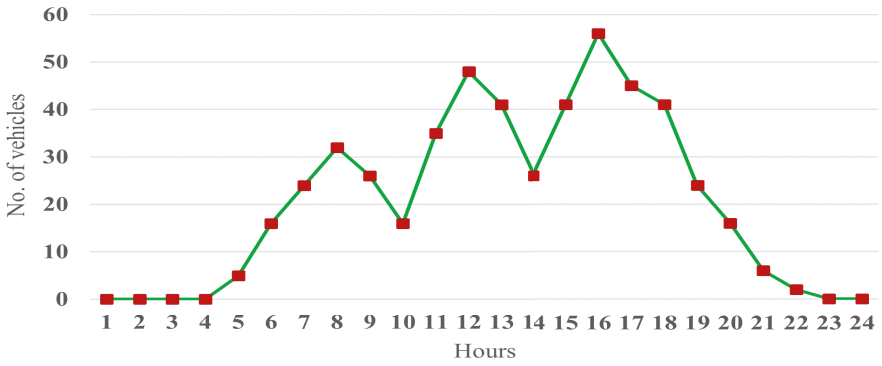

Figure 5. Arrival pattern of EVs at FCS.

Table 3. Input parameters.

Parameters	Value
Capacity of RPL/CPL	200
No. of vehicles at CPL	178
No. of vehicles at RPL	204

Table 3. *Cont.*

Parameters	Value
No. of vehicles at IFCS	500
No. of chargers at CPL	35
No. of chargers at RPL	30
No. of chargers at IFCS	10
Initial SOC range of vehicles at CPL	20–50
Final SOC range of vehicles at CPL	85–95
Initial SOC range of vehicles at RPL	20–40
Final SOC range of vehicles at RPL	85–95
Initial SOC range of vehicles at IFCS	20–50
Final SOC range of vehicles at IFCS	75–85
Battery capacity of vehicles at RPL	24–40
Battery capacity of vehicles at CPL	24/30
Battery capacity of vehicles at IFCS	30/50

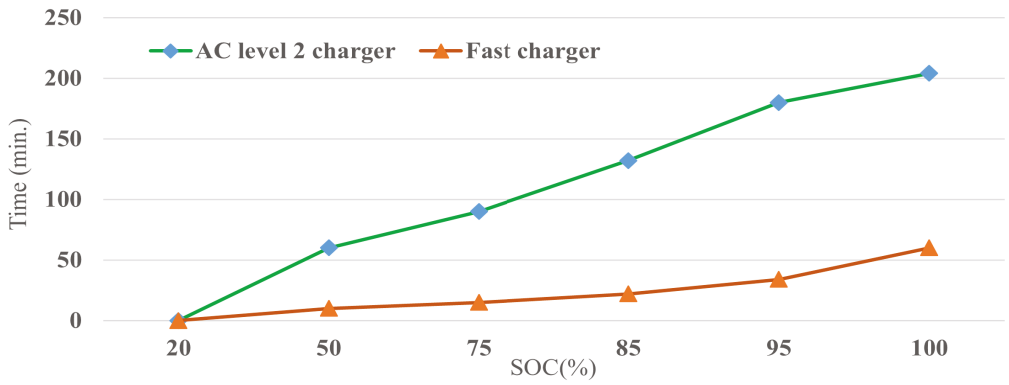

Figure 6. Battery charging behavior curve for AC level-2 chargers and fast chargers.

The IEEE 33-bus distribution system is utilized to analyze the impact of EVPLs on the distribution grid. The objective function is formulated to minimize total power losses in

the network. An Optimal Power Flow (OPF) approach, integrated with the Horse Herd Optimization (HHO) algorithm, is employed to determine the siting for the RPL, CPL, I-FCS, and sizing of a rooftop SPV on RPL and CPL. Table 4 presents the impact of EVPLs on system power losses and voltage profiles under various load scenarios. These results are obtained by placing EV loads at optimal locations identified using the HHO algorithm. The flowchart for the HHO is shown in Figure 7. To analyze the effectiveness of HHO, the formulated objective is solved by the GA and PSO algorithm also. The results, as shown in Table 5, verifies the superiority of HHO over GA and PSO, as through HHO, we found minimum power losses and lower computation time.

HHO works better than GA and PSO because it can adaptively balance exploration and exploitation. HHO changes its movement methods based on how the herd behaves, which helps it get away from local optima more easily. GA, on the other hand, uses crossover and mutation, which can cause premature convergence in complex search spaces. HHO is better than PSO because it uses random movements and adaptive parameter tweaking to keep the solution population diverse throughout the optimization process. PSO uses fixed velocity updates that might induce stalling near suboptimal solutions. This allows HHO to better explore in the solution space in the early phases and take advantage of favorable areas in later stages. Because of this, HHO obtains a solution faster and with better quality, as seen by the significant drops in power loss, better voltage stability, and shorter computing time. Table A1 presents the Sensitivity of HHO results to population size and iterations.

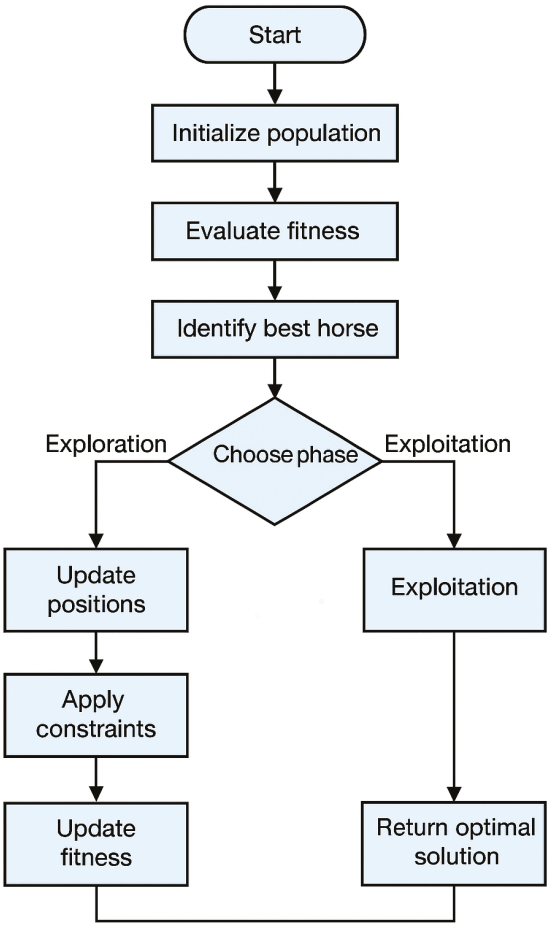

Figure 7. Horse Herd Optimization flowchart.

Table 4. Optimization (HHO) results.

Load	Optimum Location	Power Loss	Minimum Voltage
Base load	-	2.38 MW	0.9131
Case study	2, 19, 22	2.65 MW	0.9125
2* Case study	2, 19, 23	3.26 MW	0.9120
3* Case study	2, 19, 23	3.88 MW	0.9110
4* Case study	2, 19, 23	4.64 MW	0.9109

Table 5. Different optimization results.

Optimization Method	Worst Fitness (MW)	Best Fitness (MW)	Mean Fitness	CPU Time (s)	Standard Deviation
GA	2.6883	2.6746	2.6830	36.53	0.0054
PSO	2.6803	2.6659	2.6721	25.31	0.0053
HHO	2.6663	2.6518	2.6545	20.76	0.0048

This study focuses on the analysis of a commercial and residential parking lot, each with a capacity for 200 electric vehicles (EVs). By concentrating on individual parking lots, the research enables a more detailed and comprehensive approach to modeling solar PV system sizing, EV charging demand, vehicle coordination algorithms, and financial feasibility from the perspective of a small corporate parking lot owner. Selecting a fleet size of 200 EVs—rather than generalizing to smaller or larger corporate fleets—highlights the economic viability and potential benefits for a medium-sized retail complex or business facility. As the capital costs of EVs and charging infrastructure continue to decrease, parking lot owners may scale the system further and increase the share of electrified staff vehicles over time. Additionally, modeling on a per-vehicle basis allows for a more accurate representation of arrival behavior, charging requirements, and alignment with solar generation, as opposed to analyzing aggregate fleet-wide charging loads. A standard single parking space in the U.S. measures approximately 9 ft by 18 ft, equating to a total area of about 32,400 square feet (or roughly 3010 square meters) for a 200-vehicle lot. Solar PV panels are installed on the rooftop, utilizing approximately 90% of the available area.

An SPV system is assumed to be installed on the roof of RPL and CPL. The optimal size of the PV system is determined using the HHO algorithm. Annual solar generation data have been sourced from the National Renewable Energy Laboratory (NREL) [25], and the analysis is performed using the average daily generation profile. The daily solar generation pattern is illustrated in Figure 8. Calculations related to area requirements, energy performance, economic viability, and environmental impact of the PV system are discussed in the preceding section. Monthly electricity generation data are used to calculate the PR of SPV. As shown in Figure 9, the annual average PR of the rooftop SPV is calculated to be 72.38%, with monthly values ranging from a low of 68.22% in May to a high of 75.77% in January. The selection of the optimal PV technology for the rooftop is based on energy density as a performance metric, with the system in this study achieving an energy density of 231.53 kWh/m^2. The Energy Payback Time (EPBT) is evaluated by determining the net energy output of the system each year until the cumulative energy generated equals the energy invested. The estimated EPBT for the rooftop PV system is 5.25 years. The EROI, a measure of system efficiency and productivity, is calculated using Equation (10), resulting in a value of 5.71. The Cost of Energy (COE) is evaluated based on a 30-year life cycle. Capital costs are calculated excluding land acquisition, as the system is installed on an existing rooftop. A 5% annual discount rate, as currently offered by the Indian

government to promote renewable energy adoption, is applied in the economic analysis. Annual maintenance and repair costs are estimated at 1% of the capital cost, with the NPV of these expenses presented in Table 6. Replacement costs are also considered using NPV, with Power Conditioning Units (PCUs) assumed to require replacement twice during the 30-year lifespan due to their 15-year operational life. Salvage value is calculated at 20% of the initial capital cost at the end of the system's life, including PCU components. The life-cycle cost of the rooftop SPV, in terms of NPV, is summarized in Table 6. The total lifetime electricity output is determined by accounting for PV module degradation over time. Using the NREL-generated annual electricity data and applying the degradation rate across the 30-year period, the COE is calculated. The resulting cost of electricity from the SPV is estimated at 1.45 INR/kWh.

Table 6. Various costs of the rooftop PV system.

Particular	Value
Capital cost (Rs.)	24,669,090
Maintenance and repair cost (Rs.)	3,791,716
Replacement cost (Rs.)	2,126,969
Salvage cost (Rs.)	4,118,837
Life-cycle cost (Rs.)	26,468,938
Cost of electricity (Rs/kWh)	1.45
System cost (Rs/W_p)	61.67

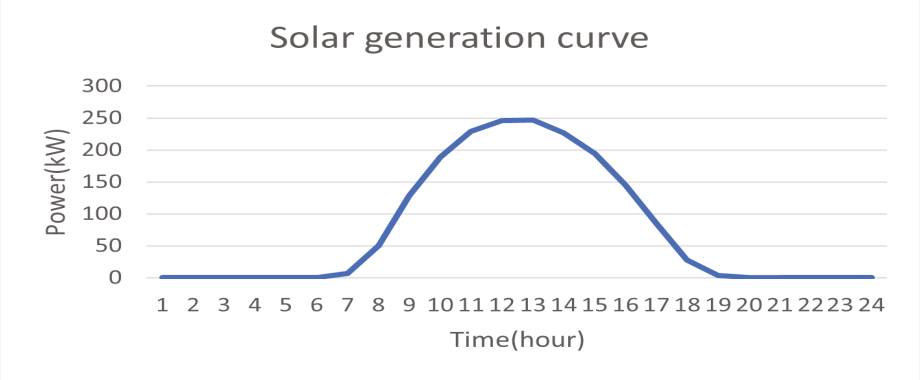

Figure 8. Solar generation curve.

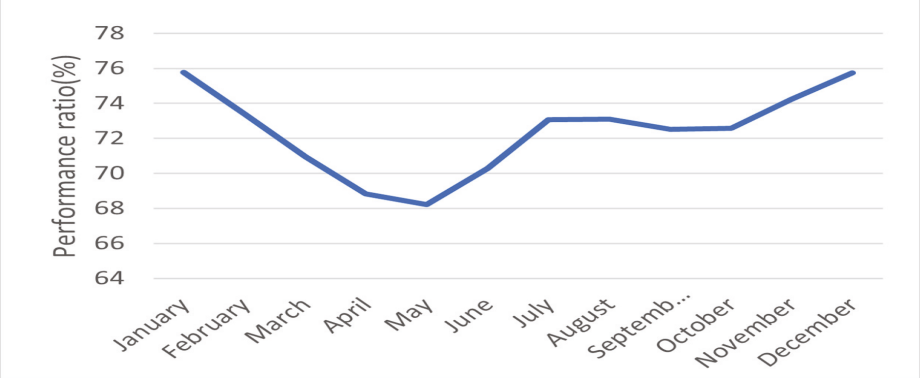

Figure 9. Monthly variation in PR of the SPV system.

As previously discussed, calculating the EPBT of a photovoltaic system requires an assessment of its embodied energy—which includes the total energy consumed in the process

of manufacturing, transportation, installation, and commissioning of the system components. For a 5 kW SPV system, the embodied energy is estimated to be 42,719.0 kWh [16]. To determine the energy consumed per kilowatt of installed capacity, this value is divided by the system's rated power, resulting in 8543.8 kWh/kW. This specific energy value is used to estimate the embodied energy for other rooftop PV systems in this study, which are similarly mounted on building rooftops and use identical polycrystalline silicon (poly-Si) PV modules. Based on this, the total embodied energy for the studied SPV is calculated to be 3,417,520 kWh. To assess the EPBT, the system's net annual energy generation is computed year by year until the cumulative energy output equals the total embodied energy. Using this approach, the EPBT for the SPV is estimated at 5.25 years.

Photovoltaic (PV) systems do not emit CO_2 during their operational phase. However, carbon emissions are associated with the embodied energy required for manufacturing, transporting, and installing the system components. The net CO_2 emissions of rooftop PV systems are therefore assessed based solely on their embodied energy. Using this approach, the rooftop PV system in this study is estimated to offset approximately 862.64 tons of CO_2 emissions annually. The net carbon footprint mitigation over the system's lifetime is calculated using Equation (22), which considers the annual energy output adjusted for a degradation rate of 0.6% per year. This accounts for the gradual decline in energy production due to PV module aging. Over a 30-year operational life, the net CO_2 mitigation achieved by an SPV system is estimated to be 23,306.5 tons of CO_2.

This study also includes a cost–benefit analysis of the CPL from the perspective of the EVPL owner. Electric vehicles are charged using solar energy when available; otherwise, electricity is drawn from the grid. Figure 10, Figure 11, and Figure 12 represent the power drawn from the grid in different scenarios at RPL, CPL, and I-FCS, respectively. The economic evaluation is based on real-time electricity pricing, as described in [26] and illustrated in Figure 13. Any hour during which the electricity price exceeds 95% of the peak rate is categorized as a high Real-Time Pricing (RTP) zone. Vehicle charging is scheduled to avoid these high-RTP periods, thereby minimizing electricity costs. As shown in Table 7, the integration of a 400 kW solar PV system at the CPL substantially reduces the average daily energy cost from USD 218.52 to USD 105.72, representing a 51.60% reduction. Furthermore, implementing a vehicle charging schedule based on RTP zones results in an additional 4.68% cost savings. The cost–benefit analysis clearly demonstrates the significant economic advantage of incorporating solar PV systems and intelligent charging strategies in EV parking lots.

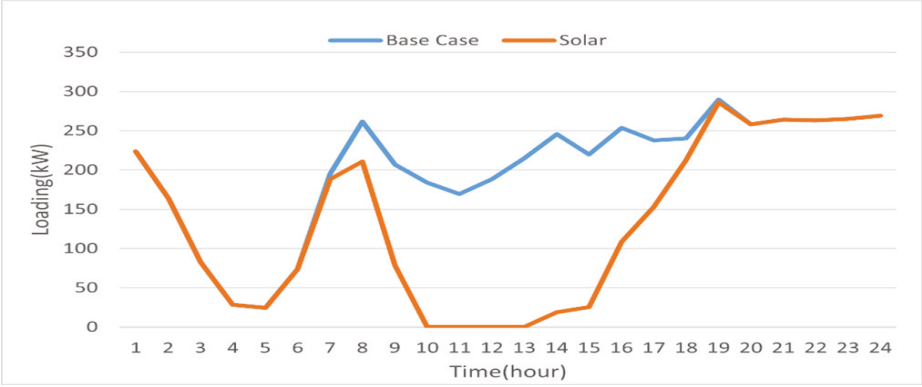

Figure 10. Power drawn from grid at RPL in different scenarios.

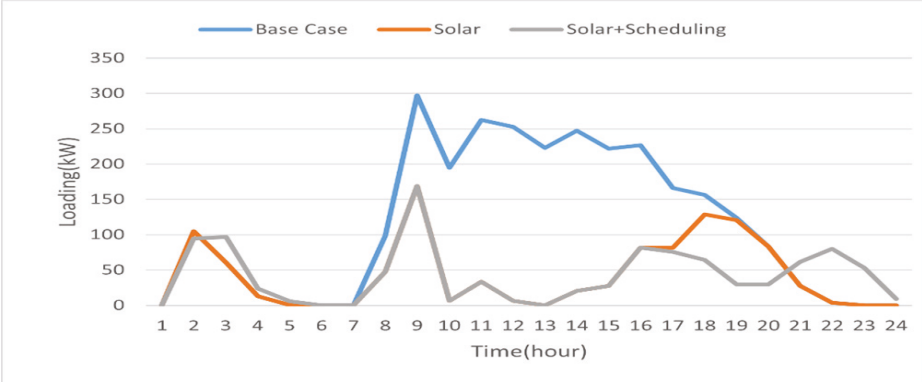

Figure 11. Power drawn from grid at CPL in different scenarios.

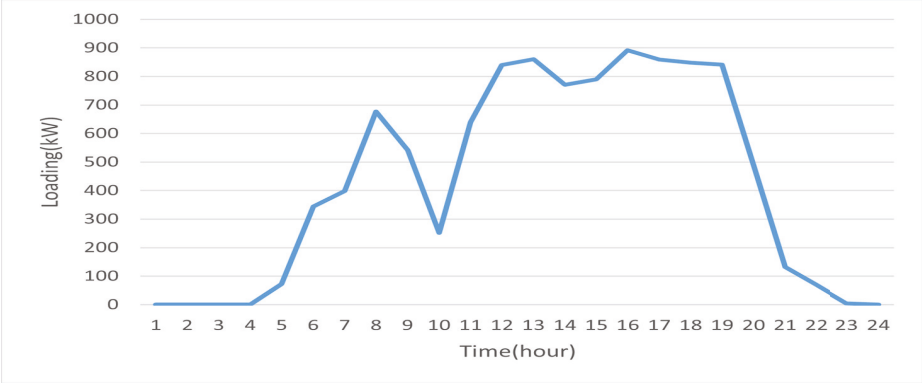

Figure 12. Power drawn from grid at I-FCS.

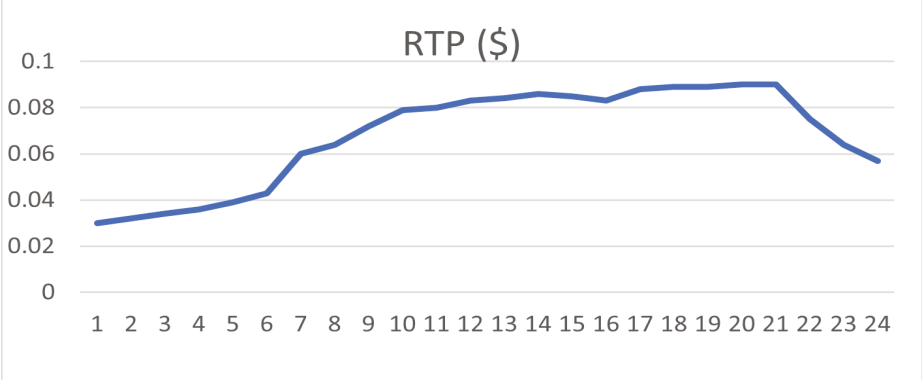

Figure 13. Real-time pricing.

Table 7. Cost–benefit analysis at CPL.

Scenario → Cost ↓	Before Solar	After Solar	After Solar + Scheduling
Power purchased from grid (USD/day)	218.52	75.38	70.43
Solar generation (USD/day)	-	30.34	30.34
Total purchasing cost (USD/day)	218.52	105.72	100.77

5. Conclusions

This work addresses multi-zone optimization across residential, commercial, and industrial areas for a combined siting of FCS, CPL, and RPL. In addition, PV sizing is also

determined. The optimization problem is solved using HHO to optimize power loss. Comparative analyses on IEEE-33 bus demonstrate that it outperforms well-known optimization algorithms such as GA and PSO in achieving lower energy losses and computation time. In addition, the techno-economic evaluation of a 400 kW rooftop PV system in Jaipur indicated a promising performance ratio of 72.38%, EPBT of 5.25 years, EROI of 5.71, and COE of Rs. 1.45/kWh. The rooftop photovoltaic system reduced carbon footprint by 59.21%, which shows the significant impact on the environment. In this study, cost–benefit analysis of CPL is also performed from the prospective of the EVPL owner. Results show that 400 kW of the solar PV system in CPL significantly reduced the per-day energy cost from USD 218.52 to USD 105.72, i.e., 51.60%. The per-day energy purchasing cost is further reduced by 4.68% by using vehicle scheduling. The efficacy of the proposed work is demonstrated on a 33-bus distribution system.

Policy Implications: The results have direct implications for policymakers and utility planners aiming to accelerate EV adoption while maintaining grid stability. The demonstrated cost reductions and carbon footprint mitigation from optimally sited, solar-integrated charging infrastructure support policies that incentivize rooftop PV deployment at commercial and residential parking facilities. Furthermore, the integration of intelligent charging scheduling aligns with demand-response programs and dynamic pricing schemes, which can help flatten peak loads and defer costly grid reinforcements. Regulatory frameworks that encourage coordinated planning between transport and power sectors, coupled with targeted subsidies for renewable-powered EVSE, can leverage the demonstrated techno-economic benefits for large-scale implementation.

Limitations and future scope: While the proposed framework demonstrates strong performance for the IEEE-33 bus system, several limitations should be noted. The case study is based on a single test network with fixed demand profiles and does not account for seasonal or stochastic variations in EV arrival patterns, solar irradiance, or electricity prices. Additionally, the analysis assumes ideal communication and control infrastructure without considering implementation delays or uncertainties. Future research could extend the model to larger and meshed distribution systems, incorporate real-time adaptive control under variable conditions, and evaluate hybrid renewable-storage integration. Exploring multi-objective formulations that also include reliability indices, user satisfaction metrics, and regulatory constraints would further enhance practical applicability.

Author Contributions: Conceptualization, K.C., M.K.S. and K.R.N.; methodology, K.C. and K.R.N.; software, K.C.; validation, K.R.N., P.N.B. and G.S.; formal analysis, K.R.N. and M.K.S.; investigation, K.C.; resources, M.K.S. and G.S.; data curation, K.C.; writing—original draft preparation, K.C.; writing—review and editing, M.K.S. and K.R.N.; visualization, K.C.; supervision, K.R.N., M.K.S. and G.S.; project administration, P.N.B.; funding acquisition, P.N.B. All authors have read and agreed to the published version of the manuscript.

Funding: This research received no external funding.

Data Availability Statement: The raw data supporting the conclusions of this article will be made available by the authors upon reasonable request.

Conflicts of Interest: The authors declare no conflicts of interest.

Nomenclatures

Index	Definition
$E_{a,out}$	PV system's annual energy generation (kWh)
A_a	Total area of array (m^2)
E_{em}	Embodied energy (kWh)
C	Capital cost (Rs.)
C_{MR}	Maintenance and repair cost (Rs.)
C_R	Replacement cost (Rs.)
C_S	Salvage cost (Rs.)
M	The SPV system's average yearly maintenance and repair costs
R_{15}	Replacement cost of PCU at 15 years' interval
P_o	Capital cost
C_E	Cost of grid electricity (INR/kWh)
E_{req}	Energy required to charge the battery to desired SOC
V_c	Battery capacity of the vehicle
SOC_{req}	Required SOC of EV battery
SOC_{cr}	Current SOC of EV battery
E_T	Total energy required for charging all the vehicles
E_{avl}	Energy available for discharging scenario
SOC_{min}	Minimum SOC limit that the battery can discharge
T_c	Charging time
P_{ch}	Charging power
$P_{L,k}$	Loading by the kth vehicle
$V_{c,k}$	Battery capacity of the kth vehicle
C_{bs}	Cost of charging before implying solar (USD/day)
P_{bs}	Energy extracted from grid before implying solar (kWh/day)
σ_i	Real-time price at i^{th} hour (USD/kWh)
C_{as}	Cost of charging after implying solar (USD/day)
P_{as}	Energy extracted from grid after implying solar (kWh/day)
C_s	Cost of generating solar power (USD/day)
$T_{ar,k}$	Arrival time of the kth vehicle
$T_{d,k}$	Charging duration of the kth vehicle
$T_{dep,k}$	Departure time of the kth vehicle
$SOC_{k,t}$	SOC of the kth vehicle at any t instant
$Ch_{r,t}$	Charging rate of the battery at any t instant
$Ch_{r_{max},t}$	Maximum charging rate of the charger at any t instant
$P_{s,t}$	Solar energy utilization at any t instant
$P_{s_{max,t}}$	Maximum solar energy available at any t instant

List of Acronyms

Acronym	Definition
RPL	Residential Parking Lot
CPL	Commercial Parking Lot
I-FCS	Industrial Fast Charging Station
SPV	Solar Photovoltaic
EV	Electric Vehicle
PL	Parking Lot
PV	Photovoltaic
HHO	Horse Herd Optimization
SOC	State of Charge
RTP	Real-Time Pricing
PR	Performance Ratio
EPBT	Energy Payback Time
COE	Cost of Electricity
LCC	Life-Cycle Cost
PCU	Power Conditioning Unit
CFe	Carbon Footprint Emission
CFm	Carbon Footprint Mitigation

Appendix A. Sensitivity of HHO Parameter

The performance of the Horse Herd Optimization (HHO) algorithm was evaluated under different parameter settings to assess robustness. In particular, the herd size (population) and maximum iterations were varied, and their impact on feeder real power losses and CPU time was recorded for the IEEE-33 bus test case. Table A1 summarizes the results.

Table A1. Sensitivity of HHO results to population size and iterations.

Population Size	Max Iterations	Best Fitness (MW)	Mean Fitness (MW)	Std. Dev. (MW)	CPU Time (s)
20	100	2.6554	2.6618	0.0072	15.42
30 (baseline)	100	2.6518	2.6545	0.0048	20.76
40	100	2.6515	2.6539	0.0045	26.94
30	80	2.6521	2.6553	0.0051	17.10
30	120	2.6517	2.6543	0.0048	24.92
30	150	2.6517	2.6542	0.0047	30.31

References

1. Oruganti, K.S.P.; Vaithilingam, C.A.; Rajendran, G.; Ramasamy, A. Cost-benefit analysis of sustainable solar-powered workplace electric vehicle charging station. In *Theoretical, Modelling and Numerical Simulations Toward Industry 4.0*; Springer: Singapore, 2020; pp. 71–86.
2. Deshmukh, S.S.; Pearce, J.M. Electric vehicle charging potential from retail parking lot solar photovoltaic awnings. *Renew. Energy* **2021**, *169*, 608–617. [CrossRef]
3. Li, Y.; Pei, W.; Zhang, Q.; Xu, D.; Ma, H. Optimal layout of electric vehicle charging station locations considering dynamic charging demand. *Electronics* **2023**, *12*, 1818. [CrossRef]
4. Altaf, M.; Yousif, M.; Ijaz, H.; Rashid, M.; Abbas, N.; Khan, M.A.; Waseem, M.; Saleh, A.M. PSO-based optimal placement of electric vehicle charging stations in a distribution network in smart grid environment incorporating backward forward sweep method. *IET Renew. Power Gener.* **2024**, *18*, 3173–3187. [CrossRef]
5. Asghari Rad, H.; Jafari-Nokandi, M.; Hosseini, S.M. Optimal Allocation of Plug-in Electric Vehicle Parking Lots for Maximum Serviceability and Profit in the coupled distribution and transportation networks. *Sci. Iran.* **2024**, *31*, 1178–1196. [CrossRef]

6. Babu, K.V.S.M.; Chakraborty, P.; Pal, M. Planning of fast charging infrastructure for electric vehicles in a distribution system and prediction of dynamic price. *Int. J. Electr. Power Energy Syst.* **2024**, *155*, 109502.
7. Prajapati, S.; Fernandez, E. Solar PV parking lots to maximize charge operator profit for EV charging with minimum grid power purchase. *Energy Sources Part A Recover. Util. Environ. Eff.* **2025**, *47*, 3319–3329. [CrossRef]
8. Mudgal, Y.; Tiwari, R. Residential Parking Lot Pricing Strategy Considering Scheduling of Electric Vehicles. *J. Inst. Eng. (India) Ser.* **2024**, *106*, 1129–1141. [CrossRef]
9. Baherifard, M.A.; Kazemzadeh, R.; Yazdankhah, A.S.; Marzband, M. Intelligent charging planning for electric vehicle commercial parking lots and its impact on distribution network's imbalance indices. *Sustain. Energy Grids Netw.* **2022**, *30*, 100620. [CrossRef]
10. Nafeh, A.E.S.A.; Omran, A.E.F.A.; Elkholy, A.; Yousef, H.M. Optimal economical sizing of a PV-battery grid-connected system for fast charging station of electric vehicles using modified snake optimization algorithm. *Results Eng.* **2024**, *21*, 101965. [CrossRef]
11. Khalid, M.; Thakur, J.; Bhagavathy, S.M.; Topel, M. Impact of public and residential smart EV charging on distribution power grid equipped with storage. *Sustain. Cities Soc.* **2024**, *104*, 105272. [CrossRef]
12. Citroni, R.; Mangini, F.; Frezza, F. Efficient integration of ultra-low power techniques and energy harvesting in self-sufficient devices: A comprehensive overview of current progress and future directions. *Sensors* **2024**, *24*, 4471. [CrossRef] [PubMed]
13. Junid, A.; Yap, E.H.; Ng, P.K. Electric vehicle charging at telco base station and bidirectional charging at hillslope descent technical-commercial cost-benefit study and scheduling-reservation system. In Proceedings of the 2018 International Conference on Smart Grid and Clean Energy Technologies (ICSGCE), Kajang, Malaysia, 29 May–1 June 2018; pp. 137–144.
14. Varone, A.; Heilmann, Z.; Porruvecchio, G.; Romanino, A. Solar parking lot management: An IoT platform for smart charging EV fleets, using real-time data and production forecasts. *Renew. Sustain. Energy Rev.* **2024**, *189*, 113845. [CrossRef]
15. Sharma, S.; Niazi, K.; Verma, K.; Rawat, T. Coordination of different DGs, BESS and demand response for multi-objective optimization of distribution network with special reference to Indian power sector. *Int. J. Electr. Power Energy Syst.* **2020**, *121*, 106074. [CrossRef]
16. Yadav, S.K.; Bajpai, U. Performance evaluation of a rooftop solar photovoltaic power plant in Northern India. *Energy Sustain. Dev.* **2018**, *43*, 130–138. [CrossRef]
17. Quansah, D.A.; Adaramola, M.S.; Appiah, G.K.; Edwin, I.A. Performance analysis of different grid-connected solar photovoltaic (PV) system technologies with combined capacity of 20 kW located in humid tropical climate. *Int. J. Hydrogen Energy* **2017**, *42*, 4626–4635. [CrossRef]
18. Jordan, D.C.; Kurtz, S.R. Photovoltaic degradation rates—An analytical review. *Prog. Photovoltaics Res. Appl.* **2013**, *21*, 12–29. [CrossRef]
19. Government of India. CEA Annual Report 2022–23. 2023. Available online: https://cea.nic.in/annual-report/?lang=en (accessed on 15 May 2025).
20. Kanwar, N.; Gupta, N.; Niazi, K.; Swarnkar, A. Optimal distributed generation allocation in radial distribution systems considering customer-wise dedicated feeders and load patterns. *J. Mod. Power Syst. Clean Energy* **2015**, *3*, 475–484. [CrossRef]
21. Guner, S.; Ozdemir, A. Stochastic energy storage capacity model of EV parking lots. *IET Gener. Transm. Distrib.* **2017**, *11*, 1754–1761. [CrossRef]
22. Anggraini, D.; Amelin, M.; Söder, L. Electric Vehicle Charging Considering Grid Limitation in Residential Areas. In Proceedings of the 2024 IEEE Transportation Electrification Conference and Expo (ITEC), Chicago, IL, USA, 19–21 June 2024; pp. 1–6.
23. Zhang, Y.; You, P.; Cai, L. Optimal charging scheduling by pricing for EV charging station with dual charging modes. *IEEE Trans. Intell. Transp. Syst.* **2018**, *20*, 3386–3396. [CrossRef]
24. Vashisth, S.; Agrawal, P.K.; Gupta, N.; Niazi, K.; Swarnkar, A. Multi-stage planning of fast charging stations for PEVs using traffic-based approach. *Sustain. Energy, Grids Netw.* **2022**, *30*, 100662. [CrossRef]
25. NREL. NREL Solar Calculator. 2025. Available online: https://pvwatts.nrel.gov/ (accessed on 1 May 2025).
26. Sharma, B.; Gupta, N.; Niazi, K.; Swarnkar, A. Estimating impact of price-based demand response in contemporary distribution systems. *Int. J. Electr. Power Energy Syst.* **2022**, *135*, 107549. [CrossRef]

Disclaimer/Publisher's Note: The statements, opinions and data contained in all publications are solely those of the individual author(s) and contributor(s) and not of MDPI and/or the editor(s). MDPI and/or the editor(s) disclaim responsibility for any injury to people or property resulting from any ideas, methods, instructions or products referred to in the content.

energies

MDPI

Article

Height-Dependent Inter-Array Temperature Difference and Position-Dependent Intra-Array Temperature Gradient

Akash Kumar, Nijanth Kothandapani, Sai Tatapudi, Sagar Bhoite and GovindaSamy TamizhMani *

Photovoltaic Reliability Laboratory, Arizona State University, Mesa, AZ 85212, USA
* Correspondence: manit@asu.edu

Abstract

This study investigates the influence of array height, irradiance, and wind speed on temperature difference and thermal gradients in photovoltaic (PV) arrays operating in hot, arid conditions. A field experiment was conducted in Mesa, Arizona (latitude 33° N), using two fixed-tilt PV module arrays installed at different elevations—one at 1 m and the other at 2 m above ground level. Each array comprised seven monocrystalline PV modules arranged in a single row with an 18° tilt angle optimized for summer performance. Data were collected between June and September 2025, and the analysis was restricted to 10:00–13:00 h to avoid shading and ensure uniform irradiance exposure on both arrays. Measurements included module backsheet temperatures at the center and edge modules, ambient temperature, plane-of-array (POA) irradiance, and wind speed. By maintaining identical orientation, tilt, and exposure conditions across all PV configurations, the influence of array height was isolated by comparing module operating temperatures between the 1-m and 2-m installations (inter-array comparison). Under the same controlled conditions, the setup also enabled an examination of how the intra-array comparison affects temperature gradients along the PV modules themselves, thereby revealing edge-center thermal non-uniformities. Results indicate that the 2 m array consistently operated 1–3 °C cooler than the 1 m array, confirming the positive impact of elevation on convective cooling. This reduction corresponds to a 0.4–0.9% improvement in module efficiency or power based on standard temperature coefficients of crystalline silicon modules. The 1 m array exhibited a mean edge–center intra-array temperature gradient of −1.54 °C, while the 2 m array showed −2.47 °C, indicating stronger edge cooling in the elevated configuration. The 1 m array displayed a broader temperature range (−7 °C to +3 °C) compared to the 2 m array (−5 °C to +2 °C), reflecting greater variability and weaker convective uniformity near ground level. The intra-array temperature gradient became more negative as irradiance increased, signifying intensified edge cooling under higher solar loading. Conversely, wind speed inversely affected ΔT, mitigating thermal gradients at higher airflow velocities. These findings highlight the importance of array height (inter-array), string length (intra-array), irradiance, and wind conditions in optimizing PV system thermal and electrical performance.

Keywords: photovoltaic (PV) systems; module temperature; array height; thermal gradients; convective cooling; heat transfer; arid climate

1. Introduction

The operating temperature of photovoltaic (PV) modules is one of the most influential factors affecting system efficiency, energy yield, and long-term reliability. While

the electrical design of a PV system determines its output potential, the thermal environment defines how closely that potential can be achieved in the field. Among the many site-specific parameters governing PV module temperature, array height and string length play particularly critical roles, as they directly influence convective heat exchange between the modules and surrounding air. Understanding the thermal impact of array geometry is therefore essential for modern PV array and plant design, especially in hot and low-wind climates where cooling is predominantly governed by natural convection. Array height determines the extent of air circulation beneath and around modules; higher elevations promote stronger airflow and turbulence, which enhance convective heat removal, reduce operating temperature, and improve conversion efficiency. Conversely, low-mounted systems—such as those installed close to the ground on short supports—experience reduced ventilation, higher heat retention, and larger thermal gradients. These differences not only affect instantaneous efficiency but also contribute to accelerated material aging, potential-induced degradation (PID), and other temperature-related performance losses. A clear understanding of the influence of array height on convective cooling [1], row spacing and its technoeconomic implications for thermal management [2], and module arrangement effects on airflow and heat transfer within PV arrays [3] enables system designers to optimize racking structures, ground clearance, and layout, while mounting dimensions and detailed temperature distribution studies further demonstrate how local geometry governs module thermal behavior and long-term durability [4,5]. The present work advances the literature by simultaneously resolving height-dependent inter-array temperature differences and position-dependent intra-array thermal gradients under controlled, real-world field conditions in a hot-arid climate. Unlike earlier studies that primarily focus on mean module temperatures, array-level performance, or modeled airflow behavior, this study explicitly quantifies edge–center temperature non-uniformities along a single-row array and demonstrates how these gradients systematically vary with array height, irradiance, and wind speed. By employing two otherwise identical fixed-tilt arrays that differ only in elevation and by isolating mid-day, shade-free operating conditions, the analysis provides a clear separation between inter-array and intra-array thermal effects. This dual-scale thermal characterization offers new insight into how array height influences not only overall cooling but also thermal uniformity along long strings—an aspect that is increasingly relevant for modern PV systems with extended string lengths due to higher system voltages and reliability-driven design considerations.

As photovoltaic architectures evolve from traditional 600 V legacy strings to today's 1500 V commercial standards—and toward 2000 V future configurations—the number of modules per string has increased substantially [6–8]. These extended strings form longer continuous arrays, which inherently restrict airflow through central sections and elevate internal thermal coupling between adjacent modules. The result is a higher effective thermal mass and reduced convective exchange, especially in glass/glass PV modules that already possess lower heat dissipation rates. Under low-wind or stagnant air conditions, these factors cause persistent temperature gradients between the center and edge modules, where edge regions benefit from lateral cooling while the inner modules retain heat for longer durations. Such non-uniform thermal profiles can exacerbate mismatch losses, accelerate thermomechanical stress, and amplify degradation rates over time. As system voltages and string lengths continue to grow, quantifying and mitigating these intra-array temperature gradients has become an important step toward thermally robust PV plant design.

In our previous work, long-term thermal mapping of PV modules and plants revealed significant temperature non-uniformities both within modules and across arrays. Center cells within a module typically operated at higher temperatures than edge cells, while centrally located arrays within a PV plant tended to run hotter than edge or corner ar-

https://doi.org/10.3390/en19010111

rays [9]. Building on these findings, the present study examines temperature variations between arrays of different mounting heights (inter-array comparison) and evaluates the temperature gradients between center and edge modules within each array (intra-array comparison). This study does not include datasets or analyses related to thermal gradients between edge and center modules for arrays of differing string lengths. The study focuses on how irradiance, wind speed, array height, and string length jointly influence module temperature distributions and their resulting impact on performance. The field experiment was conducted under actual desert conditions in Mesa, Arizona, providing high-fidelity data for hot-climate PV operation. This work isolates the geometric and aerodynamic effects of array configuration using identical modules, orientation, and operating conditions by systematically quantifying height- and string length-induced temperature differences.

2. Methodology

2.1. Experimental Setup

The field experiment was conducted in Mesa, Arizona (latitude 33° N), where two fixed-tilt photovoltaic module arrays were installed at different heights—one at 1 m and the other at 2 m above ground level (Figure 1). Each array consisted of seven monocrystalline PV modules arranged in a single row, with an 18° tilt angle optimized for summer production and thermal evaluation. The longitudinal (north–south) separation between the two arrays was maintained at 0.2 m to ensure identical irradiance exposure while minimizing mutual shading. The site was selected to ensure unobstructed sunlight throughout the day during the four-month test period.

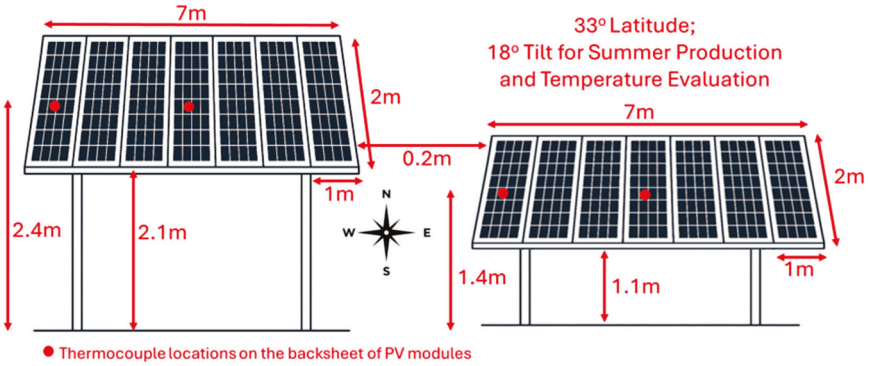

Figure 1. PV array setup showing 1 m and 2 m module heights and geometric parameters.

The experiments were conducted from June 2025 through September 2025, capturing the summer operating conditions most representative of high-temperature PV performance in hot, arid climates. To measure the thermal distribution on the back surface of the PV modules, type-K thermocouples were securely attached to the center of the middle module and the center of an edge module in each array (Figure 1). This configuration allowed for simultaneous monitoring of both inter-array (1 m vs. 2 m) temperature differences and intra-array (edge–center) temperature gradients under identical environmental conditions.

2.2. Instrumentation and Data Acquisition

Incident solar irradiance on the array plane was measured using a plane-of-array (POA) irradiance sensor. Wind speed and ambient temperature were recorded using meteorological sensors positioned near the arrays. All instruments were connected to a data acquisition (DAQ) system programmed to record data at 1- or 2-min intervals, depending on the parameter. The following parameters were continuously monitored and stored with time stamps: backsheet temperature, ambient temperature, wind speed, and POA irradiance.

https://doi.org/10.3390/en19010111

The performance and thermal characteristics of the modules used in this study are provided in Table 1.

Table 1. Performance and Thermal Characteristics of the Test Modules.

Parameter	Symbol	Value
Maximum power at STC	$P_{\max}$	320 Wp
Open circuit voltage at STC	V_{OC}	45.9 V
Short circuit current at STC	I_{sc}	9.41 A
Nominal Operating Cell Temperature	NOCT	46 °C
Temperature coefficient of I_{sc}	$T_{C,I_{SC}}$	0.042% °C^{-1}
Temperature coefficient of V_{oc}	$T_{C,V_{OC}}$	−0.304% °C^{-1}
Temperature coefficient of $P_{\max}$	$T_{C,P_{\max}}$	−0.43% °C^{-1}

Nominal Operating Cell Temperature (NOCT) is defined in IEC 61215:2005 as the equilibrium temperature reached by a photovoltaic (PV) module operating under open-circuit conditions when exposed to a total irradiance of 800 W/m^2, an ambient air temperature of 20 °C, and a wind speed of 1 m/s, with the rear surface freely ventilated [10]. The experimental setup specified in the standard requires that the test modules be surrounded by non-operating (dummy) modules to replicate the thermal environment of a real PV array and minimize edge-cooling effects. Temperature sensors are affixed to the back of representative cells, and measurements taken over several weeks are extensively processed to obtain the eventual NOCT value. The NOCT test characterizes the module's thermal behavior under standardized, yet realistic, field conditions and provides a reference for estimating operating temperatures in system performance models. The manufacturer-reported NOCT value of 46 °C aligns closely with the average NOCT of approximately 46 °C reported for glass/backsheet photovoltaic modules in the California Energy Commission (CEC) equipment open-source database listing about 20,000 modules [11]. This consistency indicates that the tested modules exhibit typical thermal behavior for conventional crystalline silicon glass/backsheet constructions, supporting the representativeness of this module for use in thermal analyses of the industry.

2.3. Data Filtering and Analysis

To ensure data quality and avoid shading effects from nearby structures or between the two arrays, only the data collected between 10:00 h and 13:00 h were used for analysis. This time window corresponds to near-solar-noon conditions when the sun's position minimizes the risk of shading on the 1 m array caused by the adjacent 2 m array's edge. Raw data were screened to remove outliers resulting from sensor noise, cloud transients, or data gaps. The processed dataset was analyzed to evaluate both inter-array and intra-array thermal behavior, focusing on three main aspects:

1. Temperature difference between arrays with different heights (see Section 3.1): The difference in module backsheet temperature between the 1 m and 2 m arrays was statistically evaluated as a function of irradiance, wind speed, month, and time of day.
2. Temperature gradient within each array (see Section 3.2): The edge–center temperature gradient ($\Delta T_{\text{edge-center}}$) was computed and statistically analyzed for both arrays to assess spatial temperature variation and compare gradient magnitudes.
3. Combined effects of weather parameters (see Section 3.3): A summary on the combined effects of irradiance, wind speed, and ambient temperature on the inter-array and intra-array ΔT values is provided.

https://doi.org/10.3390/en19010111

3. Results and Discussion

3.1. Temperature Difference Between 1 m and 2 m PV Arrays

3.1.1. Results

This section examines the thermal behavior of photovoltaic (PV) arrays installed at two different heights—1 m and 2 m above ground level, based on time-series and statistical analyses of module temperature differences. The two plots presented below—a smoothed ΔT time series (Figure 2) and a histogram of temperature differences (Figure 3) provide complementary insights into the cooling effects of array elevation on module performance and temperature uniformity. The temperature difference (ΔT) is defined as the mean module temperature at 2 m minus that at 1 m; thus, negative values indicate that the 2 m array operates at lower temperatures. Both datasets cover the summer season (June–October), when solar irradiance and ambient temperatures are highest, and convective cooling plays a significant role in module thermal behavior.

Temporal Evolution and Seasonal Behavior: The smoothed ΔT versus time plot shown in Figure 2 includes a ±1σ confidence band to represent short-term variability. This time-series plot illustrates the seasonal variation in ΔT. Throughout most of the period, ΔT remains negative, confirming that the 2 m array consistently operates cooler than the 1 m array. The fluctuations reflect changes in irradiance, wind speed, and ambient temperature. Peaks in ΔT magnitude occur during high irradiance periods (late June, mid-August, late September), when the difference in convective heat transfer between the two configurations becomes most evident.

Statistical Characteristics and Distribution of ΔT: The histogram of ΔT shown in Figure 3 provides a quantitative trend on the ΔT distribution. The mean ΔT is −1.71 °C and the mode is −2.10 °C, indicating that most temperature differences cluster between −3 °C and −1 °C. This distribution is slightly right-skewed, suggesting that occasional low-wind or cloudy periods produce smaller temperature differences. Nevertheless, the consistent negative mean demonstrates that the 2 m configuration maintains a cooler operating condition across all environmental variations.

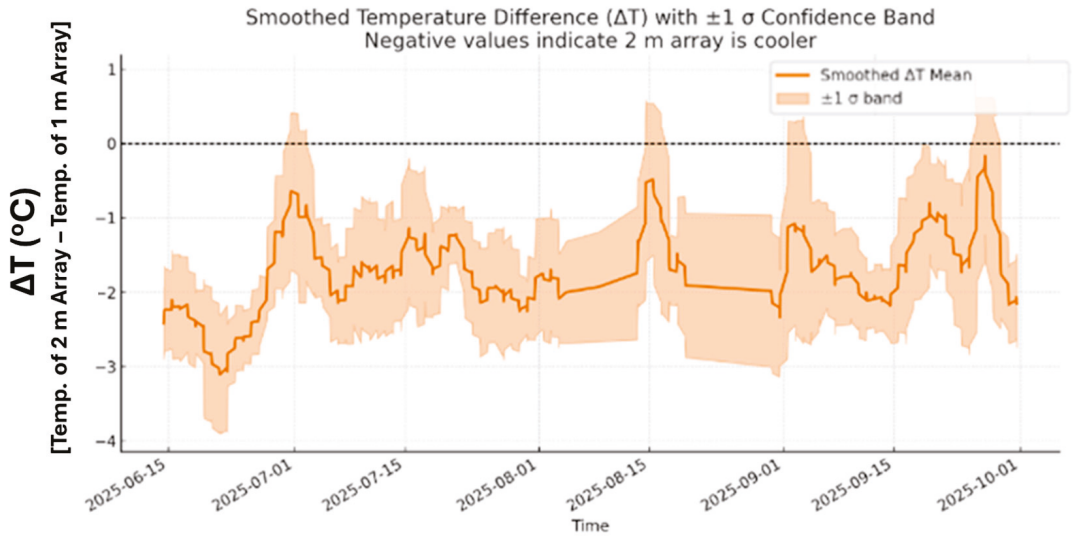

Figure 2. Smoothed temperature difference (ΔT) between the 2 m array and the reference configuration as a function of time (June-September 2025 data between 10:00 h and 13:00 h). The solid line shows the temporally smoothed mean ΔT, while the shaded region represents the ±1 σ confidence band, reflecting short-term variability. Negative ΔT values indicate periods during which the 2 m array operates at a lower temperature than the 1 m array. The dashed horizontal line at ΔT = 0 denotes thermal parity between configurations, highlighting intervals of relative cooling or warming over the measurement period.

https://doi.org/10.3390/en19010111

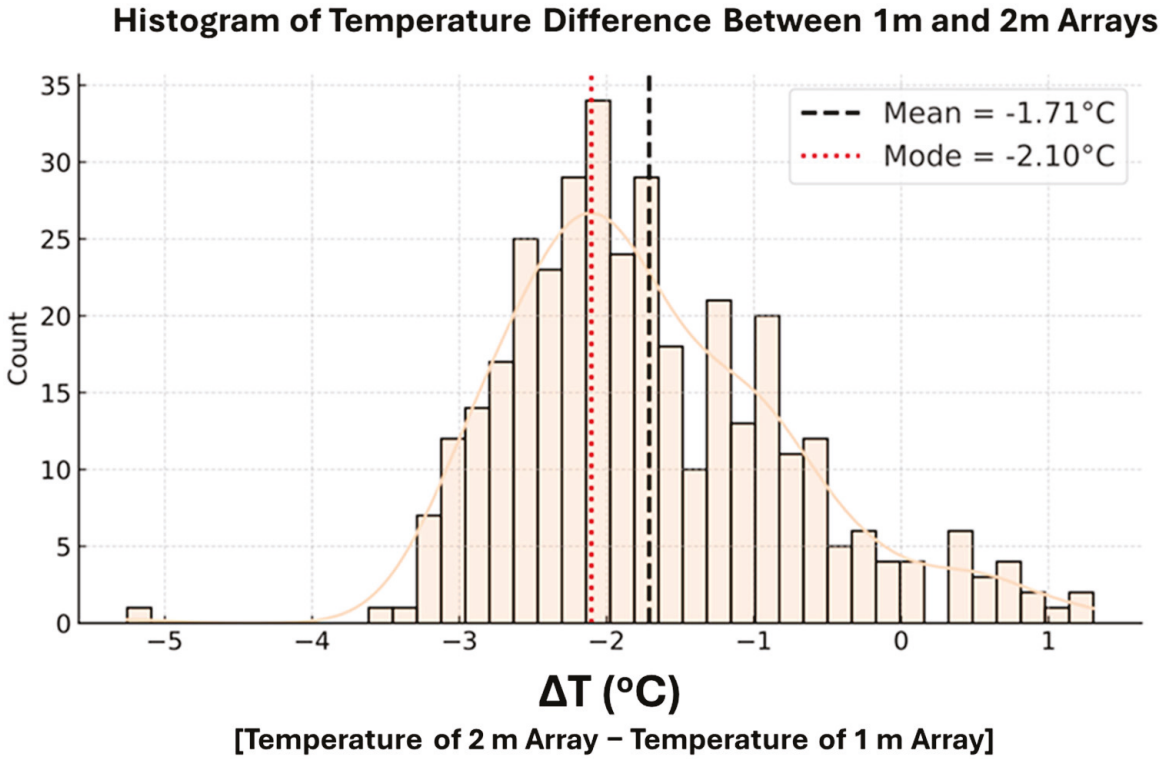

Figure 3. Histogram of the temperature difference (ΔT) between the 1 m and 2 m arrays. ΔT is defined as the temperature of the 2 m array minus that of the 1 m array. The distribution illustrates the frequency of observed temperature differences over the measurement period (June-September 2025 data between 10:00 h and 13:00 h). The dashed vertical line denotes the mean ΔT, while the dotted vertical line indicates the modal value. The predominance of negative ΔT values indicates that the 2 m array operates at a lower temperature than the 1 m array for most observations, with the distribution shape reflecting variability and asymmetry in the thermal response.

3.1.2. Discussion

The cooler operation of the 2 m array is primarily attributed to enhanced natural convection and air turbulence. At 2 m height, air circulation beneath and around the modules is more effective, reducing the boundary layer thickness and increasing the convective heat transfer coefficient. In contrast, the 1 m array experiences limited airflow and partial stagnation within the ground boundary layer, leading to reduced heat dissipation and higher overall module temperatures. This aligns with theoretical expectations from convective heat-transfer models, where the Nusselt number increases with both wind speed and free-air exposure. From a performance standpoint, cooler operation at 2 m translates into improved electrical efficiency. For crystalline silicon PV modules, every 1 °C decrease in operating temperature typically increases conversion efficiency by about 0.36–0.45%. Thus, a consistent 1–2 °C reduction in temperature yields roughly a 0.4–0.9% gain in power output. This estimated power gain is theoretically inferred from industry standards, databases, and published literature, and is not derived from direct I–V measurements of the individual modules investigated in this study. Lower operating temperatures also reduce thermomechanical stress and material degradation over time, especially solder bond degradation [12,13]. The 1 m configuration, while more compact and cost-efficient structurally, sacrifices some performance and thermal efficiency due to constrained airflow. In this study, a single ground surface and albedo condition were considered; however, variations in ground properties may influence module thermal behavior at a secondary level and warrant further investigation.

https://doi.org/10.3390/en19010111

3.2. Temperature Gradient Between Edge and Center Modules

3.2.1. Results

The following discussion analyzes the (Edge–Center) ΔT distributions for the 1 m and 2 m height photovoltaic (PV) arrays. Each histogram shown in Figures 4 and 5 represents the temperature difference between the module edge and its center, with negative values indicating that the edges are cooler due to convective air movement. The plots include overlaid kernel density estimate (KDE) curves, mean (black dashed line), and mode (red dotted line) indicators to illustrate key trends in the thermal distribution.

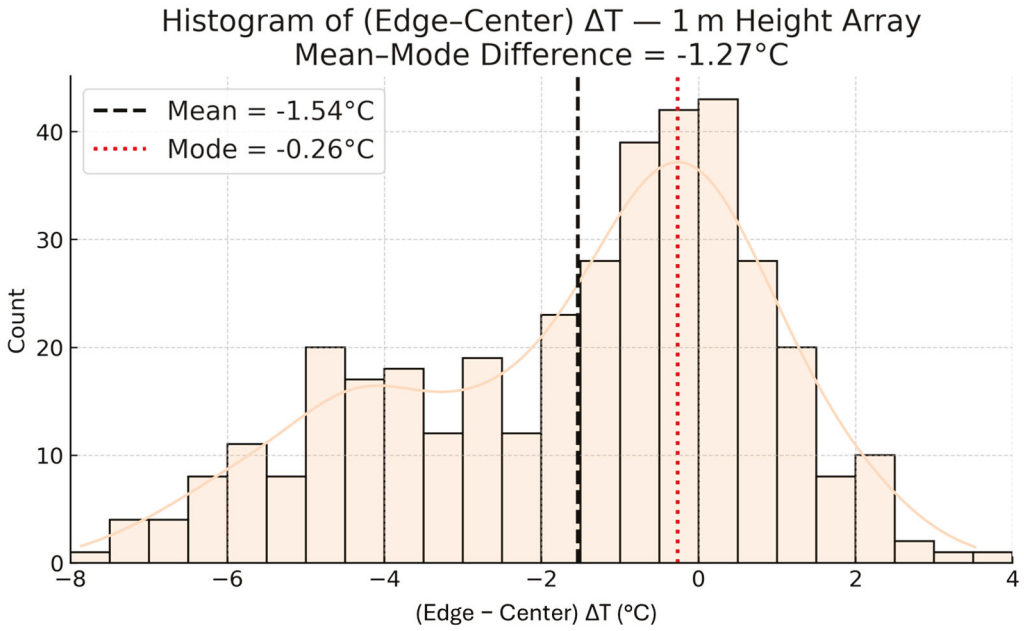

Figure 4. Histogram of (Edge-Center) ΔT—1 m Height Array (June-September 2025 data between 10:00 h and 13:00 h).

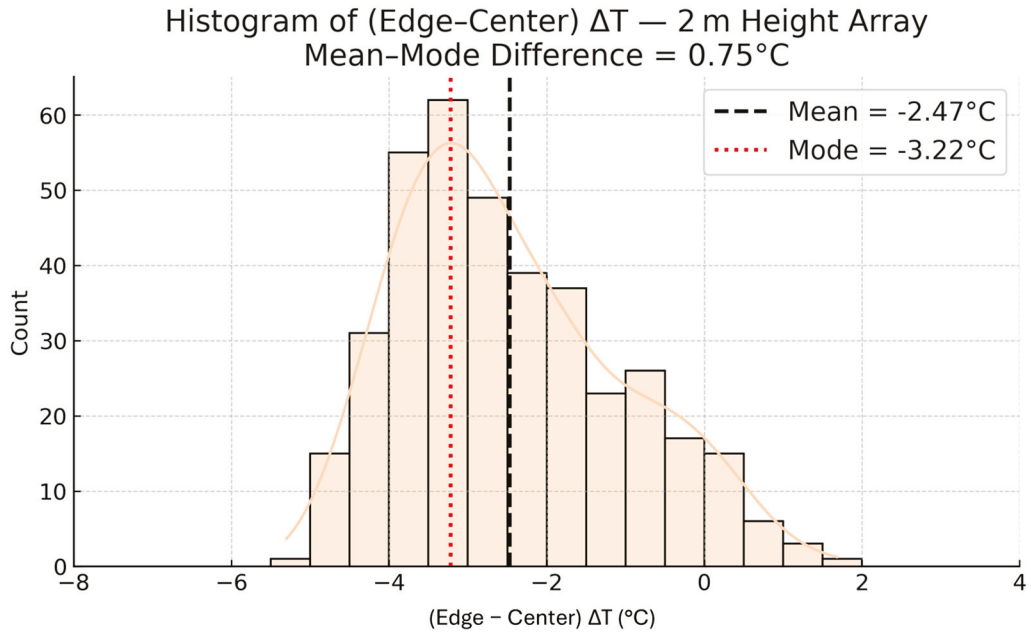

Figure 5. Histogram of (Edge-Center) ΔT—2 m Height Array (June-September 2025 data between 10:00 h and 13:00 h).

The 1 m array shown in Figure 4 exhibits a mean ΔT of −1.54 °C and a mode of −0.26 °C, while the 2 m array shown in Figure 5 indicates a mean of −2.47 °C and a mode

https://doi.org/10.3390/en19010111

of −3.22 °C. These differences reveal that modules elevated to 2 m experience stronger convective cooling at the edges due to enhanced airflow. In contrast, the 1 m array, being closer to the ground, encounters restricted airflow, resulting in reduced edge cooling and warmer overall module temperatures. The 1 m array's distribution spans approximately −7 °C to +3 °C, indicating greater variability and a broader spread. This suggests less stable thermal behavior influenced by fluctuating ground-level airflow and boundary-layer effects. The 2 m array's narrower range, centered between −5 °C and +2 °C, implies more consistent convective cooling. The mean–mode differences (−1.27 °C for 1 m and +0.75 °C for 2 m) indicate skewness: the 1 m array leans toward smaller gradients, while the 2 m array exhibits more strongly negative ΔT values, confirming improved cooling efficiency. Since the degradation rates of most PV module failure mechanisms increase exponentially with temperature, the center modules in a series-connected string—being the hottest—are expected to determine the end-of-life of the entire string.

To assess the statistical relevance of the observed temperature differences, the full distributions of ΔT were analyzed in addition to their mean and mode values. The results show consistent and systematic shifts in both the inter-array (1 m vs. 2 m) and intra-array (edge–center) temperature distributions, with limited overlap and clear separation relative to the spread of the data. These distributional characteristics indicate that the observed differences are statistically meaningful and not attributable to random variability or measurement uncertainty. Because field-measured thermal data exhibit non-Gaussian behavior, emphasis was placed on distributional analysis and comparative confidence intervals rather than parametric hypothesis testing. The persistence of the observed trends across the test samples supports the conclusion that array height and module position exert a significant influence on module operating temperature and thermal gradients under hot-arid conditions.

3.2.2. Discussion

Figures 6 and 7 show that the (Edge–Center) ΔT generally becomes more negative with increasing irradiance, indicating that the panel edges tend to cool more effectively than the center under higher thermal loading. Across most irradiance bins, ΔT remains slightly below zero, reflecting preferential convective heat removal at the boundaries where airflow is less restricted. The variability in ΔT widens at higher irradiance levels, suggesting that localized cooling effectiveness becomes increasingly sensitive to moment-to-moment wind conditions as the modules heat up. The accompanying wind-speed trends highlight that sharper decreases in ΔT often coincide with periods of enhanced air movement, reinforcing that (Edge–Center) temperature differences are strongly governed by the interplay between irradiance-driven heating and wind-driven convective cooling.

3.3. Combined Parameter Influence—Summary

Temperature difference between two array heights: The 2 m array consistently exhibits more negative mean ΔT values than the 1 m array, confirming stronger convective cooling at greater elevation. At 2 m, air circulation beneath and around the modules is less obstructed by ground interference, promoting higher convective heat transfer. Conversely, the 1 m array operates closer to the ground boundary layer, where airflow stagnation reduces convective efficiency. At high irradiance levels (900–1100 W/m^2), the mean ΔT of the 2 m array is approximately 1 °C more negative than that of the 1 m configuration, underscoring the benefit of increased elevation for thermal management.

https://doi.org/10.3390/en19010111

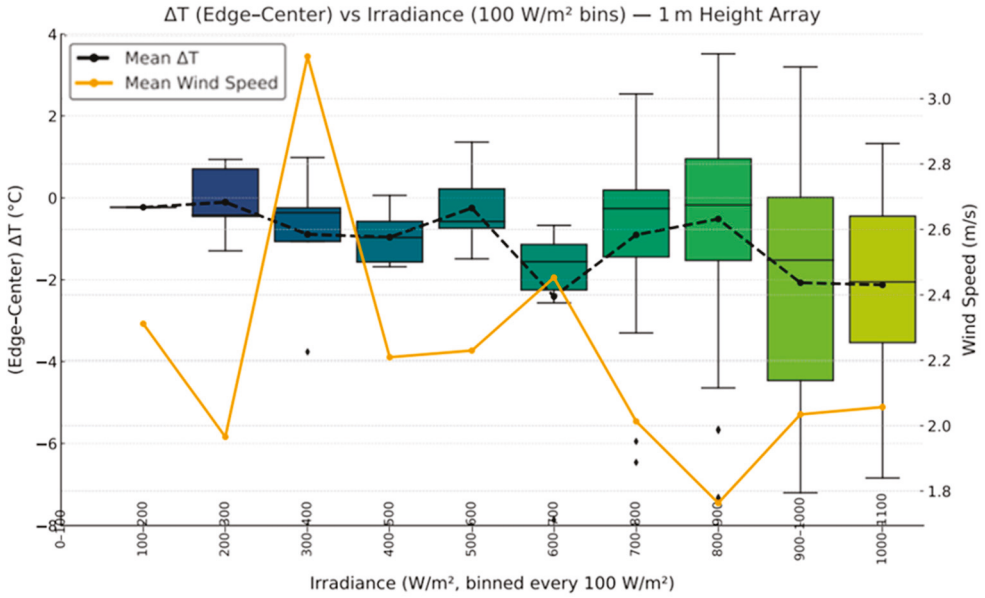

Figure 6. (Edge-Center) ΔT vs. Irradiance for 1 m Height Array. This plot includes irradiance bins of 100 W/m^2, mean ΔT (black dashed line), and mean wind speed (orange line).

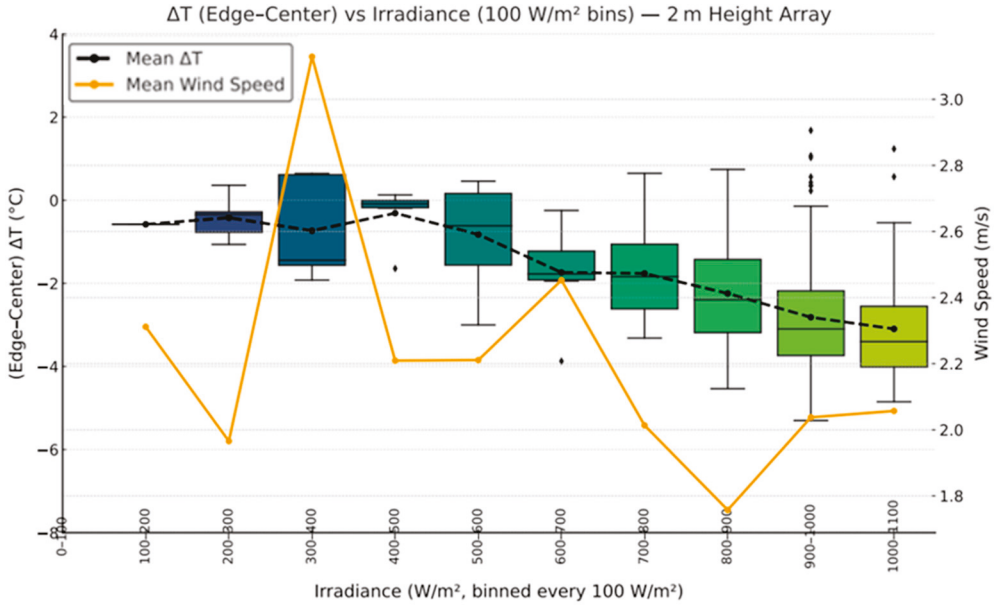

Figure 7. (Edge-Center) ΔT vs. Irradiance for 2 m Height Array. This plot includes irradiance bins of 100 W/m^2, mean ΔT (black dashed line), and mean wind speed (orange line).

Temperature gradient between modules within an array: Both 1 m and 2 m arrays with identical string length display increasingly negative ΔT values with rising irradiance, particularly beyond 500 W/m^2. This trend reflects the greater edge–center thermal contrast as solar heating intensifies. Under higher irradiance, module centers retain heat more efficiently due to limited exposure to airflow, while the edges, being more exposed, dissipate heat faster through convection. At irradiance levels above 800 W/m^2, broader ΔT distributions emerge, indicating increased variability caused by increased string length, fluctuations in ambient airflow and wind turbulence.

Combined influence of weather parameters: Wind speed serves as a crucial moderating factor. At low irradiance (<400 W/m^2), higher wind speeds coincide with smaller ΔT magnitudes, as stronger convection minimizes temperature gradients across the module surface. As wind speed increases, the ΔT magnitude tends to decrease. This inverse rela-

https://doi.org/10.3390/en19010111

tionship shows that wind promotes thermal uniformity and counteracts radiative heating. In both arrays, when wind speeds drop below approximately 2 m/s, the ΔT magnitude increases sharply—most notably within the 800–900 W/m^2 range, where radiative effects dominate. The combined effects of irradiance and wind speed can be interpreted through convective and radiative heat transfer mechanisms. Higher irradiance increases absorbed solar energy, raising module temperature and enhancing buoyancy-driven flow. The 2 m array benefits from higher Reynolds number (higher turbulent flow) and Nusselt number (higher convective heat transfer) due to stronger air motion, yielding greater convective efficiency. By contrast, the 1 m array resides within the near-ground boundary layer, where reduced turbulence limits heat exchange. These physical mechanisms collectively explain the observed differences in ΔT and reinforce the importance of module height in promoting convective cooling.

In this study, the thermal analysis focuses on ambient temperature, plane-of-array irradiance, and wind speed, which are widely recognized as the dominant environmental parameters governing PV module operating temperature in established thermal models. Factors such as wind direction, turbulence intensity, and atmospheric humidity were not explicitly included, as their influence on module temperature is generally considered secondary under typical outdoor operating conditions. Nevertheless, these variables may contribute second-order effects to convective cooling and thermal uniformity, and their role warrants further investigation in future studies incorporating detailed airflow measurements or numerical modeling.

4. Conclusions

The inter-array temperature comparison results presented in this study show that the 2 m array consistently operated 1–3 °C cooler than the 1 m array, confirming the beneficial influence of elevation on convective heat dissipation. The increased mounting height allowed for greater air circulation and turbulence beneath and around the modules, enhancing convective heat removal. This cooling effect translates into measurable gains in performance and long-term reliability for photovoltaic (PV) systems.

Intra-array temperature analysis revealed distinct temperature gradients between the edge and center modules, demonstrating the role of localized convection in shaping module temperature profiles. The 1 m array exhibited a mean edge–center temperature gradient of −1.54 °C, while the 2 m array showed −2.47 °C, indicating stronger edge cooling in the elevated configuration due to improved airflow exposure. Because the center modules in a series-connected string typically operate at higher temperatures, they are more susceptible to accelerated degradation and are therefore expected to dictate the end-of-life of the entire string.

The study also examined the combined effects of irradiance and wind speed on temperature gradients. The gradient became increasingly negative with higher irradiance, suggesting intensified edge cooling under stronger solar loading. Conversely, wind speed exhibited an inverse relationship with ΔT, as higher airflow velocities reduced temperature differentials by promoting convective uniformity across the module surface.

Overall, the findings highlight the importance of array height and module position within an array as key design parameters for enhancing module cooling, improving thermal uniformity, and increasing both energy yield and reliability in crystalline silicon PV installations, particularly in hot and arid climates. The analysis framework and observed trends are also applicable to other existing and emerging PV technologies, including perovskite and cadmium telluride modules. While the present study is based on a limited number of modules and a single tilt angle, future work should extend the investigation to a statistically significant number of arrays with long strings, additional seasons, and multiple

https://doi.org/10.3390/en19010111

sites in order to fully quantify and generalize configurational, seasonal, and site-specific variability in thermal differences and gradients.

Author Contributions: Conceptualization, G.T.; Methodology, A.K. and G.T.; Software, S.T.; Formal analysis, G.T.; Investigation, A.K., N.K., S.T., S.B. and G.T.; Resources, G.T.; Data curation, A.K. and G.T.; Writing—original draft, A.K. and G.T.; Writing—review & editing, A.K., N.K., S.T., S.B. and G.T.; Visualization, G.T.; Supervision, G.T.; Project administration, G.T.; Funding acquisition, G.T. All authors have read and agreed to the published version of the manuscript.

Funding: This research was funded by the Salt River Project (SRP). The funder was not involved in the study design, collection, analysis, interpretation of data, the writing of this article or the decision to submit it for publication.

Data Availability Statement: The original contributions presented in this study are included in the article. Further inquiries can be directed to the corresponding author.

Acknowledgments: The technical contributions and support provided by our ASU-PRL colleagues, including Arjun Aaraamudhan Seshathri, Anand Anil Kumar and Rishi Ravindra Dhavale, are sincerely appreciated.

Conflicts of Interest: The authors declare no conflicts of interest.

References

1. Smith, S.E.; Viggiano, B.; Ali, N.; Silverman, T.J.; Obligado, M.; Calaf, M.; Cal, R.B. Increased panel height enhances cooling for photovoltaic solar farms. *Appl. Energy* **2022**, *323*, 119819. [CrossRef]
2. Prilliman, M.; Smith, S.E.; Stanislawski, B.J.; Keith, J.M.F.; Silverman, T.J.; Calaf, M.; Cal, R.B. Technoeconomic analysis of changing PV array convective cooling through changing array spacing. *IEEE J. Photovolt.* **2022**, *12*, 6. [CrossRef]
3. Stanislawski, B.; Margairaz, F.; Cal, R.B.; Calaf, M. Potential of module arrangements to enhance convective cooling in solar photovoltaic arrays. *Renew. Energy* **2020**, *157*, 851–858. [CrossRef]
4. Zhang, W.; Gong, T.; Ma, S.; Zhou, J.; Zhao, Y. Study on the influence of mounting dimensions of PV array on module temperature in open-joint photovoltaic ventilated double-skin façades. *Sustainability* **2020**, *13*, 5027. [CrossRef]
5. Wen, Y.; Li, X.; Hu, W.; Yang, F.; Yang, K.; Wang, J. Experimental research on the temperature distribution characteristics of photovoltaic array. *Appl. Therm. Eng.* **2025**, *265*, 125507. [CrossRef]
6. IHS Markit. Higher Voltage Standards Help Reduce LCOE for PV Systems. 2021. Available online: https://cdn.ihsmarkit.com/www/pdf/0221/Higher-Voltage-Standards-Help-Reduce-LCOE-for-PV-Systems.pdf (accessed on 12 November 2025).
7. Casey, J.P. Breaking the 2,000 V PV System Threshold. *PV Tech*, 12 March 2025. Available online: https://www.pv-tech.org/breaking-the-2000v-pv-system-threshold/ (accessed on 8 October 2025).
8. Nelson, B. Driving Innovation Together: The Path to 2000 V Systems in Utility-Scale Renewable Energy Projects. 2025. Available online: https://electrification.us.abb.com/insights/driving-innovation-together-path-2000v-systems-utility-scale-renewable-energy-projects-0 (accessed on 8 October 2025).
9. Pavgi, A.; Oh, J.; Kuitche, J.; Tatapudi, S.; TamizhMani, G. Thermal Uniformity Mapping of PV Modules and Plants. In Proceedings of the IEEE 44th Photovoltaic Specialist Conference (PVSC), Washington, DC, USA, 25–30 June 2017.
10. *IEC 61215:2005*; Crystalline Silicon Terrestrial Photovoltaic (PV) Modules–Design Qualification and Type Approval. International Electrotechnical Commission: Geneva, Switzerland, 2005.
11. California Energy Commission (CEC). PV Module List-Full Data, California Energy Commission. 2025. Available online: https://www.energy.ca.gov/media/2367 (accessed on 12 September 2025).
12. Sinha, A.; Buddha, V.S.P.; Schneller, E.J.; Davis, K.O.; TamizhMani, G. Solder bond degradation of fielded PV modules: Climate dependence of intermetallic compound growth. In Proceedings of the 46th IEEE Photovoltaic Specialists Conference (PVSC), Chicago, IL, USA, 16–21 June 2019; pp. 1393–1397.
13. Gopalakrishna, H.; Sinha, A.; Carpenter, J.; Niverty, S.; Chawla, N.; Jordan, D.; Tamizhmani, G. Activation Energy for End-of-Life Solder Bond Degradation: Thermal Cycling of Field-Aged PV Modules. *IEEE J. Photovolt.* **2020**, *10*, 1762–1771. [CrossRef]

Disclaimer/Publisher's Note: The statements, opinions and data contained in all publications are solely those of the individual author(s) and contributor(s) and not of MDPI and/or the editor(s). MDPI and/or the editor(s) disclaim responsibility for any injury to people or property resulting from any ideas, methods, instructions or products referred to in the content.

https://doi.org/10.3390/en19010111

energies

MDPI

Article

Instantaneous Power Generation of Monofacial and Bifacial Photovoltaic Modules Under Tracker-Induced Albedo Variations

Marian Kampik [1], Krzysztof Bodzek [2], Arkadiusz Domoracki [2] and Grzegorz Jarek [2,*]

[1] Department of Measurement Science, Electronics and Control, Faculty of Electrical Engineering, Silesian University of Technology, 44-100 Gliwice, Poland; marian.kampik@polsl.pl
[2] Department of Power Electronics, Electrical Drives and Robotics, Faculty of Electrical Engineering, Silesian University of Technology, 44-100 Gliwice, Poland; krzysztof.bodzek@polsl.pl (K.B.); arkadiusz.domoracki@polsl.pl (A.D.)
* Correspondence: grzegorz.jarek@polsl.pl

Abstract

This paper presents an experimental comparison of the instantaneous power generation of standard and bifacial photovoltaic modules under real operating conditions. The study focuses on short-term effects caused by spatially variable albedo and tracker-induced changes in module orientation. Both modules were installed on the same mobile single-axis tracking platform and had identical rated front-side power, which ensured nearly identical operating conditions and independent MPPT operation. The experimental campaign included five ground surfaces: grass, river sand, grey paver, light aggregate, and dark aggregate. For each surface, electrical parameters and albedo were recorded over the full investigated geometrical range, covering relative solar azimuth from -60° to $+60^\circ$ and module tilt from 0° to 90°. The measured increase in power generation of the bifacial module relative to the standard module depended strongly on the ground surface. Over the full investigated range, the gain was 6.4% for grass, 11.3% for river sand, 5.9% for grey paver, 13.6% for light aggregate, and 4.5% for dark aggregate. These results confirm that, in bifacial photovoltaic systems with tracking, the ground surface and its reflective properties significantly affect the rear-side contribution and instantaneous power output. Consequently, albedo should not be treated as a constant or spatially homogeneous parameter when assessing short-term bifacial PV performance.

Keywords: bifacial photovoltaic module; albedo coefficient; tracker system

1. Introduction

Modern photovoltaic systems are designed within the paradigm of minimizing the levelized cost of energy (LCOE), while simultaneously increasing the energy yield per unit area and maximizing the use of the available grid connection capacity. From this perspective, bifacial modules have become cost-effective solutions both technically and economically. A review of the literature indicates that bifacial technologies are mature, but reliable estimates and analyses of the impact of albedo under field conditions are still necessary [1,2]. At the same time, ongoing research shows that combining bifacial modules with a single-axis solar tracking system can be competitive for most locations, because the gains add up in the annual energy balance [3]. In a review report on trackers with bifacial modules, prepared within the IEA PVPS framework, it was emphasized that

this configuration has become the dominant architecture in the utility-scale segment and that its development is strongly linked to the growing availability of modules [4]. It is worth noting that the market share of bifacial cells is reaching about 90% in 2024 (with the expectation of maintaining a high share in subsequent years), which indicates a structural change in technology supply [5]. In turn, in a document devoted to bifacial trackers it was additionally pointed out that with such a high penetration of bifacial cells, some of them still end up in monofacial modules (e.g., through the use of light-impermeable backsheet foil on the rear side), which complicates the straightforward identification of "bifacial cell" with "bifacial module" in market analyses and system design [4].

From the perspective of scientific research, it is important that classical approaches to PV system design (annual energy yield, LCOE) [3,6] dominate in publications. At the same time, with the increasingly widespread use of trackers and bifacial modules, the importance of short-term phenomena is growing, including non-uniform rear-side irradiance, dynamic shading by structural elements, and the time- and space-dependent variability of albedo [4,7].

A monofacial module converts the energy of radiation reaching the front side, whereas a bifacial module utilizes power from radiation incident on both the front and rear sides. The yield from the rear side depends on the cell technology, the module design (e.g., glass–glass), the transparency of the back layer, and the optical properties of the structure and its surroundings [1,2]. Consequently, for bifacial modules it becomes crucial to separate the influence of reflected radiation, albedo measurements, as well as control algorithms aimed at assessing the potential gains from the use of such technology. The standard approach to analysing the increased yield focuses on procedures for measuring the I–V characteristics of the bifacial modules themselves in natural or simulated light [8]. A parallel problem is the use of standard energy rating schemes (e.g., IEC 61853 [9]) for bifacial modules. The literature indicates that the classical energy rating prepared for monofacial modules does not explicitly include rear-side irradiance, which necessitates extending the models and/or the definition of test conditions to account for the rear-side contribution in a comparable and repeatable manner [10].

From the experimental point of view, the differences between simulated and operational conditions are also important (under conditions of variable irradiance, varying proportions of diffuse and reflected components, and possible shading). Studies indicate that laboratory comparison of effects may turn out to depend on the level of irradiation and operating conditions. This means that transferring a single catalogue parameter to hourly or minute-by-minute models is subject to limited reliability [11].

Comparisons between monofacial and bifacial modules in real outdoor conditions are most meaningful when both types of devices are operated under geometric and electrical conditions that are matched as closely as possible. (the same mounting configuration, similar temperature and wind exposure, consistent MPPT, and data recording with comparable resolution). In practice, many field tests provide only comparable, rather than "identical" conditions, which makes it difficult to separate the influence of geometry, albedo, and positioning algorithms from the influence of the module technology [7,12].

Albedo (in radiometric terms: the fraction of short-wave radiation reflected from a surface) is one of the most sensitive input parameters of yield models for bifacial systems, because it directly determines the available reflected radiation [13,14]. At the same time, albedo is not a constant quantity. It changes with the type of surface, its moisture, contamination, seasonality, the state of vegetation, as well as with the geometry of illumination and observation and the radiation spectrum [13–15]. From a design perspective, the literature shows that the profitability of bifacial solutions is strongly dependent on albedo.

https://doi.org/10.3390/en19112641

Analyses indicate that at low albedo the advantage of bifacial modules over monofacial ones decreases, whereas at higher albedo the energy gain can increase significantly [3,6].

In engineering practice, albedo is obtained through three main approaches: (i) onsite measurements (albedometer/pyranometers), (ii) satellite data (e.g., MODIS products), and (iii) tabulated values or fixed assumptions in simulation tools. Each of these methods has its limitations. Review and methodological studies point to problems of spatial scaling (satellite pixel resolution vs. farm terrain heterogeneity) and to the difficulty of transferring regional albedo to effective albedo for a specific geometry [14,16].

An onsite approach potentially offers the highest resolution and best representativeness for a specific project, but it introduces metrological requirements such as the selection and calibration of sensors, mounting height, representativeness of the field of view, and the impact of shading and terrain obstacles. Publications devoted to the uncertainty of estimating bifacial gain indicate that the albedo measurement strategy can make a measurable contribution to the uncertainty of predicted energy production, and thus to the financial risk of the project [15]. Similarly, metrological reports and studies emphasize that in systems with non-uniform ground surfaces (e.g., albedo-boosting materials, buildings, agrivoltaics), it may be reasonable to treat albedo as a spatially varying quantity and to estimate its average from grid-based measurements [17]. In this context, the "map" approach becomes justified: instead of a single albedo value (constant or monthly), albedo is considered as a spatial field changing over time. Imaging and mapping methods for albedo are being extensively developed for the needs of geophysics, agriculture, and climatology, for example using UAVs and photogrammetric techniques. For example, Refs. [18,19] present a workflow for estimating landscape albedo from UAV cameras and comparing it with Landsat data, as well as the concept of a multi-sensor UAV payload for albedo and spectral measurements with high spatial resolution. For European conditions, studies demonstrating the mapping of the albedo of the active surface during the growing season based on UAV and satellite data [20] are also of interest.

Horizontal single-axis trackers (HSAT) introduce an additional degree of freedom, namely the time-dependent angular position of the photovoltaic modules. This dynamic reorientation leads to temporal variations in both the incident direct irradiance and the reflected or diffuse components of solar radiation [7,21]. Research on tracker control algorithms includes both classical approaches (algorithms and backtracking implementations in large-scale farms) and more recent developments (backtracking that takes terrain shape into account, and movement optimization with respect to the diffuse component) [22–24]. Research indicates that "smart tracking" can offer additional energy benefits by adjusting the angle to make better use of diffuse radiation and to reduce adverse shading and mismatch effects [21]. The literature also presents control algorithms that explicitly take bifacial parameters and albedo into account when optimizing tracker motion [25].

In the comparative literature, two main modelling approaches are distinguished: (i) models based on configuration factors (view factors, usually 2D and assuming "infinite" rows), and (ii) models based on ray tracing (3D representation of geometry and ray tracking). Validation studies based on field measurements consistently demonstrate that forecasting accuracy is sensitive, among other factors, to ground clearance, surface albedo, the fraction of diffuse irradiance, and installation and construction details. Investigations assessing the correspondence between simulations and empirical data for both fixed-tilt and horizontal single-axis tracking (HSAT) systems document the achievable level of convergence as well as the typical discrepancies among modelling tools and their respective error sources [26–28].

At the level of computational tools, a significant contribution to the popularization of ray tracing in PV was made by the bifacial radiance package, described in the literature

https://doi.org/10.3390/en19112641

as an open tool for simulating bifacial PV systems using the RADIANCE engine [29]. In parallel, hybrid models are being developed (e.g., 3D view factor with deterministic shadow geometry), an example of which is the DUET model, designed to determine irradiance profiles while accounting for non-uniformities and subsequently combining I–V characteristics in order to capture mismatch effects [30].

A special class of effects are interactions between structural elements. The torque tube and the supporting elements of trackers generate both shadows on the rear side and reflections (sometimes beneficial, sometimes detrimental), which change the local irradiance distributions and can reduce or increase mismatch. Studies of torque tube parameters indicate a significant impact of geometry (axis height, installation gaps) on rear-side irradiance and on rear-side shading losses [31]. Conversely, studies focused on optical reflections from the torque tube in tracked bifacial photovoltaic systems have demonstrated that such reflections can influence both the instantaneous energy yield and inter-string mismatch. Moreover, and of relevance to the present work, this effect is typically evaluated over an extended temporal horizon and may exhibit dynamic behaviour [32].

The literature review shows that there is a large number of articles concerning global yield and LCOE analyses for monofacial/bifacial and fixed-tilt/tracking configurations [3,6], validation of rear POA and bifacial gain models for selected geometries and locations [26–28], as well as the development of simulation tools (VF, RT, hybrid) and mismatch loss modelling [29–31]. In addition, the development of perovskite bifacial photovoltaic modules is the subject of articles [33].

However, the available reports synthesizing the state of knowledge on bifacial trackers and rear POA irradiance metrology emphasize that reliable "closure" of the energy balance for bifacial tracking is limited by the simultaneous variability of geometry (tracker motion), shading (rows and structural elements), and albedo (in time and space) [4,7,17]. In practice, many analyses treat albedo as a constant (or monthly) value, and the spatial distributions of reflected radiation are, at best, indirectly estimated from models rather than from direct field measurements [13,15].

On the basis of a review of the available studies, two particularly significant gaps can be identified that directly justify the topic of this article:

- First, the literature is dominated by averaged approaches (annual/monthly), whereas short-term power profiles (instantaneous power generation) are published less frequently.
- Secondly, despite the existence of field studies comparing monofacial and bifacial modules, there is a lack of experiments in which a monofacial and a bifacial module operate on the same tracker and in the same geometry (allowing the influence of the module technology to be separated from the influence of the tracking and shading algorithm), which ensures not only comparable but practically identical conditions.

This prompted the authors to conduct comparative research focused on analysing the instantaneous power delivered by classic and bifacial panels. The authors' unique contribution, therefore, is the analysis of energy yields conducted under the same solar radiation conditions, using classic and bifacial panels with identical technical parameters. The research was conducted in several locations to compare the effect of albedo on instantaneous power generation.

2. Materials and Methods

For the purposes of the research, an experimental setup was developed for the parallel testing of monofacial and bifacial photovoltaic modules. Its design makes it possible to evaluate the operating parameters of both solutions under identical environmental conditions, while maintaining the same exposure to solar radiation. This system makes it possible to directly compare the performance of both types of modules, while at the

https://doi.org/10.3390/en19112641

same time measuring albedo. An additional advantage is its mobility, which makes it possible to conduct research on various types of substrates. The modules were mounted on a single-axis solar tracker, which makes it possible to analyze energy yield for different positions relative to the sun. This solution provides more reliable comparative results and significantly shortens the measurement time.

To avoid ambiguity, the term identical operating conditions refers to the external boundary conditions of the experiment, including the same tracker position, module orientation, mounting structure, measurement time, front-side irradiance exposure, and ambient conditions. Full optical equivalence of the rear-side irradiance field was not assumed, because only the bifacial module converts rear-side radiation into electrical power. However, both modules were exposed to the same surrounding surfaces, support structure, tracker-induced shading, and environmental conditions during each measurement series. Therefore, the experiment compares the actual electrical response of the standard and bifacial modules under matched field conditions, including the real influence of reflected irradiance and structural shading.

2.1. Mobile Laboratory Stand

The mechanical system of the test stand (Figure 1) was mounted on a mobile platform, which made it possible to conduct research for different types of surfaces and in various locations. The structure was equipped with a single-axis tracking system, in which automatic control was implemented solely in the horizontal axis, corresponding to changes in azimuth with respect to the position of the Sun. The range of automatic positioning is from −60° to +60° relative to the direction of incoming solar radiation, where a deviation of −60° corresponds to the east direction and +60° to the west direction. The tilt angle of the modules can be set manually in the range from 0° (flat) to 90° (vertical). This method of movement control enables analysis of the impact of both azimuth and, to some extent, tilt on instantaneous energy generation and the albedo coefficient.

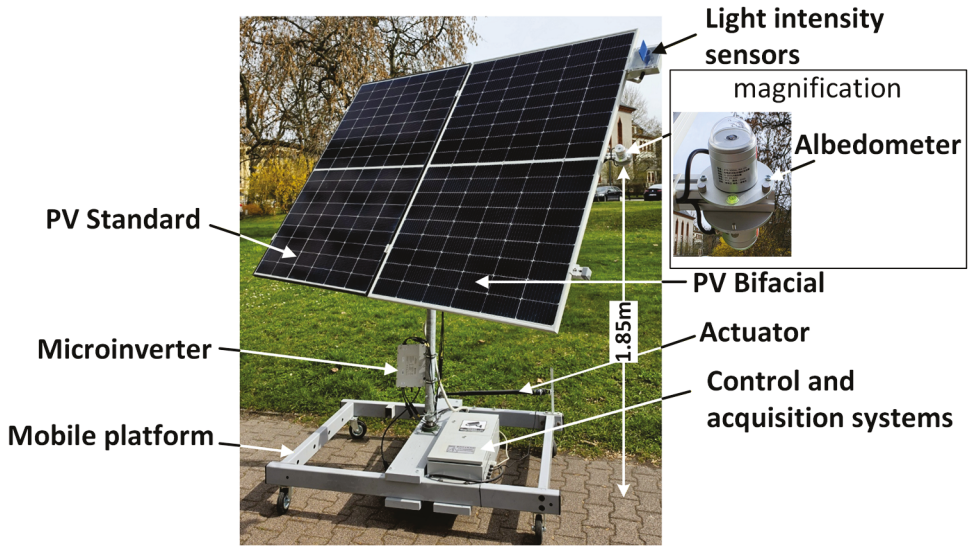

Figure 1. Mobile laboratory stand with PV modules and the single-axis positioning system.

Control in the horizontal axis is implemented using a linear actuator. Motion control is based on signals from two LDR light-intensity sensors (Okystar, Shenzhen, China) operating in a differential configuration. These sensors are housed in a single enclosure, and their operation is separated by an opaque screen that serves as an optical barrier. The screen prevents mutual interference between measurements taken by both sensors by eliminating disturbances caused by reflected or scattered light. In addition, the screen

https://doi.org/10.3390/en19112641

limits the admission of light coming from outside the main direction of incidence, which makes it possible to obtain more precise results. The system is implemented in the form of a compact housing (Figure 2), which contains the light sensors and the screen. The housing protects the sensors from adverse weather conditions such as rain and dust, while ensuring stable measurement results. This solution provides automatic tracking of the apparent motion of the Sun along the horizontal axis, while maintaining a simplified and repeatable manual procedure for setting the tilt angle.

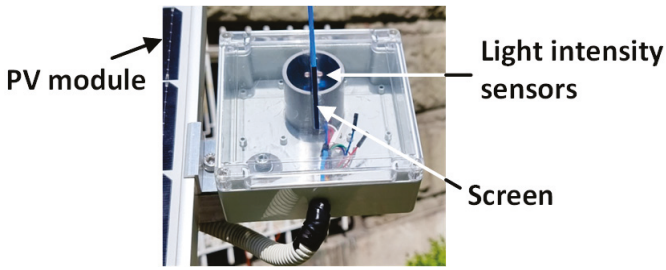

Figure 2. Light intensity sensor with screen for positioning system.

The control and measurement part of the workstation consists of a SIMATIC S7-1200 PLC (Siemens, Munich, Germany) cooperating with the distributed ET200 input/output system (Siemens, Munich, Germany). This setup performed both the actuator control functions and the acquisition of measurement data from the DC and AC channels. On the DC side of each PV module, the output voltage and current were recorded. The current was measured using LA25-NP transducers (LEM, Meyrin, Switzerland), while the voltage was measured using LV25-P transducers (LEM, Meyrin, Switzerland). Similar measurement circuits were also used to record the actuator's current and voltage, which makes it possible to monitor the operating state of the executive system and analyze its load during position changes. The signals from the transducers were fed directly to the PLC data acquisition system, which ensured synchronous recording of the electrical parameters of the test stand and the albedo calculations (Figure 3). Sampling time of the PLC system was 100 ms.

For converting the electrical energy generated by the PV modules, a HMS-1000-2T microinverter (Hoymiles, Hangzhou, China) [34] was used. It is equipped with two inputs that enable independent maximum power point tracking for each PV module. Such a solution eliminates the influence of the common operating point on the DC side and allows for a direct comparison of the performance of the monofacial and bifacial modules under the same irradiation conditions. On the AC side, the measurement of energy fed into the grid was performed using an energy meter communicating with the master system via the RS-485 interface. The applied architecture enables simultaneous recording of instantaneous parameters on the DC side and on the AC side.

A useful feature of the developed test stand is the ability to measure the albedo coefficient of the ground surface. This measurement was carried out using two sensor channels with a ZTS-300AL-RA-120 type albedometer (Mertani, Yogyakarta, Indonesia), enabling simultaneous measurement of incident radiation and radiation reflected from the ground. This made it possible to determine the instantaneous albedo value directly at the research site and to correlate this quantity with the instantaneous energy production of the bifacial module. Integrating the albedo channel into the common data acquisition system allowed for synchronous analysis of the relationships between the module mounting geometry, radiation conditions, and the electrical parameters of the system.

Before starting the series of measurements, all key measurement channels were calibrated. The energy meter was calibrated using a PQM-707 power quality analyzer (Sonel, Świdnica, Poland). The voltage and current measurement channels, built using LEM LA25-

https://doi.org/10.3390/en19112641

NP (LEM, Geneva, Switzerland) and LEM LV25-P transducers (LEM, Geneva, Switzerland), were calibrated with PC5000a multimeters (Sanwa Electric Instrument Co., Ltd., Japan, Tokyo). The radiation and albedo measurement channels were calibrated using a IRM-1 solar irradiance meter (Sonel, Świdnica, Poland). The adopted calibration procedure made it possible to reduce systematic errors and ensure the comparability of results obtained for different positions of the test stand and different types of ground surface.

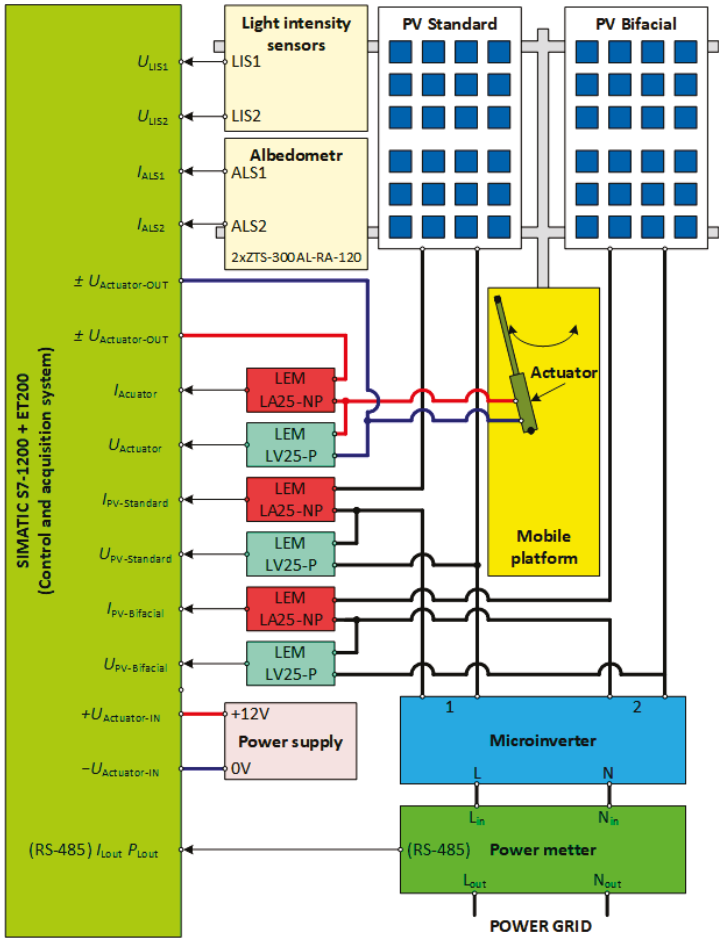

Figure 3. Control and data acquisition system architecture for a mobile laboratory stand.

2.2. Microinverter and PV Module

The Hoymiles HMS-1000-2T microinverter is designed to work with two photovoltaic modules and provides independent maximum power point tracking (MPPT) for each DC input. The microinverter has a rated output power of 1000 VA, allowing it to operate with modules in the 400–670+ W power range. It uses a passive cooling system based on natural convection, eliminating the need for fans. Detailed technical specifications of the microinverter are presented in Table 1.

The microinverter communicates wirelessly with the DTU-Pro-S gateway, which transmits data to the S-Miles Cloud monitoring system (Hoymiles, Hangzhou, China). This solution enables remote supervision of the device's operation, regardless of the measurement and data acquisition system used at the test stand. It should be noted, however, that standard data logging in the DTU-Pro-S is performed with limited time resolution, i.e., every 15 min. Access to the data is possible both via a web interface and a mobile application. The application, when directly connected to the DTU-Pro-S or using the S-Miles Toolkit tool (Hoymiles, Hangzhou, China), also enables the reading of current values and alarm signals. Example screenshots from the application, corresponding to low and high energy

https://doi.org/10.3390/en19112641

production, are shown in Figure 4. It can be observed that the bifacial module connected to port 2 generates instantaneous power that is higher by 12.5% and 4.5%, respectively, for the analysed cases of low and high energy production. This method of presenting electrical parameters is sufficient for monitoring the standard operation of the system in photovoltaic installations; however, it limits research capabilities. Therefore, the measurements used for the comparative analysis of module operation are based on the calibrated measurement paths of the test stand and the data acquisition system.

Table 1. Technical specifications of the Hoymiles HMS-1000-2T microinverter [34].

Parameter	Hoymiles HMS-1000-2T
Commonly used module power, W	400 to 670+
Maximum input voltage, V	65
MPPT voltage range, V	16–60
Start-up voltage, V	22
Maximum input current, A	2 × 14
Maximum input short-circuit current, A	2 × 20
Number of MPPTs	2
Number of inputs per MPPT	1
Rated output power, VA	1000
Peak efficiency, %	96.7
Nominal MPPT efficiency, %	99.8
Night power consumption, mW	<50
Type of isolation	Galvanically isolated HF transformer
Cooling	Natural convection, fanless
Communication	Sub-1G
Monitoring	Hoymiles S-Miles Cloud





Micro-SN：114472822375
Data Update Time：2025-04-26 15:22:30
Input Port1
PV Current：1.71A PV Voltage：31.5V
PV Power：54.1W
Input Port2
PV Current：1.96A PV Voltage：31V
PV Power：60.9W
Output Port
Grid Voltage：230.2V Grid Frequency：50Hz

(**a**)

Micro-SN：114472822375
Data Update Time：2025-04-26 14:52:30
Input Port1
PV Current：13.72A PV Voltage：30V
PV Power：412.2W
Input Port2
PV Current：13.99A PV Voltage：30.8V
PV Power：430.7W
Output Port
Grid Voltage：233.8V Grid Frequency：50Hz

(**b**)

Figure 4. Actual inverter readout for: (**a**) low; (**b**) high energy production.

https://doi.org/10.3390/en19112641

The research stand was equipped with two photovoltaic modules from Jolywood: the monofacial module JW-HT108N-415W and the bifacial module JW-HD108N-415W (Jolywood Solar Technology, Taizhou, China). Both modules use n-type monocrystalline cells, which makes their basic electrical parameters on the front side similar. Under standard test conditions (STC), the rated front-side power of both modules is 415 W. For both modules, the voltage at the maximum power point is 31.7 V and the open-circuit voltage is 37.7 V. The fundamental difference between them results from their mechanical design and from the fact that the JW-HD108N module also enables conversion of radiation reaching the rear side.

The higher power of the bifacial module results from its ability to use reflected light, which provides an advantage in installation conditions that favour a high albedo coefficient; for example, it increases to 448 W (for an albedo of approx. 30%). Electrical parameters such as MPPT voltage (31.7 V), open-circuit voltage (37.7 V), MPPT current (13.10 A for the monofacial module and 14.13 A for the bifacial one) and short-circuit current (13.91 A for the monofacial module and 14.99 A for the bifacial one) make these modules comparable. The difference in currents stems from the additional energy yield generated by the bifacial module. The modules have identical cell dimensions (182.0 × 91.0 mm) and overall dimensions (1728 × 1134), which allows them to be used with the same mounting structures. However, a difference appears in weight. The bifacial module weighs 24.5 kg, whereas the monofacial module weighs 22.5 kg. This is due to the use of double glass in the bifacial module, which increases its durability but at the same time adds load to the structure.

The temperature coefficient for power, which specifies the decrease in power with increasing temperature, is −0.320%/°C for the monofacial module and −0.310%/°C for the bifacial module. The bifacial module is therefore characterized by slightly better temperature stability. Selected parameters of the modules used in the test stand are listed in Table 2.

Table 2. Comparison of the monofacial and bifacial Jolywood modules used in the test stand [35].

Parameter (STC *)	415W JW-HT108N	415W JW-HD108N
Type	N-type monocrystalline, half-cell, single-glass	N-type bifacial, dual-glass
Rated front-side power, W	415	415
Example power at 10% rear-side gain, W	–	448 **
MPP voltage, V	31.7	31.7
MPP current at front-side STC, A	13.10	13.10
MPP current at 10% rear-side gain, A	–	14.13 **
Open-circuit voltage, V	37.7	37.7
Short-circuit current at front-side STC, A	13.91	13.91
Short-circuit current at 10% rear-side gain, A	–	14.99 **
Efficiency, %	21.18	21.18
Cell dimensions, mm	182.00 × 91.00	182.00 × 91.00
Number of cells	108 (12 × 9)	108 (12 × 9)
Module dimensions, mm	1728 × 1134 × 35	1728 × 1134 × 30
Front/rear glass thickness, mm	3.2/–	2.0/2.0
Weight, kg	22.5	24.5
Temperature coefficient of Pmax, %/°C	−0.320	−0.310

* Standard test conditions: irradiance 1000 W/m^2, cell temperature 25 °C, AM 1.5. ** Values corresponding to an example of 10% additional power gain (albedo 30).

In the first stage of the research, measurements of the electrical parameters of both photovoltaic modules were carried out during the execution of a forced motion sequence

https://doi.org/10.3390/en19112641

of the positioning system. The purpose of this part of the experiment was to verify the correct operation of the control system and the measurement path, as well as to assess the behaviour of both modules with varying orientation relative to the direction of incident solar radiation. The sequence lasted 500 s and included successive changes in the position of the modules: starting from the reference position of 0° with respect to the Sun, moving west to +60°, then moving east to −60°, returning to the 0° position, moving again to +60°, and a final return to the reference position. The time required to complete the full movement over the 120° range was approximately 105 s. This motion dynamics ensured smooth operation of the system and limited the influence of transient states resulting from changes in the orientation of the modules. At higher positioning speeds, these disturbances would have to be compensated by the MPPT systems assigned to the individual inputs of the microinverter. The voltage, current, and power waveforms of both modules, recorded with a time step of 100 ms, are shown in Figure 5.

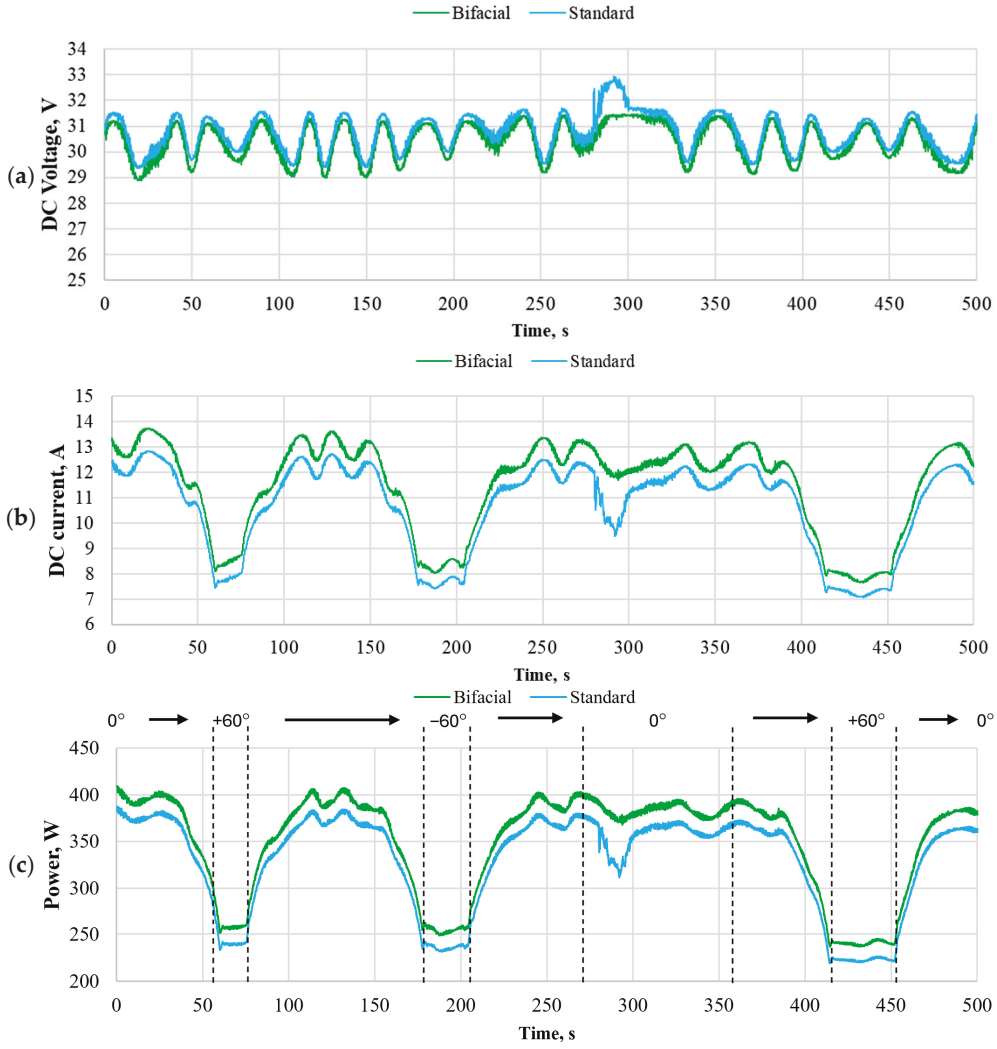

Figure 5. Waveforms of: (**a**) voltage, (**b**) current and (**c**) module power for the forced motion sequence of the positioning system relative to the Sun's position (0°).

The voltage changes of both modules were relatively small and resulted mainly from the operation of the maximum power point tracking algorithm. The voltage fluctuations did not exceed approximately ±2 V, while the difference between the monofacial and bifacial modules reached at most about 1 V. The short-term increase in voltage observed in the 280–300 s interval was associated with a temporary deterioration of irradiance conditions, most likely due to passing cloud cover. Much more pronounced changes concerned the

https://doi.org/10.3390/en19112641

output current, especially during transitions between successive positions of the modules. Throughout the entire analysed range, the bifacial module generated a current higher by about 0.5–1.0 A compared to the monofacial module, which should be attributed to the additional absorption of radiation by its rear surface. For a change in position of a full 120°, the current of both modules varied approximately in the range of 10–14 A. Temporary cloudiness resulted in a significant reduction in current values, with this effect being more pronounced for the monofacial module.

The power profiles reflected the combined changes in voltage and current. At the extreme positions, the power decreased to about 250 W, while near the optimal position it exceeded 400 W. Throughout the entire investigated range, the bifacial module mounted on grass achieved a power output about 5–10% higher compared to the monofacial module. Over the entire analysed range of this verification test, the average measured power output increase of the bifacial module was 6.1% compared with the monofacial module.

This difference was particularly evident during short-term variations in irradiance conditions, which indicates that the bifacial module makes more effective use not only of the direct component, but also of reflected and diffuse radiation.

2.3. Albedo Measurements

Measurements of the albedo coefficient were carried out at a test stand with a single-axis tracking system, under the conditions shown in Figure 6. The measurement campaign was conducted on 12 March 2026, around midday, under high solar irradiance and an ambient temperature of approximately 20 °C. Stable atmospheric conditions prevailed during the measurements. The sky was mostly clear, with only small clouds observed locally near the horizon, which did not cause periodic shading of the solar disk or significant changes in the direct radiation component. The adopted conditions can therefore be considered representative for analysing the influence of module orientation and tracker position on the distribution of effective albedo.



Figure 6. View of the measurement site used for albedo measurements on a grass surface.

The measurements were carried out over the full analysed range of tracker motion, described by the relative solar azimuth from −60° to +60°, in 5° increments. Additionally, a measurement series was performed for seven values of the module tilt angle, covering the range from 0° to 90°. This selection of the measurement grid made it possible to determine the two-dimensional distribution of albedo as a function of two basic geometric parameters, i.e., the relative azimuth with respect to the direction of incident radiation and the tilt angle of the active surface of the module. The adopted measurement resolution represents a compromise between the accuracy of reproducing spatial variations and the time required to carry out the entire campaign under the most stable possible insolation conditions.

The total time needed to carry out the entire measurement series was about 30 min. Limiting the duration of the experiment was of significant methodological importance, as it

https://doi.org/10.3390/en19112641

reduced the impact of changes in the Sun position and slow atmospheric variations on the comparability of successive measurement points. Since the series was performed around midday, under stable irradiance conditions, without observed cloud transients or periodic shading of the solar disk, the resulting data set was treated as quasi-stationary from the point of view of the experimental boundary conditions. Therefore, the obtained albedo distributions should be interpreted as geometry-dependent values representative of the specific short-term field conditions during the measurement campaign.

To visualize the spatial distribution of albedo, a heat map was used, created on the basis of a discrete matrix of measurement data defined at grid nodes corresponding to successive azimuth and tilt values. In the analysed case, the grid step was $\Delta x = 5^\circ$ in the azimuth direction and $\Delta y = 15^\circ$ in the tilt direction. To obtain a continuous and clear graphical representation, as in Figure 7, two-dimensional bicubic interpolation was applied. It should be emphasized that in order to improve the visualization quality of the albedo distribution the bicubic interpolation was used solely at the stage of presenting the results. It did not constitute a stage of filtering or modifying the source data. This means that the input values used for the analysis remained consistent with the original measurement matrix, and the smoothing concerned only the method of determining values between grid points during the rendering of the heat map.

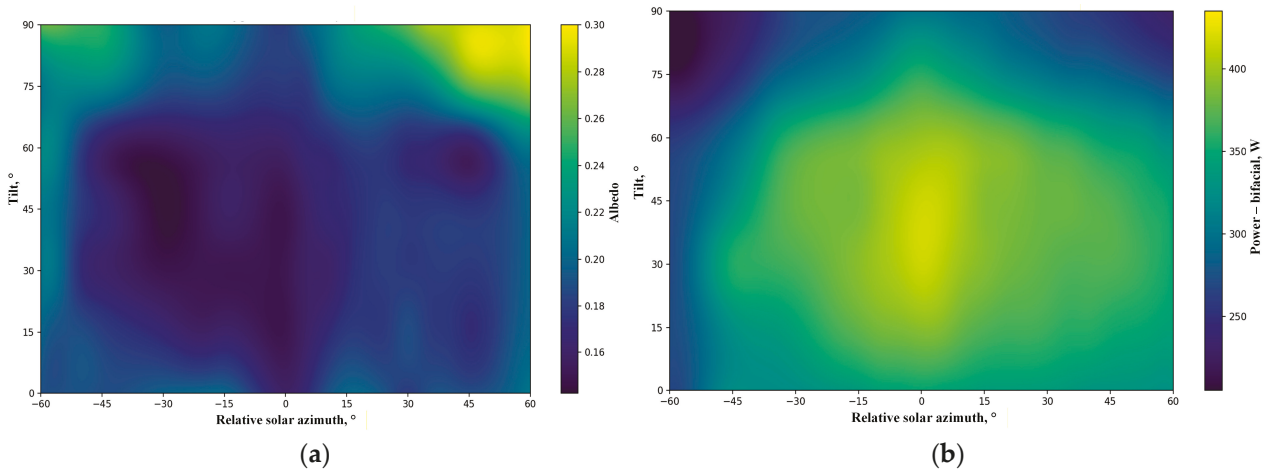

Figure 7. Heatmaps of: (**a**) albedo; (**b**) bifacial module power output as a function of relative solar azimuth and tilt angle.

The obtained heat maps confirm that for a grass-covered ground, the albedo coefficient cannot be treated as a constant surface property, but rather as an effective parameter of the module–ground system, dependent on the geometry of the tracker configuration. In the analysed range of relative solar azimuth from -60° to $+60^\circ$ and for module tilt from 0° to 90°, a clearly non-uniform, two-dimensional distribution of albedo was determined. The map shows that the albedo values varied over a wide range, approximately from about 0.15 to 0.30. The lowest values were observed mainly for negative relative azimuths and tilt angles of about 30–60°, whereas the highest values occurred for large tilts and positive relative azimuths, particularly in the region of about $+45^\circ$ to $+60^\circ$ and 75–90°. This means that the amount of reflected radiation available to the rear side of the bifacial module was strongly dependent on the system orientation, and the albedo distribution was clearly anisotropic in character.

However, the power distribution of the bifacial module shows a different character than the albedo distribution. The maximum generated power occurred for a relative azimuth close to 0°, that is, for a setup most similar to the optimal orientation of the front side with respect to the direction of incidence of direct radiation. The highest power values

https://doi.org/10.3390/en19112641

were observed for tilt angles of about 30–50°, while a deviation of the system from an azimuth of 0° caused a gradual decrease in production, especially for larger tilts. This result is of significant interpretative importance: although the albedo of grass showed considerable variability in the two-dimensional measurement grid and locally reached elevated values, the additional gain from the rear side did not compensate for the losses resulting from the deterioration of the operating conditions of the front side of the bifacial module when departing from the optimal orientation with respect to the Sun. In other words, under the conditions analysed, the dominant influence on the instantaneous energy production was still exerted by the direct component of the radiation incident on the front of the module, while the contribution of reflected radiation acted as an addition, increasing the yield, but not sufficient to shift the production maximum away from the position corresponding to a relative azimuth of 0°.

At the same time, the results confirm the positive impact of bifacial technology across the entire analysed operating range. The average increase in production of the bifacial module compared to the standard module was 6.8%, which means that even for a surface with moderate albedo, such as dry grass, the energy harvested by the rear side of the module constituted a significant component of the overall energy balance. However, this increase was additive rather than compensatory, i.e., it boosted production across the entire range of analysed configurations, but did not eliminate losses resulting from a non-optimal orientation of the module with respect to the Sun.

As a further development of the analysis based on the heat maps, Figure 8a presents the albedo profiles for individual module tilt angles as a function of the relative solar azimuth. A clear dependence of the albedo coefficient on the system geometry is visible, with the curves for different tilts being neither parallel nor symmetric with respect to the 0° position. For small tilt angles, especially 0° and 15°, the variation of albedo as a function of relative solar azimuth is limited, and the values remain clustered within a relatively narrow range. As the tilt angle increases, both the amplitude of the changes and the diversity of the shapes of the characteristics grow. The greatest variability is observed for a tilt of 90°, for which the albedo increases from about 0.22 at negative azimuths to nearly 0.30 at extreme positive azimuths. For a tilt of 75°, the profile has a similar character, although with a slightly lower maximum.

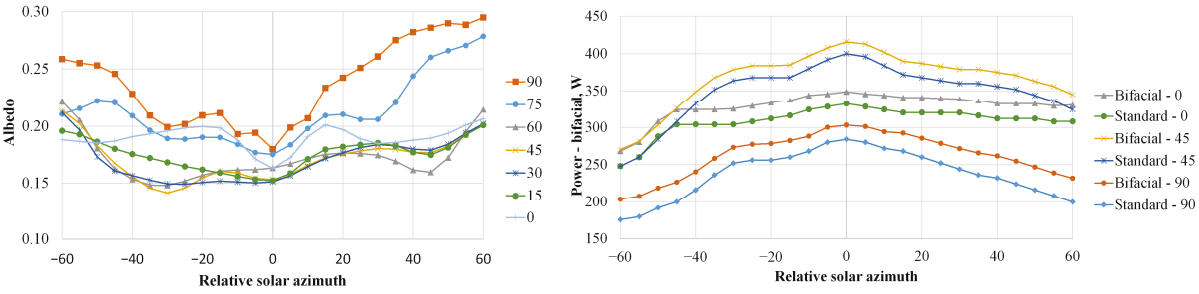

(**a**) (**b**)

Figure 8. Dependence on relative solar azimuth: (**a**) albedo for selected tilt angles; (**b**) bifacial and standard module power output for tilt angles of 0°, 45°, and 90°.

Figure 8b shows the power distributions corresponding to these conditions for tilt angles of 0°, 45°, and 90°, separately for the standard and bifacial modules. The power maximum for both technologies occurs near a relative solar azimuth of 0°, which confirms that, in the analysed case, the most energetically favourable position is determined primarily by the irradiation conditions on the front side. The highest power values were obtained for a tilt of 45°, for which the bifacial module reached values exceeding 420 W, while the

https://doi.org/10.3390/en19112641

monofacial module reached about 400 W. For a tilt of 0°, the characteristics are clearly more flattened, and the power variation with respect to azimuth is smaller. In turn, for a tilt of 90°, the lowest power levels and the greatest sensitivity to changes in orientation relative to the Sun were recorded.

Across the entire analysed range, the bifacial module generated more power than the standard module; however, this advantage did not cause the production maximum to shift away from the central position.

The main objective of the measurement series was to determine the relationship between the power output of the bifacial and standard modules, as well as to estimate the gain in yield resulting from the use of bifacial technology. The experiment was conducted in two operating modes. For approximately two-thirds of the time, the modules operated in automatic solar tracking mode, while during the remaining time forced changes in orientation were carried out in order to obtain data for different tilt angles. The parameters were recorded with high temporal resolution, at a 100 ms interval, which also made it possible to analyse the results under dynamically changing illumination conditions. Figure 9 shows the relationship between the instantaneous power of the bifacial module and the instantaneous power of the standard module.

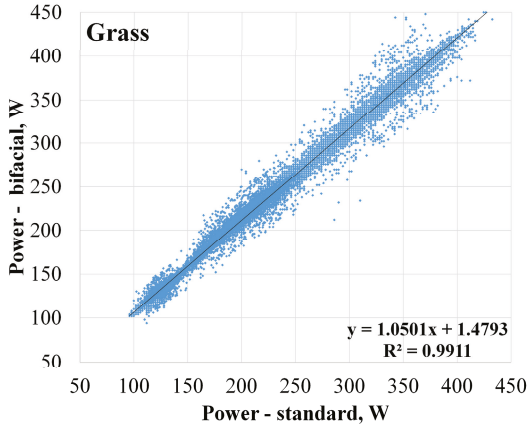

Figure 9. Relationship between bifacial and standard module power for the grass surface.

The analysis of the obtained results confirmed that the bifacial module achieved a higher instantaneous power than the monofacial module over the entire considered operating range. Based on the distribution of the measurement points, a linear approximating function was determined, yielding a very good fit to the experimental data, described by the coefficient of determination $R^2 = 0.9911$.

A slope coefficient of 1.0501 indicates that, over the entire measurement range, the power of the bifacial module was on average about 5.2% higher than that of the standard module. The positive intercept means that the relative advantage of the bifacial module is greater at lower power levels. Consequently, for the power range from about 100 to 400 W, the average power gain of the bifacial module can be estimated at around 6%. At a power level of about 100 W, the advantage of the bifacial module was around 6.5%; for the 200–300 W range it was about 5.5–5.8%; and at the maximum power of about 420 W it was around 5.3%.

The applied methodology creates a coherent research environment in which the impact of the module's technology, the geometry of the setup, and the local radiation conditions on instantaneous energy production can be reliably separated. The key value of this approach lies in combining the mobility of the test stand, the shared working geometry of both modules, independent MPPT paths, and synchronous measurement of electrical parameters and albedo. This makes it possible to move from simplified, literature-based

https://doi.org/10.3390/en19112641

averaged assumptions to a direct field assessment of the short-term effects of bifacial module operation on the same tracker and over different types of ground surfaces. In this sense, the mobile test stand and the adopted research method fulfil the objectives set out in the introduction, namely they enable an analysis of the actual impact of albedo, orientation, and tracking system motion on instantaneous energy yield, while maintaining a high comparability of experimental conditions.

3. Results

The grass case (Figures 7 and 9) is treated as the reference, and analogous observations for the remaining four surfaces are compiled in Appendix A (photographs of the locations) and on comparative maps and charts (Figures A2 and A3). The analysed types of ground surface include:

- River sand—light sand (a mineral surface with increased albedo);
- Grey paver—grey paving blocks (artificial surface with moderate albedo);
- light aggregate—light aggregate (high-reflectivity surface);
- dark aggregate—dark aggregate (the surface with the lowest reflectivity in the tested set).

In practice, this means that the share of reflected radiation reaching the rear side of the bifacial module was analysed for surfaces with extremely different properties.

Figure 10 shows the measured albedo values as a function of the relative solar azimuth for a constant module tilt of 45° and five types of ground surface. This figure represents a selected cross-section of the two-dimensional albedo distributions at a fixed tilt angle of 45°, extracted from the full azimuth–tilt measurement maps. Therefore, the values shown in Figure 10 should not be interpreted as the maximum albedo values over the entire tilted range investigated. The maximum albedo depends strongly on the module tilt angle. For example, in the grass case shown in Figure 7, values close to 0.30 occur at large tilt angles, mainly 75–90°, which are outside the fixed-tilt condition analyzed in Figure 10.

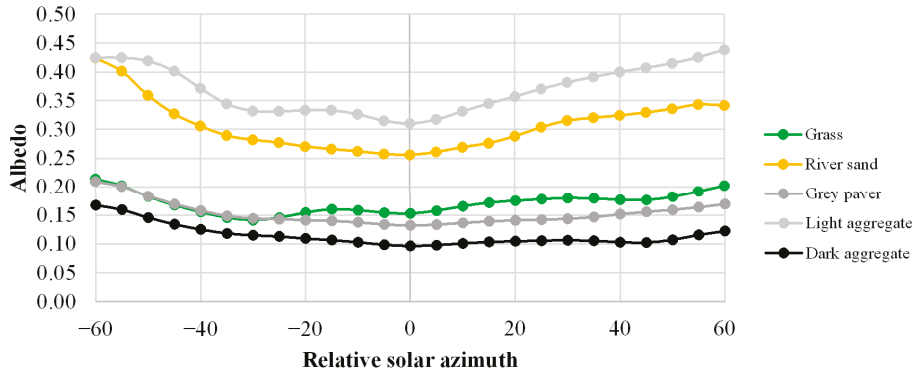

Figure 10. Measured albedo as a function of relative solar azimuth for a module tilt angle of 45° across five surface types.

The resulting characteristics confirm a clear differentiation in the reflective properties of the analysed surfaces. Across the entire azimuth range, the highest albedo values were recorded for light aggregate, for which the albedo coefficient varied approximately from 0.31 to 0.44. Slightly lower values were obtained for river sand, in the range of about 0.25–0.42. Surfaces with moderate reflective properties were represented by grass and grey paver, for which the albedo was approximately in the ranges 0.14–0.20 and 0.13–0.17, respectively. The lowest values, over the entire analysed range, were obtained for dark aggregate, where the albedo remained at about 0.10–0.12.

https://doi.org/10.3390/en19112641

For all examined surfaces, a similar pattern of variation is visible, with a minimum occurring near the relative azimuth from about −20° to 0°, and higher values for large positive and negative azimuths. The characteristics therefore have a shape similar to a broad "U" curve, although their shape is not perfectly symmetrical with respect to the central position. This effect is particularly evident for light aggregate and river sand, where, after passing through the minimum, there is a systematic increase in albedo up to the extreme values. For grass, grey paver, and dark aggregate, the amplitude of the changes is smaller, but the direction of change remains the same.

It should be emphasized that the observed increase in albedo with a change in relative azimuth does not imply an absolute increase in the amount of radiation reflected from the ground. It results primarily from the definition of albedo as the ratio of reflected radiation to incident radiation. As the system deviates from the position of the Sun, the intensity of radiation on the front side, which constitutes the denominator of this ratio, decreases, while the reflected component does not change proportionally to the same extent. As a result, the value of the albedo coefficient increases, even though the total level of irradiance available to the module does not necessarily increase (Figure 10; analogously Figures A2 and 7). This is important for the interpretation of the results, because higher albedo at larger azimuth deviations does not necessarily lead to an increase in energy production.

These results therefore indicate that even for a fixed tilt of 45°, albedo cannot be treated as a constant parameter assigned solely to the type of ground surface. Its value also depends on the geometry of the system's configuration with respect to the Sun, as well as on the relationship between the reflected and direct components of the radiation. At the same time, the ordering of the surfaces in terms of albedo level is consistent with the previously observed differences in the energy yield of the bifacial module. The highest albedo for light aggregate and river sand corresponds to the highest gains in production, while the lowest albedo for dark aggregate translates into the smallest bifacial effect. Figure 10 therefore provides direct confirmation that, at a tilt of 45°, the reflective properties of the ground remain one of the key factors shaping the additional yield of a bifacial module, although their interpretation requires considering the geometric definition of the albedo coefficient itself.

Figure 11 shows the power of the bifacial module as a function of the relative solar azimuth for a fixed tilt angle of 45° and for the five analysed types of ground surface. All characteristics have a similar shape and exhibit a clear maximum near a relative azimuth of 0°, which confirms that for this mounting geometry the highest energy yield occurs when the position is closest to perpendicular incidence of radiation on the front side of the module. As the deviation from this position increases, both toward negative and positive azimuths, the power gradually decreases, with the drop being particularly evident for the extreme positions.

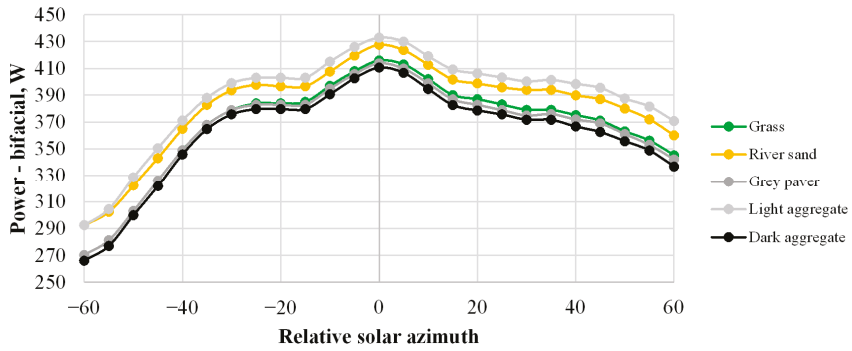

Figure 11. Power output of bifacial modules vs. relative solar azimuth (tilt angle 45°) for five ground surfaces.

https://doi.org/10.3390/en19112641

The highest power values across the entire analysed range were obtained for the light aggregate surface, for which the maximum exceeded 430 W. Slightly lower values were recorded for river sand, while the next group consisted of grass and grey paver, whose characteristics were very close to each other in the middle azimuth range. The lowest power values across the entire range were obtained for dark aggregate. This means that with a constant tilt of 45°, the type of ground surface still significantly affects the energy production of the bifacial module, and the differences between the surfaces are preserved over practically the entire range of changes in the relative azimuth.

These results are consistent with the earlier albedo analysis for the same tilt angle. Surfaces with a higher reflectance coefficient, especially light aggregate and river sand, provide a greater share of radiation reaching the rear side of the module, which translates into higher instantaneous power values. At the same time, the shape of all the curves confirms that, despite the positive impact of reflected radiation, the dominant factor determining the position of the production maximum remains the irradiance on the front side. The additional gain resulting from higher albedo increases the power level across the entire operating range, but does not shift the maximum beyond the position corresponding to a relative azimuth of 0°.

Table 3 lists the operating parameters of the bifacial module for two methods of data aggregation. The Full Range variant covers the entire analysed range of operating geometries, i.e., a relative solar azimuth from −60° to +60° and a module tilt angle from 0° to 90°. The Tilt 45° variant, on the other hand, refers to the results obtained for a fixed tilt of 45°, corresponding to the setting closest to perpendicular incidence of solar radiation during the measurements, while maintaining changes in relative azimuth over the same range.

Table 3. Bifacial module power output and production increase compared to standard module across five ground surfaces.

Parameters	Grass	River Sand	Grey Paver	Light Aggregate	Dark Aggregate
			Bifacial—Full Range		
Maximum power, W	415.9	427.6	413.8	432.9	410.6
Minimum power, W	203.6	234.3	207.8	244.7	206.7
Average power, W	333.0	348.2	331.2	355.4	326.9
Increased, %	6.4	11.3	5.9	13.6	4.5
			Bifacial—Tilt 45°		
Maximum power, W	415.9	427.6	413.8	432.9	410.6
Minimum power, W	270.3	292.5	270.3	292.5	266.0
Average power, W	367.8	382.3	365.8	388.8	361.8
Increased, %	5.2	9.3	11.2	11.2	3.5

For the Full Range variant, the highest average power values and the greatest increase in output compared to the standard module were obtained for surfaces with the highest reflective potential. The best results were recorded for light aggregate, for which the average power of the bifacial module was 355.4 W and the production increase was 13.6%. Slightly lower values were obtained for river sand: 348.2 W and 11.3%, respectively. For the remaining surfaces, the bifacial effect was clearly smaller and amounted to 6.4% for grass, 5.9% for grey paver, and 4.5% for dark aggregate. The highest maximum power was also obtained for light aggregate (432.9 W), while the lowest was recorded for dark aggregate (410.6 W).

For the Tilt 45° variant, the same order of surfaces was maintained in terms of average power. The highest value was obtained for light aggregate (388.8 W), followed by river sand

https://doi.org/10.3390/en19112641

(382.3 W), and lower values for grass (367.8 W), grey paver (365.8 W), and dark aggregate (361.8 W). The increase in production compared to the standard module amounted to 11.2% for light aggregate and grey paver, 9.3% for river sand, 5.2% for grass, and 3.5% for dark aggregate. This means that for a 45° tilt the impact of the type of ground surface on the yield of the bifacial module remains distinct; however, its magnitude depends not only on the albedo level itself, but also on the operating geometry of the system.

It is noteworthy that the maximum power values in both parts of the table are identical. This indicates that the global maximum power in the analysed dataset occurred precisely for the tilt angle of 45°. At the same time, the minimum values for the Tilt 45° variant are higher than for the Full Range, which results from the elimination of less favourable tilt configurations.

This form of regression indicates that the relative gain is close to the slope of the line (5% for grass, $\alpha = 1.0501$). The positive intercept suggests a slightly higher relative difference at lower power levels within the analysed dataset; however, this should be interpreted only as an observed tendency under the measurement conditions of this study, not as a separately validated cloudy-sky or full-shade effect.

Analogous relationships for the remaining surfaces are shown in Figure A3 in Appendix A. The slope of the line increases for lighter substrates ($\alpha = 1.1132$; $R^2 = 0.9916$, river sand: $\alpha = 1.0914$; $R^2 = 0.9817$) and decreases for darker ones (dark aggregate: $\alpha = 1.0335$; $R^2 = 0.9941$), which is qualitatively consistent with the albedo distribution and the observed increases in production (Figures A3 and 10, Table 3).

The obtained results indicate three key conclusions that are important for the assessment of bifacial modules under field conditions. The position of the maximum power point is determined mainly by the operating conditions of the front side and occurs near a relative solar azimuth of 0° (Figures A2, 7 and 11; Table 3), while the reflected radiation increases the power level but does not shift the geometric optimum. Albedo is a parameter dependent on geometry. In particular, it increases at large azimuth deviations, largely because the irradiance on the front side decreases (albedo being defined as the ratio of reflected to incident component). It calls for careful interpretation of high albedo values in energetically sub-optimal configurations (Figure 10; analogously Figures A2 and 7).

The gain from bifacial modules depends on the type of ground surface as well as on the geometric configuration. Consequently, a reliable assessment of the benefits of bifacial technology should simultaneously consider the actual albedo and its geometric variability, as well as the distribution of the system's operating geometry, since these two factors determine both the average power level and the range of instantaneous power. This is particularly important for modules operating on trackers.

The results also confirm that the efficiency of a bifacial module is determined both by the reflective properties of the ground and by the geometry of the module's orientation relative to the Sun. Averaging over the full range of azimuth and tilt reduces the observed bifacial effect, whereas for the optimal tilt the advantage of the bifacial module is more pronounced.

4. Discussion

The use of ground-reflected radiation by the rear side of a bifacial module is difficult to describe with a single constant albedo value. The obtained heat maps show that, in tracking systems, effective albedo depends not only on the surface type, but also on the tracker geometry and module tilt angle.

The determined output power distributions for bifacial modules operating above five test surfaces (grass, river sand, grey paver, light and dark aggregate) exhibit a classic, highly symmetrical concentric form, referred to in the literature as the "bullseye" effect.

https://doi.org/10.3390/en19112641

Peak power generation consistently occurs in the central areas of the geometric maps, corresponding to a relative solar azimuth of around 0° (normal incidence of rays, east–west axis) and a module tilt angle within the optimal range of 30° to 60°, depending on the season and time of day. This chart architecture confirms the fundamental principle that the dominant component of system production remains the direct irradiance incident on the front of the module. This relationship shows a direct coupling with Lambert's cosine law for the frontal surface, where illuminance intensity decreases with the cosine of the angle of incidence.

In stark contrast to the phenomenon described above, the heat maps for the albedo coefficient itself show a very different behaviour. They exhibit strong irregularity, a lack of symmetry, and significant spatial noise. The highest recorded albedo values do not coincide with the optimum energy production. On the contrary, the reflection coefficient reaches its extrema at very high sensor tilt angles and at extreme azimuths. Furthermore, the definition of albedo (the ratio of reflected to incident radiation) becomes metrologically distorted. At extreme deviations, the denominator (radiation incident on the frontal plane) tends toward its minimum much faster than the numerator (the sum of radiation reflected from the ground and scattered).

The conclusion that follows from this is extremely important for tracker control logic. Specifically, the tendency of algorithms to position the module based on searching for the maximum albedo point under clear-sky conditions is not justified, because higher albedo at large azimuth deviations does not generate an absolute increase, but only changes the proportion of production between the module sides [16].

However, it should be emphasized that validating the benefits of bifacial technology requires isolating random phenomena from systematic ones. To this end, linear regression models were developed for the collected empirical results from five separate substrates, relating the instantaneous power of a standard module to the power of a bifacial module operating on a shared tracking axis and equipped with independent MPPT paths. The results, expressed in the form of a linear equation, allow for good representation.

The light aggregate provided the highest relative increase in the power of the bifacial module, amounting to 11.3% compared with the standard module. The high regression fit indicates stable and repeatable optical conditions for this surface. This result is consistent with the high reflectance of the bright mineral substrate and the increased rear-side irradiance reaching the bifacial module.

River sand provided one of the highest bifacial gains, with a measured increase of 9.1% compared with the standard module. However, the corresponding regression showed a lower coefficient of determination than for the other surfaces, which indicates a larger scatter of the measured points. Since soil moisture was not measured during the campaign, this scatter cannot be attributed quantitatively to moisture variations. It should rather be interpreted as the combined effect of the natural heterogeneity of the sand surface, local differences in surface texture, possible non-uniform compaction, and uncontrolled environmental conditions during the measurement. Consequently, sandy surfaces can provide a high bifacial effect, but their response should be interpreted with caution when no direct information on surface moisture and local surface condition is available.

The grass surface provided a moderate bifacial gain of 5.0%. This confirms that natural biological surfaces do not necessarily provide a high effective rear-side contribution, even when they appear visually bright. The result can be related to the non-uniform structure of vegetation and partial absorption or scattering within the grass layer. Since moisture and spectral reflectance were not measured directly, these mechanisms should be treated as possible explanatory factors rather than independently verified effects.

https://doi.org/10.3390/en19112641

This result remains consistent with the conclusions of report [17], which indicated that broadband radiometric instruments, such as pyranometers, do not fully reflect the spectral and angular response of silicon photovoltaic cells. For biological surfaces and moist substrates, this may lead to noticeable discrepancies between the measured rear-side irradiance and the actual conversion effect achieved by a bifacial module. For this reason, the direct comparison of the synchronous operation of a standard and a bifacial module, used in the study, should be regarded as a particularly useful approach, as it makes it possible to assess the actual energy effect without the need for indirect inference based solely on irradiance measurements.

Although frequently indicated as a potentially beneficial substrate for installations mounted above parking lots or carports, the grey concrete paver provided only a 4.5% power gain for the bifacial module. This result suggests that the actual optical properties of pavement in operation may significantly differ from the parameters declared for new or laboratory-clean material. Under real operating conditions, concrete and paving surfaces undergo gradual optical degradation due to the deposition of dust, tire wear particles, traffic-related residues, operational soiling, and periodic moisture. These contaminants fill the pores and irregularities of the material, reducing its operational albedo and thus limiting its ability to illuminate the rear side of the module. The relatively small intercept in the regression and the low slope of the characteristic confirm that, in the examined configuration, the paving blocks only moderately reflected light.

The lowest power gain was recorded for the dark aggregate, for which the bifacial module achieved only a 3.35% increase compared with the standard module. At the same time, the regression fit was very high, which indicates that the response of this surface was stable, but consistently unfavourable from the perspective of bifacial module performance. In the present experiment, this result can be directly attributed to the low reflectance of the dark surface and the correspondingly reduced rear-side irradiance. The possible thermal influence of dark substrates was not quantified, because no dedicated surface-temperature or cell-temperature measurements were performed. Therefore, thermal effects should be treated only as a potential secondary mechanism requiring separate experimental verification. Consequently, among the analysed surfaces, dark aggregate should be regarded as the least favourable substrate for bifacial applications primarily due to its low optical reflectance.

Standard IEC 61724-1 defines the effective irradiance received by the module G_{eff} in algebraic form as [36]:

$$G_{eff} = \left(1 + \varphi_{Pmax} \cdot \frac{G_r}{G_{POA}}\right) \cdot G_{POA}, \quad (1)$$

where

φ_{Pmax}—bifacial power coefficient (typically 0.7–0.75)
G_r—rear irradiance
G_{POA}—front irradiance.

In addition, a multiplier called the Bifacial Irradiance Factor (BIF) was introduced, representing the expression in parentheses in Equation (1). The measurement problem focuses on determining the value of G_r itself, and four main approaches are generally used for its determination.

The analytical approach based on GHI, DHI, front-side POA and constant albedo is computationally useful, but it poorly reflects real field conditions. It does not account for local and temporal variability of albedo, the impact of moisture, surface aging, or spatially variable shading, all of which clearly emerged in the study's heatmaps.

The multi-sensor method records rear-side irradiation better, but it remains highly susceptible to non-uniformity of the irradiance field behind the module. Moving shadow

https://doi.org/10.3390/en19112641

zones, the influence of the tracker axis, and structural elements cause point measurements to become unstable and, in addition, they may be affected by spectral mismatch error. The undisturbed rear-side measurement method improves signal stability, but at the cost of representativeness, because it eliminates part of the actual geometric interactions and self-shading effects.

The approach that best reflects reality is the one using a bifacial reference device. Such a module simultaneously incorporates the influence of geometry, shading, albedo variability, and spectral response, and therefore most accurately reproduces the actual energy effect of a bifacial module's operation under field conditions.

The proposed mobile measurement station was built using a method similar to a solution employing a bifacial reference device. By using a dual-input microinverter, variables that are difficult to calculate analytically, including the impact of transverse shadows from the linear actuator axis and noise caused by the surrounding urban infrastructure on gray paving blocks and vegetatio, were fully integrated. In this way, the main errors of pyranometers were eliminated, and the final measurement of electrical power was obtained directly, representing the best possible approximation. The resulting R^2 correlations above 0.98 indicate that the direct electrical comparison provides a stable basis for assessing the relative performance of the tested modules under the analysed conditions.

Discussion of the influence of albedo requires taking dynamic shadows into account. Simplified analytical models usually assume homogeneous reflection of radiation from the ground, whereas field observations have revealed significant deviations from this assumption. For some of the surfaces studied, especially grey paving blocks and grass, external objects such as trees and lampposts cast shadows in the reflection area. As a result, the rear side of the module operated under conditions of a strongly non-uniform irradiance field.

Additional disturbances were introduced by the structural elements of the tracker, primarily the torque tube and cables, which locally limited irradiance in the central part of the module. In HSAT systems, differences in local irradiance between the central and edge zones can reach 20–30%. Due to the series connection of the cells, such non-uniformity leads to current mismatch, a reduction in module power, and activation of the bypass diodes. The results therefore indicate that in bifacial systems over a non-uniform ground surface, the power conversion architecture is of key importance. The use of a microinverter with two independent MPPT channels reduced the impact of mismatch and enabled reliable recording of bifacial gains.

Installations with bifacial modules must consider a greater variability of instantaneous power production than classical standard systems. In conventional PV farm design, it is usually assumed that the DC side is oversized relative to the AC side, expressed by a DC/AC ratio of about 1.20–1.35, which makes it possible to use the inverter more effectively on an annual basis at the cost of occasional clipping under high-irradiance conditions. In the case of bifacial modules, this assumption needs to be revised, because the additional power from the rear side may lead to a significant increase in current and instantaneous power. For a module with a rated power of 400 W operating above bright aggregate, an experimentally confirmed gain of around 11.3% means it is possible to reach approximately 445–450 W. If the inverter is selected according to the standard rules applicable to monofacial installations, part of this additional yield may be lost due to current and power limitations on the AC side. This means that the benefits resulting from the high ground albedo will not be fully utilized. For this reason, the design of bifacial installations requires appropriate selection of inverters in terms of permissible input current, resistance to higher current values, and more cautious selection of the DC/AC ratio.

https://doi.org/10.3390/en19112641

The obtained results have implications for tracker control under clear-sky conditions. The maximum power occurred near a relative solar azimuth of 0°, whereas higher albedo values observed at large azimuth deviations did not coincide with the maximum power output. This confirms that, under the tested clear-sky conditions, maximizing measured albedo alone is not equivalent to maximizing electrical power. Therefore, the rear-side contribution should be treated as an additive gain rather than as a factor shifting the optimal tracker position. The influence of cloudy conditions or a high diffuse-radiation share was not quantified separately in this study. A dedicated "Cloudy vs. Clear Sky" analysis would require long-term measurements for each ground surface under comparable diffuse-radiation conditions and is planned as a continuation of this work.

The obtained results confirm that the bifacial effect under field conditions is determined not only by the properties of the ground itself, but also by the local geometry of the system, the radiation structure, and the environmental conditions. A key conclusion from the discussion is that albedo cannot be treated as a constant and homogeneous parameter, and the rear-side yield of bifacial modules is highly variable in space. This means that simplified models based on constant albedo and point irradiance measurements may lead to interpretative errors. In addition, soil moisture, surface temperature, and cell temperature were not measured directly; therefore, their influence is discussed only as a possible source of uncertainty and not as an independently verified effect.

Potential sources of uncertainty include, above all, the anisotropy of reflection, the limited representativeness of the sensors' field of view, the influence of local shading and structural elements, the variable share of diffuse radiation, spectral mismatch between the sensors and the PV module, and the lack of full control over the influence of temperature on the electrical parameters. An additional limitation of this article is the scale of the test setup, which improves the control of module-to-module comparison but does not fully reproduce farm conditions. However, it is suitable for interpreting phenomena and for analysing the operation of individual (or distant) trackers. Nevertheless, the use of direct comparison not only of albedo but also of power makes the results highly useful, because the comparison conditions in each area are maintained with parameters that are as similar as possible, using the same, rather than a similar, setup.

5. Conclusions

The conducted field experiment and the metrological analysis of the operation of bifacial modules in a SAT configuration indicate that the ground albedo cannot be treated as a constant or spatially homogeneous parameter. Under real operating conditions, the distribution of rear-side irradiance is shaped by local reflection anomalies, dynamic shading, and the influence of the tracker's structural elements, which significantly limits the representativeness of point measurements performed with standard pyranometers. For the grass reference case, the effective albedo varied from approximately 0.15 to 0.30 depending on relative solar azimuth and module tilt, while for a fixed tilt angle of 45° the measured albedo ranged from about 0.10–0.12 for dark aggregate to about 0.31–0.44 for light aggregate. For this reason, the most reliable approach is to use a reference bifacial module, which integrates the effects of system geometry, optical conditions, and local disturbances directly at the level of energy conversion in the cells.

The geometry-dependent albedo distributions obtained in this study do not invalidate simulation approaches based on fixed albedo values. A constant albedo may still be suitable for simplified long-term yield simulations. However, for short-term analyses of bifacial modules operating with a tracking system, it should be treated as an approximation. In such cases, experimentally determined albedo maps can be used to derive effective average albedo values or to validate more detailed view-factor and ray-tracing models.

https://doi.org/10.3390/en19112641

The results obtained for grass-covered ground show that biological surfaces have limited usefulness as a substrate for enhancing the bifacial effect. This is determined both by the spectral properties of vegetation and by its non-uniform reflection geometry, so the actual power gain over natural ground cover remains moderate. In the grass case, the regression between bifacial and monofacial module power showed a very strong linear relationship, with $R^2 = 0.9911$ and a slope of $\alpha = 1.0501$, corresponding to an average bifacial gain of approximately 5.0%. At low power levels, this relative advantage increased to about 6.5%, which indicates a proportionally higher contribution of diffuse and reflected radiation under reduced front-side irradiance. This also means that conventional albedo measurements may, under such conditions, lead to an overestimation of the potential energy yield.

The highest effectiveness was demonstrated by light-colored mineral substrates, which provided the greatest and most stable increase in the power output of the bifacial module. The highest relative gain was obtained for light aggregate, reaching 11.3% compared with the monofacial module, whereas the gain over grass-covered ground was limited to approximately 5.0%. River sand also provided a high bifacial effect, reaching about 9.1%, while dark aggregate showed the weakest response, with a gain of about 3.35%. Their advantage results primarily from a high reflectance coefficient and favorable diffusive properties. The thermal influence of the substrate should be treated as a possible secondary effect, requiring direct temperature measurements in future work. The choice of substrate therefore affects mainly the optical operating conditions of the installation, while its thermal impact should be evaluated with dedicated measurements.

The results also confirm that the maximum instantaneous power is governed primarily by front-side irradiance. For the tested tracker geometry, the power maximum occurred near a relative solar azimuth of 0°, while the highest albedo values observed at large azimuth deviations did not coincide with the maximum power output. Thus, rear-side irradiance acted as an additive contribution to power generation, but it did not shift the geometric optimum of the tracker. This finding is important for tracker control strategies, because it indicates that maximizing the measured albedo alone is not equivalent to maximizing the electrical output of a bifacial module under clear-sky conditions.

A significant limitation remains the power conversion architecture. The additional yield resulting from high albedo may be partially lost due to inverter current limitations, clipping, and mismatch caused by non-uniform rear-side illumination. However, these effects were not isolated quantitatively in the present experiment; therefore, they should be interpreted as design implications rather than as independently measured loss components. In practice, this means the need for a more cautious selection of the DC/AC ratio and the use of solutions that mitigate the effects of mismatch in bifacial systems.

The results obtained indicate that the design and assessment of bifacial installations should be based on a spatially differentiated description of the radiative environment, taking into account the optical, spectral, and environmental properties of the ground. The most relevant quantitative outcome of the study is that the bifacial gain varied substantially with the substrate: from about 3.35–5.0% for low- or moderate-reflectance natural surfaces to about 11.3% for light aggregate. This confirms that the energy benefit of bifacial modules cannot be characterized by a single generic gain value but must be evaluated with respect to the actual ground surface and tracker operating geometry. Only such an approach makes it possible to reliably estimate the actual energy effect and correctly evaluate the cost-effectiveness of bifacial solutions under field conditions.

Author Contributions: Conceptualization, K.B. and M.K.; methodology, M.K.; software, K.B.; validation, A.D., G.J. and K.B.; formal analysis, K.B.; investigation, G.J. and A.D.; resources, G.J.; data curation, A.D.; writing—original draft preparation, K.B.; writing—review and editing, A.D. and G.J.;

https://doi.org/10.3390/en19112641

visualization, K.B.; supervision, M.K.; project administration, M.K.; funding acquisition, K.B. and A.D. All authors have read and agreed to the published version of the manuscript.

Funding: This research received no external funding.

Data Availability Statement: The original contributions presented in this study are included in the article and Appendix A. Further inquiries can be directed to the corresponding author.

Conflicts of Interest: The authors declare no conflicts of interest.

Abbreviations

The following abbreviations are used in this manuscript:

LCOE	Levelized Cost of Electricity
IEA PVPS	International Energy Agency Photovoltaic Power Systems Programme
PV	Photo Voltaic
MPPT	Maximum Power Point Tracking
UAV	Unmanned Aerial Vehicle
HSAT	Horizontal Single-Axis Tracker
POA	Plane of Array
VF	View Factor
RT	Ray Tracking
LDR	Light Dependent Resistor
PLC	Programmable Logic Controller
DC	Direct Current
AC	Alternating Current
DTU	Data Transfer Unit
STC	Standard Test Conditions
BIF	Bifacial Irradiance Factor
GHI	Global Horizontal Irradiance
DHI	Diffuse Horizontal Irradiance
DNI	Direct Normal Irradiance

Appendix A

Views of the measurement sites used for albedo determination on four representative surface types: river sand, grey paver, light aggregate, and dark aggregate; are presented in Figure A1.

The heatmaps presented in Figure A2 illustrate the variation of surface albedo and bifacial module power output as a function of relative solar azimuth and tilt angle for four tested surfaces: river sand, grey paver, light aggregate, and dark aggregate. Measurements were conducted under controlled outdoor conditions, ensuring consistent meteorological parameters comparable solar irradiance throughout the data acquisition period.

The albedo values are presented using a scale adjusted to the range of measured results, as the spatial distribution and variability of surface reflectance are of primary analytical importance. In contrast, the bifacial module power output is shown using a uniform scale (maximum 435 W, minimum 205 W), allowing for a straightforward comparison of energy yield across different surface types.

https://doi.org/10.3390/en19112641

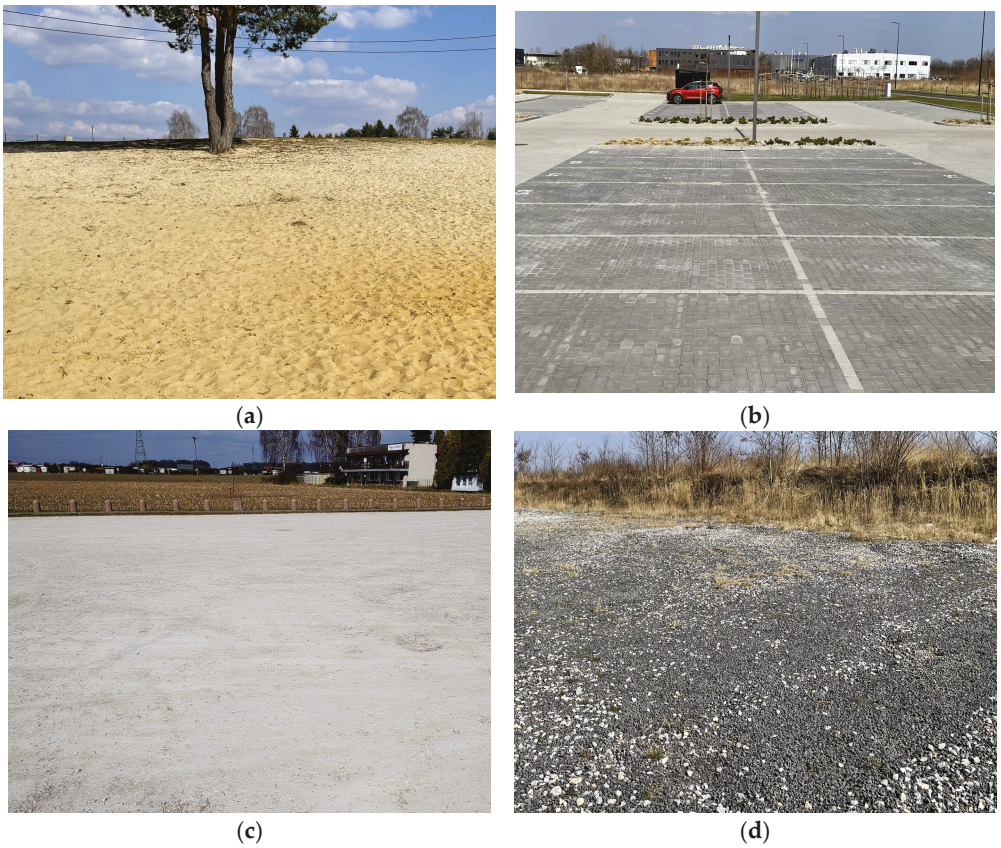

Figure A1. Views of the measurement sites used for albedo measurements on: (**a**) river sand; (**b**) grey paver; (**c**) light aggregate; (**d**) dark aggregate.

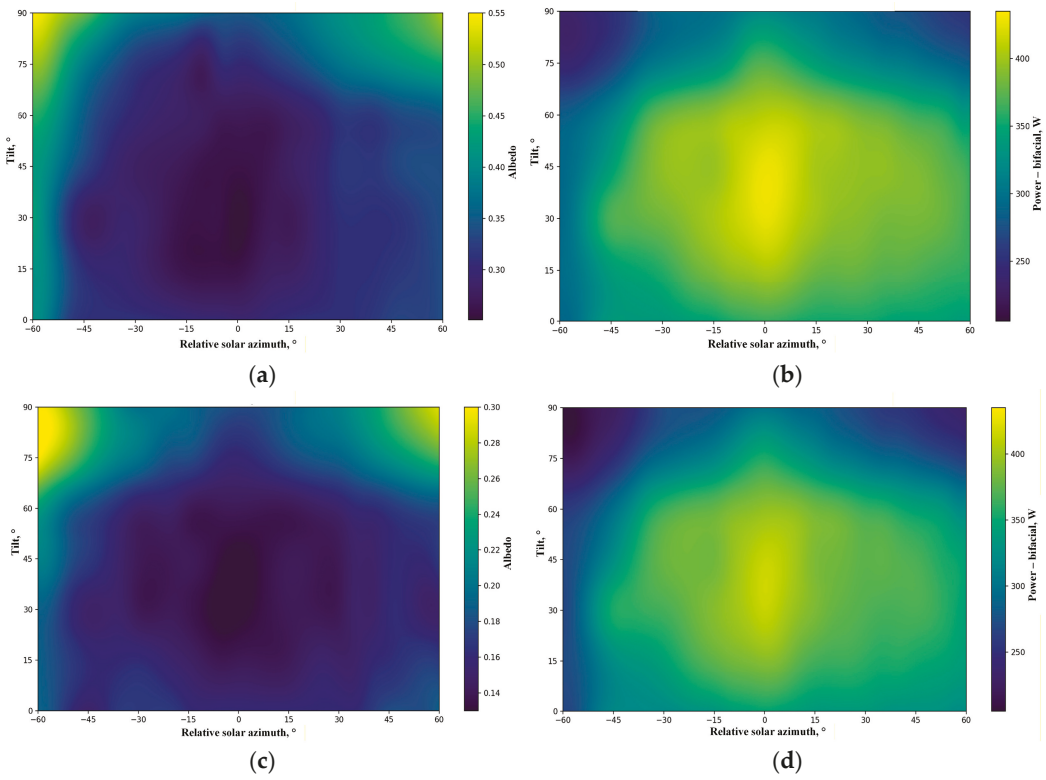

Figure A2. *Cont.*

https://doi.org/10.3390/en19112641

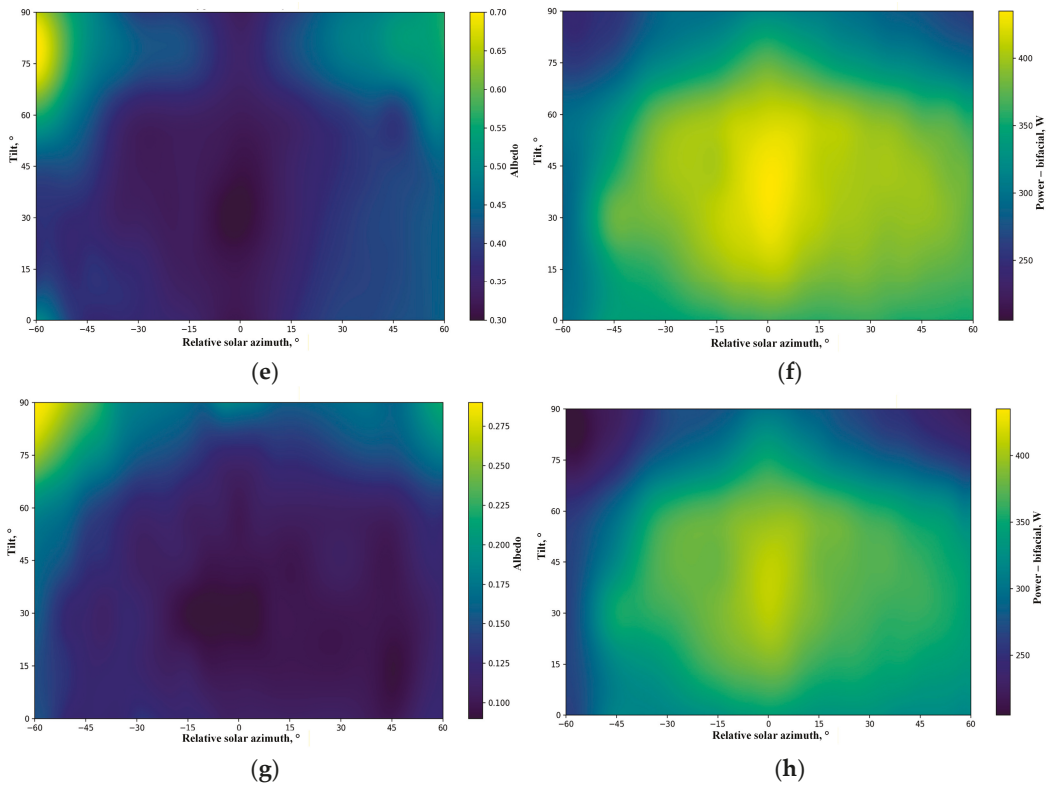

Figure A2. Heatmaps of: (**a**,**b**) albedo and bifacial module power output as functions of relative solar azimuth and tilt angle for river sand; (**c**,**d**) grey paver; (**e**,**f**) light aggregate; and (**g**,**h**) dark aggregate.

Figure A3 presents the relationship between the power output of bifacial and monofacial photovoltaic modules obtained for four surface types: river sand, grey paver, light aggregate, and dark aggregate. The plots illustrate the correlation between measured power values under comparable irradiance and temperature conditions, allowing evaluation of the bifacial gain as a function of surface albedo.

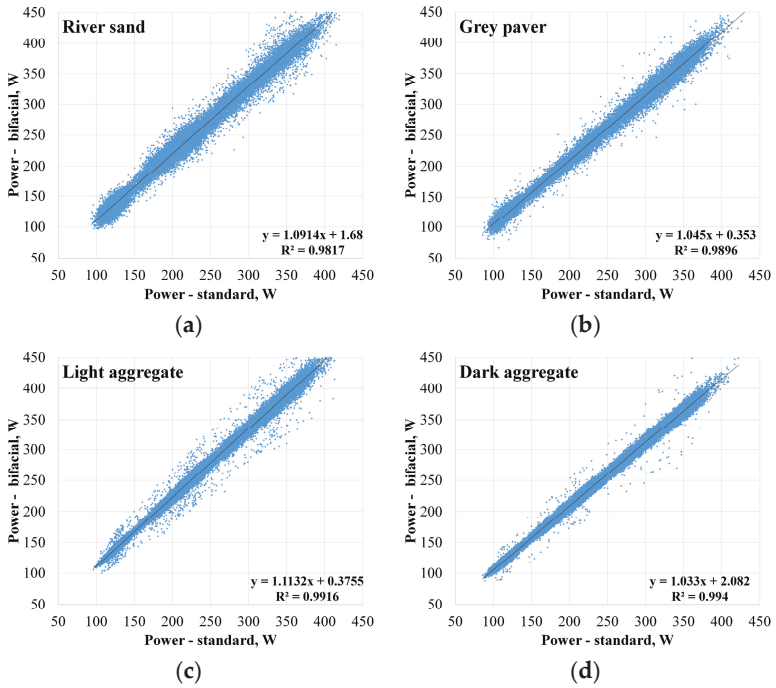

Figure A3. Relationship between bifacial and standard module power output measured on four surface types: (**a**) river sand; (**b**) grey paver; (**c**) light aggregate; and (**d**) dark aggregate.

https://doi.org/10.3390/en19112641

References

1. Guerrero Lemus, R.; Vega, R.; Kim, T.; Kimm, A.; Shephard, L.E. Bifacial solar photovoltaics—A technology review. *Renew. Sustain. Energy Rev.* **2016**, *60*, 1533–1549. [CrossRef]
2. Kopecek, R.; Libal, J. Bifacial Photovoltaics 2021: Status, Opportunities and Challenges. *Energies* **2021**, *14*, 2076. [CrossRef]
3. Rodríguez-Gallegos, C.D.; Liu, H.; Gandhi, O.; Singh, J.P.; Krishnamurthy, V.; Kumar, A.; Stein, J.S.; Wang, S.; Li, L.; Reindl, T.; et al. Global Techno-Economic Performance of Bifacial and Tracking Photovoltaic Systems. *Joule* **2020**, *4*, 1514–1541. [CrossRef]
4. Stein, J.S.; Maugeri, G.; Riedel-Lyngskær, N.; Ovaitt, S.; Müller, T.; Wang, S.; Huerta, H.; Leloux, J.; Vedde, J.; Berwind, M.; et al. *Best Practices for the Optimization of Bifacial Photovoltaic Tracking Systems*; IEA PVPS Task 13, Report IEA-PVPS T13-26:2024; IEA PVPS: Paris, France, 2024. [CrossRef]
5. VDMA. *International Technology Roadmap for Photovoltaic (ITRPV)*, 15th ed.; VDMA: Frankfurt am Main, Germany, 2024.
6. Rodríguez-Gallegos, C.D.; Bieri, M.; Gandhi, O.; Singh, J.P.; Reindl, T.; Panda, S.K. Monofacial vs bifacial Si-based PV modules: Which one is more cost-effective? *Sol. Energy* **2018**, *176*, 412–438. [CrossRef]
7. Stein, J.; Reise, C.; Castro, J.B.; Friesen, G.; Maugeri, G.; Urrejola, E.; Ranta, S. *Bifacial Photovoltaic Modules and Systems: Experience and Results from International Research and Pilot Applications*; IEA PVPS Task 13, Report IEA-PVPS T13-14:2021; IEA PVPS: Paris, France, 2021. [CrossRef]
8. *IEC TS 60904-1-2:2024*; Photovoltaic Devices—Part 1–2: Measurement of Current-Voltage Characteristics of Single-Junction Bifacial Photovoltaic Devices. International Electrotechnical Commission (IEC): Geneva, Switzerland, 2024.
9. *IEC 61853-1*; Photovoltaic (PV) Module Performance Testing and Energy Rating—Part 1: Irradiance and Temperature Performance Measurements and Power Rating. International Electrotechnical Commission (IEC): Geneva, Switzerland, 2011.
10. Vogt, M.R.; Pilis, G.; Zeman, M.; Santbergen, R.; Isabella, O. Developing an energy rating for bifacial photovoltaic modules. *Prog. Photovolt. Res. Appl.* **2023**, *31*, 1466–1477. [CrossRef]
11. Muñoz-Cerón, E.; Moreno-Buesa, S.; Leloux, J.; Aguilera, J.; Moser, D. Evaluation of the bifaciality coefficient of bifacial photovoltaic modules under real operating conditions. *J. Clean. Prod.* **2024**, *434*, 139807. [CrossRef]
12. Pike, C.; Whitney, E.; Wilber, M.; Stein, J.S. Field Performance of South-Facing and East-West Facing Bifacial Modules in the Arctic. *Energies* **2021**, *14*, 1210. [CrossRef]
13. Marion, B. Albedo Data Sets for Bifacial PV Systems. In Proceedings of the 2020 IEEE 47th Photovoltaic Specialists Conference (PVSC), Calgary, AB, Canada, 15 June–21 August 2020. [CrossRef]
14. Marion, B. Measured and satellite-derived albedo data for estimating bifacial photovoltaic system performance. *Sol. Energy* **2021**, *215*, 321–327. [CrossRef]
15. Merodio, P.; Martínez-Moreno, F.; Moretón, R.; Lorenzo, E. Albedo measurements and energy yield estimation uncertainty for bifacial photovoltaic systems. *Prog. Photovolt. Res. Appl.* **2023**, *31*, 1130–1143. [CrossRef]
16. Schaaf, C.; Wang, Z. *MCD43A1 MODIS/Terra+Aqua BRDF/Albedo Model Parameters Daily L3 Global—500 m V006 [Data Set]*; NASA EOSDIS Land Processes DAAC; NASA: Washington, DC, USA, 2015. [CrossRef]
17. Gostein, M.; Ayala Peláez, S.; Deline, C.; Habte, A.; Hansen, C.W.; Marion, B.; Newmiller, J.; Sengupta, M.; Stein, J.S.; Suez, I. Measuring Irradiance for Bifacial PV Systems. In *Proceedings of the 2021 IEEE 48th Photovoltaic Specialists Conference (PVSC), Fort Lauderdale, FL, USA, 20–25 June 2021*; IEEE: New York, NY, USA, 2021; pp. 896–903. [CrossRef]
18. Cao, C.; Lee, X.; Muhlhausen, J.; Bonneau, L.; Xu, J. Measuring landscape albedo using unmanned aerial vehicles. *Remote Sens.* **2018**, *10*, 1812. [CrossRef]
19. Canisius, F.; Wang, S.; Croft, H.; Leblanc, S.G.; Russell, H.A.; Chen, J.; Wang, R. A UAV-based sensor system for measuring land surface albedo: Tested over a boreal peatland ecosystem. *Drones* **2019**, *3*, 27. [CrossRef]
20. Bartmiński, P.; Siłuch, M. Mapping the albedo of the active surface at different stages of the growing season using data from various sources. *Remote Sens. Appl. Soc. Environ.* **2022**, *28*, 100818. [CrossRef]
21. Ayala Peláez, S.; Deline, C.; Greenberg, P.; Stein, J.S.; Kostuk, R.K. Model and Validation of Single-Axis Tracking with Bifacial PV. *IEEE J. Photovolt.* **2019**, *9*, 715–721. [CrossRef]
22. Schneider, D. Control Algorithms for Large-scale Single-axis Photovoltaic Trackers. *Acta Polytech.* **2012**, *52*, 86–92. [CrossRef]
23. Anderson, K.; Mikofski, M. *Slope-Aware Backtracking for Single-Axis Trackers*; NREL/TP-5K00-76626; National Renewable Energy Laboratory: Golden, CO, USA, 2020. [CrossRef]
24. Keiner, D.; Walter, L.; ElSayed, M.; Breyer, C. Impact of backtracking strategies on techno-economics of horizontal single-axis tracking solar photovoltaic power plants. *Sol. Energy* **2024**, *267*, 112228. [CrossRef]
25. Santos de Araújo, J.V.; de Lucena, M.P.; da Silva Netto, A.V.; Gomes, F.D.S.V.; Oliveira, K.C.D.; de Souza Neto, J.M.R.; Cavalcante, S.L.; Morales, L.R.V.; Villanueva, J.M.M.; Macedo, E.C.T.D. Solar Tracking Control Algorithm Based on Artificial Intelligence Applied to Large-Scale Bifacial Photovoltaic Power Plants. *Sensors* **2024**, *24*, 3890. [CrossRef]
26. Ayala Peláez, S.; Deline, C.; MacAlpine, S.M.; Marion, B.; Stein, J.S.; Kostuk, R.K. Comparison of Bifacial Solar Irradiance Model Predictions with Field Validation. *IEEE J. Photovolt.* **2019**, *9*, 82–88. [CrossRef]

https://doi.org/10.3390/en19112641

27. Nussbaumer, H.; Janssen, G.; Berrian, D.; Wittmer, B.; Klenk, M.; Baumann, T.; Baumgartner, F.; Morf, M.; Burgers, A.; Libal, J.; et al. Accuracy of simulated data for bifacial systems with varying tilt angles and share of diffuse radiation. *Sol. Energy* **2020**, *197*, 6–21. [CrossRef]
28. Riedel-Lyngskær, N.; Berrian, D.; Alvarez Mira, D.; Aguilar Protti, A.; Poulsen, P.B.; Libal, J.; Vedde, J. Validation of Bifacial Photovoltaic Simulation Software against Monitoring Data from Large-Scale Single-Axis Trackers and Fixed Tilt Systems in Denmark. *Appl. Sci.* **2020**, *10*, 8487. [CrossRef]
29. Ayala Peláez, S.; Deline, C. bifacial_radiance: A python package for modeling bifacial solar photovoltaic systems. *J. Open Source Softw.* **2020**, *5*, 1865. [CrossRef]
30. Russell, A.C.J.; Valdivia, C.E.; Bohémier, C.; Haysom, J.E.; Hinzer, K. DUET: A Novel Energy Yield Model with 3-D Shading for Bifacial Photovoltaic Systems. *IEEE J. Photovolt.* **2022**, *12*, 1576–1585. [CrossRef]
31. Ayala Peláez, S.; Deline, C.; Stein, J.S.; Marion, B.; Anderson, K.; Muller, M. Effect of Torque-Tube Parameters on Rear-Irradiance and Rear-Shading Loss for Bifacial PV Performance on Single-Axis Tracking Systems. In *Proceedings of the 2019 IEEE 46th Photovoltaic Specialists Conference (PVSC), Chicago, IL, USA, 16–21 June 2019*; IEEE: New York, NY, USA, 2020; pp. 1–6. [CrossRef]
32. Coathup, T.J.; Lewis, M.R.; Russell, A.C.J.; Haysom, J.E.; Valdivia, C.E.; Hinzer, K. Impact of torque tube reflection on bifacial photovoltaic single axis tracked system performance. *Opt. Express* **2023**, *31*, 6143–6155. [CrossRef] [PubMed]
33. Hossain, M.I.; Chelvanathan, P.; Khandakar, A.; Thomas, K.; Rahman, A.; Mansour, S. Enhanced efficiency of bifacial perovskite solar cells using computational study. *Sci. Rep.* **2024**, *14*, 12984. [CrossRef] [PubMed]
34. Hoymiles Corporate Website. Available online: https://www.hoymiles.com (accessed on 27 March 2026).
35. Jolywood Corporate Website. Available online: https://www.jolywood.cn/en (accessed on 27 March 2026).
36. *IEC 61724-1*; Photovoltaic System Performance—Part 1: Monitoring. International Electrotechnical Commission (IEC): Geneva, Switzerland, 2017.

Disclaimer/Publisher's Note: The statements, opinions and data contained in all publications are solely those of the individual author(s) and contributor(s) and not of MDPI and/or the editor(s). MDPI and/or the editor(s) disclaim responsibility for any injury to people or property resulting from any ideas, methods, instructions or products referred to in the content.

https://doi.org/10.3390/en19112641

MDPI AG
Grosspeteranlage 5
4052 Basel
Switzerland
Tel.: +41 61 683 77 34

Energies Editorial Office
E-mail: energies@mdpi.com
www.mdpi.com/journal/energies



Disclaimer/Publisher's Note: The title and front matter of this reprint are at the discretion of the Guest Editors. The publisher is not responsible for their content or any associated concerns. The statements, opinions and data contained in all individual articles are solely those of the individual Editors and contributors and not of MDPI. MDPI disclaims responsibility for any injury to people or property resulting from any ideas, methods, instructions or products referred to in the content.





Academic Open
Access Publishing

mdpi.com

ISBN 978-3-7258-8708-8